Expansion of Cerebellar Neuron Diversity

François Grégory Claude Blot

Expansion of Cerebellar Neuron Diversity

Expansie van de diversiteit van cerebellaire neuronen

Proefschrift

ter verkrijging van de graad van doctor aan de
Erasmus Universiteit Rotterdam
op gezag van de
rector magnificus

Prof.dr. F.A. van der Duijn Schouten

en volgens besluit van het College voor Promoties.

De openbare verdediging zal plaatsvinden op

woensdag 21 april 2021 om 13.00 uur

door

François, Grégory, Claude Blot
geboren te Saint-Malo, Frankrijk.

Erasmus University Rotterdam

Promotiecommissie:

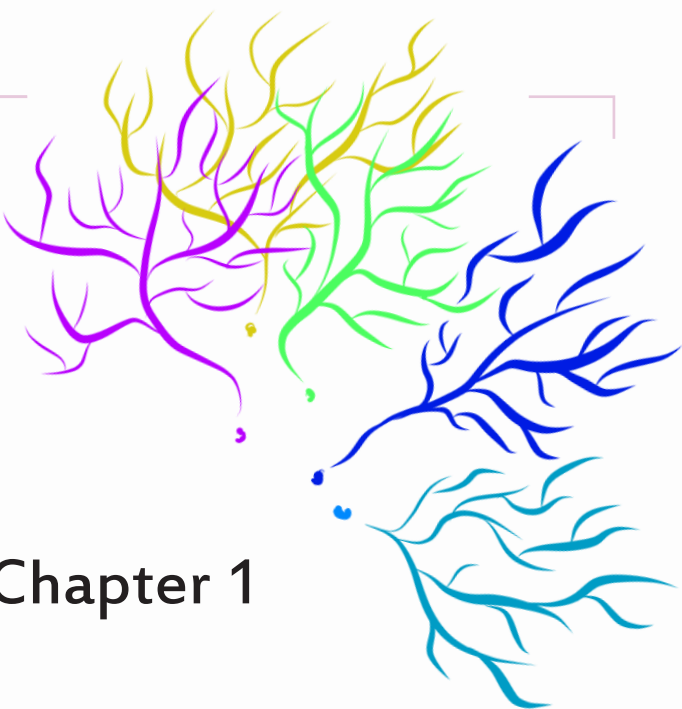|	
Promotor:	prof. dr. C.I. de Zeeuw

Overige leden: prof. dr. F.E. Hoebeek
dr. Z. Gao
dr. M.T. Mulder

Copromotor: drs. M. Schonewille

À mes parents, mon frère,
et Gibson

Contents

Chapter 1

Introduction

In 2003, Bota *et al.* (1) estimated the average neuronal diversity of a human brain at five neuron types per brain region, which based on 500 to 1 000 brain structures resulted in a crude assessment of 2 500 to 5 000 neuronal types in the entire brain. Assuming one type of neuron projects to 10-20 different types of neuron, they ended up with a range of 25 000 to 100 000 potential intertype connections to illustrate the diversity of neuronal networks. These approximations were based on the very first morphological descriptions of cerebellar and retinal neurons by Cajal (2) that have reached consensus through decades of anatomical studies. Still, neuronal diversity is largely underestimated due to two methodological biases illustrated by Bordal *et al.*: extrapolation and classification. The cytoarchitecture of a continuous brain structure is commonly extrapolated from the detailed characterization of one or a few restricted parts of it and not from a refined analysis of the structure in its integrity. As a result of these extrapolations, current anatomical descriptions omit local specificities. The classification is the essential issue as the definition of neuronal types and subtypes can be arbitrary and vary depending on the measured parameter. Then, the question remains: what is the full extent of neuronal diversity?

Seemingly identical cells are commonly clustered together based on one or several biological features. Morphology, spatial distribution and basic biochemical properties were historically the first parameters used to define types and subtypes of neurons. The identification of distinct molecular features (immunohistology), connections (tracing) and biophysical properties (electrophysiology) came later to consolidate the already defined groups and to subdivide neuron types into numerous subtypes. While the inconsistencies of experimental measures among types and subtypes were often reduced to biological noise or experimental artefacts, the biological relevance of the cell-to-cell variability recently emerged (3) with the development of new tools and methods of higher resolution and better accuracy. As examples, single cell RNA sequencing recently allowed to characterize new neuronal subtypes (4–6), while new genetic construct and tracing tools allowed to discriminate new neuronal pathways (7). Such studies imply that we have been underestimating the range of discrete networks, and question our current models regarding brain processing (8, 9).

The work presented in this thesis illustrates the extent of the neuronal diversity which fits two attributes: **non-homogeneous** and **non-random**. First, "non-homogeneous" stresses the large diversity of cell types, subtypes and single cell properties. Second, "non-random" highlight the integration of such diversity in specific networks that ultimately shine light on the biological relevance of even the most subtle nuances. The cerebellum offers an ideal

playground to uncover the extend and the role of neuronal diversity as it is the most densely populated brain structure while being one of the most organized. The major functions of the cerebellum in sensory integration and motor functions make it the optimal tool to study brain circuits. In its most simplistic depiction, the cerebellum is a multilaminar structure composed of the molecular layer (ML), the Purkinje cell layer (PCL), the granular cell layer (GCL) and the white matter (WM). Seven major types of neurons are distributed through the width of the cortex: basket (BC) and stellate (SC) cell (or molecular layer interneurons: MLI), Purkinje cell (PC), Golgi cell (GoC), Lugaro cell (LC), unipolar Brush cell (UBC), granule cell (GC). The cerebellum is commonly described in the field as an assemble of parallel microcircuits, or modules (10). The first portrayal of the compartmentalized cytoarchitecture of the cerebellum is attributed to Brodal and his work on the organized olivo-cerebellar connectivity in cat (11), in 1940. My current level in German did not allow me to go further backwards in the literature, but some translated sections referred to a work from the early twentieth century on the organized distribution of olivary projections. Following this work, the organization of the cortico-nuclear projections was quickly added to the modular map (12). Two decades later the first description of parasagittal domains based on molecular expression pattern in the cerebellar cortex was made (13). The parasagittal distribution of afferent olivary fibers, molecular compartmentalization of Purkinje cell in the cortex, and segregated downstream cerebellar nuclei targets gave rise to the first definition of the cerebellar modules. Piece by piece, experimental evidence brought to light the inter- as well as intra-modular diversity. However, the extend of network heterogeneity is largely underestimated and overlooked in the current models of cerebellar processing (14). While the range of functionalities we attribute to the cerebellum is still growing, it becomes essential to assess the full extent of cerebellar neurons diversity, and the functional relevance that can be attributed to a multitude of discrete and diverse parallel networks. Below I will analyze the mosaic of neuronal diversity stratum by stratum:

White matter

Often forgotten in the recent literature, studies of the cerebellar white matter were among the first to show regional differences. Voogd observed parasagittal compartments of fibers in the cat cerebellar white matter already back in 1964 (15). This was later observed in mouse (16) and chicken (17), defining the only known atlas of compartmentalized myeloarchitecture (18).

These domains defined by fibers density and diameter reflect diversity of PCs and myelination. In addition, evidences of a local microcircuit hidden in the cerebellar white matter emerged. Thomas Langer identified in 1985 a sparse neuronal population nested in the core of the cerebellar white matter of the flocculus, hereon named the Basal Interstitial Nucleus (BIN) of the Cerebellum (19) (**Fig. 1A-B**). Neglected for decades, this cell type represents a unique local cerebellar structure as it receives glutamatergic input from the gigantocellular reticular nuclei (Fig. 1C) and projects massively to the floccular cortex, acting directly on glomeruli (this thesis). This uncharacterized circuit shows how local cytoarchitecture can hide unknown neuronal types.
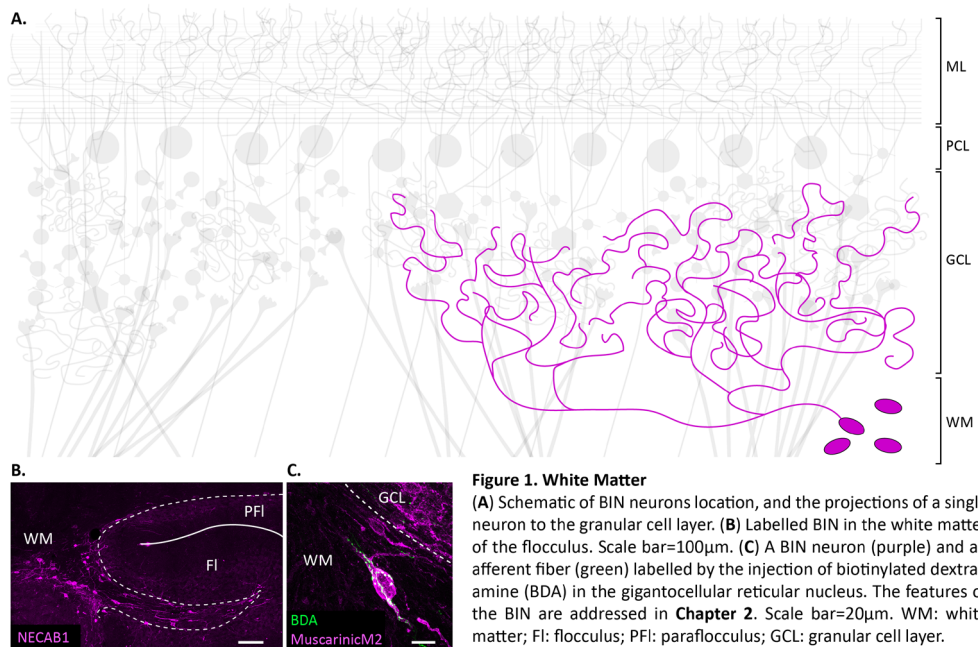

Figure 1. White Matter
(**A**) Schematic of BIN neurons location, and the projections of a single neuron to the granular cell layer. (**B**) Labelled BIN in the white matter of the flocculus. Scale bar=100µm. (**C**) A BIN neuron (purple) and an afferent fiber (green) labelled by the injection of biotinylated dextran amine (BDA) in the gigantocellular reticular nucleus. The features of the BIN are addressed in **Chapter 2**. Scale bar=20µm. WM: white matter; Fl: flocculus; PFl: paraflocculus; GCL: granular cell layer.

Granular Cell Layer

<u>Mossy Fibers</u>:

MFs are easily identified by their characteristic "rosette" shape and represent the major sensory-motor input to the cerebellum. The MF terminals contact granule cell dendrites to form a glomerulus (Fig. 2B). Decades of neuronal tracing using wide range of technics (BDA, CtB, HRP, AAV, Rabies) allowed to list all main projections to the cerebellar cortex. The distribution of these inputs between lobules gave rise to the first subdivision of the cerebellar cortex: vestibulocerebellum, spinocerebellum, cerebrocerebellum (20). The
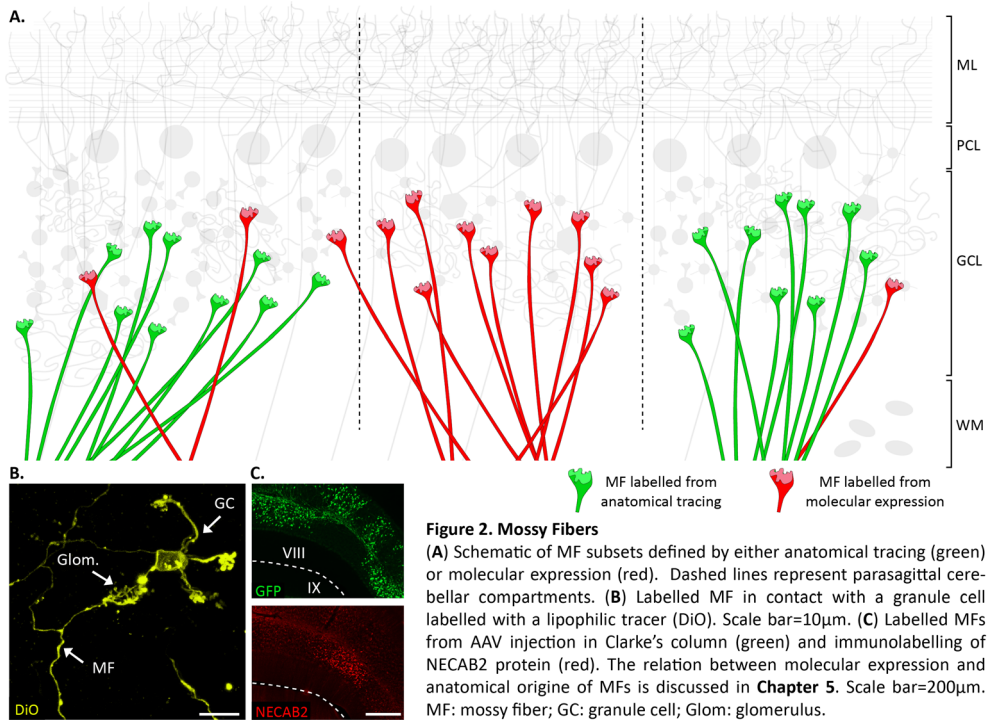
Figure 2. Mossy Fibers
(**A**) Schematic of MF subsets defined by either anatomical tracing (green) or molecular expression (red). Dashed lines represent parasagittal cerebellar compartments. (**B**) Labelled MF in contact with a granule cell labelled with a lipophilic tracer (DiO). Scale bar=10µm. (**C**) Labelled MFs from AAV injection in Clarke's column (green) and immunolabelling of NECAB2 protein (red). The relation between molecular expression and anatomical origine of MFs is discussed in **Chapter 5**. Scale bar=200µm. MF: mossy fiber; GC: granule cell; Glom: glomerulus.

vestibulocerebellum, established as the oldest part of the cerebellum, is defined as the regions receiving massive primary and secondary vestibular MFs. These MFs are projecting mainly to the flocculonodular lobules of the cerebellum to transduce the information essential for vestibular adaptation, from eye movement to postural balance. The spinocerebellum encompasses all territories receiving MFs originating in the spinal cord. Converging mainly to the vermis, it drives a large range of adaptive motor process (locomotion, limb movement, visuo-motor). The cerebrocerebellum, also known as neocerebellum, represents the most recent addition to the cerebellum from the evolutionary standpoint, as it receives input from the cerebrum via the pontine nuclei. These MFs end in the hemispheres, assumed to be the center of the higher cognitive functions of the cerebellum. Refined anatomical studies showed that this map is only a superficial description of MF afferents as, within lobules, MF territories draw parasagittal compartments (21).

Early investigations of choline acetyltransferase, glutamatergic vesicular transporters 1 and 2, somatostatin and calretinin expression showed that MFs can also be classified in subtypes based on their molecular signature (Chat (22), VGluT1/2 (23), SST28 (24)). Such molecular features could be decisive for MF neuronal transmission and grant unique properties to each subtype. As example, expression of VGluT1 or VGluT2 relates

to release probability (25) and synaptic plasticity (26). So far, none of the molecular profiles have been directly linked to distinct MF synaptic properties. However, the diversity of synaptic signatures among MFs was demonstrated by Chabrol *et al.* (27), who discriminated five groups of MF inputs in the lobule X. Interestingly these five modalities originate from only three distinct brain regions: the Scarpa's ganglion, the medial vestibular nucleus, and the prepositus hypoglossi, demonstrating the diversity hidden in a single anatomical class of MFs.

The terminal fields of MF sub-populations defined by either neuronal tracing or molecular features relate to the cerebellar compartments drawn by the PC subtypes (**Fig. 2A and C**). However, the topographical distributions do not perfectly overlap as a MF territory can span over multiple PC modules. The exact relation existing between these two distributions remains unclear.
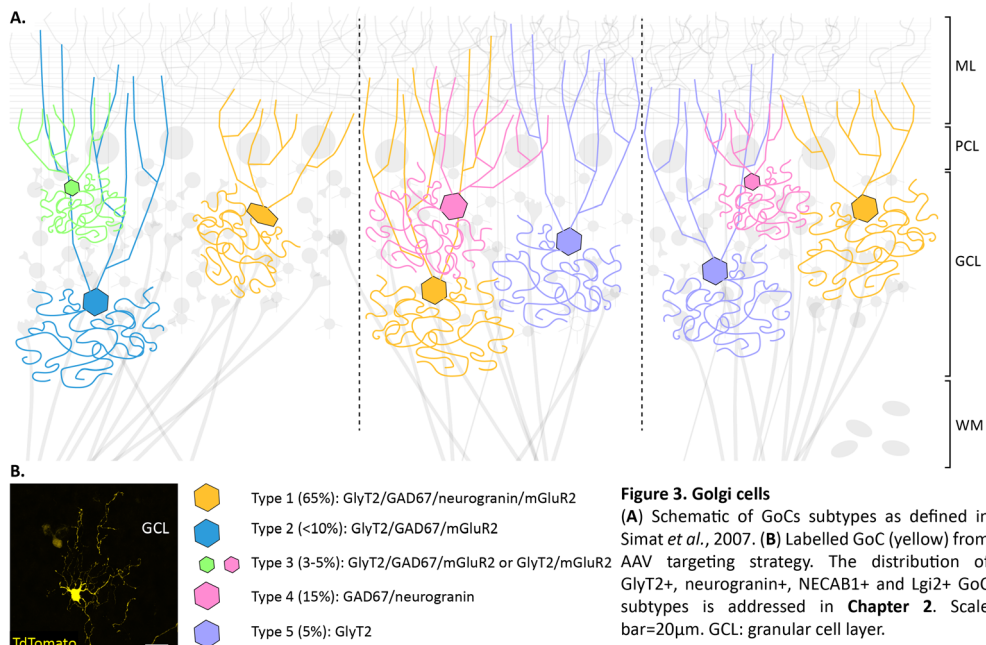
Golgi cells:

Golgi cells (GoC) are a dense population of inhibitory interneurons of various size and shape in the cerebellar cortex: circular, fusiform or polygonal. As a source of inhibitory feedback, they are contacted by the granule cells in the molecular layer and project back onto the glomeruli in the granular cell layer. Camillo Golgi was the first to point out the plurality of such inhibitory interneurons (28), which still holds today as the term "Golgi cell" encompasses a multitude of subtypes either GABA/Glycinergic, GABAergic only, or glycinergic only. The expression of mGluR2 and mGluR5 was found to discriminate the two major non-overlapping populations of GoCs representing respectively 90% and 10% of GoCs (29). Immunoreactivity for mGluR2, neurogranin, Gad67, GlyT2, muscarinic M2, together with morphological distinctions, raised the current classification to at least five GoC subtypes (30–32) (**Fig. 3**). The range and nature of GoC subtypes have always been heavily debated due to this panel of neurochemical and morphological signatures (33). Meanwhile, the relevance of this diversity at a network level has been illustrated in Ankri *et al.*(34), in which authors showed that neurogranin-positive spontaneously active GoC population is the primary target of inhibitory nucleo-cortical projections. Therefore, "type 4" GoCs (30) represent a unique route of inhibitory control of the glomeruli from the cerebellar nuclei.

The intra- and inter-lobule distribution of GoCs is relatively ambiguous. Despite the known heterogeneity, no extensive map of subtypes distribution has been established as of today. The cartography of ChaT-positive, mGluR2, mGluR5 and muscarinicM2-positive Golgi cells along

the cerebellar cortex was initiated in rat, rabbit and human (22, 29, 35, 36). Geurts *et al.* (37) used morphometrical measures to distinguish vermal and hemispheric GoC subtypes. These maps established the distribution across lobules, or vermis/hemispheres distinctions, but nothing is known regarding variable distribution across parasagittal modules. The only known correlation between GoCs and parasagittal compartments is the restriction of GoC dendrites to the boundaries defined by PC subtypes (38). The unresolved cartography of GoC questions whether they are disconnected or anchored to the parasagittal compartmentalization.

Lugaro cells, Globular cells, and other inhibitory interneurons representative of the diversity of GCL remain a neglected aspect of the cerebellar cytoarchitecture. Although, one can assume a certain subtype diversity (37) and subtle organization along the cortex.

A.

ML

PCL

GCL

WM

B.

GCL

TdTomato

Type 1 (65%): GlyT2/GAD67/neurogranin/mGluR2

Type 2 (<10%): GlyT2/GAD67/mGluR2

Type 3 (3-5%): GlyT2/GAD67/mGluR2 or GlyT2/mGluR2

Type 4 (15%): GAD67/neurogranin

Type 5 (5%): GlyT2

Figure 3. Golgi cells
(**A**) Schematic of GoCs subtypes as defined in Simat *et al.*, 2007. (**B**) Labelled GoC (yellow) from GlyT2+ AAV targeting strategy. The distribution of GlyT2+, neurogranin+, NECAB1+ and Lgi2+ GoC subtypes is addressed in **Chapter 2**. Scale bar=20µm. GCL: granular cell layer.

<u>Unipolar Brush Cells</u>:

Sole excitatory interneurons of the cerebellar cortex, UBCs gain their name from the brush-like structure of their primary dendrite (**Fig. 4B**). They receive a unique extrinsic MF input, and project to multiple local granule cell and other UBCs via a rosette-like terminal defined as intrinsic MF (39). Morphologically uniform, UBCs can be distinguished in four subtypes based on the chemical signatures: Calr.+/PLCβ4-, PLCβ4+/mGluR1α+, PLCβ4+/

Calr.-/mGluR1α-, and Calr.+/PLCβ4+/mGluR1α- (40–42). However, UBCs are commonly resumed to only two subtypes. It was proposed that 30% of all UBCs are inhibited in response to glutamatergic input, labeling them as OFF-UBCs, putative Calr+ cells (43). In contrast, 70% of all UBCs are excited in response to glutamatergic input, labeling them as ON-UBCs, putative mGluR1α+ cells. These characteristic responses would result from distinct intrinsic biophysical properties (44), synaptic elements (mGluR1α mediated current), and possibly from the profile of their respective MF input (27). UBC subtypes have been associated to discreet networks as primary vestibular input selectively target mGluR1 α+/Calr.-/ON-UBCs while secondary vestibular input contact both ON- and OFF-UBCs (45, 46). Supposedly this unique pathway would converge to granule cells receiving secondary vestibular MF input to amplify the signal from the vestibular organ largely diluted in the massive multisensory integrated signal from the vestibular nuclei.

UBCs are, after PCs, the best example of a non-random neuronal distribution throughout the cerebellar cortex. Unevenly distributed between lobules, rich UBC domains appeared to match with the density of vestibular input received. More importantly, the intra-lobule distribution follows the modular organization defined by PC subtypes (**Fig. 4**). This topography has been clearly established in the vermis of lobule IX and X, but remains elusive in other part of the cerebellum such as the flocculus (47). The relative distribution of individual four subtypes remains although clearly unresolved.

Figure 4. Unipolar Brush cells
(**A**) Schematic of UBCs subtypes distribution as observed in the lobule IX by Chung et al., 2009. The distribution do not account for the co-expression of these markers. (**B**) Labelled UBC from PLCβ4 immunostaining. Scale bar=5μm. (**C**) Distribution of PLCβ4+ UBCs in the flocculus, in respect to the domains 9+ and 9- defined by KCTD12 expression. The composition of floccular domains is addressed in **Chapter 5**.

Granule cells 1/2 - from MF to GC:

Small circular neurons, a GC presents 3 to 5 dendrites each receiving one mossy fiber rosette to form a glomerulus (48) (**Fig. 2B**). The number of cerebellar GCs in an adult human brain is estimated at 50 billion, representing by itself 75% of the entire neuronal population in the central nervous system (CNS). Despite a general assumption that GCs are all strictly identical, morphological diversity among GCs is known. Only 60% of GCs present an axon originating from their soma (axo-somatic), while for 40% of GCs the axon originates from a dendrite (axo-dendritic) (48, 49) (**Fig. 5**). Morphology is not the only feature that hints at GCs diversity. GCs molecular heterogeneity can be seen in adult cerebellum with nitric oxide synthase staining (50), Otx1 and 2 immunostainings (51), and transgenic reporter expression (52). It is mainly through their distinct clonal origins and the transient expression of cadherins, protocadherins (53) and ephrins during cerebellar development that we can grasp the diversity of GCs. The morphological and molecular plurality of GCs questioned the canonical conception of GC electrophysiological properties. While some defined them as electrotonically compact with no dendritic filtering due to their short dendrites (~15um)(49), others suggest that axo-dendritic and axo-somatic morphological specificities influence signal integration (48). This suggests a certain diversity in GC properties. Recent experimental evidences discriminated GCs on their excitability, describing adaptive (66.7%), non-adaptive 20.6%) and accelerating (12.7%) responses to long term current injections (2sec) (54). They showed that accelerating GC response is associated to TRPM4 current, which demonstrate that some features might not be shared by all GCs. However, as the TRPM4 expression pattern remained insufficiently described, it is unclear which molecular processes are driving this electrophysiological behavior in a specific subset of GCs.

The spatial organization of GC subtypes in relation to other cortical compartments is evident during development through the alignment of GCs stream of migration from the external granular cell layer (EGL) to the internal granular cell layer (IGL) (also known as "raphes") with the compartments defined by PC subtypes (53, 55). In adult cerebella, the nitric oxide synthase immunostaining revealed clusters that correlate to PC compartments. The distribution of morphological subtypes remains unknown. Up until now, the concept of GCs heterogeneity is not considered in models of cortical integration of sensory input.

Molecular Layer

Granule cells 2/2 - from GC to PC:

GC's axon is composed of an ascending part and a segment running transversally below the surface of the cerebellum, called the parallel fiber (PF). The synapses located on the ascending segment were described as the ones with the highest probability of vesicle release along the GC's axon (56, 57), which explains that stimulation of a patch of GCs essentially affects PCs directly above (58). Yet, the PF remains the segment with the highest number of synapses. Spreading up to 3 mm along the cortex in mice (59), the parallel fiber present synapses assumed to be randomly distributed with an average of 1 bouton every 4 µm (57). As the width of PC dendritic tree is of 7µm in coronal plan, a single PF would make 1 to 2 synaptic contact(s) with a PC. However, no studies established the level of organization in the distribution of synapses along the parallel fiber, or the proportion of PF-PC synapses compared to PF-MLI synapses. While little is known about PF-synapses distribution from the anatomical point of view, physiological studies point toward an underlying regional organization of PF output. Stimulation of GC patches results in two distinct effects, 1) the excitation of the overlying PC region, 2) the inhibition of distinct regions of PCs distributed along the PF (60, 61). The recent study from Valera *et al.* (62) was one of the first to overlay the distant activated groups with the known PC molecular subtypes. Similar observations were done *in vivo* where PF stimulation resulted in parasagittal patches of inhibition (63) assumed to match with PC compartments. Synapses distribution, post-synaptic targets, strength of the synapses, all could be in play to explain the domain specific PC response.

A certain heterogeneity can be observed in regards to the PF itself. GC time of birth and clonal origin relate to PF features as early born GCs will project their PF in the deeper part of the ML, closer to PCs, while late born GCs will project more to the surface of the ML. The PFs of the upper layer present a smaller diameter than deep PF, resulting in a gradient of PF thickness (**Fig. 5A**). As a non-myelinated axon, the result of the diameter variability on action potential propagation has been questioned (48). Model predictions established that PF diameter variability is too small to have a measurable effect. However, the existence of myelinated PF in the deepest part of the ML in some species (cat, marmoset and macaque), suggest that PF features have an impact on propagation speed (64). This demonstrates a complex radial and longitudinal organization of PFs and their synapses. At a time in which the importance of cerebellar granule cell in cognitive function is

advocated (64), it is essential to highlight the heterogeneity of this population and detail how they relate to signal integration.
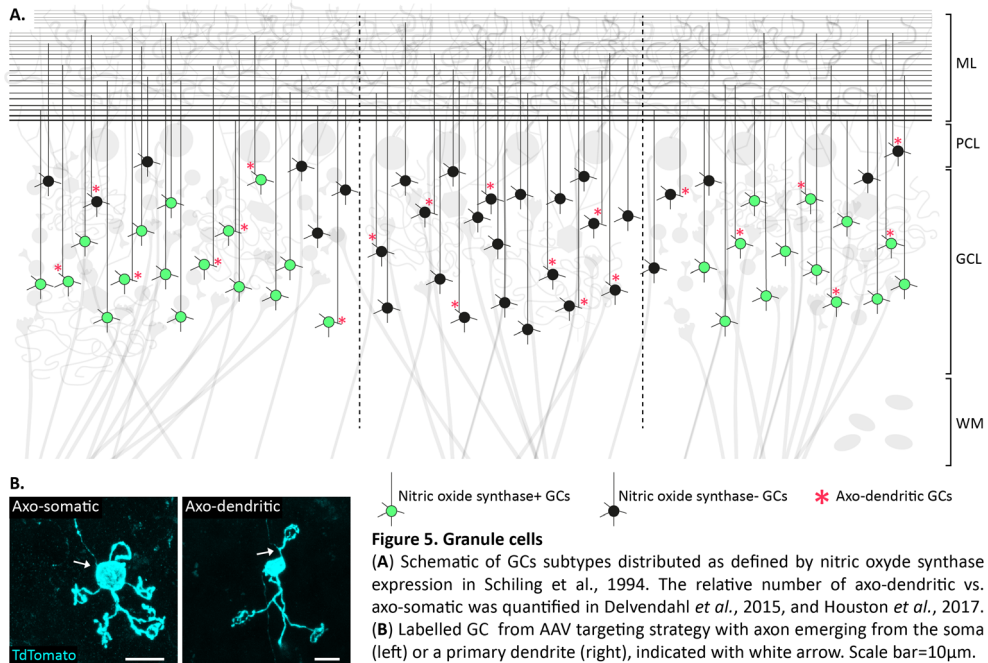

Figure 5. Granule cells
(**A**) Schematic of GCs subtypes distributed as defined by nitric oxyde synthase expression in Schiling et al., 1994. The relative number of axo-dendritic vs. axo-somatic was quantified in Delvendahl *et al.*, 2015, and Houston *et al.*, 2017. (**B**) Labelled GC from AAV targeting strategy with axon emerging from the soma (left) or a primary dendrite (right), indicated with white arrow. Scale bar=10µm.

Molecular Layer Interneurons:

Basket (BC) and Stellate (SC) cells are the two types of inhibitory interneurons found in the molecular layer of the cerebellum. Both are contacted by the parallel fiber and project to multiple PCs distributed along the sagittal plan. The main distinctions between these two cell types are their respective axonal morphology and synaptic structure. BC terminals have a characteristic "pinceau" (brush) shape that enwraps the PC axon initial segment. SC axons disperse in the molecular layer, primarily in the sagittal plane, and contact the distal domain of PC dendrites. A radial distribution of both types was observed as BC populate the lower third of the molecular layer while SC populate the upper two-third (65). The sagittal compartmentalization of their axonal processes hinted toward the alignment with cerebellar modules, but only recent studies exposed a correlation between MLI and PC compartments. The expression of HCN1, Kv1.1, PSD95 and GAD67 revealed a pattern of morphologically distinct pinceau terminals distributed accordingly to the known PC compartments (66). This new anatomical data came to consolidate the previously established physiological evidences of local contribution of MLI neurons. *In vivo* stimulation of a PF bundle (beam)

in CrusI showed a consistent off-beam inhibitory response (63). Parasagittal discrete PC domains juxtaposed to the stimulated beam were revealed to be specifically inhibited by local interneuron network. This non-uniformity of MLI inhibition was directly correlated with the known PC subtypes. *In vitro* work supports the correlation between MLI clusters and PC subtypes. However, at higher spatial resolution the output connectivity map did not allow align MLI cluster with PC subtypes. It appeared that MLI cluster span over several PC domains of different identities (62). The mechanisms behind the transversal clusters of MLI are still unknown as so far, no markers allow to discriminate subtypes of MLI.

<u>Climbing Fibers</u>:

Olivo-cerebellar projections, or CFs, represent the second input pathway to the cerebellum. They embody the learning component of the cerebellar cortex as the PC's complex spike triggered by the CF represents the putative "error signal" essential for motor adaptation. The organized distribution of inferior olive compartments in the cerebellum was the first feature to describe cerebellar modules (reviewed in (67)). While the parasagittal organization of olivary sub-nuclei has been mapped in details, little is known about their molecular and electrophysiological diversity. Enkephalin(68), peripherin (69), the cocaine- and amphetamine-regulated
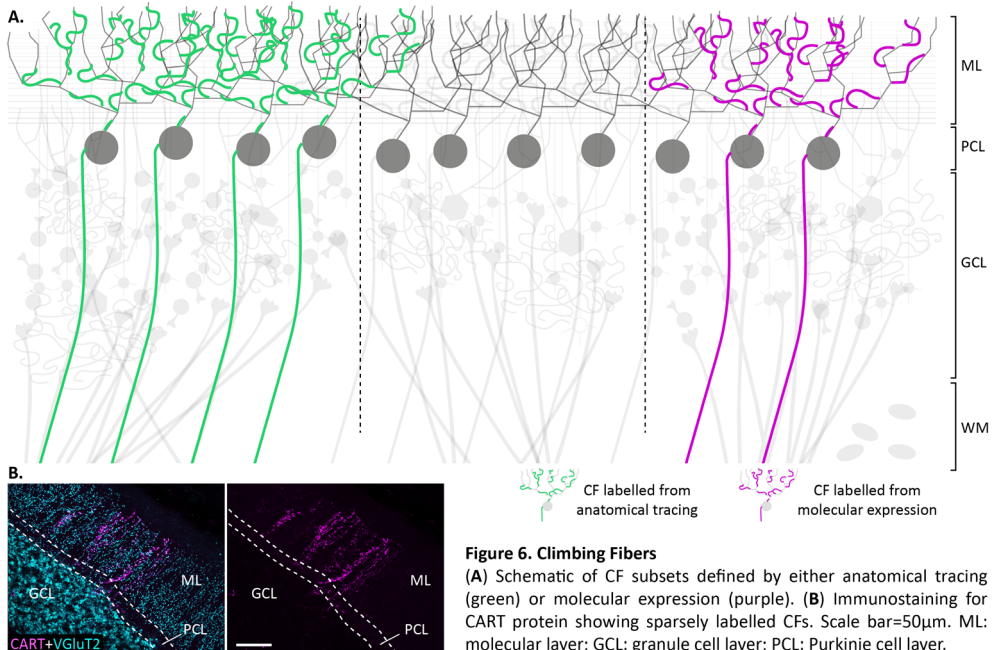

Figure 6. Climbing Fibers
(**A**) Schematic of CF subsets defined by either anatomical tracing (green) or molecular expression (purple). (**B**) Immunostaining for CART protein showing sparsely labelled CFs. Scale bar=50µm. ML: molecular layer; GCL: granule cell layer; PCL: Purkinje cell layer.

transcript CART 55-102 peptide (70), and the corticotropin-releasing factor (71) allow for molecular discrimination of certain CF subsets (**Fig. 6**). In addition, CFs of distinct modules present differential probability of release related to their respective vesicular pools (72). Response to CF has been shown to be different across PC modules, resulting in distinct types of learning processes. However, most of the heterogeneity of complex spike responses along the cerebellar cortex is so far attributed to PC identity and post-synaptic molecular composition. The molecular diversity among CFs could translate a broad spectrum of pre-synaptic features.
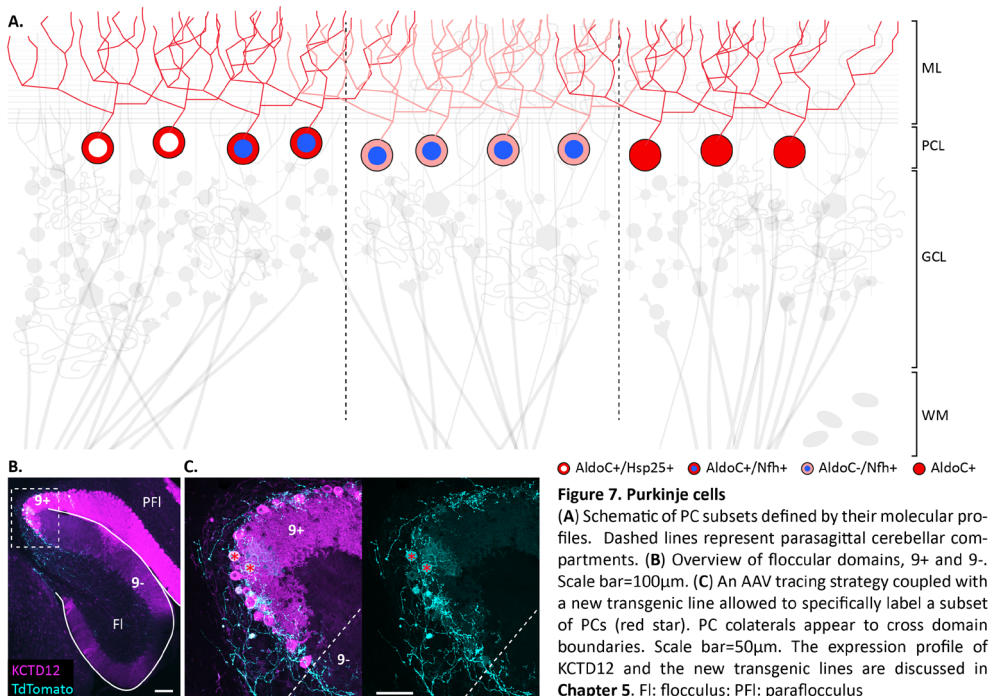
Purkinje Cell Layer

Purkinje Cell:

PCs are the converging point for all sensory input to the cerebellum, and the sole cortical output. Defined as the principal neuron of the cerebellum, PCs are characterized by their fan shape dendritic arborization oriented in the parasagittal plan. In 1963, Scott (13) demonstrated with 5'-nucleosidase immunostaining the existence of parasagittal domain in the mouse cortex defined by different levels of expression among PCs. In 1990, Brochu (73) identified a novel antigene named zebrinII, later recognized as AldolaseC (AldoC), to distinguish similar PC subpopulations (**Fig. 7A**). The topographical afferent and efferent fiber distributions were subsequently mapped over the cortical domains delineated by AldoC expression, showing that juxtaposed PC compartments are connected to distinct divisions of the inferior olive and respectively project to diverging pathways in the cerebellar or vestibular nuclei (74). The life work of Richard Hawkes contributed in making AldoC the reference marker for parasagittal arrays of PCs. First, with the identification of several proteins delineating similar (Hnk-1 (75), Sphk1 (76), PlcB3 (77), $GABA_{B2}$ (78)) or complementary (Map1a (79), PlcB4 (77)) expression patterns. Second, with the overlay of AldoC expression defined boundaries with pathophysiological landmarks observed in several cerebellar neurodegenerative disorders (80). Later, with the comparative anatomy of AldoC pattern performed in several species which showed the evolutionary conservation through mammals (81–83) and avians (84–86). The definition of PC subtypes changed into a binary classification as AldoC-positive (AldoC+) and AldoC-negative (AldoC-) PCs. In its more recent history, the AldoC pattern found physiological relevance. AldoC+ and AldoC- PCs were showed to operate at different simple spike and indirectly complex spike

frequencies (87, 88) and to present different synaptic properties (89). The relative function of each subtypes and the possible cross talk between them (**Fig. 7C**) remains uncertain.

Assuming that PC diversity can be reduced to only two clearly distinct subpopulations underestimates the biological reality. Not without reason, the expression of AldoC is illustrated with a grayscale in the reference atlas of the cerebellar patterning (90), to depict nuances of protein levels suggesting more than a dual-modality system. The use of the endogenous AldoC expression was also questioned by the recent generation of an AldoC-reporter mouse line (91) which forced to redraw the previously defined compartments. Finally, a list of molecular markers delineating similar but not strictly identical PC subpopulations hints toward a higher level of heterogeneity among PCs (Hsp25 (92), Nfh (93)) (**Fig. 7A**). Trying to decipher the functionality of the modules while overlooking the extent of PC diversity may result in major misinterpretations.

○ AldoC+/Hsp25+   ◉ AldoC+/Nfh+   ◉ AldoC-/Nfh+   ● AldoC+

Figure 7. Purkinje cells
(**A**) Schematic of PC subsets defined by their molecular profiles. Dashed lines represent parasagittal cerebellar compartments. (**B**) Overview of floccular domains, 9+ and 9-. Scale bar=100μm. (**C**) An AAV tracing strategy coupled with a new transgenic line allowed to specifically label a subset of PCs (red star). PC colaterals appear to cross domain boundaries. Scale bar=50μm. The expression profile of KCTD12 and the new transgenic lines are discussed in **Chapter 5**. Fl: flocculus; PFl: paraflocculus

Pathophysiology

In 1905 Andre Thomas published a case study of a cerebellar ataxia patient (94). During the post mortem anatomical investigation he described that : "*Sur certaines lamelles les cellules de Purkinje ont completement disparu alors que les lamelles, immédiatement adjacent, ont conservé à peu près le nombre normal de cellules ; la transition entre les regions saines et les regions malades y est en quelque sorte brusque*". My level in French was sufficient to understand that this is the first known description of cerebellar patterned degeneration. Thomas described in this ataxia patient alternated juxtaposed regions of the cerebellum either preserved from the degeneration or heavily affected. To explain such regional susceptibility to neurodegeneration he wrote in his opening statement: "… there is still a category of diseases in which it is impossible to infer meningeal or vascular lesions in order to explain the slow and progressive disappearance of certain groups of nerve cells…" (directly translated from the text).

Patterned PC degeneration is a common trait observed in several cerebellar pathologies in human and rodent models (**Fig. 8**). Hawkes and Sarna exhaustive review on the topic (80) concluded with the definition of four types of cerebellar neurodegeneration: type 1 = AldoC- PCs
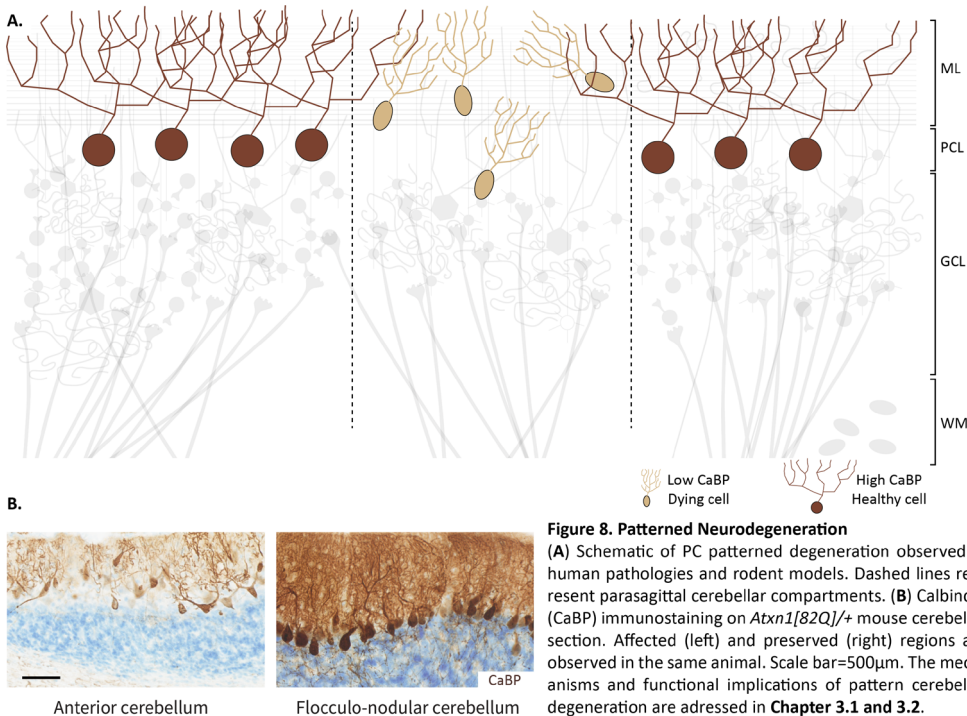

Figure 8. Patterned Neurodegeneration
(**A**) Schematic of PC patterned degeneration observed in human pathologies and rodent models. Dashed lines represent parasagittal cerebellar compartments. (**B**) Calbindin (CaBP) immunostaining on *Atxn1[82Q]/+* mouse cerebellar section. Affected (left) and preserved (right) regions are observed in the same animal. Scale bar=500μm. The mechanisms and functional implications of pattern cerebellar degeneration is adressed in **Chapter 3.1 and 3.2**.

Anterior cerebellum   Flocculo-nodular cerebellum

preferentially degenerate; type 2= AldoC+ PCs preferentially degenerate; type 3 = the neurodegeneration follows a pattern but do not correlate with a known molecular expression; type 4 = the neurodegeneration follows a clear random distribution. Although, this crude classification might be inaccurate as the characterization of new molecular pattern leads to the re-evaluation of type 3 models as demonstrated with the *lurcher* mutant (95, 96). Patterned degeneration (1, 2 and 3) was described in a wide range of conditions, such as genetic mutations (97–101), brain ischemia (102), viral infections (103), prion diseases (104), and alcohol-related cerebellar degeneration (105). Several other pathologies entered in type 1, 2 or 3, and many more could if it was not for the lack of refined anatomical descriptions. The recurrent selective survival of discrete molecular subtypes suggests endogenous predispositions to neurodegeneration independent of the type of insult. The differential expression of proteins involved in cellular stress response (Hsp25), bioenergetic processes (AldoC) and bioactive lipid synthesis (Sphk1) points toward distinct metabolic balances inherent to PC subtypes.

Functionality

The understanding of cerebellar compartments at a functional level remains mostly unresolved. Current models use behaviors assumed to be predominantly driven by only one of the two main modalities to decipher their respective properties. Eyeblink conditional training commonly embodies the AldoC- pathway, while eye-movement adaptation represents the AldoC+ pathway (106, 107). Dissociation of the modules allowed to further understand the learning processes behind each modality. The perception of the module as independent units is not utterly wrong. The overall confinement of the afferent pathways and the assumed limited cortical crosstalk (108) suggest that parasagittal domains behave with a relative independence at the input stage. However, understanding how modules act relative to each other's and not only independently is key. Several lines of evidences made it clear that a specific behavioral task is controlled by an ensemble of parallel compartments of different identities. Retrograde trans-synaptic tracing experiments showed that cortical compartments of distinct molecular signatures (e.g. A1 zone = AldoC+ and B zone = AldoC-) converge toward individual muscles (e.g. Tibialis anterior) (109). Moreover, the slight discrepancies between MF, CF and PC topography also suggest that a sensory input domain encompasses multiple PC compartments. This was confirmed experimentally as cluster of PCs defined by the physiological response to MF or GC evoked stimulation,

span upon the borders of compartments defines by AldoC expression (62, 110). At the behavioral level, the work done on the neuronal map of the vestibulo-ocular system of the pigeon cerebellum showed that each individual functional zone in the flocculus and the uvula encompass both AldoC+ and AldoC- PC domains (111).

Still, the current limits to the comprehension of the cerebellar compartments functions are the lack of anatomical knowledge and the constrains of spatial resolution. While MFs and CFs afferents have been extensively described, PC's downstream pathways have been neglected. The map of cortical projections to the cerebellar and vestibular nuclei (CN and VN) is based on crude anatomical discrimination of the CN/VN, and not discreet networks defined by molecular or physiological properties of CN/VN neurons. The attempts for more refined anatomical description are still limited by the lack of cellular resolution (112). The difficulty lies in that efferent pathways appear less topographically organized and more interlaced (113, 114). In addition, multi-synaptic anatomical studies describing connections from the cerebellum to the muscles are scarce. As example, the efferent pathways connecting the cerebellum to the orbicularis oculi (eye lid closure) or lateral/medial rectus (eye movement) are poorly described and barely incorporate the modular map (eyeblink: (115, 116); eye-movement: (117, 118)). Building a conceptual understanding of modular domains on such incomplete anatomical work is risky.

One could argue that the bigger issue is the lack of spatial resolution to monitor and control individual microcircuit. While several genetic tools or viral strategies have been developed to target the different types of neurons in the cerebellar cortex, none has been established to selectively isolate a sub-type.

Flocculus

The flocculus is the control centre of two major eye movement adaptations, the vestibulo-ocular (VOR) and the optokinetic reflex (OKR). Vestibular, visual, visuo-motor and proprioceptive sensory inputs (MF pathway) as well as visual error signal (CF pathway) are integrated in the floccular PCs which drives ocular movements to counteract involuntary head motions and retinal slip. The flocculus receives MF inputs essentially from the nucleus prepositus (PrH), the VN and the nucleus reticularis tegmenti pontis (NRTP), all multi-sensory integration centres. The primary vestibular MF inputs (Scarpa's ganglion) appear present but sparse (Barmack *et al.* 1993, Osanai *et al.* 2011). From the inferior olive (IO) the flocculus receive

climbing fiber afferents originating in the ventro-lateral outgrowth (VLO) and the dorsal cap of kooy (DC). Floccular PCs project back to the VN and PrH.

Assumed to be completely described in its anatomy and functions, the flocculus has been at the centre of cerebellar network modelling. In mouse, the flocculus was found to be organised in five functional micro-zones define by PCs modulation in response to either optokinetic stimulation along the horizontal axis (zone 1 and 3), stimulation along the vertical axis (zone 2 and 4), or the absence of response to either stimulations (zone C2) (119). They relate to the micro-zones described in rat and rabbit, and to a certain extent, the ones described in cat (presenting three more subdivisions) and monkeys (120). The distinct modulations observed in these micro-zones are commonly attributed to the tonotopy with afferent (olivo-cerebellar) and efferent (cortico-vestibular) projections.

The molecular diversity of PCs in the flocculus on the other hand is an unresolved question. In rabbit, muscarinic-m2 immunoreactivity discriminated subtypes of PCs in the flocculus (22). Superimposed on the functional map of preferential rotation axis response, it defined zone C2/1 positive for muscarinic-m2 and zone 2/4 mainly negative. PC molecular signature would then correlate to a preferential stimulus response (hypothesis #1). In pigeon, a functional zone includes two juxtaposed AldoC+ and AldoC- domains equal in size. The complementation of distinct molecular domains would then be responsible for a functional zone (hypothesis #2). In mouse, Hsp25 expression describes discreet domains but discriminate the flocculus from the ventral paraflocculus more than distinct floccular microzones. The seemingly homogeneous expression of AldoC in all floccular PC led to the depiction of the flocculus as a single compartment. Hence, a cerebellar task would be completely performed by a single modality (hypothesis #3). The existence or not of distinct molecular compartments in the flocculus would elaborate different hypothesis in regard to the functional involvement of cerebellar modules at the behavioural level. The three hypotheses then mutually reject each other. One could discard hypothesis #1 as it results from assumptions and not experimental confirmation. Hypothesis #2 and #3 oppose the current map of AldoC expression in two distinct species. The recent re-mapping of AldoC expression in the mouse flocculus bears the answer. The novel AldolaC-Venus knock-in reporter mouse (91) parcelled the flocculus in two micro-domains: the AldoC+ caudal aspect (9+), and AldoC- rostral aspect (9-) (**Fig. 7B**). While their physiology, anatomy, and functions remain unknown, the allocation of two modalities to the flocculus questions the current models founded on hypothesis #3 and would support models based on the hypothesis #2.

Scope of the thesis

The scope of my thesis is to demonstrate that neuronal diversity goes beyond our current models. The different works presented in the following chapters focus on refined anatomical investigation applied to molecular, connectivity and behavioral studies.

In chapter 2 we defined the neuronal network of the BIN. Molecular identification and neuronal tracing showed that BIN neurons are a unique inhibitory input to the granular cell layer of the flocculus receiving glutamatergic afferent projections from a discreet population of neurons located in the gigantocellular reticular nucleus. BIN neurons provide a preponderant feedforward inhibition that complements feedback inhibition pathways formed by cerebellar interneurons. This unique modality of the floccular network is a common trait of all mammals studied, suggesting an evolutionary pressure to maintain this neuronal population in the visuo-motor control circuit.

In chapter 3.1 we detailed the pathophysiological traits of a spino-cerebellar ataxia type I (SCA-I) transgenic mouse model, Atxn1[82Q]-/+. The PC neurodegeneration observed in this model follow a well-established pattern as the vestibulocerebellum and CrusI lobule maintain morphologically and physiologically healthy PC features, contrasting with the deterioration of the other cerebellar lobules. Despite an advanced neurodegeneration in the cerebellar cortex, the preserved PC regions related to conserved cerebellar functions.

In chapter 3.2 we identified a molecular pathway responsible for cerebellar patterned neurodegeneration. In the Atxn1[82Q]-/+, the sphingolipid metabolism is affected and unbalanced principally in cerebellar region primarily affected by the degeneration. Deletion of a major enzyme in the sphingolipid metabolic pathway allowed to partially rescue neurodegenerative pathology in Atxn1[82Q]-/+ mice. The new degenerative pattern emerging relates to the known PC diversity.

In Chapter 4 we uncovered new microcircuits embedded in the floccular network. We found that recently identified 9- and 9+ domains of the flocculus present distinct molecular, electrophysiological, and anatomical features. The molecular and physiological characteristics of 9- PCs take down the concept of bimodal organization of the cerebellum as PC properties define a module halfway between AldoC+ and AldoC- microzones. Meanwhile the anatomical data, mapped over the known floccular microcircuit, add a degree of complexity to this model of cerebellar processing. Within this study we identified and characterized two transgenic Cre lines which allow to genetically target distinct PC sub-populations.

In chapter 5 we illustrated the functional relevance of distinct molecular expressions in PC subtypes. The deletion of TRPC3 channel resulted in a specific alteration of AldoC- PCs properties while AldoC+ PCs are unaltered. While the expression pattern of TRPC3 partially correlate with the absence of effects of the deletion on AldoC+ PCs, the complex spatial expression does not appear to fully explain such results.

In chapter 6 we exposed a novel type of transient homeostatic process in PCs. We discovered *in vitro* that decreased axonal fidelity in PCs induces the formation of an ephemeral structure along the axon. The so-called "swellings" were also observed *in vivo* and we suggested they relate to learning mechanism. This major morphological change correlating with intrinsic firing at a define time stresses that PC heterogeneity goes beyond the spatial and temporal resolution of the cerebellar compartments.

In conclusion, the different works presented in the following chapters build on the foundations of neuronal diversity to further refine cerebellar anatomy and its biological meaning. We have reached an infinite complexity, let's go beyond.

1. M. Bota, H. W. Dong, L. W. Swanson, From gene networks to brain networks. *Nat. Neurosci.* (2003) https:/doi.org/10.1038/nn1096.

2. S. Ramón y Cajal, *Histologie du Systeme Nerveux de l'Homme et des Vertebres. Maloine, Paris: 1911. chap. II* (1909).

3. S. J. Altschuler, L. F. Wu, Cellular Heterogeneity: Do Differences Make a Difference? *Cell* (2010) https:/doi.org/10.1016/j.cell.2010.04.033.

4. B. B. Lake, *et al.*, Neuronal subtypes and diversity revealed by single-nucleus RNA sequencing of the human brain. *Science (80-.).* (2016) https:/doi.org/10.1126/science.aaf1204.

5. K. D. Harris, *et al.*, Classes and continua of hippocampal CA1 inhibitory neurons revealed by single-cell transcriptomics. *PLoS Biol.* (2018) https:/doi.org/10.1371/journal.pbio.2006387.

6. E. Boldog, *et al.*, Transcriptomic and morphophysiological evidence for a specialized human cortical GABAergic cell type. *Nat. Neurosci.* (2018) https:/doi.org/10.1038/s41593-018-0205-2.

7. E. Puighermanal, *et al.*, Functional and molecular heterogeneity of D2R neurons along dorsal ventral axis in the striatum. *Nat. Commun.* (2020) https:/doi.org/10.1038/s41467-020-15716-9.

8. K. Padmanabhan, N. N. Urban, Intrinsic biophysical diversity decorrelates neuronal firing while increasing information content. *Nat. Neurosci.* (2010) https:/doi.org/10.1038/nn.2630.

9. E. Marder, A. L. Taylor, Multiple models to capture the variability in biological neurons and networks in *Nature Neuroscience*, (2011) https:/doi.org/10.1038/nn.2735.

10. N. L. Cerminara, E. J. Lang, R. V. Sillitoe, R. Apps, Redefining the cerebellar cortex as an assembly of non-uniform Purkinje cell microcircuits. *Nat. Rev. Neurosci.* (2015) https:/doi.org/10.1038/nrn3886.

11. A. Brodal, Experimentelle Untersuchungen über die olivocerebellare Lokalisation. *Zeitschrift für die gesamte Neurol. und Psychiatr.* (1940) https:/doi.org/10.1007/BF02871362.

12. J. Jansen, A. Brodal, Experimental studies on the intrinsic fibers of the cerebellum. II. The cortico nuclear projection. *J. Comp. Neurol.* (1940) https:/doi.org/10.1002/cne.900730204.

13. T. G. Scott, A unique pattern of localization within the cerebellum [34]. *Nature* (1963) https:/doi.org/10.1038/200793a0.

14. L. S. Popa, A. L. Hewitt, T. J. Ebner, The cerebellum for jocks and nerds alike. *Front. Syst. Neurosci.* (2014) https:/doi.org/10.3389/fnsys.2014.00113.

15. J. Voogd, Cerebellar zones: A personal history. *Cerebellum* (2011) https:/doi.org/10.1007/s12311-010-0221-6.

16. E. Marani, Topographic Histochemstry of the Cerebellum: 5′-Nucleotidase, Acetylcholinesterase, Immunology of Fal. *Prog. Histochem. Cytochem.* (1986) https:/doi.org/10.1016/S0079-6336(86)80003-1.

17. H. K. P. Feirabend, H. Choufoer, J. Voogd, White matter of the cerebellum of the chicken (Gallus domesticus): A quantitative light and electron microscopic analysis of myelinated fibers and fiber compartments. *J. Comp. Neurol.* (1996) https:/doi.org/10.1002/(SICI)1096-9861(19960527)369:2<236::AID-CNE5>3.0.CO;2-4.

18. H. K. P. Feirabend, J. Voogd, Myeloarchitecture of the cerebellum of the chicken (Gallus domesticus): An atlas of the compartmental subdivision of the cerebellar white matter. *J. Comp. Neurol.* (1986) https:/doi.org/10.1002/cne.902510104.

19. T. P. Langer, Basal interstitial nucleus of the cerebellum: Cerebellar nucleus related to the flocculus. *J. Comp. Neurol.* (1985) https:/doi.org/10.1002/cne.902350104.

20. J. Voogd, What we do not know about cerebellar systems neuroscience. *Front. Syst. Neurosci.* (2014) https:/doi.org/10.3389/fnsys.2014.00227.

21. J. A. Heckroth, L. M. Eisenman, Parasagittal organization of mossy fiber collaterals in the cerebellum of the mouse. *J. Comp. Neurol.* (1988) https:/doi.org/10.1002/cne.902700307

22. D. Jaarsma, *et al.*, Cholinergic innervation and receptors in the cerebellum. *Prog. Brain Res.* (1997) https:/doi.org/10.1016/s0079-6123(08)63359-2.

23. S. A. Gebre, S. L. Reeber, R. V. Sillitoe, Parasagittal compartmentation of cerebellar mossy fibers as revealed by the patterned expression of vesicular glutamate transporters VGLUT1 and VGLUT2. *Brain Struct. Funct.* (2012) https:/doi.org/10.1007/s00429-011-0339-4.

24. C. L. Armstrong, *et al.*, A novel somatostatin-immunoreactive mossy fiber pathway associated with HSP25-immunoreactive Purkinje cell stripes in the mouse cerebellum. *J. Comp. Neurol.* (2009) https:/doi.org/10.1002/cne.22167.

25. G. Liu, Presynaptic control of quantal size: Kinetic mechanisms and implications for synaptic transmission and plasticity. *Curr. Opin. Neurobiol.* (2003) https:/doi.org/10.1016/S0959-4388(03)00078-3.

26. M. C. Weston, R. B. Nehring, S. M. Wojcik, C. Rosenmund, Interplay between VGLUT isoforms and endophilin A1 regulates neurotransmitter release and short-term plasticity. *Neuron* (2011) https://doi.org/10.1016/j.neuron.2011.02.002.

27. F. P. Chabrol, A. Arenz, M. T. Wiechert, T. W. Margrie, D. A. Digregorio, Synaptic diversity enables temporal coding of coincident multisensory inputs in single neurons. *Nat. Neurosci.* (2015) https://doi.org/10.1038/nn.3974.

28. , 10. CAMILLO GOLGI <I>Sulla fina anatomia</I> <I>degli</I> <I>organi centrali</I> <I>del</I> <I>sistema nervoso</I> a cura di Alberto Oliverio 1995, 264 pp., Giunti, Firenze. *Nuncius* (2012) https://doi.org/10.1163/221058799x00557.

29. A. Neki, *et al.*, Metabotropic glutamate receptors mGluR2 and mGluR5 are expressed in two non-overlapping populations of Golgi cells in the rat cerebellum. *Neuroscience* (1996) https://doi.org/10.1016/0306-4522(96)00316-8.

30. M. Simat, F. Parpan, J. M. Fritsch, Heterogeneity of glycinergic and gabaergic interneurons in the granule cell layer of mouse cerebellum. *J. Comp. Neurol.* (2007) https://doi.org/10.1002/cne.21142.

31. D. Jaarsma, *et al.*, The basal interstitial nucleus (BIN) of the cerebellum provides diffuse ascending inhibitory input to the floccular granule cell layer. *J. Comp. Neurol.* (2018) https://doi.org/10.1002/cne.24479.

32. F. Prestori, L. Mapelli, E. D'Angelo, Diverse Neuron Properties and Complex Network Dynamics in the Cerebellar Cortical Inhibitory Circuit. *Front. Mol. Neurosci.* (2019) https://doi.org/10.3389/fnmol.2019.00267.

33. S. Dieudonné, Submillisecond kinetics and low efficacy of parallel fibre-Golgi cell synaptic currents in the rat cerebellum. *J. Physiol.* (1998) https://doi.org/10.1111/j.1469-7793.1998.845bj.x.

34. L. Ankri, *et al.*, A novel inhibitory nucleo-cortical circuit controls cerebellar Golgi cell activity. *Elife* (2015) https://doi.org/10.7554/eLife.06262.

35. S. de Lacalle, L. B. Hersh, C. B. Saper, Cholinergic innervation of the human cerebellum. *J. Comp. Neurol.* (1993) https://doi.org/10.1002/cne.903280304.

36. D. Jaarsma, M. R. Diño, C. Cozzari, E. Mugnaini, Cerebellar choline acetyltransferase positive mossy fibres and their granule and unipolar brush cell targets: A model for central cholinergic nicotinic neurotransmission. *J. Neurocytol.* (1996) https://doi.org/10.1007/bf02284845.

37. F. J. Geurts, J. P. Timmermans, R. Shigemoto, E. De Schutter, Morphological and neurochemical differentiation of large granular layer interneurons in the adult rat cerebellum. *Neuroscience* (2001) https://doi.org/10.1016/S0306-4522(01)00058-6.

38. R. V. Sillitoe, S. H. Chung, J. M. Fritschy, M. Hoy, R. Hawkes, Golgi cell dendrites are restricted by purkinje cell stripe boundaries in the adult mouse cerebellar cortex. *J. Neurosci.* (2008) https://doi.org/10.1523/JNEUROSCI.4145-07.2008.

39. E. Mugnaini, G. Sekerková, M. Martina, The unipolar brush cell: A remarkable neuron finally receiving deserved attention. *Brain Res. Rev.* (2011) https://doi.org/10.1016/j.brainresrev.2010.10.001.

40. M. G. Nunzi, R. Shigemoto, E. Mugnaini, Differential expression of calretinin and metabotropic glutamate receptor mGluR1α defines subsets of unipolar brush cells in mouse cerebellum. *J. Comp. Neurol.* (2002) https://doi.org/10.1002/cne.10344.

41. E. B. E. Becker, The Moonwalker Mouse: New Insights into TRPC3 Function, Cerebellar Development, and Ataxia. *Cerebellum* (2014) https://doi.org/10.1007/s12311-014-0564-5.

42. S. H. Chung, H. Marzban, M. Watanabe, R. Hawkes, Phospholipase Cβ4 expression identifies a novel subset of unipolar brush cells in the adult mouse cerebellum. *Cerebellum* (2009) https://doi.org/10.1007/s12311-009-0092-x.

43. C. Borges-Merjane, L. O. Trussell, ON and OFF unipolar brush cells transform multisensory inputs to the auditory system. *Neuron* (2015) https://doi.org/10.1016/j.neuron.2015.02.009.

44. J. A. Kim, G. Sekerková, E. Mugnaini, M. Martina, Electrophysiological, morphological, and topological properties of two histochemically distinct subpopulations of cerebellar unipolar brush cells. *Cerebellum* (2012) https://doi.org/10.1007/s12311-012-0380-8.

45. M. R. Diño, A. A. Perachio, E. Mugnaini, Cerebellar unipolar brush cells are targets of primary vestibular afferents: An experimental study in the gerbil. *Exp. Brain Res.* (2001) https://doi.org/10.1007/s002210100790.

46. T. S. Balmer, L. O. Trussell, Selective targeting of unipolar brush cell subtypes by cerebellar mossy fibers. *Elife* (2019) https://doi.org/10.7554/eLife.44964.

47. G. Sekerková, M. Watanabe, M. Martina, E. Mugnaini, Differential distribution of phospholipase C beta isoforms and diaglycerol kinase-beta in rodents cerebella corroborates the division of unipolar

brush cells into two major subtypes. *Brain Struct. Funct.* (2014) https:/doi.org/10.1007/s00429-013-0531-9.

48. C. M. Houston, *et al.*, Exploring the significance of morphological diversity for cerebellar granule cell excitability. *Sci. Rep.* (2017) https:/doi.org/10.1038/srep46147.

49. I. Delvendahl, I. Straub, S. Hallermann, Dendritic patch-clamp recordings from cerebellar granule cells demonstrate electrotonic compactness. *Front. Cell. Neurosci.* (2015) https:/doi.org/10.3389/fncel.2015.00093.

50. K. Schilling, H. H. H. W. Schmidt, S. L. Baader, Nitric oxide synthase expression reveals compartments of cerebellar granule cells and suggests a role for mossy fibers in their development. *Neuroscience* (1994) https:/doi.org/10.1016/0306-4522(94)90293-3.

51. G. D. Frantz, J. M. Weimann, M. E. Levin, S. K. McConnell, Otx1 and Otx2 define layers and regions in developing cerebral cortex and cerebellum. *J. Neurosci.* (1994) https:/doi.org/10.1523/jneurosci.14-10-05725.1994.

52. G. Giacomo Consalez, R. Hawkes, The compartment restriction of cerebellar interneurons. *Front. Neural Circuits* (2012) https:/doi.org/10.3389/fncir.2012.00123.

53. R. Luckner, K. Obst-Pernberg, S. Hirano, S. T. Suzuki, C. Redies, Granule cell raphes in the developing mouse cerebellum. *Cell Tissue Res.* (2001) https:/doi.org/10.1007/s004410000292.

54. S. Masoli, M. Tognolina, U. Laforenza, F. Moccia, E. D'Angelo, Parameter tuning differentiates granule cell subtypes enriching transmission properties at the cerebellum input stage. *Commun. Biol.* (2020) https:/doi.org/10.1038/s42003-020-0953-x.

55. C. L. John, C. L. Cepko, Granule cell raphes and parasagittal domains of Purkinje cells: Complementary patterns in the developing chick cerebellum. *J. Neurosci.* (1998) https:/doi.org/10.1523/jneurosci.18-22-09342.1998.

56. R. Llinas, General discussion: Radial connectivity in the cerebellar cortex: A novel view regarding the functional organization of the molecular layer. *Exp. Brain Res.* (1982) https:/doi.org/10.1007/978-3-642-68560-6_10.

57. L. Li, *et al.*, Visualizing the distribution of synapses from individual neurons in the mouse brain. *PLoS One* (2010) https:/doi.org/10.1371/journal.pone.0011503.

58. D. Rokni, R. Llinas, Y. Yarom, The Morpho/Functional Discrepancy in the Cerebellar Cortex: Looks Alone are Deceptive. *Front. Neurosci.* (2008) https:/doi.org/10.3389/neuro.01.036.2008.

59. N. H. Barmack, V. Yakhnitsa, Distribution of granule cells projecting to focal Purkinje cells in mouse uvula-nodulus. *Neuroscience* (2008) https:/doi.org/10.1016/j.neuroscience.2008.07.030.

60. J. M. Bower, D. C. Woolston, Congruence of spatial organization of tactile projections to granule cell and Purkinje cell layers of cerebellar hemispheres of the albino rat: Vertical organization of cerebellar cortex. *J. Neurophysiol.* (1983) https:/doi.org/10.1152/jn.1983.49.3.745.

61. D. Cohen, Y. Yarom, Patches of synchronized activity in the cerebellar cortex evoked by mossy-fiber stimulation: Questioning the role of parallel fibers. *Proc. Natl. Acad. Sci. U. S. A.* (1998) https:/doi.org/10.1073/pnas.95.25.15032.

62. A. M. Valera, *et al.*, Stereotyped spatial patterns of functional synaptic connectivity in the cerebellar cortex. *Elife* (2016) https:/doi.org/10.7554/eLife.09862.

63. W. Gao, G. Chen, K. C. Reinert, T. J. Ebner, Cerebellar cortical molecular layer inhibition is organized in parasagittal zones. *J. Neurosci.* (2006) https:/doi.org/10.1523/JNEUROSCI.2434-06.2006.

64. K. D. Wyatt, P. Tanapat, S. S. H. Wang, Speed limits in the cerebellum: Constraints from myelinated and unmyelinated parallel fibers. *Eur. J. Neurosci.* (2005) https:/doi.org/10.1111/j.1460-9568.2005.04053.x.

65. S. L. Palay, V. Chan-Palay, *Cerebellar Cortex* (1974) https:/doi.org/10.1007/978-3-642-65581-4.

66. J. Zhou, *et al.*, Purkinje cell neurotransmission patterns cerebellar basket cells into zonal modules defined by distinct pinceau sizes. *Elife* (2020) https:/doi.org/10.7554/ELIFE.55569.

67. S. L. Reeber, J. J. White, N. A. George-Jones, R. V. Sillitoe, Architecture and development of olivocerebellar circuit topography. *Front. Neural Circuits* (2012) https:/doi.org/10.3389/fncir.2012.00115.

68. J. S. King, R. H. Ho, G. A. Bishop, Anatomical evidence for enkephalin immunoreactive climbing fibres in the cerebellar cortex of the opossum. *J. Neurocytol.* (1986) https:/doi.org/10.1007/BF01611856.

69. L. Errante, *et al.*, The intermediate filament protein peripherin is a marker for cerebellar climbing fibres. *J. Neurocytol.* (1998) https:/doi.org/10.1023/A:1006991104595.

70. S. L. Reeber, R. V. Sillitoe, Patterned expression of a cocaine- and amphetamine-regulated

transcript peptide reveals complex circuit topography in the rodent cerebellar cortex. *J. Comp. Neurol.* (2011) https:/doi.org/10.1002/cne.22601.

71. K. Sawada, H. Sakata-Haga, S. Hisano, Y. Fukui, Topological relationship between corticotropin-releasing factor-immunoreactive cerebellar afferents and tyrosine hydroxylase-immunoreactive Purkinje cells in a hereditary ataxic mutant, rolling mouse Nagoya. *Neuroscience* (2001) https:/doi.org/10.1016/S0306-4522(00)00533-9.

72. M. Paukert, Y. H. Huang, K. Tanaka, J. D. Rothstein, D. E. Bergles, Zones of enhanced glutamate release from climbing fibers in the mammalian cerebellum. *J. Neurosci.* (2010) https:/doi.org/10.1523/JNEUROSCI.5118-09.2010.

73. G. Brochu, L. Maler, R. Hawkes, Zebrin II: A polypeptide antigen expressed selectively by purkinje cells reveals compartments in rat and fish cerebellum. *J. Comp. Neurol.* (1990) https:/doi.org/10.1002/cne.902910405.

74. I. Sugihara, Y. Shinoda, Molecular, topographic, and functional organization of the cerebellar nuclei: Analysis by three-dimensional mapping of the olivonuclear projection and aldolase C labeling. *J. Neurosci.* (2007) https:/doi.org/10.1523/JNEUROSCI.1579-07.2007.

75. L. M. Eisenman, R. Hawkes, Antigenic compartmentation in the mouse cerebellar cortex: Zebrin and HNK□1 reveal a complex, overlapping molecular topography. *J. Comp. Neurol.* (1993) https:/doi.org/10.1002/cne.903350410.

76. N. Terada, *et al.*, Compartmentation of the Mouse Cerebellar Cortex by Sphingosine Kinase. *J. Comp. Neurol.* (2004) https:/doi.org/10.1002/cne.11002.

77. J. R. Sarna, H. Marzban, M. Watanabe, R. Hawkes, Complementary stripes of phospholipase Cβ3 and Cβ4 expression by Purkinje cell subsets in the mouse cerebellum. *J. Comp. Neurol.* (2006) https:/doi.org/10.1002/cne.20912.

78. S. H. Chung, C. T. Kim, R. Hawkes, Compartmentation of gaba b receptor2 expression in the mouse cerebellar cortex. *Cerebellum* (2008) https:/doi.org/10.1007/s12311-008-0030-3.

79. F. Touri, Differential distribution of MAP1a and aldolase c in adult mouse cerebellum. *Eur. J. Neurosci.* (1996) https:/doi.org/10.1111/j.1460-9568.1996.tb01167.x.

80. J. R. Sarna, R. Hawkes, Patterned Purkinje cell death in the cerebellum. *Prog. Neurobiol.* (2003) https:/doi.org/10.1016/S0301-0082(03)00114-X.

81. J. Y. Kim, *et al.*, Purkinje cell compartmentation of the cerebellum of microchiropteran bats. *J. Comp. Neurol.* (2009) https:/doi.org/10.1002/cne.22147.

82. H. Marzban, R. Hawkes, On the architecture of the posterior zone of the cerebellum. *Cerebellum* (2011) https:/doi.org/10.1007/s12311-010-0208-3.

83. R. V. Sillitoe, C. R. Malz, K. Rockland, R. Hawkes, Antigenic compartment of the primate and tree shrew cerebellum: A common topography of zebrin II in Macaca mulatta and Tupaia belangeri. *J. Anat.* (2004) https:/doi.org/10.1111/j.0021-8782.2004.00282.x.

84. J. M. P. Pakan, A. N. Iwaniuk, D. R. W. Wylie, R. Hawkes, H. Marzban, Purkinje cell compartmentation as revealed by zebrin II expression in the cerebellar cortex of pigeons (Columba livia). *J. Comp. Neurol.* (2007) https:/doi.org/10.1002/cne.21266.

85. A. N. Iwaniuk, *et al.*, Compartmentation of the cerebellar cortex of hummingbirds (Aves: Trochilidae) revealed by the expression of zebrin II and phospholipase Cβ4. *J. Chem. Neuroanat.* (2009) https:/doi.org/10.1016/j.jchemneu.2008.10.001.

86. H. Marzban, *et al.*, Antigenic compartment of the cerebellar cortex in the chicken (Gallus domesticus). *J. Comp. Neurol.* (2010) https:/doi.org/10.1002/cne.22328.

87. H. Zhou, *et al.*, Cerebellar modules operate at different frequencies. *Elife* (2014) https:/doi.org/10.7554/eLife.02536.

88. J. Xiao, *et al.*, Systematic regional variations in Purkinje cell spiking patterns. *PLoS One* (2014) https://doi.org/10.1371/journal.pone.0105633.

89. J. I. Wadiche, C. E. Jahr, Patterned expression of Purkinje cell glutamate transporters controls synaptic plasticity. *Nat. Neurosci.* (2005) https://doi.org/10.1038/nn1539.

90. I. Sugihara, P. N. Quy, Identification of aldolase C compartments in the mouse cerebellar cortex by olivocerebellar labeling. *J. Comp. Neurol.* (2007) https:/doi.org/10.1002/cne.21219.

91. H. Fujita, *et al.*, Detailed expression pattern of Aldolase C (Aldoc) in the cerebellum, retina and other areas of the CNS studied in Aldoc-Venus knock-in mice. *PLoS One* (2014) https:/doi.org/10.1371/journal.pone.0086679.

92. C. L. Armstrong, A. M. Krueger-Naug, R. W. Currie, R. Hawkes, Constitutive expression of the 25-kda heat shock protein Hsp25 reveals novel parasagittal bands of Purkinje cells in the adult mouse cerebellar cortex. *J. Comp. Neurol.* (2000) https:/doi.org/10.1002/(SICI)1096-

9861(20000117)416:3<383::AID-CNE9>3.0.CO;2-M.

93. R. V. Sillitoe, D. Stephen, Z. Lao, A. L. Joyner, Engrailed homeobox genes determine the organization of Purkinje cell sagittal stripe gene expression in the adult cerebellum. *J. Neurosci.* (2008) https:/doi.org/10.1523/JNEUROSCI.2059-08.2008.

94. A.Thomas, Atrophie lamellaire des cellules de Purkinje. *Rev. Neurol. (Paris).* **Vol. 13**, 917–24 (1905).

95. D. Tano, *et al.*, Novel developmental boundary in the cerebellum revealed by zebrin expression in the Lurcher (Lc/+) mutant mouse. *J. Comp. Neurol.* (1992) https:/doi.org/10.1002/cne.903230111.

96. C. A. Duffin, R. McFarland, J. R. Sarna, M. W. Vogel, C. L. Armstrong, Heat shock protein 25 expression and preferential purkinje cell survival in the lurcher mutant mouse cerebellum. *J. Comp. Neurol.* (2010) https:/doi.org/10.1002/cne.22309.

97. J. A. Heckroth, L. C. Abbott, Purkinje cell loss from alternating sagittal zones in the cerebellum of leaner mutant mice. *Brain Res.* (1994) https:/doi.org/10.1016/S0006-8993(09)90014-2.

98. S. H. Chung, M. Calafiore, J. M. Plane, D. E. Pleasure, W. Deng, Apoptosis inducing factor deficiency causes reduced mitofusion 1 expression and patterned Purkinje cell degeneration. *Neurobiol. Dis.* (2011) https:/doi.org/10.1016/j.nbd.2010.10.016.

99. J. R. Sarna, R. Hawkes, Patterned Purkinje cell loss in the ataxic sticky mouse. *Eur. J. Neurosci.* (2011) https:/doi.org/10.1111/j.1460-9568.2011.07725.x.

100. T. Miyazaki, *et al.*, Ca v2.1 in cerebellar Purkinje cells regulates competitive excitatory synaptic wiring, cell survival, and cerebellar biochemical compartmentalization. *J. Neurosci.* (2012) https:/doi.org/10.1523/JNEUROSCI.2755-11.2012.

101. P. Strømme, *et al.*, X-linked Angelman-like syndrome caused by Slc9a6 knockout in mice exhibits evidence of endosomal-lysosomal dysfunction. *Brain* (2011) https:/doi.org/10.1093/brain/awr250.

102. J. P. Welsh, *et al.*, Why do Purkinje cells die so easily after global brain ischemia? Aldolase C, EAAT4, and the cerebellar contribution to posthypoxic myoclonus. *Adv. Neurol.* (2002).

103. B. L. Williams, K. Yaddanapudi, M. Hornig, W. I. Lipkin, Spatiotemporal Analysis of Purkinje Cell Degeneration Relative to Parasagittal Expression Domains in a Model of Neonatal Viral Infection. *J. Virol.* (2007) https:/doi.org/10.1128/jvi.02245-06.

104. A. Ragagnin, *et al.*, Cerebellar compartmentation of prion pathogenesis. *Brain Pathol.* (2018) https:/doi.org/10.1111/bpa.12503.

105. J. H. Lee, S. H. Heo, D. Il Chang, Early-stage alcoholic cerebellar degeneration: Diagnostic imaging clues. *J. Korean Med. Sci.* (2015) https:/doi.org/10.3346/jkms.2015.30.11.1539.

106. C. I. De Zeeuw, M. M. Ten Brinke, Motor learning and the cerebellum. *Cold Spring Harb. Perspect. Biol.* (2015) https:/doi.org/10.1101/cshperspect.a021683.

107. C. I. De Zeeuw, Bidirectional learning in upbound and downbound microzones of the cerebellum. *Nat. Rev. Neurosci.* (2020) https:/doi.org/10.1038/s41583-020-00392-x.

108. L. Witter, S. Rudolph, R. T. Pressler, S. I. Lahlaf, W. G. Regehr, Purkinje Cell Collaterals Enable Output Signals from the Cerebellar Cortex to Feed Back to Purkinje Cells and Interneurons. *Neuron* (2016) https:/doi.org/10.1016/j.neuron.2016.05.037.

109. T. J. H. Ruigrok, A. Pijpers, E. Goedknegt-Sabel, P. Coulon, Multiple cerebellar zones are involved in the control of individual muscles: A retrograde transneuronal tracing study with rabies virus in the rat. *Eur. J. Neurosci.* (2008) https:/doi.org/10.1111/j.1460-9568.2008.06294.x.

110. D. J. Graham, D. R. Wylie, Zebrin-immunopositive and -immunonegative stripe pairs represent functional units in the pigeon vestibulocerebellum. *J. Neurosci.* (2012) https:/doi.org/10.1523/JNEUROSCI.0197-12.2012.

111. I. Craciun, C. Gutiérrez-Ibáñez, J. R. Corfield, P. L. Hurd, D. R. Wylie, Topographic organization of inferior olive projections to the zebrin II stripes in the pigeon cerebellar uvula. *Front. Neuroanat.* (2018) https:/doi.org/10.3389/fnana.2018.00018.

112. H. Fujita, T. Kodama, S. Du Lac, Modular output circuits of the fastigial nucleus for diverse motor and nonmotor functions of the cerebellar vermis. *Elife* (2020) https:/doi.org/10.7554/eLife.58613.

113. M. Shin, *et al.*, Multiple types of cerebellar target neurons and their circuitry in the vestibule-ocular reflex. *J. Neurosci.* (2011) https:/doi.org/10.1523/JNEUROSCI.0768-11.2011.

114. H. Matsuno, *et al.*, Distribution and structure of synapses on medial vestibular nuclear neurons targeted by cerebellar flocculus purkinje cells and vestibular nerve in mice: Light and electron microscopy studies. *PLoS One* (2016) https:/doi.org/10.1371/journal.pone.0164037.

115. S. Morcuende, J. M. Delgado-García, G. Ugolini, Neuronal premotor networks involved in eyelid responses: Retrograde transneuronal tracing with rabies virus from the orbicularis oculi muscle in the rat. *J. Neurosci.* (2002) https:/doi.org/10.1523/jneurosci.22-20-08808.2002.

116. J. Gonzalez-Joekes, B. G. Schreurs, Anatomical characterization of a rabbit cerebellar eyeblink premotor pathway using pseudorabies and Identification of a local modulatory network in anterior interpositus. *J. Neurosci.* (2012) https:/doi.org/10.1523/JNEUROSCI.2088-12.2012.
117. W. Graf, N. Gerrits, N. Yatim-Dhiba, G. Ugolini, Mapping the oculomotor system: The power of transneuronal labelling with rabies virus. *Eur. J. Neurosci.* (2002) https:/doi.org/10.1046/j.1460-9568.2002.01994.x.
118. I. Billig, C. D. Balaban, Zonal organization of the vestibulo-cerebellum in the control of horizontal extraocular muscles using pseudorabies virus: I. Flocculus/ventral paraflocculus. *Neuroscience* (2004) https:/doi.org/10.1016/j.neuroscience.2004.01.051.
119. M. Schonewille, *et al.*, Zonal organization of the mouse flocculus: Physiology, input, and output. *J. Comp. Neurol.* (2006) https:/doi.org/10.1002/cne.21036.
120. J. Voogd, D. R. W. Wylie, Functional and Anatomical Organization of Floccular Zones: A Preserved Feature in Vertebrates. *J. Comp. Neurol.* (2004) https:/doi.org/10.1002/cne.11022.

Chapter 2

The basal interstitial nucleus (BIN) of the cerebellum provides diffuse ascending inhibitory input to the floccular granule cell layer

Dick Jaarsma, François G. C. Blot, Bin Wu, Subramanian Venkatesan, Jan Voogd, Dies Meijer, Tom J.H. Ruigrok, Zhenyu Gao, Martijn Schonewille, and Chris I. De Zeeuw

Abstract

The basal interstitial nucleus (BIN) in the white matter of the vestibulocerebellum has been defined more than three decades ago, but has since been largely ignored. It is still unclear which neurotransmitters are being used by BIN neurons, how these neurons are connected to the rest of the brain and what their activity patterns look like. Here, we studied BIN neurons in a range of mammals, including macaque, human, rat, mouse, rabbit and ferret, using tracing, immunohistological and electrophysiological approaches. We show that BIN neurons are GABAergic and glycinergic, that in primates they also express the marker for cholinergic neurons choline acetyl transferase (ChAT), that they project with beaded fibers to the glomeruli in the granular layer of the ipsilateral floccular complex, and that they are driven by excitation from the ipsilateral and contralateral medio-dorsal medullary gigantocellular reticular formation. Systematic analysis of co-distribution of the inhibitory synapse marker VIAAT, labeled BIN axons and Golgi cell marker mGluR2 indicate that BIN axon terminals complement Golgi cell axon terminals in glomeruli, accounting for a considerable proportion (> 20%) of the inhibitory terminals in the granule cell layer of the floccular complex. Together, these data show that BIN neurons represent a novel and relevant inhibitory input to the part of the vestibulocerebellum that controls compensatory and smooth pursuit eye movements.

Significance statement

In this study we uncover the connectivity and activity of a neglected population of neurons identified in the macaque cerebellum and named the basal interstitial nucleus (BIN). We characterized BIN neurons in a variety of mammalian species, ranging from mice to men. BIN neurons receive excitatory input from the medullary reticular formation and provide GABAergic input to granule cells in the flocculus, i.e. part of the vestibullocerebellum controlling compensatory eye movements. Our data disclose a novel inhibitory pathway in the cerebellum, and further outline the variability of the microcircuitry of different parts of the cerebellar cortex.

Author contributions

DJ, designed research and wrote the paper; DJ, FB, BW, TJHR, MS and ZG performed research; MS, DM, JV, TJHR, CIdZ contributed unpublished reagents/analytic tools; DJ, FB, ZG, SV analyzed data; CIdZ edited the paper.

The basal interstitial nucleus (BIN) of the cerebellum provides
diffuse ascending inhibitory input to the floccular granule cell layer.

2

Introduction

The cerebellar cortex is well known for its relatively simple stereotyped trilaminar histo-architecture and sagittally organized modules (Voogd and Glickstein, 1998; Cerminara *et al.*, 2015), and represents a powerful model system for investigating the organization and computations of complex central nervous system circuitries (Dean *et al.*, 2010; De Zeeuw *et al.*, 2011; Gao *et al.*, 2012). The cerebellar cortex receives two main types of excitatory afferent systems, the climbing fiber system and the mossy-parallel fiber system, that converge on a single output neuron, the Purkinje cell that in turn provides inhibitory control of the cerebellar and vestibular nuclei. Climbing fibers arise from the inferior olive and innervate about 8-15 Purkinje cells each, providing an exceptionally strong direct synaptic connection with well over ~1,000 release sites distributed over a large portion of the dendritic tree (Palay and Chan-Palay, 1974; Davie *et al.*, 2008; Gao *et al.*, 2012). Mossy fibers originate from various sources in the brainstem and spinal cord and modulate Purkinje cell activity indirectly via the granule cells and inhibitory interneurons (Jelitai *et al.*, 2016). With about 100-200 rosettes per mossy fiber, each innervating about 10-20 granule cells that in turn may form synaptic terminals with more than 500 Purkinje cells, the mossy fibers represent a highly divergent system (Harvey and Napper, 1988; Jakab and Hamori, 1988; Rancz *et al.*, 2007; Gao *et al.*, 2012). One of the key questions regarding the cerebello-cortical circuitry is how mossy fiber activity is translated into granule cell activity and subsequently integrated into Purkinje cell activity (Powell *et al.*, 2015; Valera *et al.*, 2016; Sudhakar *et al.*, 2017).

Mossy fibers are morphologically heterogeneous, encode diverse modalities and may evoke greatly distinct patterns of excitatory responses in granule cells across different parts of the cerebellar cortex (Arenz *et al.*, 2009; Huang *et al.*, 2013; Chabrol *et al.*, 2015; Gao *et al.*, 2016). Therefore, it is feasible that also the down-stream cerebellar cortical circuitries display modality and task-depending variabilities (Arenz *et al.*, 2009; Witter and De Zeeuw, 2015; Valera *et al.*, 2016). For example, the activity patterns and learning mechanisms of different cerebellar modules may be dominated by Purkinje cells with different intrinsic electrophysiological and biochemical properties (Zhou *et al.*, 2014; Cerminara *et al.*, 2015; De Zeeuw and Ten Brinke, 2015). In addition, the flocculus and nodulus of the vestibulocerebellum, which are involved in compensatory eye and body movements (Ito, 1982; Schonewille *et al.*, 2006; Lisberger, 2009; Voogd *et al.*, 2012) show a marked enrichment of unipolar brush cells (UBCs), an excitatory granular layer interneuron, which can prolong the excitatory drive of the mossy fiber system

(Gao *et al.*, 2012; Sekerková *et al.*, 2014; van Dorp and De Zeeuw, 2015; Zampini *et al.*, 2016). Furthermore, there is evidence for heterogeneity of inhibitory granule cell layer interneurons across distinct lobules (Neki *et al.*, 1996; Simat *et al.*, 2007; Ankri *et al.*, 2015; Eyre and Nusser, 2016).

In the present study, we show that the granule cell layer of the flocculus receives an inhibitory input from a hitherto largely neglected population of neurons, the basal interstitial nucleus (BIN), which was originally identified by Langer in macaque (Langer *et al.*, 1985; Langer, 1985). We found that BIN cells in human, rodents, ferret and rabbit are, just like in macaque, mainly located in the white matter of the lateral vestibulocerebellum, and that they are GABAergic and glycinergic. In addition, we show in rodents that BIN neurons receive a relevant and unique excitatory input from the medio-rostral medullary reticular formation. Our data indicate that the BIN represents a novel inhibitory afferent system, which may play an essential role in the proper conversion of mossy fiber activity into Purkinje cell firing in the flocculus.

Materials and Methods

Primary antibodies, mutant mouse models and key resources are summarized in Table 1.

<u>Animals:</u>

All animal experiments were performed in accordance with the guidelines the Dutch national and European legislation and were approved by the animal welfare committee for animal experiments of the Erasmus Medical Center. Male and female C57BL/6 mice, aged 2- 6 months of age, were obtained from the ErasmusMC animal core facility. BALB/c mice were from Charles River. GlyT2GFP transgenic mice that express enhanced green fluorescent protein under the control of the glycine transporter type 2 promoter were kindly provided by Dr. Fritschy (Zeilhofer *et al.*, 2005) and maintained as hemizygotes in C57BL/6 background in the ErasmusMC animal core facility. VGluT2-ires-Cre knock-in mice, generated by Dr. Lowell (Vong *et al.*, 2011), were obtained from Jackson Laboratories (JAX#016963), and maintained as homozygotes in the Erasmus MC animal core facility. Young (3-4 weeks) and adult (3-6 months) male Wistar rats were obtained from Charles River. Animals were group housed until surgery, fed ad libitum, and kept at 12:12 light/dark cycle.

The basal interstitial nucleus (BIN) of the cerebellum provides diffuse ascending inhibitory input to the floccular granule cell layer.

2

Cerebella from adult pigmented Dutch belted rabbits (n = 2), ferret (n = 2), and macaque monkey (n = 4) were derived from animals used in other studies (Jaarsma *et al.*, 1995; Ruigrok *et al.*, 2011; van Riel *et al.*, 2013; Siegers *et al.*, 2014).

Human tissue:

Human cerebella were obtained via the Dutch National body donation program. Donors gave their informed and written consent to the donation of their bodies to the Erasmus MC for research and education purposes. In this study we used cerebellar tissue from two male donors who died at 74 and 78 years of age. Cerebellar specimens were dissected within 48 h following death and fixed in formalin for 6-8 weeks.

Stereotaxic injections:

For stereotaxic injections of Cholera toxin B-subunit (CTB) in rat flocculus, animals (n = 2) were anesthetized with an intraperitoneal injection of thiazinehydrochloride (3 mg/kg) and ketamine (100 mg/kg), placed in a stereotactic frame, and their caudal vermis was exposed by removing overlying skin and neck muscles and opening of the atlanto-occipital membrane and dura. Carprofen (Rimadyl Cattle i.p. 5 mg/kg) and lidocaine (s.c. 0,4 mg/ml) were used to reduce perisurgical pain. The flocculus was approached by a glass micropipette (tip diameter 10 - 20 μm), placed horizontally at an angle of 50 degrees with the rostrocaudal axis, and penetrating the cerebellum 6.5 mm starting from the midline at the border of lobule IX-B and -C (Ruigrok, 2003). 100 nl CTB (1% w/v in phosphate buffered saline, pH 7.2, 0.1 M) was injected with mechanical pressure at a speed of 10 nl/min. After injection, the pipette was left in place for >10 minutes before being slowly withdrawn. After a survival period of 5 to 7 days, rats were deeply anesthetized with an overdose of Nembutal (200 mg/kg) and transcardially perfused with an initial flush of 500 ml 0.9% saline, followed by 1 liter of 4% paraformaldehyde (PFA) in 0.12 M phosphate buffer (PB, pH 7.4).

Methods for stereotaxic injections in mice were largely as previously reported (Schonewille *et al.*, 2006; Boele *et al.*, 2013; Gao *et al.*, 2016). During surgery mice were anesthetized with a mixture of isoflurane/oxygen (5% for induction, 1.5-2.0% for maintenance), while carprofen (Rimadyl Cattle i.p. 5 mg/kg), buprenorphine (Temgesic, i.p. 0.05 mg/kg), lidocaine (s.c. 0,4 mg/ml) and bupivacaïne (s.c. 0,1 mg/ml) were applied to reduce perisurgical pain. Ophthalmic ointment was applied to the eyes to prevent corneal drying

TABLE 1 Reagents and resources

Antibody (concentration)	Immunogen	Source, catalog #, RRID
Ms anti-calbindin (1:10000)	Bovine kidney calbindin-D	Sigma, C8666; RRID:AB_2313712
Rabbit anti-calbindin (1:10000)	Recombinant rat calbindin D-28k	Swant, CB38; RRID:AB_10000340
Rabbit anti-calretinin (1:5000)	Recombinant human calretinin-22k	Swant, 6B3; RRID:AB_10000320
Goat anti-CTB (1:5000)	Purified cholera toxin B subunit	List Labs, #703; RRID:AB_2313637
Goat anti-ChAT (1:500)	Purified ChAT from human placenta	Millipore, AB144P; RRID:AB_11214092
Rabbit anti-GABA (1:1000)	GABA conjugated to BSA	Sigma, A2052; RRID:AB_477652
Rabbit anti-GAD65/67 (1:2000)	rat GAD65 C-terminus (aa572-585)	Millipore, AB1511, RRID:AB_90715
Ms anti-GAD67, clone 1G10.2 (1:1000)	Recombinant GAD67 protein	Millipore, MAB5406; RRID:AB_2278725
Rabbit anti-GFP (1:5000)	Purified GFP from Aequorea Victoria	AbCam, #290; RRID:AB_303395
Rat anti-Lgi2 (1:10 culture supernatant)	Lgi2-Fc fusion protein	Dies Meijer, clone Lgi2-10D6
Ms anti-mGluR2 Clone mG2Na-s (1:2000)	GST-fusion protein containing aa87-134 of mouse mGluR2	AbCam, ab15672; RRID:AB_302021
Rat anti-muscarinic M2 receptor, clone M2-2-B3 (1:500)	GST-fusion protein containing i3 loop (aa225-359) of M2 receptor	Millipore, MAB367; RRID:AB_94952
Rabbit anti-Necab1 (1:1000)	Recombinant human Necab1 fragment (aa206-278)	Sigma, HPA023629; RRID:AB_1848014
Ms anti NeuN, clone A60 (1:4000)	Purified cell nuclei from mouse brain	Millipore, MAB377; RRID:AB2298772
Ms anti-Neurogranin, clone 898502 (1:100)	Recombinant human neurogranin	R&D systems, MAB7947
Rabbit anti-Neurogranin (1:2000)	Recombinant rat neurogranin	Millipore, AB5620; RRID:AB_91937
Guinea pig anti-VIAAT (1:1000)	Recombinant rat VIAAT fragment (aa2-115)	Synaptic Systems, 131004;RRID: AB_887873
Rabbit anti-VIAAT (1:1000)	Peptide corresponding to aa75-87 of rat VIAAT	Synaptic Systems, 131003;RRID: AB_887869
Guinea Pig anti-VGluT1 (1:4000)	Unspecified peptide from rat VGluT1	Millipore, AB5905;RRID: AB_2301751
Rabbit anti-VGluT1 (1:4000)	Recombinant rat VGluT1 fragment (aa456-560)	Synaptic Systems, 135 002,RRID: AB_2315546
Guinea pig anti-VGluT2 (1:2000)	KLH-conjugated peptide corresponding to rat VGluT2 C-terminus	Millipore, AB2251; RRID:AB_1587626
Ms anti-VGluT2 (1:1000)	Recombinant rat VGLUT2	Millipore, MAB5504; RRID:AB_2187552
Rabbit anti-VGluT2 (1:2000)	Recombinant rat VGluT2 fragment (aa510-582)	Synaptic systems, 135402; RRID: AB_2187539
Tracers	**Source**	**Catalog #, RRID**
Cholera toxin b-subunit (CTB), low salt	List Biological Labs	#104
biotin dextran amine 10 kDa (BDA-10000)	ThermoFisher	D1956; RRID:AB_2307337
AAV-vector	**Source**	**Catalog #**
AAV1.CAG.CI.eGFP.WPRE.rBG	Penn Vector Core	AV-1-PV1963
AAV1.CAG.Flex.eGFP.WPRE.bGH (AllenInstitute854)	Penn Vector Core	AV-1-ALL854
Mutant mouse models	**Source/reference**	**MGI number/Catalog #**
GlyT2-GFP	Zeilhofer et al., 2005	MGI:105090
VGluT2-ires-cre	Jackson Laboratories	JAX#016963

and damage. Body temperature was monitored and kept constant at 37°C throughout the entire surgical procedure. Mice were positioned on a custom-made mouse stereotaxic head-holding frame following the Paxinos mouse brain atlas (Paxinos and Franklin, 2001), small craniotomies (diameter ~3 mm) were made in corresponding sites, and injections were performed using glass pipettes (tip opening 8 - 15 µm) with mechanical pressure or iontophoresis. After each injection, the pipette was left in place for >10 minutes before being slowly withdrawn. For retrograde tracing, 40-100 nl of CTB (1% w/v in phosphate buffered saline, pH 7.2) was injected with mechanical pressure (speed 10 nl/min). For anterograde tracing biotinylated dextran amine 10 kDa (BDA, 10% w/v in saline, ThermoFisher) was applied with mechanical pressure (20-100 nl) or iontophoresis (pulses of 4 µA, 10 min). Alternatively, anterograde tracing was performed using AAV viral vector expressing enhanced GFP (Harris *et al.*, 2012; Wang *et al.*, 2014): 50-100

The basal interstitial nucleus (BIN) of the cerebellum provides diffuse ascending inhibitory input to the floccular granule cell layer.

2

nl purified AAV1.CAG.CI.eGFP.WPRE.rBG (AAV-GFP, 10^{12}-10^{13} GC/ml) or AAV1.CAG.Flex.eGFP.WPRE.bGH (AAV-Flex-GFP), purchased from UPenn Vector Core (Table 1, https://pennvectorcore.med.upenn.edu/gtp/default.php), were pressure injected. To examine BIN axons in the flocculus, AAV-GFP was injected in C57BL/6 mice (n=10) using the following coordinates: 1.4 posterior of Lambda, 2.4 mm lateral and 2.6 mm ventral of the pial surface. The same coordinates were used for CTB injections in the BIN of C57BL/6 mice (n=4) to characterize brain stem neurons that innervate BIN neurons. This retrograde approach was complemented by an anterograde tracing approach with BDA injections made throughout the medulla oblongata and the pontine reticular formation of C57BL/6 mice (n=20). Coordinates of BDA injections in the medullary gigantocellular reticular nucleus that resulted in labeling of fibers innervating BIN neurons were 2,3-2,6 mm posterior of lambda, 0,2-0,4 mm lateral, 4,6 - 4,8 ventral of the pial surface. These coordinates were also used for AAV-Flex-GFP injections in VGluT2-Cre mice (n=2) to demonstrate that medullary gigantocellular reticular nucleus projections to BIN neurons were VGluT2+ neurons. For a subset of BDA injections (n = 15 mice) the squamosal part of the occipital bone was freed and the atlanto-occipital membrane and dura were opened, to approach the medulla oblongata from caudal with the pipette positioned at an angle of 45° in the rostro-caudal direction. For injection in the inferior olive, penetrations were made with reference to the obex and guided by electrophysiological recording, and injections were made using iontophoresis (Ruigrok *et al.*, 1992). Also injection in the medial vestibular prepositus hypoglossal nuclei were guided by electrophysiological recordings. CTB injections in the floccular cortex were performed in alert, head-fixed restrained GlyT2GFP (n=3) and C57BL/6 (n=2) mice placed on a platform in the center of a random dotted drum to enable identification of floccular zones on the basis of complex spike modulation of Purkinje cells triggered by optokinetic stimulation (Schonewille *et al.*, 2006). In these mice, a head fixation pedestal was fixed to the skull with dental cement (Charisma, Heraeus Kulzer, NY, USA) 5 days prior to injection, and a recording chamber was made following craniotomy of the occipital bone (Schonewille *et al.*, 2006).

Post-injection survival times for injected mice were 5-8 days (CTB, BDA) or 2-3 weeks (AAV). Mice were deeply anesthetized with an overdose of Nembutal (i.p. 200 mg/kg), transcardially perfused with 20 ml saline followed by 100 ml 4% PFA in 0.12 M PB, and brains were removed, post-fixed for 2 h in 4% PFA, and embedded in 12% gelatin further processed for histology.

Immunohistology:

The following material was processed for immunohistology: brains from mouse and rat who received tracer injections; brains from additional transcardially 4% PFA perfused mice (n= 12; C57BL/6 or BALB/c), rats (n =4), rabbits (n=2) and macaque (n= 4), immersion (6-8 weeks) formalin-fixed brains from ferret (n=2), and formalin-fixed blocks from humans containing the flocculus, tonsils and deep nuclei. Brain samples were embedded in 11% gelatin (type B, J.T. Baker, #2124), incubated overnight in 30% sucrose at 4 °C, and cut into 40 or 50 μm coronal sections on a sliding freezing microtome (Leica SM 2000R). Sections were serially collected in 8 (mouse, rat), 20 (ferret, rabbit, macaque) or 40 (human) vials with phosphate buffered saline (PBS, pH 7.2) such that each vial contained a complete series of sections. Sections were processed free-floating for diaminobenzidine (DAB, 0.05%)-immunoperoxidase histochemistry or immunofluorescence (Kuijpers *et al.*, 2013). Following preincubation in PBS containing 0,4% Triton X-100 (PBST) and normal horse serum (NHS) and for 1 h at room temperature, sections were incubated 48-60 h at 4°C with the primary antibodies in PBST with 2% NHS. For immunoperoxidase histochemistry, sections were subsequently incubated with biotinylated secondary antibodies raised in donkey (diluted 1:400; Jackson, Burlingame, CA) for 2 h at room temperature, followed by incubation in avidin-biotin-immunoperoxidase complex (ABC; diluted 1:400; Vector Laboratories) and the reaction with DAB as described by the manufacturer. To visualize BDA in anterograde tracing experiments, sections following the preincubation step, were incubated with ABC and processed for DAB staining. Sections were mounted on glass-slides, air-dried, and counterstained with Thionin (1%) to outline cell nuclei and Nissl substance in neurons. Immunoperoxidase-stained sections were analyzed using a Leica (Nussloch, Germany) DM-RB microscope, or scanned with a Hamamatsu NanoZoomer 2 whole slide imager and analyzed with NDP.view (Hamamatsu) software. Immunoperoxidase histochemistry was performed with series of sections of BDA and CTB tracing experiments to examine injection area and map projection fibers and retrogradely labeled neurons, respectively. In addition, immunoperoxidase histochemistry was used for mapping BIN neurons using the following antibodies: goat anti-ChAT (1:500; Millipore AB144P), rabbit anti-Glutamic acid decarboxylase 65 and 67 (GAD; 1:2000; Millipore AB1511), mouse anti-GAD67 (1:1000; Millipore MAB5406), rabbit anti-Necab1 (1:1000; Sigma HPA023629), or mouse anti-NeuN (1:2000; Millipore).

For immunofluorescence, sections were incubated with multiple combinations of primary antibodies (see table 1), followed by incubation with fluorescently-labeled secondary antibodies raised in donkey, diluted 1:400 in

The basal interstitial nucleus (BIN) of the cerebellum provides diffuse ascending inhibitory input to the floccular granule cell layer.

2

PBST-2%NHS, and carrying Alexa Fluor 405 (A405), A488, Cy3-, or A647 as fluorophores (Jackson Immunoresearch or ThermoFisher). Typically, in triple labelling experiments A488, Cy3 and A647-labeled secondary antibodies were used, and section were counterstained with Dapi to visualize cell nuclei, while in quadruple labelling experiments A405-labeled secondary antibody was used, and Dapi was omitted. In sections from BDA tracing experiments, BDA was labeled with A488 streptavidin (ThermoFisher). Sections stained for immunofluorescence were mounted on coverslips, placed on glass slides with Vectashield mounting medium, and were examined with Zeiss LSM 510 and LSM700 confocal laser scanning microscopes.

Antibody characterization:

Primary antibodies used for immunohistology were from commercial sources with the exception of a rat monoclonal antibody against Lgi2 (Table 1). The commercial primary antibodies have been well characterized in previous studies (Jaarsma *et al.*, 1995; Jaarsma *et al.*, 1996; Singec *et al.*, 2004; Simat *et al.*, 2007; Gao *et al.*, 2016; Zhang *et al.*, 2016). Validation of labeling specificity in this study is based on the expected distribution pattern compared to these studies. The rat-anti Lgi2 antibody (clone Lgi2-10D6) was raised against a full length Lgi2-Fc fusion protein. Immunization of rats with antigen, and production of hybridoma cell lines was performed by Absea (http://www.absea-antibody.com). The labelling specificity for Lgi2 was determined using cerebellar sections from Lgi2 knockout mice, which did not show any labelling. Furthermore, the labelling pattern in the cerebellar cortex is consistent with the expected distribution based on mRNA expression in Allan Brain Atlas (Lein *et al.*, 2007). Further details of the production and validation of the rat-anti Lgi2 antibody will be reported elsewhere.

Immuno-electron microscopy:

Two mice receiving an AAV-GFP injection in the BIN were perfused with 100 ml 0.12 M PB buffered 4% PFA with 0.5% glutaraldehyde, and further processed for anti-GFP immuno-peroxidase DAB electron microscopy: the cerebellum was removed, post-fixed overnight in 4% PFA, and cut in 60 μm coronal sections on a vibratome. Sections were subjected to a freeze-thaw procedure to improve antibody penetration and incubated for 96 h at 4°C with rabbit-anti-GFP antibody (1:5000, Abcam) in Tris-buffered saline (TBS, pH7.4), followed by incubation with biotinylated-goat-anti-rabbit secondary antibody (1:200 in TBS, overnight at 4°C), and incubation with ABC (1:400

in TBS overnight at 4°C), and subsequent reaction with DAB. Subsequently, sections were rinsed and post-fixed in 1% osmium tetroxide, stained with 1% uranyl acetate, dehydrated and embedded in araldite (Durcupan ACM; Fluka, Buchs, Switzerland). Semi-thin (500 nm) and ultrathin (50-70 nm) sections were cut on an ultramicrotome (Leica, Wetzlar, Germany). Semi-thin were mounted on glass slides and stained with toluidine blue and analyzed light-microscopically. Ultrathin sections were mounted on formvar-coated grids, contrasted with 2% uranyl acetate and 1% lead citrate (Fluka), and examined using a Phillips CM100 electron microscope at 80 kV (Philips, Eindhoven, Netherlands). A subset of grids were processed for GABA immunogold labelling. The grids were rinsed in TBS with 0.1% Triton X-100, pH 7.6 (TBST), and incubated overnight at 4ºC with rabbit anti-GABA (Sigma, 1:1500 in TBST) antibody. The grids were subsequently rinsed twice with TBST and incubated for 1 h at room temperature in goat anti-rabbit IgG labeled with 10 nm gold particles (Aurion) diluted 1:50 in TBST.

<u>Slice recording:</u>

3-4 weeks old Wistar rats were decapitated under isoflurane anesthesia. 300 µm thick cerebellar coronal slices containing the flocculus were cut on a vibratome (VT1200s, Leica, Wetzlar, Germany) in icecold slicing medium containing (in mM): 240 Sucrose, 5 KCl, 1.25 Na_2HPO_4, 2 $MgSO_4$, 1 $CaCl_2$, 26 $NaHCO_3$ and 10 D-Glucose, bubbled with 95% O_2 and 5% CO_2. Slices were incubated at 34°C for 1 h in the oxygenated ACSF containing (in mM): 124 NaCl, 2.5 KCl, 1.25 Na_2HPO_4, 1 $MgSO_4$, 2 $CaCl_2$, 26 $NaHCO_3$ and 25 D-Glucose and kept at room temperature (21 ± 1 °C) before use. Experiments were performed with a constant flow of oxygenated ACSF (1.5-2.0 ml/min) at 34 ± 1 °C. Putative BIN neurons were identified under DIC visualization based on their distribution in the floccular white matter, and their relative large size compared to other white matter cells. Patch-clamp recordings were performed using an EPC-10 double amplifier controlled by the Patchmaster software (HEKA electronics, Lambrecht, Germany) (Gao *et al.*, 2016). All recordings were low-pass filtered at 5 kHz and digitized at 20 kHz. Borosilicate glass pipettes (WPI) were filled with intracellular solution containing the following (in mM): 120 K-gluconate, 9 KCl, 10 KOH, 3.48 $MgCl_2$, 4 NaCl, 10 HEPES, 4 Na_2ATP, 0.4 Na_3GTP and 17.5 sucrose (pH 7.25) and had pipette resistances of 3-5 MΩ. Spontaneous action potential firing of BIN neurons were recorded in loose cell-attached mode prior to attaining the whole-cell configuration. After obtaining stable whole-cell configuration, a series of constant depolarizing current pulses with

The basal interstitial nucleus (BIN) of the cerebellum provides
diffuse ascending inhibitory input to the floccular granule cell layer.

2

incremental amplitudes (20 pA/step) was applied to each cell to elicit voltage
action potential firing patterns. For voltage clamp recordings of spontaneous
EPSCs (sEPSCs), cells were recorded for >3 mins at -65 mV. At the end of
the recording, a 5 mV hyperpolarizing voltage step was applied and the cell
capacitance were calculated based on the decay of capacitive current.

For morphological characterization of recorded BIN neurons,
neurobiotin (1% w/v) was added to the intracellular solution. After recording,
slices were fixed in 4% PFA at room temperature for 2 h, washed in PBS
overnight, and processed for immunofluorescence with guinea-pig anti
VGluT1, mouse anti-mGluR2, and rabbit α-GAD as primary antibodies; A405
donkey anti-guinea-pig IgG, Cy3 donkey anti-mouse, and Cy5 donkey anti-
rabbit as secondary antibodies; and A488 streptavidin (1:400, ThermoFisher)
to visualize neurobiotin. Slices were carefully mounted in Vectashield and
examined with LSM 700 confocal microscopes (Carl Zeiss, Jena, Germany).
The slices were scanned at 0.5 x 0.5 x 2 μm (xyz) resolution using a Plan-
Apochromat 20x (n.a. 0.8) objective and the tile function. The confocal stacks
were used to trace the dendritic and axonal arborization of biocytin filled cells
using Neurolucida software (MicroBrightField, Inc., Colchester, VT).

Analyses:

To map and count BIN neurons in different species, series of sections
processed for bright-field microscopy were examined and plotted using an
Olympus microscope fitted with a Lucivid miniature monitor and Neurolucida
software (MicroBrightField, Inc., Colchester, VT), while fluorescently-
labeled section selected areas were scanned at a 0.625 x 0.625 x 2.5 μm
(xyz) resolution using a LSM 700 confocal microscopes (Carl Zeiss, Jena,
Germany) with Plan-Apochromat 20x (n.a. 0.8) objective and the tile function,
and analyzed using ImageJ. To plot and count BIN neurons in macaque
cerebellum we used 1 in 5 transverse thionin-stained serial sections (section
thickness 40 μm, 160 μm interval between sections), and 1 in 10 GAD- and
ChAT-immunoperoxidase stained series (360 μm between sections). Only
cells with a visible nucleus were counted. In case of human cerebellum,
ChAT-stained serial sections in a final frequency of 1 in 10 (section thickness
50 μm, 450 μm interval between section) were used for counting and plotting
BIN neurons. For mapping the distribution of BIN neurons in rat, we used 1 in
4 CTB-immunoperoxidase/thionin stained series of transverse sections (120
μm interval) of previously documented (rat #798, rat #802, rat #836; Ruigrok,
2003) CTB experiments, and 1 in 4 CTB/GAD immunofluorescent stained
series from 2 additional CTB tracing injections in rat flocculus (rat B1, rat B2).

To estimate the relative size of the injection in each section, the ratio of the area of the injection occupying the floccular granule cell layer, and the area of the entire floccular granule cell layer were determined, and the means of these ratio's were calculated for each experiment. To count the total number of BIN neurons in rat cerebellum, additional 1 in 4 series stained for thionin, or GAD/NeuN immunofluorescence were used. For mapping and counting BIN neurons in mouse cerebellum, we used 1 in 4 series of transverse fluorescent sections (120 µm interval) labeled for CTB/GlyT2GFP (n = 3 mice) or CTB/Necab1 (n = 2 mice). For mapping and counting Golgi cells in the vermis 4-5 and the flocculus we used 1 in 4 series of transverse section from GlyT2GFP mice (n=4) stained for Lgi2/Necab1 or Lgi2/neurogranin.

For mapping and counting BIN neurons in ferret, we used 40 µm GAD-immunoperoxidase stained sections at frequencies of 1 in 5 (160 µm interval). For mapping BIN neurons in rabbit, we used previously documented WGA-HRP experiments with tracer injections in the floccular cortex (K227, K244, K358, K360; Tan *et al.*, 1995) and 40 µm GAD-immunoperoxidase stained sections at frequencies of 1 in 10 (360 µm interval between sections).

To analyze anterograde BDA tracing experiments with injections made throughout the brainstem, 1 in 4 sections were processed for ABC peroxidase-DAB staining to map the injection area, and examine the floccular white matter for the presence of BDA+ beaded fibers contacting BIN neurons. In case of the presence of BDA+ beaded fibers, adjacent series of sections were processed for triple labeling fluorescence to outline BDA+ fibers (visualized with A488 streptavidin), VGluT2+ excitatory synaptic boutons, and BIN neurons (with either anti-Muscarinic M2 or anti-Necab1 antibodies). BIN neurons were examined for the presence of BDA+VGluT2+ and BDA-VGluT2+ boutons using a LSM 700 confocal microscope with Plan-Apochromat 40x (n.a. 1.3) and 63x (n.a. 1.4) oil objectives. Only BDA+VGluT2+ and BDA-VGluT2+ boutons contacting BIN cell bodies and their proximal dendrites were analyzed.

To examine the proportion of VIAAT+ axon terminals in macaque flocculus and dorsal paraflocculus that where either ChAT+ or mGluR2+, Z-stacks of 20 x 20 x 10 µm (12 optical sections of 1,5 µm thickness) of glomeruli were collected from ChAT/VIAAT/mGluR2 stained sections using an 63x oil objective. Glomeruli were identified on the basis of a grossly circular arrangement of VIAAT+ boutons (e.g. Fig. 2g,h). A contour was drawn around the glomerular profile and VIAAT+ boutons within the contour were examined for the presence of ChAT and mGluR2 signal. To estimate the proportion of VIAAT+ axon terminals in mouse cerebellar lobules that where mGluR2+, Z-stacks of 100 x 100 x 3 µm (3 optical sections of 1,5 µm

The basal interstitial nucleus (BIN) of the cerebellum provides
diffuse ascending inhibitory input to the floccular granule cell layer.

2

thickness) of granule cell layer 2 μm below the surface of the section were collected from GFP/VIAAT/mGluR2 triple labeled sections using the 63x oil objective. Stacks were made in lobule III of the anterior vermis, the nodulus and the flocculus of a mice showing high levels of BIN axonal labelling in the flocculus following AAV-GFP injections in the BIN (VBIN2, VBIN3, VBIN5). VIAAT, GFP and mGluR2 signals were converted to binary images using the 'internodes' thresholding function in imageJ, and the area showing VIAAT labeling, as well as showing either VIAAT-mGluR2 or VIAAT- GFP double-labeling were determined per Z-stack (= means of 3 optical sections).

Allen mouse brain atlas:

We screened the Allen Mouse Brain Atlas (Allen Institute for Brain Science, Seattle, WA; available from www.brain-map.org, (Lein *et al.*, 2007)) for genes expressed in the mouse BIN using the AGEA (Anatomic Gene Expression Atlas) viewer modus of Allen Brain Atlas with 10400, 4800, 3000 as the seed voxel coordinates and 1.0 as the expression threshold. This modus enabled efficient visual inspection of nearly 2000 genes for expression in intermediate-large cells in the floccular white matter of the anterior flocculus. The method of screening was not exhaustive and was biased towards genes with relatively low expression in the granule cell layer, facilitating the detection of gene expression in the white matter. Genes with moderate to strong expression throughout the cerebellar white and grey matter, generally representing genes expressed by glia cells, were ignored.

Statistical analyses:

Statistical analyzes were performed with Graphpad Prism using Student's t-test and ANOVA. Data are expressed as Means ± SE.

Results

ChAT (choline acetyltransferase) immunostaining outlines the basal interstitial nucleus (BIN) in macaque cerebellum:

While analyzing the distribution of immunoreactivity of choline acetyltransferase (ChAT, the terminal biosynthetic enzyme for acetylcholine) in macaque cerebellum, we identified a group of ChAT+ cells dispersed in the white matter ventrolateral of the cerebellar nuclei (Fig. 1a). The

distribution and morphology of these ChAT+ neurons coincided with that of the basal interstitial nucleus (BIN), identified by Langer after retrograde tracing injections in the flocculus or the ventral paraflocculus (Langer *et al.*, 1985; Langer, 1985). Like BIN neurons, ChAT+ cells had relatively large polymorphic cell bodies (area = 441 ± 18 µm^2, 251-720; mean ± SE, range, n=40 cells), and formed a cluster that extended from the hilus of the ventral paraflocculus to the white matter of the most rostral folium of the nodulus, respectively, with most ChAT+ cells in the white matter medial of the stalk of the flocculus (Fig. 1a,f). While most BIN neurons had a fusiform elongated morphology with dendrites emanating from each end, other BIN neurons showed pyramidal and polygonal morphologies (Fig. 1b). Notably, ChAT+ cells were also observed in Group Y, medial of the BIN, but these cells were much smaller (104 ± 5 µm^2, mean ± SE, n=10 cells) and clearly distinguishable from ChAT+ BIN cells (Fig. 1c).   In accord with the notion that BIN neurons innervate the flocculus/ventral paraflocculus (also referred to as the floccular complex; see Voogd *et al.*, 2012), ChAT+ fibers in the BIN were oriented towards the white matter of the floccular complex, and a high density of ChAT+ fibers occurred in the white matter and granule cell layer of the floccular complex (Fig. 1a,d). In the granule cell layer, the ChAT+ fibers provided multiple beaded branches resulting in a dense plexus of ChAT+ varicose fibers (Figs 1d). These beaded ChAT+ fibers occurred throughout the floccular complex, but were absent in other cerebellar lobules, including the dorsal paraflocculus (Fig. 1e) and the nodulus. The density of ChAT+ fibers varied across different lobules of the floccular complex: grossly, ChAT+ fibers were more frequent in the flocculus than in the ventral paraflocculus and were denser in the basal than the apical part of individual folia (Fig.1f). Together, the data indicate that BIN neurons in macaque are ChAT+ and provide dense ChAT+ innervation of the granule cell layer in the floccular complex.

BIN neurons provide GABAergic input to the granule cell layer of the flocculus/ ventral paraflocculus:

        Further characterization of the neurochemical identity of macaque BIN neurons showed that BIN neurons also stained positive with anti-glutamic acid decarboxylase (GAD) antibody. GAD/ChAT double labeling showed that all ChAT+ BIN neurons stained positive for GAD (Fig. 2a, b), while an additional population of neurons inside the macaque BIN territory was negative for ChAT, but stained positive for GAD (Fig. 2a, b). These GAD+ChAT- BIN neurons showed the same size and morphologies as those
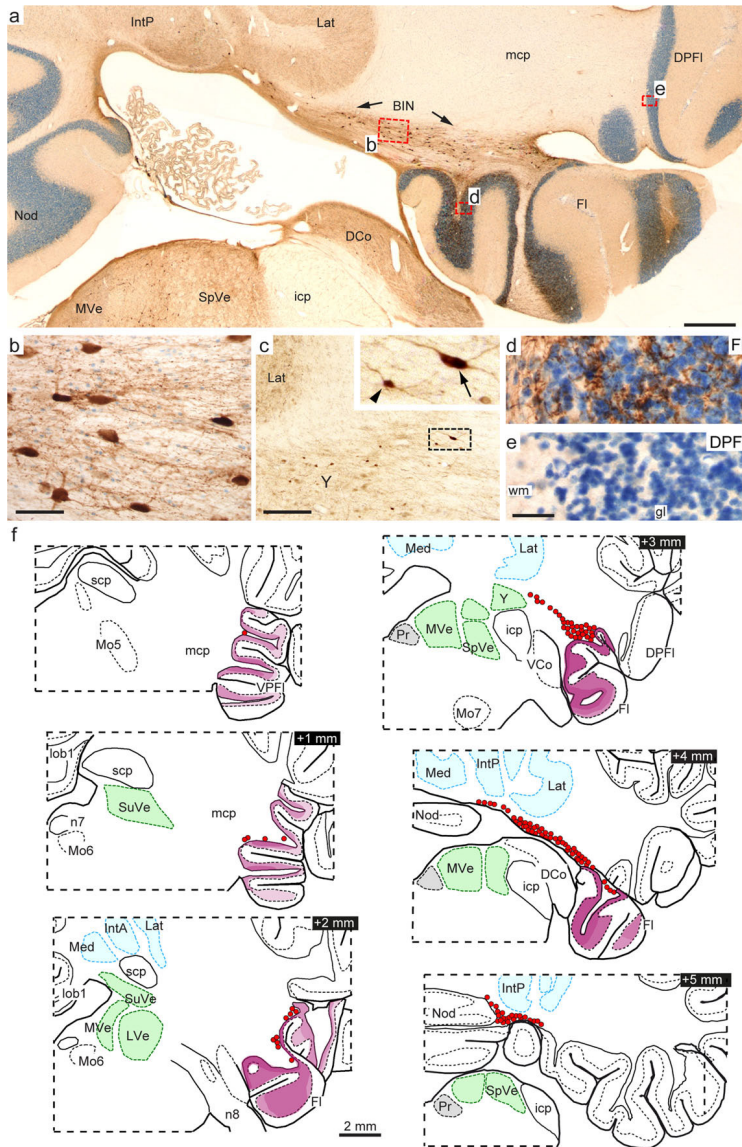
Figure 1. Choline Acetyltransferase (ChAT) immunostaining outlines the basal interstitial nucleus (BIN) in macaque cerebellum

a-e: Low-power (a) and high power (b-e) photomicrographs of ChAT immunoperoxidase diaminobenzidine (DAB) stained coronal sections of Macaque cerebellum illustrating intensely stained BIN neurons in the basal white matter between the flocculus and the cerebellar nuclei (a,b), and ChAT+ beaded fibers in the floccular granule cell layer (a,d). The photomicrograph in c illustrates that ChAT+ BIN neurons (arrow) are considerably larger than ChAT+ neurons in group Y (arrow head). No or minimal ChAT+ fibers occur in the dorsal paraflocculus (DPFl; a,e).

Sections are counterstained with thionin (blue).
f: Plots of ChAT+ BIN neurons (red dots) and relative density of ChAT+ beaded fibers (violet staining) in serial coronal macaque cerebellar sections. Cerebellar and vestibular nuclei are indicated in light blue and green, respectively.
Abbreviations: DCo, dorsal cochlear nucleus; DPFl, Dorsal paraflocculus; Fl, Flocculus; icp, inferior cerebellar peduncle; IntA, anterior interposed cerebellar nucleus; IntP, posterior interposed nucleus; Lat, lateral cerebellar nucleus; mcp, middle cerebellar peduncle; LVe, lateral vestibular nucleus; MVe, medial vestibular nucleus; Nod, Nodulus; Pr, prepositus hypoglossi; SpVe, spinal vestibular nucleus; SuVe, Superior vestibular nucleus.
Scale bars: a, 500 µm; c, 200 µm; b and e, 50 µm

of GAD+ChAT+ BIN neurons. Thus, the BIN in macaque may comprise 2 neurochemically distinct populations of neurons, GAD+ChAT+ and GAD+ChAT- neurons. Counting of serial ChAT and GAD immunoperoxidase stained sections indicated that there were about 1000 ($1.3 \pm 0.3 *10^3$, mean $\pm$ SE, n= 3) ChAT+ and 2000 ($2.2 \pm 0.2 *10^3$, n= 3) GAD+ BIN cells per half macaque cerebellum.

GAD/ChAT double labelling also showed that the cell bodies and proximal dendrites of BIN neurons were only sparsely covered by GAD+ nerve terminals. In this respect, BIN neurons were distinct from cerebellar nuclear neurons, whose cell bodies and proximal dendrites are densely innervated by GAD+ synaptic terminals from Purkinje cells axons (compare Fig. 2b and e). Analysis of GAD/ChAT double labelling in the floccular complex showed that ChAT+ axons in the granule cell layer were GAD+ (Fig. 2c), supporting the notion that ChAT+ fibers in these lobes are axons from BIN neurons. Moreover, these GAD+ChAT+ labeled axonal projections were morphologically distinct from ChAT+ mossy fibers in the nodulus that were GAD-negative (Fig. 2e). In contrast to previous monkey studies suggesting that ChAT+ fibers in the flocculus represent mossy fibers from the medial vestibular and the prepositus hypoglossal nuclei (Barmack *et al.*, 1992a; Barmack *et al.*, 1992b), we found virtually no ChAT+ fibers in the macaque flocculus that showed the typical mossy fiber morphology.

ChAT+ boutons in the flocculus/ventral paraflocculus did not stain positive for the mGluR2 metabotropic glutamate receptor (Fig. 2f), which is expressed by the majority of cerebellar Golgi cells, and is present on a large proportion of the GABAergic nerve terminals in the glomeruli (Neki *et al.*, 1996; Watanabe *et al.*, 1998; Simat *et al.*, 2007). Notably, glomeruli with ChAT+ boutons always also contained mGluR2+ boutons (Fig. 2f), indicating that BIN axon terminals complement Golgi cell axonal terminals in the same glomeruli. Triple staining of ChAT and mGluR2 with antibodies against VIAAT

The basal interstitial nucleus (BIN) of the cerebellum provides diffuse ascending inhibitory input to the floccular granule cell layer.

2

(vesicular inhibitory amino acid transporter, also termed vesicular GABA transporter, VGAT) to outline GABAergic/glycinergic inhibitory nerve terminals, showed that ChAT+ boutons, like mGluR2+ boutons, were VIAAT+ (Fig. 2g), further indicating that ChAT+ fibers in the macaque flocculus are GABAergic. In addition to ChAT+mGluR2-VIAAT+ and ChAT-mGluR2+VIAAT+ boutons we also found ChAT-mGluR2-VIAAT+ boutons in the floccular glomeruli (Fig. 2g). Analysis of 50 floccular glomeruli in ChAT/VIAAT/mGluR2 triple-stained sections showed that about two-thirds (64 ± 2 %; mean ± SE) of the VIAAT+ boutons were ChAT-mGluR2+, while about one-third of the VIAAT+ boutons were mGluR2-, consisting of ChAT+mGluR2- (21 ± 1.4%) and ChAT-mGluR2- (15 ± 1.7%) boutons. We also performed triple staining of ChAT and VIAAT with VGluT1 to outline mossy fiber nerve endings (rosettes). This staining indicated that the distribution of ChAT+VIAAT+ boutons in floccular glomeruli resembles that of ChAT-VIAAT+ boutons (Fig. 2h). Together these data indicate that a portion of inhibitory boutons in the macaque floccular glomeruli does not arise from mGluR2+ Golgi cells, and that about half of these mGluR2- boutons represent axon terminals from ChAT+ BIN neurons. For comparison, in the dorsal paraflocculus, which is not innervated by BIN afferents, we found more than 90% (94 ± 1%) of VIAAT+ boutons in the glomeruli to be mGluR2+.

In ChAT/VIAAT/mGluR2 stained sections we also noted ChAT+VIAAT+ boutons in glomeruli with a dendritic brush of unipolar brush cells (UBCs), which also may stain positive for mGluR2 (Jaarsma *et al.*, 1998). Double labeling for ChAT and calretinin, which outlines a subset of UBCs (Sekerková *et al.*, 2014), showed the presence of ChAT+ boutons surrounding calretinin+ UBC brushes (Fig. 2i). However, we also found calretinin+ brushes that were not surrounded by ChAT+ boutons. This was particularly evident in a region of the ventral paraflocculus that shows a dramatic enrichment of UBCs and virtually no ChAT+ fibers (Fig. 2j). These data indicate that ChAT+ boutons do not have a simple all or none relationship with glomeruli containing UBC dendritic brushes.

ChAT-staining outlines the BIN in human cerebellum:

To examine whether a BIN-like population of neurons also occurs in other species, we first examined human cerebellum. Using ChAT staining, we found a population of ChAT+ neurons in the basal white matter, reminiscent of BIN neurons in macaque (Fig. 3a,b). ChAT+ neurons were distributed in an area extending from the nodulus to the peduncles of the flocculus and the accessory paraflocculus (i.e. the human homologue of the macaque ventral paraflocculus; Voogd *et al.*, 2012), ChAT+ neurons being most abundant near

the base of the floccular peduncle (Fig. 3a,b). As in macaque, these ChAT+ neurons showed variable morphologies, had moderately large cell bodies (area = 533 ± 31 µm^2, 281-770; mean ± SE, range, n=20 cells), and stained positive for GAD (Fig. 3c,d). These data indicate that also in human cerebellum the BIN can be outlined using ChAT and GAD staining. Based on analysis of 1 out of 10 sections we estimate that about 5000 (4.6 ± 0.7*10^3; Mean ± SE, n= 2) ChAT+ BIN neurons occur on each side of the cerebellum in human. The quality of the GAD staining did not allow counting of GAD+ BIN cells in human series.

As in macaque, ChAT+ fibers emanating from the human BIN were oriented towards the white matter of the flocculus and the accessory paraflocculus, and the flocculus/accessory paraflocculus showed a correspondingly high density of ChAT+ fibers in the white matter as well as a dense network of ChAT+ beaded fibers in the granule cell layer (Fig. 3e,f). However, in contrast to macaque, the human cerebellum also showed a subset of Golgi cells that were ChAT+ (Fig. 3f,g; see also de Lacalle *et al.*, 1993), and, hence, ChAT+ innervation in the human flocculus/accessory paraflocculus may also derive from Golgi cells. The overall density of granular layer ChAT+ innervation in these lobules was higher than in other lobules. A particularly high density of ChAT+ fibers occurred in the areas of the floccular granule cell layer that contained ChAT+ Golgi cells (Fig. 3f), suggesting that in these areas ChAT+ axons are from both BIN neurons and Golgi cells. We were not able to further characterize the identities of ChAT+ boutons in the human floccular complex with reliable mGluR2 and VIAAT immuno-staining, probably due to limited possibilities of fixation and antigen epitope preservation of our human brain specimen.

Retrograde tracing and GAD-staining outlines the BIN in rat cerebellum:

To further examine the occurrence of BIN neurons in other species we moved to rat. No ChAT+ neurons are present in the white matter of rat cerebellum (Jaarsma *et al.*, 1996; Jaarsma *et al.*, 1997). However, following floccular cortical injections with cholera toxin B subunit (CTB) (Ruigrok, 2003), we identified retrogradely labeled neurons in the hilus and the white matter of the ipsilateral flocculus (Fig. 4a-c). These retrogradely labeled neurons occurred throughout the rostro-caudal extent of the floccular white matter (Fig. 4a), were moderately large in size, and had multipolar and fusiform morphologies (Fig. 4b,c) reminiscent of macaque BIN neurons. Furthermore, these retrogradely labeled white matter neurons were all GAD+ (Fig. 4d). Based on their localization in the white matter and their similarities with macaque BIN neurons, we designate these neurons the rat homologues of macaque BIN neurons (Ruigrok, 2003). Notably, no retrogradely labeled
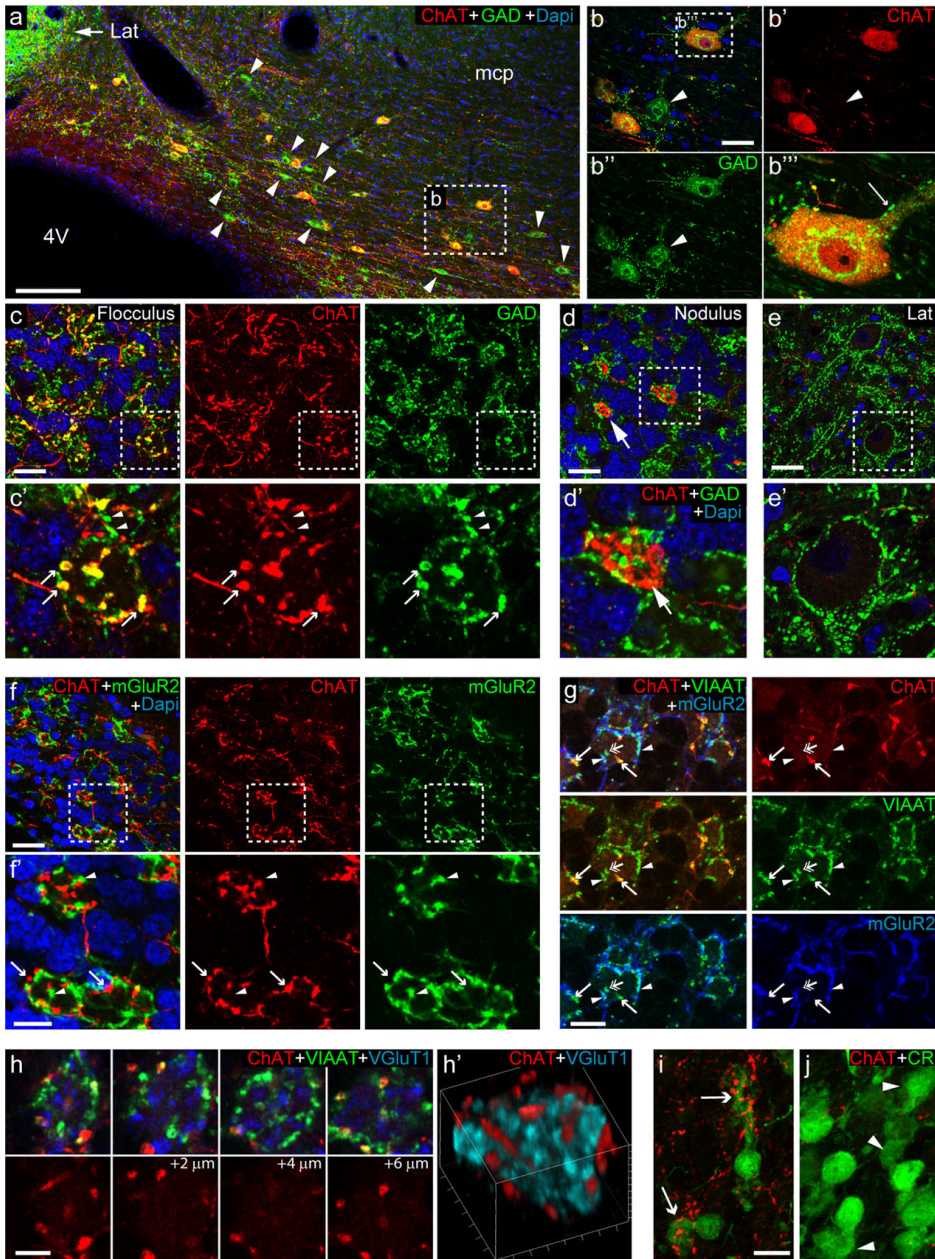
2

Figure 2. Macaque BIN neurons provide GABAergic input to the granule cell layer of the flocculus

a-e: Double labelling confocal immunofluorescence for ChAT and glutamic acid decarboxylase 65/67 (GAD) shows that ChAT+ neurons in the BIN (a,b) and ChAT+ axonal terminals in the granule cell layer of the flocculus (arrows in c) are also positive for GAD, while ChAT+ mossy fibers in the granule cell layer of the nodulus

are negative for GAD (arrow in d). Note in panel a and b, that the BIN also contains ChAT-GAD+ neurons (arrow heads in a, b). Also note that both ChAT+ and ChAT-BIN neurons are only sparsely covered by GAD+ nerve terminals (thin arrow in b'''), which differs from deep cerebellar nuclear neurons whose cell bodies and proximal dendrites are densely innervated by GAD+ synaptic terminals (e). Note in c' that ChAT+GAD+ boutons (arrows) complement ChAT-GAD+ boutons (arrow heads) in the same glomerulus.

f, g: ChAT/mGluR2 double staining (f) and ChAT/mGluR2/VIAAT triple staining (g), shows that ChAT+ fibers and boutons (arrows in f and g) are always mGluR2-, and complement mGluR2+ boutons (arrow heads in f and g) in glomeruli in the floccular granule cell layer. Both ChAT+ and mGluR2+ boutons stain positive for VIAAT. In g, also note the presence of ChAT-mGluR2-VIAAT+ nerve terminals (double-headed arrow).

h: Serial confocal optical sections and 3D-reconstructions of an exemplary mossy fiber ending labeled by VGluT1 that is surrounded by ChAT+VIAAT+ and ChAT-VIAAT+ nerve endings.

i, j: High magnifications of ChAT/calretinin (CR) double staining in the granule cell layer of the ventral paraflocculus showing examples of CR+ UBCs with a substantial number of ChAT+ nerve endings surrounding their brush-like dendritic arbor (arrows in i) as well as CR+ UBCs with virtually no ChAT+ nerve endings surrounding the 'brush' (arrow heads in j).

Scale bars: a, 100 µm; b-f, 25 µm; g, 10 µm; h, 5 µm; i, 20 µm.

BIN neurons occurred in an animal where the injection was centered in the ventral paraflocculus (e.g. case 902 in Ruigrok, 2003).

The rat BIN neurons could also be identified in thionin and NeuN stained sections, based on their size and localization in the white matter (Fig. 4c,e). Based on CTB tracing, GAD/NeuN staining and morphological criteria we propose that the BIN area in rat is rostro-medially delimited by the medial and inferior cerebellar peduncles, and more caudo-medially by the lateral cerebellar nuclei and group Y (Fig. 4a). Ventro-medially some BIN neurons may populate the cochlear nuclear superficial granule cell layer that borders the floccular white matter (Fig. 4a,b). Based on counting of GAD/NeuN and thionin stained serial sections, we estimate that in rat there are about 600-700 $(0.66 \pm 0.06*10^3$; Mean $\pm$ SE, n= 3) BIN neurons per side. We also estimated the number of retrogradely labeled BIN neurons in three animals following CTB injections in the floccular cortex (rat #798, rat #802 and rat #836; Ruigrok, 2003). Importantly, although injection areas covered less than 20% (15 $\pm$ 2%, mean $\pm$ SE) of the floccular granule cell layer, more than 70% (78 $\pm$ 5%) of BIN neurons were retrogradely labeled. These data suggest that projections from multiple BIN neurons converge on the same portion of the granule cell layer.
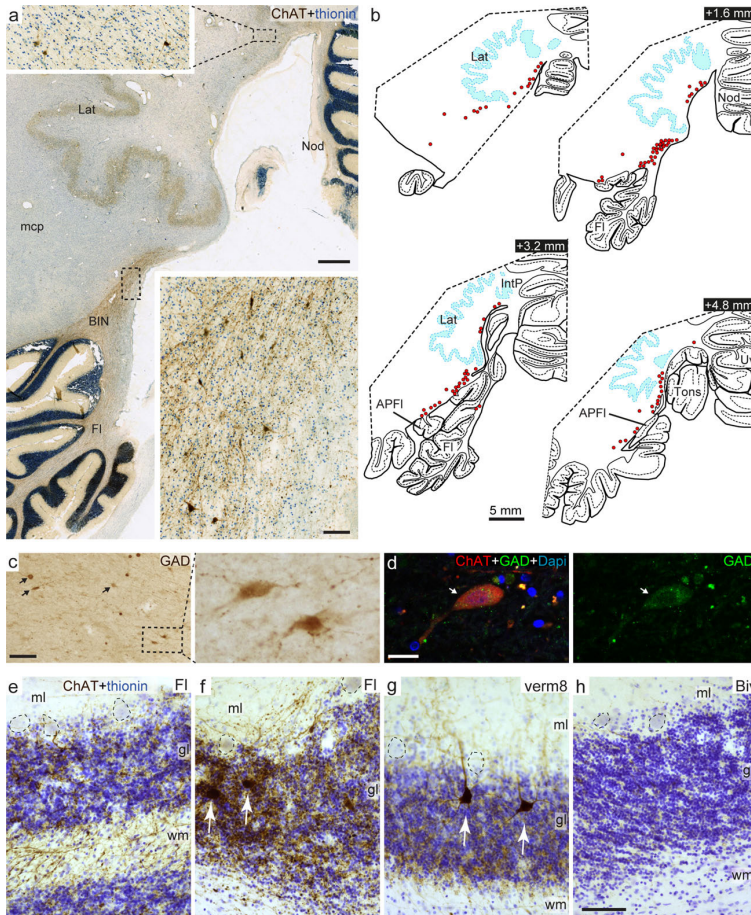
Figure 3. ChAT-staining outlines the BIN in human cerebellum

a: Low- and high-power (inserts) photomicrographs of ChAT immunoperoxidase diaminobenzidine (DAB) stained coronal sections of human cerebellum showing a cluster of ChAT stained neurons in the white matter between the flocculus and the lateral cerebellar nucleus (Lat) that is reminiscent of the BIN in macaque.

b: Plots of ChAT+ neurons in the basal white matter of human cerebellum. ChAT+ neurons are most abundant in the white matter, extending from the ventrolateral aspect of the lateral cerebellar nucleus (Lat) to the peduncles of the flocculus and the accessory paraflocculus (APFl).

c, d: GAD immunoperoxidase-DAB (c) and immunofluorescent (d) staining of BIN neurons arrows in c and d. The BIN neuron shown in d (arrow) also is ChAT+.

e-h: ChAT immunoperoxidase-DAB staining reveals variable densities of ChAT+ beaded fibers in the granule cell layer of different lobules that correlate with the presence of ChAT+ Golgi cells: in the flocculus, high densities of ChAT+ fibers occurs in parts of the granule cell layer containing ChAT+ Golgi cells (white arrows in f, g), while moderate levels of ChAT+ fibers occur in parts without ChAT+ Golgi cells (e).

Moderate levels of ChAT+ fibers also occur in lobules with ChAT+ Golgi cells, e.g. lobule 8 of the vermis (g). Lobules of the hemispheres with no ChAT+ Golgi cells do not show ChAT+ fibers (h, biventral lobule).
Scale bars: a, 1 mm (overview) and 100 µm (insert); c and h, 100 µm (also for e-g); d, 20 µm.
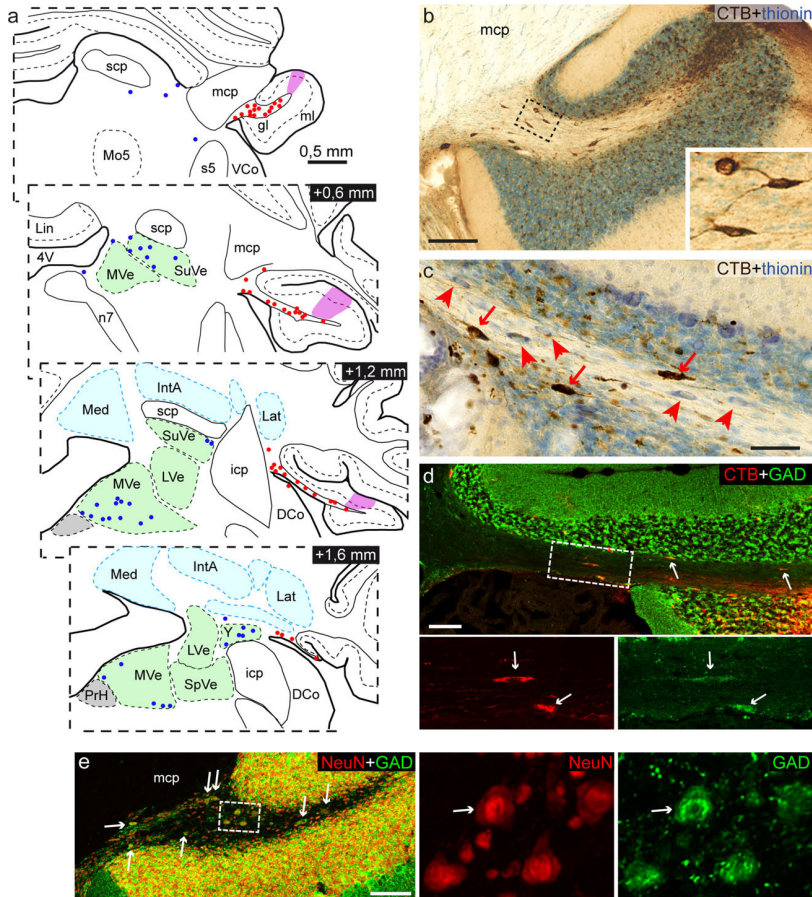
Figure 4. BIN neurons in rat

a-c: Plot (a) and photomicrographs (b, c) of retrogradely cholera toxin ß subunit (CTB) labeled BIN neurons (red dots in a; red arrows in c) following a small CTB injection in the flocculus (purple area in a); sections and plots are from rat 836 described in (Ruigrok, 2003). Note that retrogradely CTB labeled neurons also occur in the vestibular nuclei (blue dots in a). Arrowheads in c point to unlabeled BIN neurons.

d: Double labelling confocal immunofluorescence for GAD and CTB shows that retrogradely CTB labeled BIN neurons (arrows) are GAD+.

e: Double labelling confocal immunofluorescence for GAD and NeuN shows that GAD+ BIN neurons in the rat floccular white matter (arrows) are NeuN+.

Scale bars: b,d and e 100 µm; c, 50 µm.

Electrophysiological characterization of rat BIN neurons in acute slices:

To electrophysiologically characterize the BIN cells, we performed whole cell recording in acute transverse slices of rat cerebellar cortex. After recordings, cells were filled with neurobiotin for morphological analysis (Fig. 5a,b). Consistent with immunohistological data neurobiotin-filled BIN neurons showed fusiform or polygonal cell bodies with long dendrites that extend in the white matter from opposite poles of the cell. In 3 of 7 cells dendritic branches also extended into the granule cell layer to reach the Purkinje cell layer (Fig. 5a,b). The axon extended from the cell body or a proximal dendrite and produced multiple branches, many of which left the slice. In 2 of 7 cells we could trace several axonal branches innervating a substantial portion of the granule cell layer within the slice (Fig. 5a,b). The axonal branches produced a network of fine beaded fibers with multiple ramifications (Fig. 5b-d). Co-staining for mGluR2 and VGluT1 confirmed that the neurobiotin-labeled axons do not stain for mGluR2, but co-distribute with mGluR2+ axonal profiles in glomeruli identified with VGluT1-staining of the mossy fiber rosettes (Fig. 5c,d). Typically, individual branchlets of the BIN-axon innervated 10-20 glomeruli with 2-5 boutons/per glomerulus (Fig. 5c,d). These data are consistent with the notion emerging from our tracing experiments that individual BIN neurons have diffuse widespread projections, innervating large proportions of the floccular granule cell layer.

Cell attached recordings from 7 morphologically validated BIN neurons indicated that they were silent (n=5) or fired at low frequency (8.4 and 5.6 Hz respectively). The capacitance of the cells was 48 ± 10 pF (15-88; Mean ± SE, ranges, n = 7). We next determined their excitability in current clamp mode. Increasing depolarizing current injections with 20 pA increment triggered increased firing rates (Fig. 5e,f) with a rheobase current of 50 ± 10 pA (Mean ± SE, n=7), action potential (AP) threshold of -43 ± 2 mV (Fig. 5g), peak AP amplitude of 93 ± 6 mV, AP rise and decay times of 0.55 ± 0.02 and 1.18 ± 0.05 ms, respectively, and afterhyperpolarization amplitude of 12 ± 1 mV. Whole-cell voltage-clamp recoding uncovered spontaneous EPSC (sEPSC) in BIN cells (Fig. 5h-j), with sEPSC amplitudes of 17.69 ± 3.13 pA and frequencies of 3.93 ± 1.14 Hz. Together the data indicate that BIN neurons are readily excitable, receive excitatory input (see below), but show a low level of intrinsic firing activity in acute slices.

Necab1outlines BIN neurons in mouse flocculus:

To further characterize the BIN in rodents we performed retrograde CTB tracing in GlyT2GFP mice that express GFP under control of the GlyT2
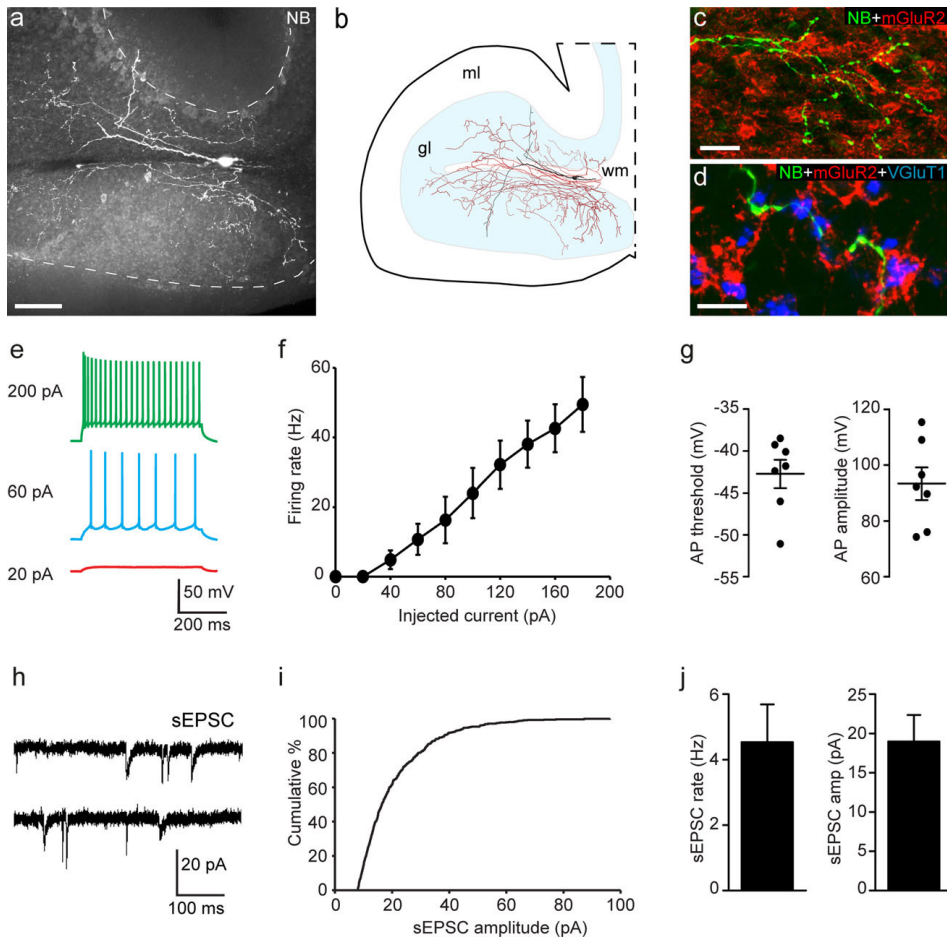
Figure 5. Evoked action potentials and spontaneous EPSC in rat BIN neurons

a-d: Example of a recorded BIN neuron filled with 1% neurobiotin (NB) visualized with A488-streptavidin. NB filling reveals an extensive axonal tree, and dendritic branches that may extend in the granule cell layer. Axonal branches are mGluR2- and contact multiple glomeruli characterized by the presence of VGluT1+ mossy fiber endings and mGluR2+ Golgi cell axons (c, d).

Scale bars: b, 100 µm; c, 25 µm; d, 10 µm.

e: Example traces of subthreshold depolarization of and evoked action potentials with increasing depolarizing current injection.

f: Average firing rate of BIN neurons (mean ± SE, n=7 cells) as a function of the injected current during the depolarizing step.

g: Action potential threshold and amplitudes (individual values and means ±SE).

h-j: Example traces (h), cumulative distribution of sEPSC activity from an exemplary BIN neuron (i), and mean ± SE of sEPSC frequencies and amplitudes (j) of recorded BIN neurons (n=6).

The basal interstitial nucleus (BIN) of the cerebellum provides
diffuse ascending inhibitory input to the floccular granule cell layer.

2

gene promoter to label glycinergic neurons (Zeilhofer *et al.*, 2005). We found that all retrogradely labeled BIN neurons were GFP+, indicating that BIN neurons are also glycinergic (Fig. 6a, b). Counting of serial GlyT2GFP sections indicated that mice have about 300 ($0.33 \pm 0.02*10^3$, mean ± SE, n = 6 flocculi from 3 animals) BIN neurons per side. Consistent with data from rat, CTB retrograde tracing in mouse showed that, while the injection areas covered less than 20%, (12 ± 3%, n = 3) of the floccular granule cell layer, more than 60% (63 ± 2%) of GFP+ BIN neurons were retrogradely labeled, indicative of widespread overlapping projection of BIN neurons. Together the data indicate that also in mice BIN neurons are distributed throughout the hilus and white matter of the flocculus.

As in macaque and rat, BIN neurons in the floccular white matter mice can be differentiated from Golgi cells in the floccular granule cell layer based on the absence of mGluR2 immunoreactivity (Fig. 6c). BIN neurons stained positive for the cholinergic muscarinic M2 receptor (Fig. 6d), which is expressed in cerebellar Golgi cells in multiple mammalian species (Jaarsma *et al.*, 1995; Jaarsma *et al.*, 1997). To further identify genes that are expressed by BIN neurons, we used the AGEA (Anatomic Gene Expression Atlas) viewer modus of Allen Brain Atlas that examines gene expression in user defined neuroanatomical areas. We screened nearly 2000 genes for distinct signal in intermediate-large cells in the white matter of the anterior flocculus. In accord with our immunohistological data, no visible signal occurs in the floccular white matter of *mGluR2* mRNA labeled sections, whereas sections stained for *Gad1 (Gad67)*, *Gad2 (Gad65)*, *GlyT2 (Slc6A5)* and *ChRM2* mRNA show labelling of intermediate-sized cells in the floccular white matter, indicative of labelling of BIN neurons (Fig. 6e). Of 89 genes with distinct labelling of BIN neurons identified in our screen, the majority (85 of 89) showed similar expression in granule cell layer interneurons, while showing variable expression in other cerebello-cortical neuronal populations. Examples of genes that like *GlyT2* and *ChRM2* are expressed in both BIN neurons and granule cell layer interneurons, include acetylcholine esterase (*AChE*) and *Lgi2* (Fig. 6e). Out of the 2000 genes examined, we identified only four genes with distinct expression in BIN neurons and no apparent expression in granule cell layer interneurons in the flocculus. For one of these, *Necab1* (N-terminal EF-hand calcium Binding protein 1) expression in BIN neurons was confirmed by immunohistology (Fig. 6f,g): Analysis of Necab1 immunostaining in GlyT2GFP mice shows that all GFP+ neurons in the floccular hilus and white matter, stain positive for Necab1, while other floccular cells, including GlyT2+ Golgi and Lugaro cells show no or very weak staining for Necab1 (Fig. 6f). Accordingly, BIN
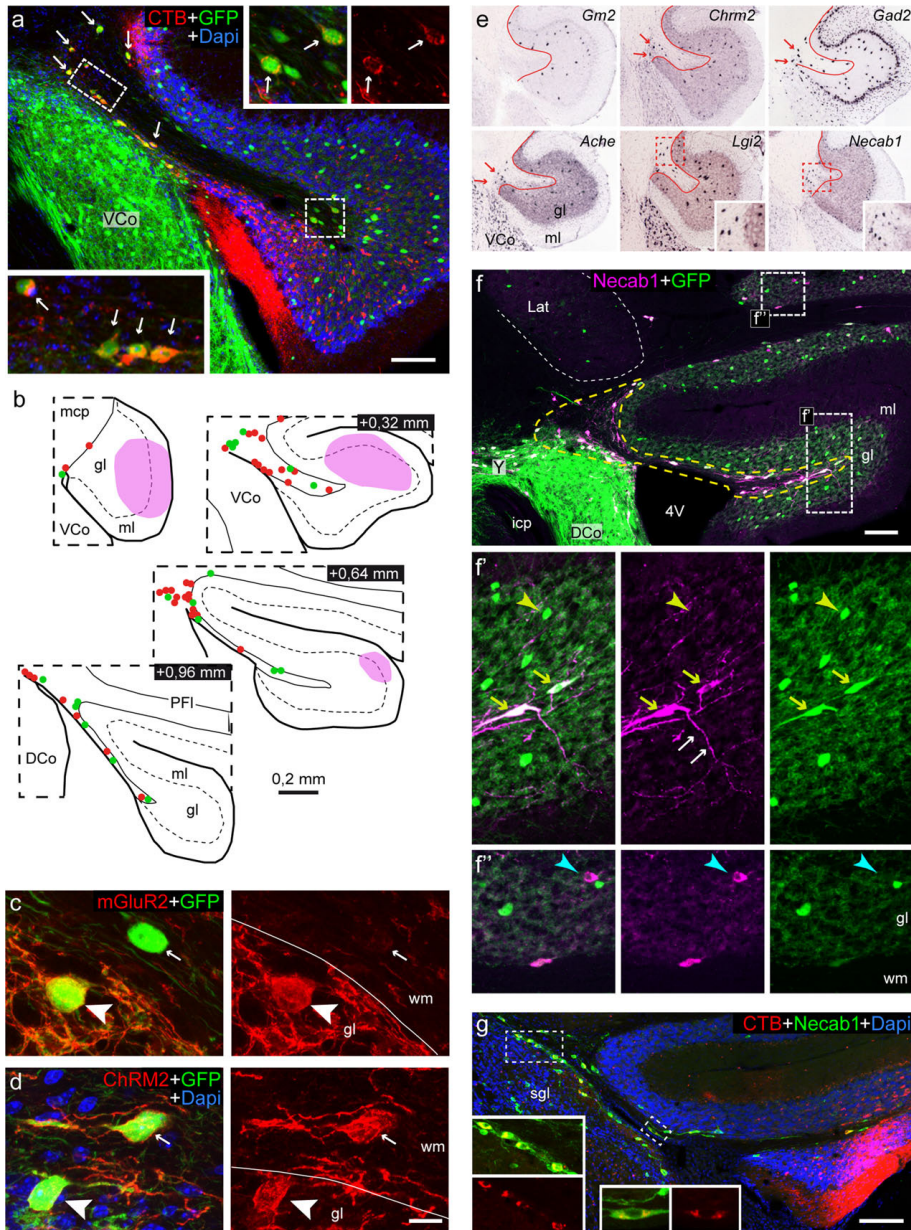
Figure 6. BIN neurons in mouse flocculus identified by retrograde CTB tracing and Necab1 immunostaining

a, b: Double labelling confocal immunofluorescent image (a) and plot (b) of CTB-labeled BIN neurons (arrows in a; red dots in b) following CTB injection in the flocculus (purple area in b outline the injection area) of GlyT2GFP transgenic mice (a is from mouse Gly1; b is from mouse Gly4). All retrogradely CTB labeled BIN neurons are also positive for GFP (arrows in a). GlyT2-GFP+ BIN neurons that are

not positive for CTB are indicated by green dots in b.

c, d: Confocal immunofluorescence of mGluR2 (c) and muscarinic M2 receptor (d) in the flocculus of a GlyT2GFP transgenic mouse. GlyT2+ Golgi cells in the granule cell layer (gl) stain positive for mGluR2 (arrow heads in c) and muscarinic M2 receptor (arrow heads in d), while GlyT2GFP BIN neurons are M2+ and mGluR2- (small arrows in c and d). wm, white matter

e: In situ hybridization image from Allan Brain Atlas showing that mGluR2 (Gm2) mRNA is expressed in granule cell layer (gl) but not in white matter cells of the flocculus, while muscarinic M2 receptor (Chrm2), GAD65 (Gad2), AChE and Lgi2 mRNA occur cells in both the granule cell layer and the white matter (red arrows). Necab1 mRNA, instead, is expressed in cells in the floccular white matter, but not in the granule cell layer.

f, g: Confocal images of Necab1 immunostaining in the flocculus of a GlyT2GFP mouse (f), and a non-trangenic mouse receiving a CTB tracer injection in the flocculus (g). Intense Necab1 staining is present in GlyT2GFP+ neurons (yellow arrows in f) and CTB-traced BIN neurons (g, see inserts). Note in f', that dendrites of some Necab1+ BIN neurons may extend in the granule cell layer (white arrows in f'). Also note in f, a population of Necab1+ neurons in the granule cell layer of the paraflocculus (cyan arrow head in f"), while no Necab1+ neurons occur in the granule cell layer of the flocculus (yellow arrow head in f' points to a GlyT2GFP+ Golgi cell in the flocculus).

Scale bars: a,f and g, 100 μm; d, 10 μm.

neurons identified by retrograde CTB-tracing were always strongly Necab1+ (Fig. 6g). Necab1 immunohistology also showed that BIN neurons may have one or more dendritic branches extending into the granule cell layer (Fig. 6f), consistent with data from rat neurobiotin-filled BIN neurons. Together, the data indicate that Necab1 selectively outlines BIN neurons in the mouse flocculus, consistent with the idea that they represent a specific class of floccular neurons.

<u>Absence of Necab1+ and Neurogranin+ Golgi cells in mouse flocculus:</u>

While granule cell layer interneurons in the flocculus show no or very weak Necab1 expression, a substantial subset of granule cell layer interneurons in other cerebellar lobules stained positive for Necab1 (Fig. 6f). The Necab1+ granule cell layer interneurons included both GlyT2GFP+ and GlyT2GFP- neurons (Fig. 6f). These data indicate that Necab1 outlines one or more subclasses of granule cell layer interneurons that are absent in the flocculus. To further characterize Necab1+ granule cell layer interneurons, and differences between the flocculus and other cerebellar lobules we compared the distribution of Necab1 with that of mGluR2 and

neurogranin in sections from GlyT2GFP mice. A previous study focusing on lobules 4-6 of the vermis (Simat *et al.*, 2007) showed that several subclasses of granule cell layer interneurons can be differentiated on the basis of differential expression of these markers, including a population of GlyT2GFP+mGluR2+neurogranin+ cells (designated type 1 Golgi cells), two populations that are GlyT2GFP+mGluR2+, but neurogranin- (type 2 and 3 Golgi cells), GlyT2GFP-GluR2-neurogranin+ cells (type 4 Golgi cells), and GlyT2GFP+ cells that are neurogranin-mGluR2- (representing Lugaro and globular cells). Consistent with this classification we found that in lobule 4-5 of the vermis (verm4/5) neurogranin occurred in GlyT2GFP+ as well as GlyT2GFP- Golgi cells (Fig. 7a), and that GlyT2GFP-/neurogranin+ cells were negative for mGluR2 (type 4 Golgi cells), while GlyT2GFP+/ neurogranin+ Golgi cells were mGluR2+ (type 1 Golgi cells). However, no neurogranin+ Golgi cells occurred in the flocculus, and furthermore also BIN neurons stained negative for neurogranin (Fig. 7b). Like neurogranin, Necab1 in verm4/5 occurred in either GlyT2GFP-/mGluR2- (potentially type 4 Golgi cells) or GlyT2GFP+/mGluR2+ (potentially type 1 Golgi cells), but not in GlyT2GFP+/mGluR2- cells (Lugaro/globular cells) (data not shown). Double labeling for Necab1 and neurogranin showed consistent codistribution of neurogranin and Necab1 in GlyT2GFP- (type 4) Golgi cells, but incomplete colocalization in GlyT2GFP+ Golgi cells (Fig. 7c). These data indicate that Necab1 is expressed in type 4 Golgi cells, to variable extent is expressed by other Golgi cell subtypes, but is not expressed in Lugaro/globular cells.

We further characterized differences in Golgi cells between the flocculus and verm4/5 using an antibody against Lgi2. Lgi2-immunostaining occurred in granule cell layer interneurons as well as BIN neurons, in accord with mRNA expression data from Allan brain atlas (Fig. 6e). Lgi2/mGluR2 and Lgi2/neurogranin double labeling in GlyT2GFP mice indicated that in verm4/5 Lgi2 is expressed in all Golgi cells, but not in Lugaro/globular cells: thus, in Lgi2/ mGluR2 labeled sections, Lgi2-immunostaining outlines GlyT2GFP+mGluR2+ cells (type 1-3 Golgi cells) and GlyT2GFP-mGluR2- cells (potentially type 4 Golgi cells), but is not present in GlyT2GFP+mGluR2- cells (Lugaro/globular cells) (data not shown). Lgi2/neurogranin staining showed that GlyT2GFP-Lgi2+ cells all stain positive for neurogranin (Fig. 7d,e) and indeed represent type 4 Golgi cells. Consistent with the notion that type 4 Golgi cells do not occur in the flocculus we found that all Lgi2+ cells in the floccular granule cell layer were GlyT2+mGluR2+, with the exception of sporadic GlyT2GFP+ cells that like BIN neurons are Necab1+ (Fig. 7f,g). Cell counts in Lgi2/Necab1/ GlyT2GFP and Lgi2/neurogranin/GlyT2GFP labeled sections indicated that the density of Lgi2+ Golgi cells is slightly, but non-significantly ($p = 0.09$;
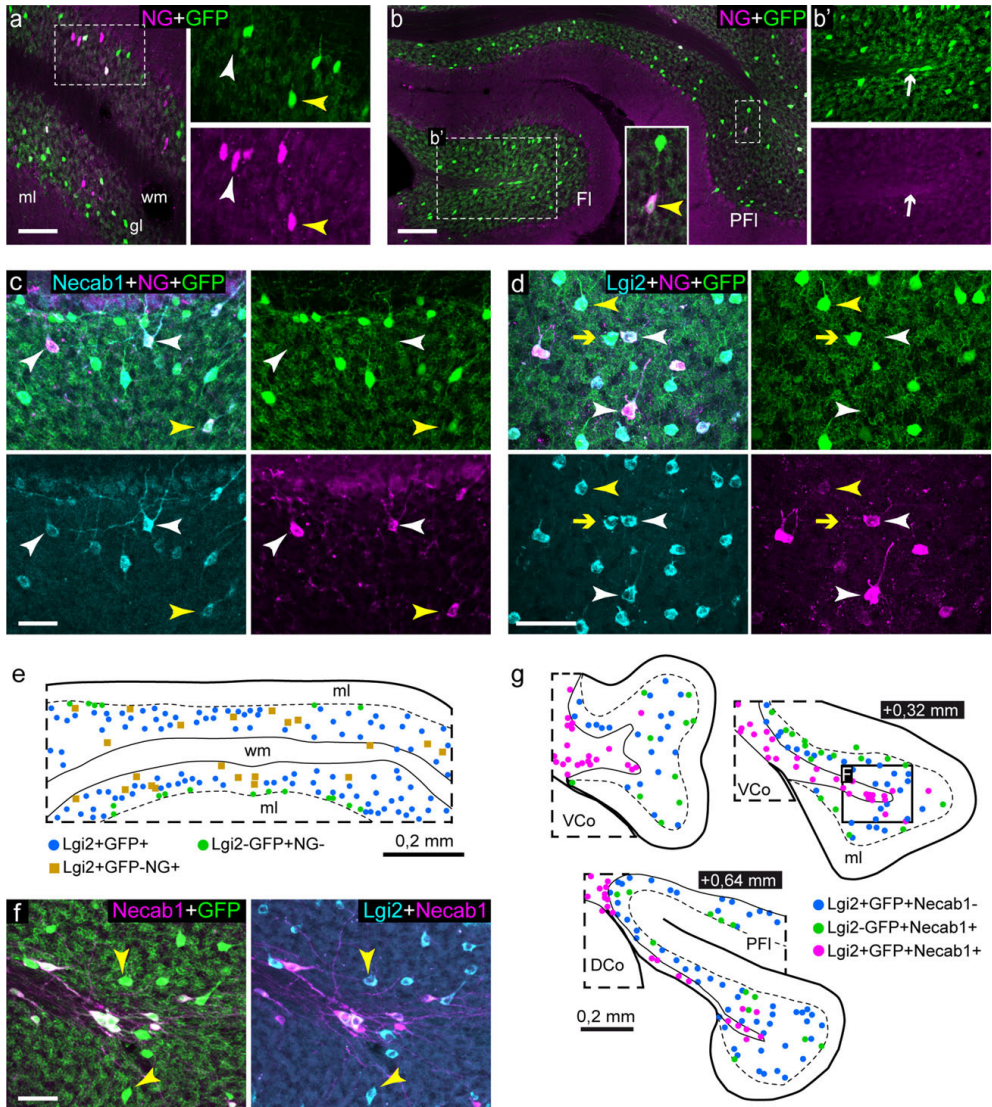
Figure 7. Absence of Necab1+ and Neurogranin+ Golgi cells in mouse flocculus

a,b: Confocal images of neurogranin-immunostaining in GlyT2GFP mouse cerebellar cortex, showing that in lobule 4-5 of the vermis (a) neurogranin (NG, rabbit antibody) labelling occurs in GFP- (white arrow head) and GFP+ Golgi cells (yellow arrow head), while in the flocculus (Fl in b) there are no neurogranin+ Golgi cells. Note in flocculus, that BIN neurons (white arrow in b') do not stain for neurogranin, while sporadic neurogranin+ cells can be observed in the adjacent ventral paraflocculus (PFl, yellow arrow head in insert in b).

c: Staining for neurogranin (mouse antibody) and Necab1 in vermis 4-5 of GlyT2GFP mouse illustrates that neurogranin and Necab1 coditribute in GFP- Golgi cells (white

arrow heads), and show variable codistribution in GFP+ Golgi cells (e.g. yellow arrow head points to GlyT+neurogranin+Necab1+ cell).

d: Staining for neurogranin (rabbit antibody) and Lgi2 in vermis 4-5 of GlyT2GFP mice shows that Lgi2 is present in neurogranin+GFP- (white arrow heads), neurogranin+GFP+ (yellow arrow heads), and neurogranin-GFP+ Golgi cells (yellow arrow).

e: Plot of vermis 4-5 in coronal section of GlyT2GFP mouse stained for Lgi2 and neurogranin; the plot outlines the distribution of type 1-3 Golgi cells (blue dots, Lgi2+GFP+), type 4 Golgi cells (light brown squares, Lgi2+GFP-NG+) and Lugaro/ globular cells (green dots, Lgi2+GFP-NG-). Lgi2+GFP- cells always were also positive for neurogranin.

f,g: Confocal image (f) and plot (g) illustrating the distribution of Golgi cells (Lgi2+GFP+Necab1-, yellow arrow heads in f, blue dots in g), Lugaro/globular cells (green dots, Lgi2+GFP-Necab1-), and BIN neurons (magenta dots, Lgi2+GFP+Necab1+) in coronal sections of the flocculus.

Scale bars: a, 100 µm; b, 200 µm; c, d, f, 50 µm.

unpaired 2-tailed *t*-test) higher in verm4/5 compared to the flocculus, with 227 ± 17 (Mean ± SE, n=3 animals) Lgi2+ cells/mm^2 in verm4/5 and 187 ± 11 (n=4) Lgi2+ cells/mm^2 in the floccular granule cell layer, respectively. In verm4/5 87% (197 ± 15) of the Lgi2+ Golgi cells were GlyT2GFP+ representing type 1-3 Golgi cells, whereas in the flocculus all Lgi2+ cells were GlyT2+. In sum, our comparison of Golgi cells between verm4-5 and flocculus using established (mGluR2, neurogranin, GlyT2) and novel markers (Lgi2, Necab1) of (subsets of) Golgi cells, uncovered differences in the neurochemical identities of Golgi cells in the flocculus versus the anterior vermis (Simat *et al.*, 2007). In particular, the absence of neurogranin+, Necab1+, and Lgi2+GlyT2GFP- Golgi cells in the flocculus indicates that type 4 Golgi cells are not present in the flocculus, all Golgi cells being mGluR2+GlyT2+.

<u>BIN neurons innervate granule cells dendrites in floccular glomeruli:</u>

Based on analysis of BIN nerve terminals in macaque and rat, we anticipate that BIN axons provide inhibitory input to granule cell dendrites, and complement inhibitory input from Golgi cells in floccular glomeruli. To further examine the axonal projections of BIN neurons we injected AAV-GFP viral particles into the white matter and hilus of the flocculus of mice (Fig. 8a). We obtained 7 injections centered in the hilus of the flocculus infecting BIN neurons and resulting in a variable degree of axonal labelling in the ipsilateral flocculus (Fig. 8b,c). Labeled axons were morphologically distinct from mossy fibers, and form a plexus of thin fibers with multiple VIAAT-positive
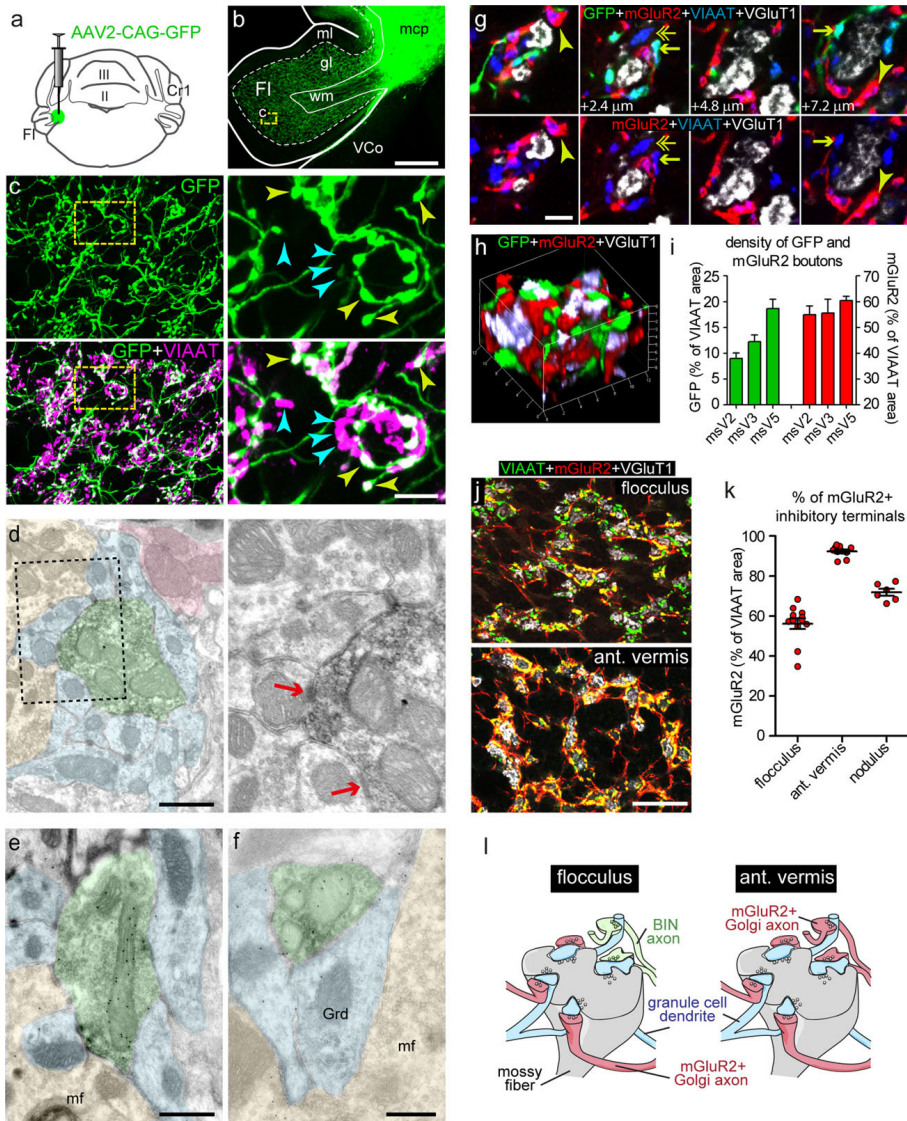
Figure 8. BIN neurons innervate granule cell dendrites in glomeruli in mouse flocculus

a-c: Injection of AAV2-CAG-eGFP virus in the white matter and the hilus of the flocculus (a,b) results in labelling of BIN neurons and their axons in the floccular granule cell layer (b,c). Co-immunostaining for VIAAT shows that GFP+ axons display VIAAT+ varicosities (white boutons, e.g. yellow arrow heads in c). Double-labeled GFP+VIAAT+ varicosities are intermingled with GFP-VIAAT+ boutons (magenta boutons, cyan arrow heads in c).

d-f: Transmission electron microscopy of anti-GFP immunoperoxidase-DAB precipitate in the floccular granule cell layer following AAV2-CAG-eGFP infection of

BIN neurons. DAB precipitate is associated with presynaptic boutons (outlined by green color coding) that form synapses (red arrows in d) with granule cell dendrites (Grd, blue color coding). Post-embedding anti-GABA immunogold-labeling shows that DAB+ axon terminals are also enriched in GABA (e, f). Mossy fiber endings and putative Golgi cell axons are coded in yellow and red, respectively.

g,h: Series of optical sections (g) and 3-dimensional reconstruction (h) of a glomerulus innervated by GFP-labeled BIN axons and labeled for mGluR2, VIAAT and VGluT1. Note that the VGluT1+ mossy fiber rosette is surrounded by GFP+mGluR2-VIAAT+ (small arrows), GFP-mGluR2+VIAAT+ (arrow heads) and single-labeled GFP-mGluR2-VIAAT+ boutons (double-headed arrow).

i: Bar graph showing the area of VIAAT+ nerve endings in floccular granule cell layer that co-distribute with GFP labeled BIN axon endings (green bars) or mGluR2 staining (red bars). Analyzed sections are from 3 mice with AAV2-CAG-GFP virus injections in the BIN showing the highest amount of BIN axonal labeling in the flocculus (mouseV2, mouseV3, mouseV5; see material and methods for details).

j,k: Exemplary confocal images (j) and graph (k) showing that in the anterior vermis more than 90% of the VIAAT+ axon endings is mGluR2+, whereas in the flocculus the proportion is 60%, as illustrated by the large proportion of single labeled VIAAT+ terminals (green boutons in upper panel in j).

l: Cartoon illustrating how BIN axon terminals may complement mGluR2+ Golgi axon terminals in floccular glomeruli.

Scale bars: b, 250 µm; c, 5 µm; d -f, 500 nm; g, 2 µm; j, 50 µm.

nerve terminals (Fig. 8c) resembling BIN fibers in macaque (Fig. 2) and rat (Fig. 5a-c). No GFP+VIAAT+ labeled axons occurred in the flocculus in case of more dorsal and medial injections that targeted the cerebellar nuclei, but did not target BIN neurons. The highest densities of labeled fibers occurred in experiments, where also BIN neurons in the floccular white matter were infected (Fig. 8b).

To characterize the post-synaptic target of AAV-GFP labeled BIN axons, we performed transmission electron microscopy of anti-GFP immunoperoxidase histochemistry with diaminobenzidine (DAB) as a substrate. Consistent with GFP fluorescence, DAB precipitate was associated with thin axonal profiles and presynaptic boutons with diameters ranging from 1 to 2 µm. Labeled axon terminals were localized in glomeruli (Fig. 8d). Analysis of 40 labeled axon terminals, revealed multiple synaptic contacts with granule cell dendrites (Fig. 8d). Post-embedding immunogold labelling for GABA showed that DAB-labeled profiles in all occasions (n=30) are enriched in GABA-immunoreactivity (Fig. 8e,f) Together the data indicate that BIN axons like Golgi cell axon terminals (Palay and Chan-Palay, 1974; Dugue *et al.*, 2005; Pietrajtis and Dieudonné, 2013; Mapelli *et al.*, 2014) primarily innervate granule cell dendrites.

The basal interstitial nucleus (BIN) of the cerebellum provides
diffuse ascending inhibitory input to the floccular granule cell layer.

2

BIN inhibitory input complements mGluR2+ Golgi axon terminals in glomeruli in the mouse flocculus:

Immunostaining of AAV-GFP labeled sections for VIAAT, mGluR2 and VGluT1 showed that GFP+ BIN axon terminals always are mGluR2-negative, but co-distribute with VIAAT+mGluR2+ boutons in the same glomeruli (Fig. 8g,h). In addition, the same glomeruli also contained VIAAT+ terminals that are both mGluR2- and GFP-negative (Fig. 8g). To obtain an estimate of the proportion of mGluR2+ Golgi versus BIN axon terminals in the floccular granule cell layer we determined the proportion of VIAAT+ boutons labeled by either GFP or mGluR2 in confocal stacks from the three AAV-GFP injections that yielded the highest level of BIN axonal labelling (i.e. VBIN2, VBIN3, VBIN5). This analysis showed that 10-20% of the area labeled by VIAAT was GFP+ whereas 50-60% of the VIAAT+ area was mGluR2+ (Fig. 8i). For comparison, we analyzed the proportion of mGluR2+ VIAAT+ boutons in the nodulus and lobules 3 and 4/5 of the anterior vermis (Fig. 8j,k). In the anterior vermis, more than 90-95% of VIAAT+ area was mGluR2+ (Fig. 8j,k), consistent with the notion that inhibitory axons in the glomeruli primarily derive from mGluR2+ Golgi cells (Ohishi *et al.*, 1994; Watanabe *et al.*, 1998; Simat *et al.*, 2007), while in the nodulus about 70% of the VIAAT+ area van mGluR2+ (Fig. 8k). The large proportion (40-50%) of VIAAT+mGluR2- boutons in the floccular granule cell layer as compared to the anterior vermis and the nodulus, can at least in part be explained by the presence of innervation from BIN neurons. In accord with data from macaque flocculus, these data indicate that BIN inhibitory input represents a significant complement of inhibitory input from Golgi cells in the floccular granule cell layer (Fig. 8l).

Rodent BIN neurons receive excitatory input from the rostro-medial medullary reticular formation:

Staining for markers of inhibitory (VIAAT, GAD) and excitatory (VGluT1, VGluT2) nerve terminals, revealed that BIN neurons have a large number of VGluT2-positive boutons contacting their cell body and proximal dendrites (Fig. 9a) consistent with our electrophysiological analysis showing sEPSC in BIN neurons (Fig. 5h-j). To learn about the origin of this excitatory input, we set out tracing experiments in mouse. VGluT2 is present in climbing fibers and multiple populations of mossy fibers (Hioki *et al.*, 2003) raising the possibility that BIN neurons are innervated by collaterals of climbing or mossy fibers. To test this possibility, we injected anterograde tracer (biotin dextran amine

10 kDa, BDA) in the inferior olive, i.e. the source of climbing fibers, and in brainstem nuclei known to provide mossy fiber input to the flocculus, including the vestibular nuclei and the prepositus hypoglossal nucleus (Ruigrok, 2003). However, none of these injections resulted in labelling of fibers contacting BIN neurons, despite abundant climbing fiber and mossy fiber labelling, respectively (data not shown). Instead a systematic anterograde tracing approach with injections throughout the medulla oblongata and the pontine reticular formation, revealed that BDA injection in the rostro-medial medullary reticular formation resulted in labeling of fibers innervating BIN neurons (Fig. 9b-e). We obtained 7 BDA injections that resulted in labeling of beaded fibers contacting the cell bodies and proximal dendrites of a substantial portion (>30%) of BIN neurons. These injections all targeted the medio-dorsal aspect of the medullary gigantocellular reticular nucleus (Gi). In 4 of 7 cases injections also included the dorsal paragigantocellular reticular nucleus (DPGi) dorsal of the Gi. However, 2 injection that targeted the DPGi, but not the Gi, resulted in labeled fibers on less than 4% of BIN neurons, indicating that afferents predominantly arise in the Gi. Similarly, BDA injections in the ventral aspect of the Gi, the pontine reticular formation rostral of the Gi, or the caudal aspect of the Gi resulted in no or minimal labeling of BIN afferents, substantiating the medio-dorsal Gi as the main source of BIN afferents. Importantly, the injections restricted to the medio-dorsal Gi that resulted in substantial labelling of BIN afferents (e.g. experiments #1541, #1606 and #1536) all produced negligible mossy fiber staining, supporting the notion that fibers innervating the cell bodies of BIN neurons do not represent mossy fiber collaterals. In all experiments labeled BIN afferent fibers were observed bilaterally, even when the injection was clearly unilateral. In addition, we observed that individual afferents may innervate several BIN neurons, and typically produce multiple (5-32) consecutive swellings on the cell body and proximal dendrites of individual BIN neurons (Fig. 9c,e). Double labelling for VGluT2 indicated that these axonal swellings in all occasions were VGluT2+ (Fig. 9e). In all neurons systematically examined for codistribution of BDA and VGluT2 (30 of 30 cells) we found that BDA+VGluT2+ boutons on BIN neurons were complemented by BDA-VGluT2+ boutons (Fig. 9e). This observation indicates that individual BIN neurons are innervated by multiple excitatory axons. To further demonstrate that VGluT2+ axon terminals innervating BIN neurons arise from neurons in the medio-dorsal Gi, we injected AAV-flex-GFP viral particles in the Gi of VGluT2-Cre mice in order to express GFP selectively in VGluT2 expressing neurons. Consistent with BDA tracing these injections resulted in bilateral GFP+ beaded fibers that made multiple synaptic connections with BIN neurons (Fig. 9f).

The basal interstitial nucleus (BIN) of the cerebellum provides
diffuse ascending inhibitory input to the floccular granule cell layer.

2

Next, to visualize the cells of origin of the BIN afferents in the Gi, we performed retrograde tracing with cholera toxin ß subunit (CTB). Comparison of CTB injections centered in the hilus of the flocculus (n=2) with injections in the floccular cortex (n=4), uncovered a population of intermediate-size (length =14 to 22 µm) polygonal CTB-labeled neurons in the dorsal Gi following hilar, but not cortical CTB injections (Fig. 9g). Consistent with anterograde tracing experiments, retrogradely-labeled neurons occurred both ipsi- and contralateral. Large neurons, characteristic for the Gi were not retrogradely labeled. The presence of intermediately sized VGluT2+ neurons in the Gi is consistent with *VGluT2* mRNA expression data documented in Allen brain atlas (Lein *et al.*, 2007) showing high levels of *VGluT2* mRNA staining in both very large and small-to-intermediate size neurons in the Gi. We therefore propose that BIN neurons receive bilateral excitatory input from intermediately sized neurons in the dorsal Gi. Together the data indicate that the BIN is part of a disynaptic afferent pathway to the floccular granule cell layer, consisting of glutamatergic fibers from the medullary reticular formation innervating BIN neurons that in turn provide inhibitory input to granule cells (Fig. 9h).

<u>Variability in the distribution of BIN neurons across mammalian species:</u>

On the basis of data from primates and rodent, the BIN can be defined as a population of GABA/glycinergic neurons in the white matter, that innervate the floccular granule cell layer. However, BIN neurons show a differential distribution in rodents and primates, i.e. a preferential localization in the floccular white matter in rodents, versus a more widespread and distant distribution in the white matter between the floccular peduncle and the cerebellar nuclei in macaque and human. This raises questions about the presence and distribution of BIN neurons in other mammalian species. Our search for BIN neurons in rabbit cerebellum indicates that their identification in other species is not always straightforward. Thionin and GAD staining shows that in rabbit a low number of neurons is present in the white matter within and dorso-medial of the flocculus. Accordingly, analysis of sections from previous tracer experiments with small injections of the anterograde/ retrograde tracer WGA-HRP in the floccular cortex (rabbits K227, K244, K358, K360; Tan *et al.*, 1995) revealed no or sporadic retrogradely labeled cells in this area. However, further analysis of these experiments revealed retrogradely labeled cells in the white matter medial of the medial cerebellar peduncle (mcp), rostral of the cerebellar nuclei (Fig. 10a,b). Retrogradely labeled cells only occurred ipsilateral. Notably, in several occasions labeled cells occurred close to the granule cell layer of the anterior vermis (Fig. 10b).
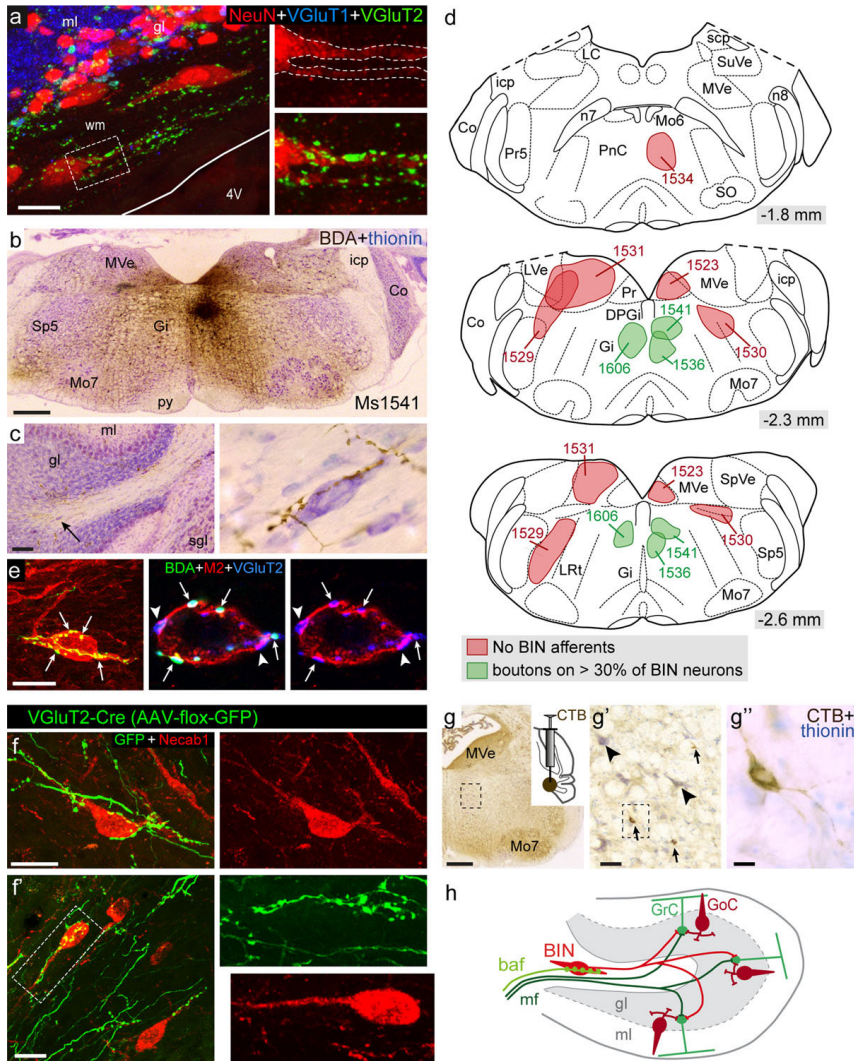
Figure 9. BIN neurons are innervated by VGluT2+ axons arising in the medial medullary reticular formation

a: Confocal image of NeuN/VGluT1/VGluT2 triple staining in rat flocculus showing that cell body and proximal dendrites of BIN neurons are covered by VGluT2+ axon terminals.

b-d: Representative images of injection spot (b) and anterogradely-labeled fibers in the floccular white matter (c), and map of injection area's of selected BDA (biotinylated dextran amine) anterograde tracing experiments (d) showing that injections targeting the gigantocellular reticular nucleus (Gi) in the rostral medullary reticular formation result in labelling of fibers contacting BIN neurons. Injections in surrounding areas (indicated in red) did not result in labeling of fibers innervating BIN neurons, but to variable extend produced labeling of mossy fibers innervating floccular granule cell layer.

e: Maximal projection (left panel, total thickness = 12 μm) and single optical

The basal interstitial nucleus (BIN) of the cerebellum provides diffuse ascending inhibitory input to the floccular granule cell layer.

2

section (middle and right panel, z = 1 µm) illustrating a BDA-labeled fiber from the Gi innervating a BIN neuron (labeled with anti-muscarinic M2 receptor antibody). Arrows in maximal projection and single optical section point to the same nerve endings. Co-staining for VGluT2+ shows that nerve endings from labeled fibers are VGluT2+, and that this cell is innervated by additional VGluT2+ nerve endings from non-labeled fibers (arrow heads).

f: Maximal projections of exemplary BIN neurons identified by (Necab1-immunostaining) innervated by GFP+-beaded fibers following AAV-floxed-GFP injection in the Gi of VGluT2-Cre mouse.

g: Immunoperoxidase-DAB staining of retrogradely labeled medium-sized neurons (arrows in G') in the Gi following CTB injection in hilus of the flocculus. Note that the large Gi neurons (arrow heads) are not labeled for CTB.

h: Schematic representation of BIN neurons and glutamatergic BIN afferent fibers (baf) from the Gi in the floccular circuitry.

Scale bars: a and f', 20 µm; b and g, 500 µm; c, 100 µm; d and g", 10 µm; g', 50 µm.

Importantly, GAD staining revealed GAD+ neurons with similar size and distribution in this region of the white matter (Fig. 10c,d). The GAD+ neurons showed morphologies reminiscent of BIN neurons in primates and rodent. Based on counting of serial sections, we estimate that on each side there are about 800 (0.8 ± 0.2 *10^3, mean ± SE, n=2) of these GAD+ neurons populating either the floccular or the anterior vermis white matter (Fig. 10c,d).

To further explore the variability in distribution of BIN neurons across mammalian species we searched for potential BIN neurons in ferret cerebellum. Analysis of thionin and GAD stained section showed that as in primates and rabbit there are only a few GAD+ neurons in the white matter of the ferret flocculus. However, a cluster of GAD+ neurons, reminiscent of BIN neurons, was present in the white matter of the transition zone between the flocculus and the ventral paraflocculus (Fig. 11). Caudo-dorsally this cluster is bordered by the lateral cerebellar nuclei. Like BIN neurons the neurons are moderately-large in size and show elongated fusiform or polygonal morphologies with dendrites emanating from two sides. With about 1000 (1.1 ± 0.1 * 10^3, mean ± SE, n=2) neurons per side, their number is compatible with BIN neurons in other species. Together the data indicate that BIN neurons also occur in rabbit and ferret cerebellum, but show different distributions than in rodent and primates.
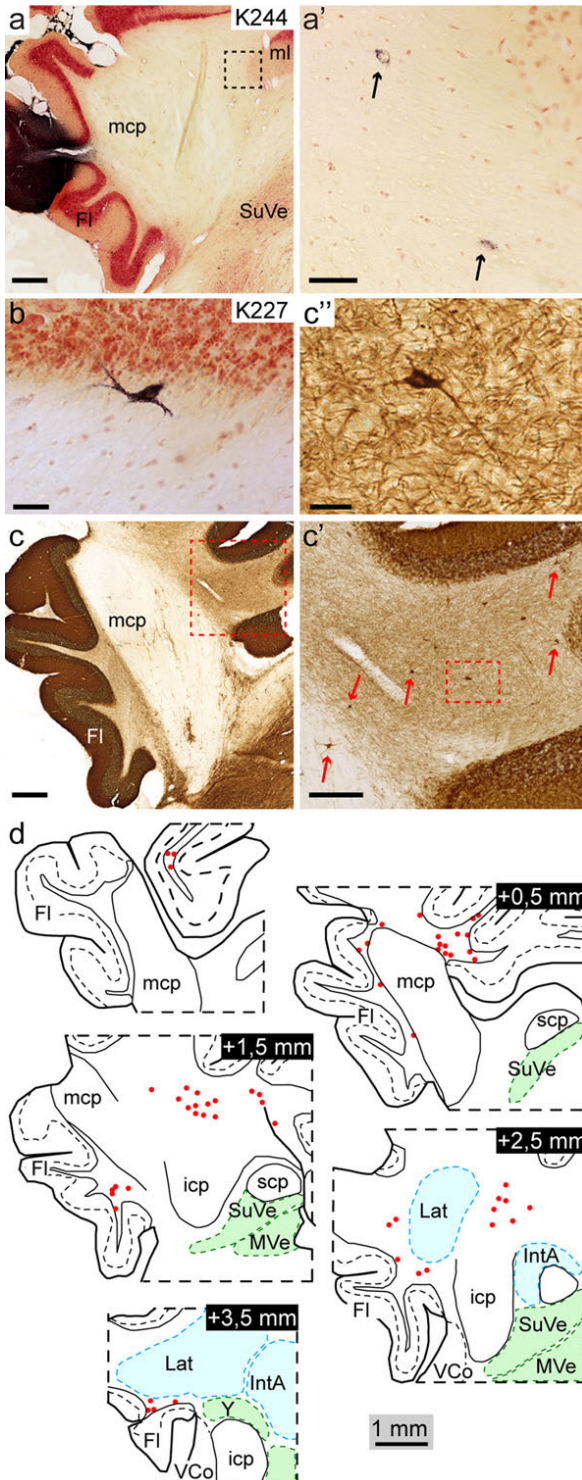
Figure 10. BIN neurons in rabbit

a, b: Low- (a) and high-magnification photomicrographs (a', b) illustrating retrogradely-labeled neurons in the white matter between the medial cerebellar peduncle (mcp) and the anterior vermis (arrows in a', b) following WGA-HRP injection in the rabbit flocculus (a). Images are from experimental animals (K244 and K227) from previously reported experiments (Tan et al., 1995).

c, d: GAD-immunoperoxidase staining reveals GAD+ neurons in the white matter medio-caudal of the mcp, while a few GAD+ neurons are present in the floccular white matter lateral of the mcp. In the plot in d, all GAD+ cells in white areas surrounding the mcp are plotted. The distribution and size of GAD+ neurons corresponded to the distribution of WGA-HRP tracing experiments.

Scale bars: a and c, 500 µm; a', 50 µm; b and c", 20 µm; c', 200µm.
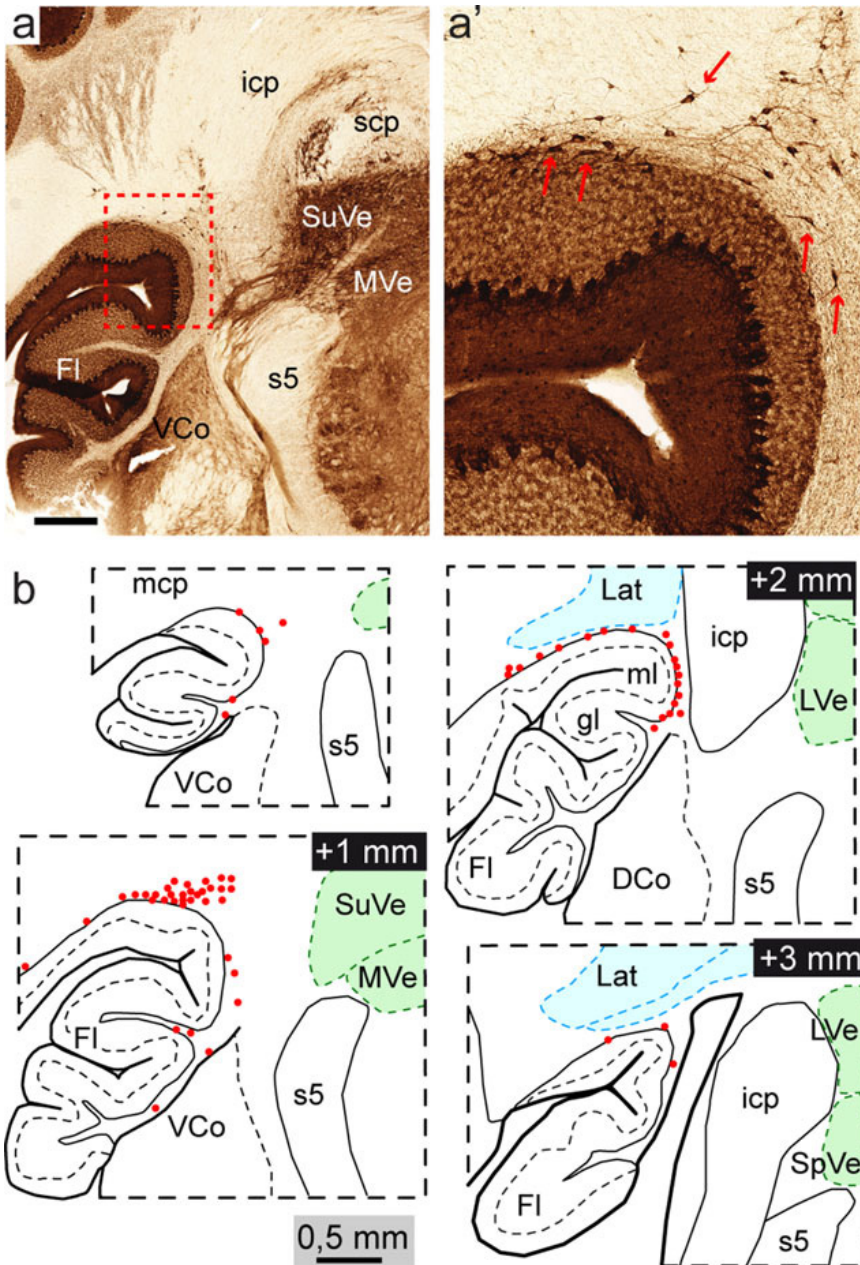
Figure 11. BIN neurons in ferret

Low-(a) and high-magnification (a') images and plots (b) of GAD-immunostaining in ferret flocculus illustrating a cluster of GAD+ neurons (red arrows in a', red dots in b) in the white matter facing the transition zone between the flocculus and the ventral paraflocculus.

Scale Bar: a, 500 μm.

TABLE 2 Number and molecular markers of BIN neurons in mammalian species examined in this study

Species	Number of neurons (*10³)[a]	Markers			
		GAD65/67	ChAT	Muscarinic M2	Necab1
Macaque	1.3 ± 0.2 (ChAT)	+	+/−	+	−
	2.2 ± 0.2 (GAD)				
Man	4.6 ± 0.7 (ChAT)	+	+/−	+	N.D.
Rat	0.66 ± 0.06 (GAD)	+	−	+	−
Mouse	0.33 ± 0.02 (GlyT2-GFP)	+	−	+	+
Rabbit	0.8 ± 0.2 (GAD)	+	−	+	N.D.
Ferret	1.1 ± 0.1 (GAD)	+	−	+	−

[a] Numbers represent mean ± SE per half cerebellum and are extrapolated from counting 1 in 4 (mouse, rat), 1 in 5 (ferret) and 1 in 10 (rabbit, macaque, man) serial sections labeled for the marker in brackets.
N.D., not determined.

Discussion

The BIN has been originally identified by Langer in macaque as a population of neurons that innervate the flocculus and the ventral paraflocculus (also designated floccular complex; Voogd *et al.*, 2012), and is located in the basal white matter between the flocculus and the cerebellar nuclei (Langer *et al.*, 1985; Langer, 1985). Although this finding was confirmed by others (Nagao *et al.*, 1997a), the BIN has been largely neglected in the literature. In addition, in some studies (Gonzalo-Ruiz *et al.*, 1988; Takikawa *et al.*, 1998) the term BIN has been used for a group of neurons that does not overlap with the BIN originally defined by Langer (Langer, 1985). In these studies, 'BIN' neurons were found to project to pontine nuclei (Gonzalo-Ruiz *et al.*, 1988) and to display saccade-related firing activity (Takikawa *et al.*, 1998). However, the cells explored in these studies were localized medial of group Y, whereas BIN neurons identified by retrograde tracing localize lateral of group Y (see Fig 1 of this study, and Fig. 3 in Langer, 1985). In a recent human brain Atlas (Ding *et al.*, 2016), the term BIcb (basal interstitial nucleus of the cerebellum) has been assigned to a population of large neurons in the roof of the 4th ventricle neurons (see Fig. 13 in Ding *et al.*, 2016). In this study, there is no reference to the study of Langer (Langer, 1985), and it is not clear whether the BIcb was intended to represent the human homologue of the macaque BIN (Ding *et al.*, 2016). On the basis of our data, we propose to reserve the term BIN (or BICb) for the population of neurons originally defined by Langer on the basis of retrograde tracing from the flocculus (Langer *et al.*, 1985; Langer, 1985). Our data indicate that these neurons represent a novel GABAergic cerebellar neuron that can be found in multiple mammalian species beyond macaque, including human, rat, mouse, rabbit and ferret (Table 2). Distinctive properties of BIN neurons are the following: they are moderately-sized GABAergic neurons localized in the white matter; they innervate floccular granule cells; and they receive excitatory input from

the medullary reticular formation. BIN neurons represent a second source of inhibition of floccular granule cells, complementing inhibitory input from Golgi cells (Fig. 9h).

We found that BIN neurons in macaque stain positive for GAD and ChAT (Figs 1 and 2) and that ChAT staining can also be used to outline the BIN in human cerebellum (Fig. 3). ChAT staining did not label BIN neurons in the other species investigated, i.e. rat, mouse, rabbit and ferret, but in these species, we identified homologous populations of neurons based on the following criteria: their localization in the white matter, their size and elongated morphologies with dendrites emanating from the two ends, their retrograde labeling after tracer injection in the flocculus, and their immunoreactivity for GAD (Figs 4, 6, 10, 11). Our data indicate that the distribution of BIN neurons shows variability across species, varying from the floccular white matter in rat and mouse, to a relatively condensed distribution in the white matter dorso-medial of the flocculus in ferret, and more widespread distributions in rabbit and primates.

A search in Allen Brain Atlas to identify molecular markers that could further aid in the identification of BIN neurons uncovered the calcium binding protein Necab1 as a marker for BIN neurons in mouse cerebellum (Fig. 6). However, Necab1 is not expressed by BIN neurons in other species. The interspecies heterogeneity of ChAT and Necab1 expression is not against our tenet that BIN neurons represent a single class of neurons across species for two reasons: First, Necab1 is also absent in rat BIN neurons, which are highly similar to mouse BIN neurons in distribution and morphology. Second, interspecies heterogeneity in the expression of neurochemical markers also occurs in other populations of cerebellar neurons, in particular Golgi cells that differentially express ChAT, neurogranin and calretinin in closely related species (Jaarsma *et al.*, 1997; Geurts *et al.*, 2001; Bastianelli, 2003; Singec *et al.*, 2003; Eyre and Nusser, 2016). In addition to Necab1, we found other proteins that might serve as neurochemical markers for BIN neurons, although the majority of these, like GlyT2, muscarinic M2 receptor, Lgi2, and acetylcholine esterase (AChE) are also expressed by Golgi cells (Figs 6, 7). In fact, our data show that also Necab1, while not being expressed by Golgi cells in the flocculus, is expressed in a subset of Golgi cells in most other lobules (Figs 6, 7). Instead mGluR2 is a marker that differentiates BIN neurons from Golgi cells, as it is not expressed in BIN neurons (Figs 2, 5, 6, 8) while being expressed by the majority of cerebellar Golgi cells and their nerve terminals (Neki *et al.*, 1996; Watanabe *et al.*, 1998; Geurts *et al.*, 2001; Simat *et al.*, 2007). Furthermore, in mouse, we found that BIN neurons do not express neurogranin (Fig. 7), another Golgi cell marker that is expressed

in at least 2 subpopulations of Golgi cells in mouse cerebellum, including a subpopulation of Golgi cells (type 4 Golgi cells) that does not express mGluR2 and GlyT2 (Singec *et al.*, 2003; Simat *et al.*, 2007). Importantly, by comparing the expression of a panel of Golgi cell markers between anterior vermis and the flocculus, we found that neurogranin+GlyT2-mGluR2- Golgi cells, while constituting 10-15% of the Golgi cells in the anterior vermis (Simat *et al.*, 2007), are not present in the flocculus, (Fig. 7). These findings on the one hand point to differences in neurochemical identities between Golgi cells in the flocculus compared to the anterior vermis (Simat *et al.*, 2007); and on the other hand, support our notion that mGluR2 may represent a useful marker to differentiate BIN neurons from Golgi cells in the flocculus.

Recently, an ascending GABAergic/glycinergic inhibitory projection from the cerebellar nuclei to the cerebellar cortex has been reported (Ankri *et al.*, 2015). These nucleo-cortical inhibitory neurons differ from BIN neurons in at least two aspects: They do not express Necab1 and they innervate Golgi cells rather granule cells (Ankri *et al.*, 2015). It has been suggested that these inhibitory nucleo-cortical neurons also innervate the floccular granule cell layer (see Fig. 2A of Ankri *et al.*, 2015). However, we did not identify retrogradely labeled neurons in the cerebellar nuclei following CTB tracer injection in the flocculus. We, therefore, speculate that the floccular projections in the study of Ankri *et al.* (2015) derive from BIN neurons. The absence of inhibitory nucleo-cortical projections to the flocculus also is consistent with the absence of neurogranin+GlyT2-mGluR2- Golgi cells in the flocculus (Fig. 7), representing a major target of this projection (Ankri *et al.*, 2015). Taken together, although BIN neurons show resemblance with either Golgi cells or inhibitory nucleo-cortical neurons and probably derive from the same lineage, they are sufficiently distinct to consider them as a novel population of cerebellar neurons.

To characterize BIN axon terminals, we took advantage of their immunoreactivity for ChAT in macaque flocculus (Fig. 2) and we used AAV-GFP anterograde tracing in mice (Fig. 8). We found that BIN axon terminals to various degrees populate glomeruli in the floccular granule cell layer and complement mGluR2+ inhibitory input from Golgi cells. Electron microscopy of anterogradely labeled BIN axons in mouse provided direct demonstration that BIN axons innervate granule cell dendrites (Fig. 8d,e). Using confocal microscopy, we found examples of ChAT+ BIN axons innervating glomeruli with UBC brushes in macaque (Fig. 2i). So far, we did not obtain ultrastructural evidence of BIN axons making synaptic contacts with UBCs. We also used confocal microscopy to examine whether AAV-GFP traced BIN axons contact Golgi cells stained with antibodies against mGluR2 or muscarinic M2 receptor,

The basal interstitial nucleus (BIN) of the cerebellum provides diffuse ascending inhibitory input to the floccular granule cell layer.

2

but so far, we did not find conclusive examples of BIN axons contacting the cell body or dendrites of Golgi cells. Thus, granule cell dendrites represent a major target of BIN axons, while further work is needed to establish to what extent other granule cell layer neurons receive direct BIN input.

To obtain an idea about the relative contribution of inhibition by BIN axons in the floccular granule cell layer, we determined the proportion of ChAT+ inhibitory boutons in macaque flocculus, and the proportion of GFP+ inhibitory boutons in AAV- GFP anterograde tracing experiments in mice. These analyses indicated that at least 20% of inhibitory boutons in the floccular granule cell layer represent BIN axon terminals. Thus, in macaque flocculus about 20% of VIAAT+ boutons stain positive for ChAT, while in mice AAV-GFP injections resulted in GFP labelling of up to 20% of VIAAT+ boutons. However, the proportion of BIN axon terminals is likely to be higher in both macaque and mouse, in view of the presence of a population of ChAT- BIN neurons in macaque (Fig. 2a,b), and unlabeled BIN neurons in the AAV- GFP tracing experiments in mice. Analysis of the proportion of Golgi axon terminals on the basis of double labelling for VIAAT and mGluR2 metabotropic glutamate receptor, indicated that about 60% of VIAAT+ axon terminals in the floccular granule cell layer is from mGluR2+ Golgi cells. Instead the proportion of mGluR2+ boutons is higher in other lobules (up to 95% in the anterior vermis; Fig. 8j,k), consistent with previous data indicating that 85-90% of Golgi cells are mGluR2+ (Neki *et al.*, 1996; Simat *et al.*, 2007) and that toxin-mediated selective ablation of mGluR2+ Golgi cells results in almost complete loss of GABAergic boutons in the granule cell layer (Watanabe *et al.*, 1998). The large proportion of mGluR2-VIAAT+ boutons in the floccular granule cell layer (about 40%) as compared to other lobules, at least in part can be explained by the presence BIN axons. mGluR2-VIAAT+ boutons also may derive from mGluR2- Golgi cells, but our data indicate that this type of Golgi cell does not occur in the flocculus (see above). Purkinje cells may represent an additional source of inhibitory boutons in the granule cell layer (Guo *et al.*, 2016) predominantly innervating Lugaro and globular cells (Simat *et al.*, 2007), but double labelling for VIAAT and the Purkinje cell marker calbindin indicated that inhibitory boutons from Purkinje cells are rare in the floccular granule cell layer (<1% of VIAAT boutons). Taken together, our data indicate that about 60% of the VIAAT+ axon terminals in the floccular granule cell layer derive from mGluR2+ Golgi cells, while at least 20% and potentially up to 40% of the residual VIAAT+ axon terminals are from BIN neurons.

What could be the function of BIN neurons in the floccular circuitry? BIN axon terminals co-distribute with mGluR2+ Golgi cell axon terminals in

the same glomeruli, and likely have complementary roles in controlling mossy fiber to granule cell signaling. Golgi cells receive excitatory granule cell and mossy fiber input and implement a local inhibitory feedback circuit that may control the precise timing and gain of granule cell firing (Cesana *et al.*, 2013; Pietrajtis and Dieudonné, 2013; Valera *et al.*, 2016). The distinctive feature of Golgi cells is their local dense axonal plexus that provides inhibitory input primarily to nearby granule cells, although some Golgi cells may have more distant projections (Pietrajtis and Dieudonné, 2013). BIN neurons instead project to large portions of the flocculus, and only produce a few axon terminals per glomerulus. This wiring pattern indicates that BIN neurons have a more global inhibitory role over widely distributed granule cells (Fig. 9h). We also show that BIN neurons receive bilateral glutamatergic input from a population of neurons in the medullary gigantocellular reticular formation. These fibers innervate the cell body and proximal dendrites of BIN neurons, and likely play an important role in controlling the activity of BIN neurons. Importantly, our data also indicate that BIN neurons are not innervated by collaterals from climbing and mossy fiber collaterals that innervate the floccular cortex, although at this point we can not exclude collateral projections on distal dendrites of BIN neurons. It had been anticipated by Langer that BIN neurons receive inhibitory input from floccular Purkinje cells (Langer, 1985). However, anterograde tracing experiments in macaque have shown that BIN neurons to not receive input from the flocculus (Nagao *et al.*, 1997b). In accord with the idea that BIN neurons do not receive Purkinje cell input, our data indicate that BIN neurons are only innervated by calbindin-negative inhibitory boutons.

Together the data indicate that BIN neurons represent a diffuse inhibitory system of floccular granule cells that is controlled by a group of neurons in the medullary formation (Fig. 9h). Understanding the information conveyed by the medullary BIN afferents, will be critical for clarifying the role of the BIN neurons in the well-established role of the flocculus in eye movement control (Ito, 1982; De Zeeuw *et al.*, 1995; Schonewille *et al.*, 2006; Voogd *et al.*, 2012; Voges *et al.*, 2017). Importantly, future studies on the function of BIN neurons would benefit from experiments in multiple mammalian species to validate whether BIN neurons indeed represent a single class of prefloccular neurons with evolutionary conserved function.

Ankri L, Husson Z, Pietrajtis K, Proville R, Lena C, Yarom Y, Dieudonne S, Uusisaari MY. 2015. A novel
inhibitory nucleo-cortical circuit controls cerebellar Golgi cell activity. Elife 4.

Arenz A, Bracey EF, Margrie TW. 2009. Sensory representations in cerebellar granule cells. Curr Opin
Neurobiol 19(4):445-451.

Barmack NH, Baughman RW, Eckenstein FP. 1992a. Cholinergic innervation of the cerebellum
of rat, rabbit, cat, and monkey as revealed by choline acetyltransferase activity and
immunohistochemistry. J Comp Neurol 317(3):233-249.

Barmack NH, Baughman RW, Eckenstein FP, Shojaku H. 1992b. Secondary vestibular cholinergic
projection to the cerebellum of rabbit and rat as revealed by choline acetyltransferase
immunohistochemistry, retrograde and orthograde tracers. J Comp Neurol 317(3):250-270.

Bastianelli E. 2003. Distribution of calcium-binding proteins in the cerebellum. Cerebellum (London,
England) 2(4):242-262.

Boele HJ, Koekkoek SK, De Zeeuw CI, Ruigrok TJ. 2013. Axonal sprouting and formation of terminals in
the adult cerebellum during associative motor learning. J Neurosci 33(45):17897-17907.

Cerminara NL, Lang EJ, Sillitoe RV, Apps R. 2015. Redefining the cerebellar cortex as an assembly of
non-uniform Purkinje cell microcircuits. Nat Rev Neurosci 16(2):79-93.

Cesana E, Pietrajtis K, Bidoret C, Isope P, D'Angelo E, Dieudonne S, Forti L. 2013. Granule cell
ascending axon excitatory synapses onto Golgi cells implement a potent feedback circuit in the
cerebellar granular layer. J Neurosci 33(30):12430-12446.

Chabrol FP, Arenz A, Wiechert MT, Margrie TW, DiGregorio DA. 2015. Synaptic diversity enables
temporal coding of coincident multisensory inputs in single neurons. Nature neuroscience
18(5):718-727.

Davie JT, Clark BA, Hausser M. 2008. The origin of the complex spike in cerebellar Purkinje cells. J
Neurosci 28(30):7599-7609.

de Lacalle S, Hersh LB, Saper CB. 1993. Cholinergic innervation of the human cerebellum. J Comp
Neurol 328(3):364-376.

De Zeeuw CI, Hoebeek FE, Bosman LW, Schonewille M, Witter L, Koekkoek SK. 2011. Spatiotemporal
firing patterns in the cerebellum. Nat Rev Neurosci 12(6):327-344.

De Zeeuw CI, Ten Brinke MM. 2015. Motor Learning and the Cerebellum. Cold Spring Harb Perspect
Biol 7(9):a021683.

De Zeeuw CI, Wylie DR, Stahl JS, Simpson JI. 1995. Phase relations of Purkinje cells in the rabbit
flocculus during compensatory eye movements. J Neurophysiol 74(5):2051-2064.

Dean P, Porrill J, Ekerot CF, Jorntell H. 2010. The cerebellar microcircuit as an adaptive filter:
experimental and computational evidence. Nat Rev Neurosci 11(1):30-43.

Ding SL, Royall JJ, Sunkin SM, Ng L, Facer BA, Lesnar P, Guillozet-Bongaarts A, McMurray B, Szafer
A, Dolbeare TA, Stevens A, Tirrell L, Benner T, Caldejon S, Dalley RA, Dee N, Lau C, Nyhus J,
Reding M, Riley ZL, Sandman D, Shen E, van der Kouwe A, Varjabedian A, Write M, Zollei L,
Dang C, Knowles JA, Koch C, Phillips JW, Sestan N, Wohnoutka P, Zielke HR, Hohmann JG,
Jones AR, Bernard A, Hawrylycz MJ, Hof PR, Fischl B, Lein ES. 2016. Comprehensive cellular-
resolution atlas of the adult human brain. J Comp Neurol 524(16):3127-3481.

Dugue GP, Dumoulin A, Triller A, Dieudonne S. 2005. Target-dependent use of co-released inhibitory
transmitters at central synapses. J Neurosci 25(28):6490-6498.

Eyre MD, Nusser Z. 2016. Only a Minority of the Inhibitory Inputs to Cerebellar Golgi Cells Originates
from Local GABAergic Cells. eNeuro 3(2).

Gao Z, Proietti-Onori M, Lin Z, Ten Brinke MM, Boele HJ, Potters JW, Ruigrok TJ, Hoebeek FE, De
Zeeuw CI. 2016. Excitatory Cerebellar Nucleocortical Circuit Provides Internal Amplification during
Associative Conditioning. Neuron 89(3):645-657.

Gao Z, van Beugen BJ, De Zeeuw CI. 2012. Distributed synergistic plasticity and cerebellar learning.
Nat Rev Neurosci 13(9):619-635.

Geurts FJ, Timmermans J, Shigemoto R, De Schutter E. 2001. Morphological and neurochemical
differentiation of large granular layer interneurons in the adult rat cerebellum. Neuroscience
104(2):499-512.

Gonzalo-Ruiz A, Leichnetz GR, Smith DJ. 1988. Origin of cerebellar projections to the region of the
oculomotor complex, medial pontine reticular formation, and superior colliculus in New World
monkeys: a retrograde horseradish peroxidase study. J Comp Neurol 268(4):508-526.

Guo C, Witter L, Rudolph S, Elliott HL, Ennis KA, Regehr WG. 2016. Purkinje Cells Directly Inhibit
Granule Cells in Specialized Regions of the Cerebellar Cortex. Neuron 91(6):1330-1341.

Harris JA, Oh SW, Zeng H. 2012. Adeno-associated viral vectors for anterograde axonal tracing with

2

fluorescent proteins in nontransgenic and cre driver mice. Curr Protoc Neurosci Chapter 1:Unit 1 20 21-18.

Harvey RJ, Napper RM. 1988. Quantitative study of granule and Purkinje cells in the cerebellar cortex of the rat. J Comp Neurol 274(2):151-157.

Hioki H, Fujiyama F, Taki K, Tomioka R, Furuta T, Tamamaki N, Kaneko T. 2003. Differential distribution of vesicular glutamate transporters in the rat cerebellar cortex. Neuroscience 117(1):1-6.

Huang CC, Sugino K, Shima Y, Guo C, Bai S, Mensh BD, Nelson SB, Hantman AW. 2013. Convergence of pontine and proprioceptive streams onto multimodal cerebellar granule cells. Elife 2:e00400.

Ito M. 1982. Cerebellar control of the vestibulo-ocular reflex--around the flocculus hypothesis. Annu Rev Neurosci 5:275-296.

Jaarsma D, Dino MR, Cozzari C, Mugnaini E. 1996. Cerebellar choline acetyltransferase positive mossy fibres and their granule and unipolar brush cell targets: a model for central cholinergic nicotinic neurotransmission. J Neurocytol 25(12):829-842.

Jaarsma D, Dino MR, Ohishi H, Shigemoto R, Mugnaini E. 1998. Metabotropic glutamate receptors are associated with non-synaptic appendages of unipolar brush cells in rat cerebellar cortex and cochlear nuclear complex. J Neurocytol 27(5):303-327.

Jaarsma D, Levey AI, Frostholm A, Rotter A, Voogd J. 1995. Light-microscopic distribution and parasagittal organisation of muscarinic receptors in rabbit cerebellar cortex. J Chem Neuroanat 9(4):241-259.

Jaarsma D, Ruigrok TJ, Caffe R, Cozzari C, Levey AI, Mugnaini E, Voogd J. 1997. Cholinergic innervation and receptors in the cerebellum. Prog Brain Res 114:67-96.

Jakab RL, Hamori J. 1988. Quantitative morphology and synaptology of cerebellar glomeruli in the rat. Anat Embryol (Berl) 179(1):81-88.

Jelitai M, Puggioni P, Ishikawa T, Rinaldi A, Duguid I. 2016. Dendritic excitation-inhibition balance shapes cerebellar output during motor behaviour. Nat Commun 7:13722.

Kuijpers M, van Dis V, Haasdijk ED, Harterink M, Vocking K, Post JA, Scheper W, Hoogenraad CC, Jaarsma D. 2013. Amyotrophic lateral sclerosis (ALS)-associated VAPB-P56S inclusions represent an ER quality control compartment. Acta Neuropathol Commun 1:24.

Langer T, Fuchs AF, Scudder CA, Chubb MC. 1985. Afferents to the flocculus of the cerebellum in the rhesus macaque as revealed by retrograde transport of horseradish peroxidase. J Comp Neurol 235(1):1-25.

Langer TP. 1985. Basal interstitial nucleus of the cerebellum: cerebellar nucleus related to the flocculus. J Comp Neurol 235(1):38-47.

Lein ES, Hawrylycz MJ, Ao N, Ayres M, Bensinger A, Bernard A, Boe AF, Boguski MS, Brockway KS, Byrnes EJ, Chen L, Chen L, Chen TM, Chin MC, Chong J, Crook BE, Czaplinska A, Dang CN, Datta S, Dee NR, Desaki AL, Desta T, Diep E, Dolbeare TA, Donelan MJ, Dong HW, Dougherty JG, Duncan BJ, Ebbert AJ, Eichele G, Estin LK, Faber C, Facer BA, Fields R, Fischer SR, Fliss TP, Frensley C, Gates SN, Glattfelder KJ, Halverson KR, Hart MR, Hohmann JG, Howell MP, Jeung DP, Johnson RA, Karr PT, Kawal R, Kidney JM, Knapik RH, Kuan CL, Lake JH, Laramee AR, Larsen KD, Lau C, Lemon TA, Liang AJ, Liu Y, Luong LT, Michaels J, Morgan JJ, Morgan RJ, Mortrud MT, Mosqueda NF, Ng LL, Ng R, Orta GJ, Overly CC, Pak TH, Parry SE, Pathak SD, Pearson OC, Puchalski RB, Riley ZL, Rockett HR, Rowland SA, Royall JJ, Ruiz MJ, Sarno NR, Schaffnit K, Shapovalova NV, Sivisay T, Slaughterbeck CR, Smith SC, Smith KA, Smith BI, Sodt AJ, Stewart NN, Stumpf KR, Sunkin SM, Sutram M, Tam A, Teemer CD, Thaller C, Thompson CL, Varnam LR, Visel A, Whitlock RM, Wohnoutka PE, Wolkey CK, Wong VY, Wood M, Yaylaoglu MB, Young RC, Youngstrom BL, Yuan XF, Zhang B, Zwingman TA, Jones AR. 2007. Genome-wide atlas of gene expression in the adult mouse brain. Nature 445(7124):168-176.

Lisberger SG. 2009. Internal models of eye movement in the floccular complex of the monkey cerebellum. Neuroscience 162(3):763-776.

Mapelli L, Solinas S, D'Angelo E. 2014. Integration and regulation of glomerular inhibition in the cerebellar granular layer circuit. Frontiers in cellular neuroscience 8:55.

Nagao S, Kitamura T, Nakamura N, Hiramatsu T, Yamada J. 1997a. Differences of the primate flocculus and ventral paraflocculus in the mossy and climbing fiber input organization. J Comp Neurol 382(4):480-498.

Nagao S, Kitamura T, Nakamura N, Hiramatsu T, Yamada J. 1997b. Location of efferent terminals of the primate flocculus and ventral paraflocculus revealed by anterograde axonal transport methods. Neurosci Res 27(3):257-269.

Neki A, Ohishi H, Kaneko T, Shigemoto R, Nakanishi S, Mizuno N. 1996. Metabotropic glutamate

The basal interstitial nucleus (BIN) of the cerebellum provides
diffuse ascending inhibitory input to the floccular granule cell layer.

2

receptors mGluR2 and mGluR5 are expressed in two non-overlapping populations of Golgi cells in the rat cerebellum. Neuroscience 75(3):815-826.

Ohishi H, Ogawa-Meguro R, Shigemoto R, Kaneko T, Nakanishi S, Mizuno N. 1994. Immunohistochemical localization of metabotropic glutamate receptors, mGluR2 and mGluR3, in rat cerebellar cortex. Neuron 13(1):55-66.

Palay SL, Chan-Palay VE. 1974. Cerebellar cortex: cytology and organization. Berlin: Springer Verlag.

Paxinos G, Franklin KBJ. 2001. The mouse brain in stereotaxic coordinates. London: Academic Press.

Pietrajtis K, Dieudonné S. 2013. Golgi Neurons. Handbook of the cerebellum and cerebellar disorders: Springer. p doi: 10.1007/1978-1094-1007-1333-1008_1034.

Powell K, Mathy A, Duguid I, Hausser M. 2015. Synaptic representation of locomotion in single cerebellar granule cells. Elife 4.

Rancz EA, Ishikawa T, Duguid I, Chadderton P, Mahon S, Hausser M. 2007. High-fidelity transmission of sensory information by single cerebellar mossy fibre boutons. Nature 450(7173):1245-1248.

Ruigrok TJ. 2003. Collateralization of climbing and mossy fibers projecting to the nodulus and flocculus of the rat cerebellum. J Comp Neurol 466(2):278-298.

Ruigrok TJ, Hensbroek RA, Simpson JI. 2011. Spontaneous activity signatures of morphologically identified interneurons in the vestibulocerebellum. J Neurosci 31(2):712-724.Ruigrok TJ, Osse RJ, Voogd J. 1992. Organization of inferior olivary projections to the flocculus and ventral paraflocculus of the rat cerebellum. J Comp Neurol 316(2):129-150.

Schonewille M, Luo C, Ruigrok TJ, Voogd J, Schmolesky MT, Rutteman M, Hoebeek FE, De Jeu MT, De Zeeuw CI. 2006. Zonal organization of the mouse flocculus: physiology, input, and output. J Comp Neurol 497(4):670-682.

Sekerková G, Watanabe M, Martina M, Mugnaini E. 2014. Differential distribution of phospholipase C beta isoforms and diaglycerol kinase-beta in rodents cerebella corroborates the division of unipolar brush cells into two major subtypes. Brain Struct Funct 219(2):719-749.

Siegers JY, Short KR, Leijten LM, de Graaf M, Spronken MI, Schrauwen EJ, Marshall N, Lowen AC, Gabriel G, Osterhaus AD, Kuiken T, van Riel D. 2014. Novel avian-origin influenza A (H7N9) virus attachment to the respiratory tract of five animal models. J Virol 88(8):4595-4599.

Simat M, Parpan F, Fritschy JM. 2007. Heterogeneity of glycinergic and gabaergic interneurons in the granule cell layer of mouse cerebellum. J Comp Neurol 500(1):71-83.

Singec I, Knoth R, Ditter M, Frotscher M, Volk B. 2003. Neurogranin expression by cerebellar neurons in rodents and non-human primates. J Comp Neurol 459(3):278-289.

Singec I, Knoth R, Ditter M, Volk B, Frotscher M. 2004. Neurogranin is expressed by principal cells but not interneurons in the rodent and monkey neocortex and hippocampus. J Comp Neurol 479(1):30-42.

Sudhakar SK, Hong S, Raikov I, Publio R, Lang C, Close T, Guo D, Negrello M, De Schutter E. 2017. Spatiotemporal network coding of physiological mossy fiber inputs by the cerebellar granular layer. PLoS Comput Biol 13(9):e1005754.

Takikawa Y, Kawagoe R, Miyashita N, Hikosaka O. 1998. Presaccadic omnidirectional burst activity in the basal interstitial nucleus in the monkey cerebellum. Exp Brain Res 121(4):442-450.

Tan J, Epema AH, Voogd J. 1995. Zonal organization of the flocculovestibular nucleus projection in the rabbit: a combined axonal tracing and acetylcholinesterase histochemical study. J Comp Neurol 356(1):51-71.

Valera AM, Binda F, Pawlowski SA, Dupont JL, Casella JF, Rothstein JD, Poulain B, Isope P. 2016. Stereotyped spatial patterns of functional synaptic connectivity in the cerebellar cortex. Elife 5.

van Dorp S, De Zeeuw CI. 2015. Forward Signaling by Unipolar Brush Cells in the Mouse Cerebellum. Cerebellum (London, England).

van Riel D, Leijten LM, Kochs G, Osterhaus AD, Kuiken T. 2013. Decrease of virus receptors during highly pathogenic H5N1 virus infection in humans and other mammals. Am J Pathol 183(5):1382-1389.

Voges K, Wu B, Post L, Schonewille M, De Zeeuw CI. 2017. Mechanisms underlying vestibulo-cerebellar motor learning in mice depend on movement direction. J Physiol 595(15):5301-5326.

Vong L, Ye C, Yang Z, Choi B, Chua S, Jr., Lowell BB. 2011. Leptin action on GABAergic neurons prevents obesity and reduces inhibitory tone to POMC neurons. Neuron 71(1):142-154.

Voogd J, Glickstein M. 1998. The anatomy of the cerebellum. Trends Neurosci 21(9):370-375.

Voogd J, Schraa-Tam CK, van der Geest JN, De Zeeuw CI. 2012. Visuomotor cerebellum in human and nonhuman primates. Cerebellum (London, England) 11(2):392-410.

Wang Q, Henry AM, Harris JA, Oh SW, Joines KM, Nyhus J, Hirokawa KE, Dee N, Mortrud M, Parry

S, Ouellette B, Caldejon S, Bernard A, Jones AR, Zeng H, Hohmann JG. 2014. Systematic comparison of adeno-associated virus and biotinylated dextran amine reveals equivalent sensitivity between tracers and novel projection targets in the mouse brain. J Comp Neurol 522(9):1989-2012.

Watanabe D, Inokawa H, Hashimoto K, Suzuki N, Kano M, Shigemoto R, Hirano T, Toyama K, Kaneko S, Yokoi M, Moriyoshi K, Suzuki M, Kobayashi K, Nagatsu T, Kreitman RJ, Pastan I, Nakanishi S. 1998. Ablation of cerebellar Golgi cells disrupts synaptic integration involving GABA inhibition and NMDA receptor activation in motor coordination. Cell 95(1):17-27.

Witter L, De Zeeuw CI. 2015. Regional functionality of the cerebellum. Curr Opin Neurobiol 33:150-155.

Zampini V, Liu JK, Diana MA, Maldonado PP, Brunel N, Dieudonne S. 2016. Mechanisms and functional roles of glutamatergic synapse diversity in a cerebellar circuit. Elife 5.

Zeilhofer HU, Studler B, Arabadzisz D, Schweizer C, Ahmadi S, Layh B, Bosl MR, Fritschy JM. 2005. Glycinergic neurons expressing enhanced green fluorescent protein in bacterial artificial chromosome transgenic mice. J Comp Neurol 482(2):123-141.

Zhang MD, Barde S, Szodorai E, Josephson A, Mitsios N, Watanabe M, Attems J, Lubec G, Kovacs GG, Uhlen M, Mulder J, Harkany T, Hokfelt T. 2016. Comparative anatomical distribution of neuronal calcium-binding protein (NECAB) 1 and -2 in rodent and human spinal cord. Brain Struct Funct 221(7):3803-3823.

Zhou H, Lin Z, Voges K, Ju C, Gao Z, Bosman LW, Ruigrok TJ, Hoebeek FE, De Zeeuw CI, Schonewille M. 2014. Cerebellar modules operate at different frequencies. Elife 3:e02536.
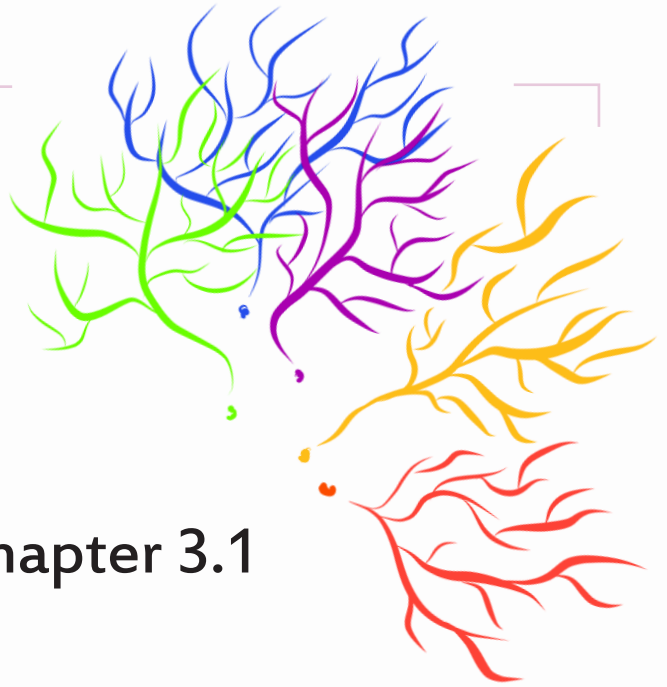
Chapter 3.1

Region-specific preservation of Purkinje cell morphology and motor behavior in the ATXN1[82Q] mouse model of Spinocerebellar Ataxia 1

Joshua J. White, Laurens W.J. Bosman, François G.C. Blot, Catarina Osório, Bram W. Kuppens, Wilhelmina H.J.J. Krijnen, Charlotte Andriessen, Chris I. De Zeeuw, Dick Jaarsma, Martijn Schonewille

Abstract

Purkinje cells are the primary processing units of the cerebellar cortex and display molecular heterogeneity that aligns with differences in physiological properties, projection patterns and susceptibility to disease. In particular, multiple mouse models that feature Purkinje cell degeneration are characterized by incomplete and patterned Purkinje cell degeneration, suggestive of relative sparing of Purkinje cell subpopulations, such as those expressing Aldolase C/zebrinII (AldoC) or residing in the vestibulo-cerebellum. Here, we investigated a well-characterized Purkinje cell-specific mouse model for spinocerebellar ataxia type 1 (SCA1) that expresses human ATXN1 with a polyQ expansion (82Q). Our pathological analysis confirms previous findings that Purkinje cells of the vestibulo-cerebellum, i.e. the flocculonodular lobes, and crus I are relatively spared from key pathological hallmarks: somatodendritic atrophy, and the appearance of p62/SQSTM1-positive inclusions. However, immunohistological analysis of transgene expression revealed that spared Purkinje cells do not express mutant ATXN1 protein, indicating the sparing of Purkinje cells can be explained by an absence of transgene expression. Additionally, we found that Purkinje cells in other cerebellar lobes that typically express AldoC, not only display severe pathology, but also show loss of AldoC expression. The relatively preserved flocculonodular lobes and crus I showed a substantial fraction of Purkinje cells that expressed the mutant protein and displayed pathology as well as loss of AldoC expression. Despite considerable pathology in these lobes, behavioral analyses demonstrated a relative sparing of related functions, suggestive of sufficient functional cerebellar reserve. Together, the data indicate that mutant ATXN1 affects both AldoC-positive and AldoC-negative Purkinje cells and disrupts normal parasagittal AldoC expression in Purkinje cells. Our results show that, in a mouse model otherwise characterized by widespread Purkinje cell degeneration, sparing of specific subpopulations is sufficient to maintain normal performance of specific behaviors within the context of the functional, modular map of the cerebellum.

Introduction

Neurodegenerative diseases, whether sporadic or genetic, typically follow a specific pattern of neural death or degeneration/atrophy affecting one or a few specific cell-types even when the genetic defect is expressed throughout the brain (30,81). The impact on a specific cell type or brain region is likely related to gene expression patterns, environmental factors and neurophysiological activity and leads to the specific set of symptoms that characterize a neurological or psychiatric disease. In genetic disorders, for a specific cell-type to be directly affected by a mutation requires that the cell expresses the mutated gene and depends on the interaction of the gene with the general homeostasis and physiology of the cell. Similarly, single mutations are able to affect only a subset of a particular neuronal cell-type, provided that there is sufficient differentiation within that type of neuron. Along these lines, molecular markers have been identified for selective populations of vulnerable or non-vulnerable motor neurons in amyotrophic lateral sclerosis (24,75), pyramidal neurons in dementia (63) and dopaminergic neurons in Parkinson's Disorder (12,27).

Cerebellar ataxias form a large group of neurodegenerative diseases, with well over 100 genetic and sporadic forms (4,49,76). In many of these, dysfunction or degeneration of cerebellar Purkinje cells is a major cause of the clinical symptoms (20,25,49,85,104). Despite this common disease target, individual forms of cerebellar ataxia show differences in the symptomatic progress of the disease (55). Possibly, these differences are at least in part explained by differential vulnerability of Purkinje cells, as has been demonstrated in mouse models (79). These mouse models represent a unique substrate to investigate factors underlying differential vulnerability of neurons, because Purkinje cells are implicated in multiple neurodegenerative disorders in which they are predominantly affected even when genetic mutations are expressed throughout the brain (49,83).

Purkinje cells can be divided in groups on the basis of differential gene expression and activity patterns (5,18,102). The highly ordered architecture of the cerebellar cortex, and modular organization of Purkinje cells enables precise behavioral, physiological and neuropathological investigation of Purkinje cells subpopulations (6).The expression of Aldolase C (AldoC also known as Zebrin II (1,13)) and other markers (98) map onto the cerebellar cortex in such a way that they form parasagittal stripes that are either predominantly AldoC-negative or -positive (18,31,89). Behaviors mediated by the cerebellum have been to linked to regions that are either AldoC-positive or -negative (101). These regional specifications mean that

lesions or degeneration within specific areas of the cerebellum would likely result in specific behavioral deficits even though redundancy of the cerebellar circuitry assures that behavior can be maintained if the lesion does not affect the entire region (40,45,46).

Consequently, studies on patterned degeneration in mouse models of Purkinje cell degeneration/atrophy have focused on the relationship with the expression of AldoC (79). In healthy animals, AldoC-negative Purkinje cells have a higher intrinsic firing rate (100,102,103), which may lead to susceptibility itself because of increased likelihood of excitotoxicity (75,96). Under pathological conditions, the situation may be more complicated as, for instance, in a mouse model for spinocerebellar ataxia type 1 (SCA1), the overall firing rates of Purkinje cells proved to be reduced (28), but this appears to follow initial Purkinje cell atrophy.

Because the mechanism of differential Purkinje cell degeneration is not well understood, we have analyzed morphological and behavioral phenotypes in ATXN1[82Q] mice, a mouse model for SCA1. ATXN1[82Q] mice express copies of a polyQ-expanded *ATXN1* gene in a Purkinje cell-specific manner, which leads to obvious Purkinje cell atrophy beginning at 3-4 weeks (16) and locomotor deficits at 5-6 weeks (23). Previous studies have indicated regional variations in the degeneration of Purkinje cells in ATXN1[82Q] mice, particularly sparing the vestibulo-cerebellum (flocculonodular lobes) (19,23). Because these regions are known to be predominantly AldoC-positive, we aimed to more systematically investigate this mouse model for a link between Purkinje cell vulnerability and AldoC expression, and to determine the extent to which differential vulnerability impacts cerebellum-dependent behaviors. However, we found that instead of AldoC, selective sparing of the flocculonodular lobe, and also crus I, correlated with no or minimal transgene expression. To examine the functional impact of the region-specific sparing of a subset of Purkinje cells, we tested behaviors related to these regions and found that, unlike the clear and progressive locomotor impairment in ATXN1[82Q] mice, the behaviors related to surviving regions are indeed preserved.

Methods

Mice:

All experiments were performed on heterozygous transgenic mice of both sexes expressing *ATXN1* with an expanded CAG repeat and their

wildtype littermates. The mutant mice overexpress human *ATXN1* cDNA
containing an 82 CAG-repeat under the Purkinje cell-specific *Pcp2* promoter
(Tg(Pcp2-ATXN1*82Q)5Horr). The generation of this mouse line has been
described as strain "B05" in (16). The mice were kept on an FVB/NHsd
background, except for those involved in compensatory eye-movement
experiments. For the latter, F1 offspring from crossings between FVB/NHsd
and C57Bl6/J mice were used. The mice were kindly provided by Dr. Harry
T. Orr at the University of Minnesota, Minneapolis, MN, USA. Mice were
group housed with a 12 h light/dark cycle and had free access to standard
laboratory food and water. All experiments were performed according to
institutional guidelines as overseen by the Animal Welfare Board of the
Erasmus MC, following Dutch and EU legislation. Prior to the start of the
experiments, a project license for the animal experiments performed for this
study was obtained from the Dutch national authority and filed under no.
AVD101002015273.

Histology:

Mice of 6 weeks, 12 weeks, 18 weeks and 24 weeks old (+/- 3 days)
were included in the experiments. Mice were deeply anesthetized with
pentobarbital (80 mg/kg administered intraperitoneally) and perfused with
saline and 4% paraformaldehyde in series. Tissue was then post-fixed in
4% paraformaldehyde for 1-2 hours before being placed in 10% sucrose in
phosphate buffer overnight at 4° C. The following day, brains were embedded
in gelatin (FujiFilm Wako, #077-03155). They were then placed in a solution
of 30% sucrose and 4% paraformaldehyde for 1-2 hours before being placed
in a solution of only 30% sucrose overnight at 4° C. The following day the
embedded brains were sectioned at 40 µm on a freezing microtome and
placed free-floating into wells of phosphate-buffered saline (PBS). Brain
sections were then incubated with primary antibodies in a solution of 4%
normal horse serum, 0.2% Triton (Sigma-Aldrich, #X100) and PBS overnight
at room temperature or 2 nights at 4° C. Sections were then washed in PBS
3-5x for 5-10 minutes and then incubated for 2 hours in secondary antibodies
in 4% Normal Horse Serum, 0.2% Triton and PBS at room temperature.
For light microscopy sections, staining was visualized with DAB solution
in H_2O_2 and dried on the slide overnight before being, counter-stained
with thionin, dehydrated and cover-slipped. For fluorescence microscopy,
sections were incubated in DAPI solution (Thermo Fisher Scientific, Cat#
D3571, RRID:AB_2307445) for 10 minutes then washed and mounted on
coverslips, dried for 30 minutes at 37° C and then mounted onto slides with

Mowiol (Calbiochem, La Jolla, CA, USA). Light microscopy images were acquired with a NanoZoomer (Hamamatsu). Fluorescent images were acquired with an LSM700 confocal (Zeiss) or Axio Imager.M2 (Zeiss). Images were adjusted for contrast and brightness in Adobe Photoshop. Primary antibodies: calbindin (Calbindin D-28K, 1:10000, mouse, Swant 300), AldoC (aldolase C, 1:1000, goat, SC-12065), p62 (SQSTM1/P62 Abcam: 56416, mouse, 1:1000), Ataxin-1 11750 (gift from Dr. Huda Zoghbi, rabbit, 1:1000). Secondary antibodies: Cy3 (1:500, donkey anti-rabbit, Jackson), Alexa-488 (1:500, donkey anti-goat, Jackson), HRP anti-mouse (1:500, Dako P0260), NeuroTrace 435 (Invitrogen). For examination of the percentage of Purkinje cells expressing mutant protein, select lobules from 3 sections each from 3 ATXN1[82Q] mice were counted.

Behavioral assays - locomotion:

Locomotor patterns were studied using the fully-automated ErasmusLadder (Noldus, Wageningen, The Netherlands), consisting of a horizontal ladder counting 37 rungs on each side in between two shelter boxes as described previously (94). Mice were acclimated to the ErasmusLadder for 20 min. the first day and then given 2 days of rest. Next, mice tested with one session a day for five days at ages 6-24 weeks. At the start of each session, the mouse was placed in one of the two shelter boxes. After a period varying from 9-11 s, a LED light turned on in the shelter box signaling that the mouse was supposed to leave the box. If the mouse left the box before the light turned on, a strong air flow drove the mouse back into the box, and the waiting period restarted. If the mouse did not leave the box within 3 s after the light turned on, a strong air flow drove the mouse out of the box. When the mouse arrived in the other box the lights and air flow were turned off and the waiting period from 9-11 s started again, after which the mouse was supposed to start the next trial, etc. A session consists of 42 consecutive crossings of the ladder with 8-12 s of rest in between trials. The sequence of consecutive mice participating in a session was identical for every experiment and inter-experimental variation of the environment was kept at a minimum. All sessions were "non-perturbed sessions" (94) implying that no obstacle rungs were elevated during the trials.

The relative fraction of different step types and step times were calculated to analyze locomotor patterns. Step time was defined as the time that elapsed between the onsets of two consecutive touches. Step types were defined based on the step direction, the distance between two consecutive touches (step length) and whether an upper or lower rung was touched. All steps that are not in the walking direction were defined as back steps. All

forward steps that terminate on an upper rung were sorted to three distinct
categories according to step length: short steps (one or two rungs further),
long steps (three or four rungs further) and jumps (five or more rungs further).
All forward steps that terminate on a lower rung were sorted in lower short
steps, lower long steps and lower jumps as is described for the upper rung
steps. The number of each step type is quantified as a percentage of the total
amount of steps per trial.

Mice were also evaluated on a 1-meter-long and 12 mm diameter
balance beam at ages 7, 12, 18 and 14 weeks. One end of the beam was
supported by a metal pole and the other end terminated in a home cage, with
the beam suspending horizontally 50 cm above the surface. Usual parameters
are the crossing time and the number of slips per run (57). However, the
latter parameter is inadequate for the assessment of the severe ATXN1[82Q]
phenotype. Hence, this is replaced by the percentage of runs where the end
of the beam is reached (percentage of successful trials).

Behavioral assays - licking:

The rhythmicity of spontaneous licking was derived from
measurements of the junction potential between an aluminum floor plate
and the spout of a normal drinking bottle in a normal home cage with the
use of an AD converter operating at a sample rate of 6 kHz (RZ2, Tucker-
Davis Technologies, Alachua, FL, USA) as described before (70). Mice were
water-deprived for 2 h prior to the start of the recording and subsequently
measured overnight (> 12 h) at the age of 7, 12, 18 and 24 weeks. The data
from the first hour was disregarded, as the mice typically showed irregular,
explorative behavior during this period. A lick was recognized in the junction
potential recording as a stereotypic event and detected by threshold crossing
using SpikeTrain (Neurasmus BV, Rotterdam, The Netherlands). All traces
were inspected visually and incorrectly detected events were corrected. We
restricted our analysis to bouts of rhythmic licking, which were defined by the
occurrence of at least two licks with a maximal inter-lick interval (ILI) of 150 ms
and minimum of 50 ms. The upper and lower cut-offs were established based
on histograms of ILIs measured in past and present recordings. The ILIs were
defined using cut-offs well over 150 ms and the graphs demonstrate a bell-
shaped curve between 50 and 150 ms which encompasses ±90% of all ILIs,
while ILIs with lengths beyond 150 ms show no such organization. Prior to
analysis, the total amount of licks was counted for each genotype to confirm
an equal magnitude of data. The average licking rate, median number of licks
per licking bout and coefficient of variance (CV2) of subsequent ILIs within

licking bouts were calculated for each mouse and averaged per genotype. The CV2 was calculated as (39).

Behavioral assays – compensatory eye movements:

Compensatory eye movements were tracked in head-fixed mice implanted with a custom-built pedestal. For surgery, mice were anesthetized with isoflurane, body temperature was maintained at 37° C and ophthalmic ointment (Duratears, Alcon®) was applied to prevent the eyes from desiccating. The scalp, after shaving and treatment with Xylocaine (AstraZenica), was opened to expose the skull. The periosteum was scraped away, again after treatment with Xylocaine, and the bone was covered with Optibond (Kerr). The pedestal was attached to the skull with Charisma (Heraeus Kulzer). Both Optibond and Charisma are cured with UV-light. As anti-inflammatory agent and analgesic, carpofen (0,5 mg/ml, Rimadyl Cattle) and bupivacaine (0,1 mg/ml, Actavis) were used respectively. The surgery was performed at least two days prior to the start of the experiment. For eye movement testing, mice were first head-fixed in the center of a turntable (Ø 60 cm), surrounded by a paper drum with random-dotted pattern (Ø 63 cm, dot size 2°) and tested for baseline optokinetic (OKR), vestibulo-ocular (VOR) and visual vestibulo-ocular (VVOR) responses. To this end, we subjected mice to 10° peak-to-peak sinusoidal rotations at 0.1-1.0 Hz of the visual stimulus (OKR), the table in the dark (VOR) or the table in the light (VVOR). The following day the ability for adaptation was tested using 6 x 5 min training sessions during with the visual stimulus rotated out-of-phase with the table in light, aiming to increase the gain of the VOR, with a VOR probe performed in darkness at the start and after every 5 minutes of training. Data were acquired with a CCD camera and video acquisition software (ISCAN Inc.) which tracked the movements of the pupil in relation to the corneal reflection created by infrared lamps. A calibration was performed at the beginning and end of each measurement, the calibration is required to turn the pixels of the video into angles when analyzing the acquired data. To determine the gain (size) and phase (timing), the eye movement and stimulus traces were differentiated to velocity signals, averaged across cycles and fitted with a sine; the amplitude of the fitted eye movement divided by stimulus was taken as the gain and the shift in time was taken as phase (in degrees of the cycle).

Results

Purkinje cell degeneration in the ATXN1[82Q] mouse is regionally specific:

The ATXN1[82Q] mouse (line B05) is a transgenic line that overexpresses human ATXN1 with an 82 CAG-repeat under control of the Purkinje cell-specific *Pcp2* promoter (16). ATXN1[82Q] mice develop progressive degeneration of Purkinje cells, predominantly consisting of gradual somatodendritic atrophy starting from 4-6 weeks and ultimately culminating in late onset Purkinje cell death after 6-8 months of age (23). Following up on previous reports that a subset of Purkinje cells are spared from pathology (23), particularly those residing in the flocculonodular lobes, we first the mapped the spatiotemporal distribution of Purkinje cell somatodendritic atrophy in sagittal and coronal sections stained for calbindin, a Purkinje cell specific marker in the cerebellum. Widespread somatodendritic atrophy is clearly visible in the majority of Purkinje cells in sagittal sections at 12 weeks the (Figure 1). The nodulus (lobule X), especially its ventral side, the flocculus including the ventral paraflocculus, and crus I instead are relatively spared (Figure 1D and Figure 1K-L). Notably, other lobules showed a few sporadic examples where Purkinje cells are spared. The same picture emerged from a more systematic analysis of coronal series from ATXN1[82Q] mice from 6 to 24 weeks of age (Figure 2). At 6 weeks of age, only mild Purkinje cell atrophy is manifested in the form of non-uniform expression of calbindin in the molecular layer of the cerebellar cortex (Figure 2A,C,E,G). Purkinje cell atrophy then progressed steadily from 12 to 18 and 24 weeks. However, the spared areas of the cerebellar cortex are spared at all ages. For instance, the flocculus still exhibits normal Purkinje cell calbindin expression and morphology at 24 weeks when the anterior vermis exhibits severe Purkinje cell atrophy (Figure 2).

Disrupted AldoC expression in ATXN1[82Q] mice:

Having established the spatial distribution of Purkinje cell somatodendritic atrophy, we next investigated the relationship of Purkinje cell atrophy and AldoC (Figure 3). Surprisingly, we found that AldoC expression was dramatically altered in ATXN1[82Q] mice at all ages investigated: many regions known to express AldoC in wild-type mice either do not express AldoC or the expression is patchy (Figure 3C-D). Closer analysis showed that AldoC expression was only spared in Purkinje cells that did not show somatodendritic atrophy. Thus, AldoC expression is largely normal in the

flocculonodular lobules and crus I. To a lesser extent, AldoC was also still expressed in lobule VI, although more patchy than is typical in wildtype mice (Figure 3). Instead, AldoC expression was mostly absent in the rest of the central and posterior cerebellum, which typically expresses large AldoC-positive bands (90). In the anterior vermis characterized by three thin stripes of AldoC-positive Purkinje cells (31), these stripes are unreliably present in ATXN1[82Q] mice.

We also compared AldoC expression with an additional marker of Purkinje cell pathology, i.e. nuclear inclusions that represent a mid-late hallmark in ATXN1[82Q] Purkinje cells (21). To label nuclear inclusions, we stained for p62/SQSTM1 (p62 hereafter), an autophagy adaptor protein that is present at high levels in many neuronal inclusions, including intranuclear inclusions of Sca1 patients (84). In ATXN1[82Q] mice at 12 weeks, we found expression of p62-positive intranuclear inclusions in all Purkinje cells with somatodendritic atrophy, including those in lobes and zones that would typically express AldoC (Figure 4). Spared AldoC-positive Purkinje cells instead do not express p62-positive intranuclear inclusions (Figure 4). Together, these data indicate that there is complex relationship between AldoC expression and preservation of Purkinje cells in ATXN1[82Q] mice. Although apparently the preserved Purkinje cells are AldoC-positive, many Purkinje cells which normally express AldoC show the same pathological changes as AldoC-negative Purkinje cells in conjunction with loss of AldoC expression.

Somatodendritic atrophy and absence of AldoC expression correlates with high levels of mutant protein expression:

The above data indicate that AldoC-expression is an unreliable predictor of sparing from toxicity in ATXN1[82Q] mice. An alternative possibility would be that preservation of a subset of Purkinje cells is linked to differential mutant protein expression. To test this, we compared transgenic ATXN1[82Q] expression between spared and affected Purkinje cells using a rabbit polyclonal anti-ATXN1 antibody (antibody 11750) that produces weak nuclear staining in wild-type Purkinje cells and very strong nuclear staining in Purkinje cells of ATXN1[82Q] mice derived from the B05 line (48,105). Indeed, we found that a substantial portion of Purkinje cells in the flocculus and the nodulus of ATXN1[82Q] mice show weak or no nuclear staining for ATXN1 (Figure 5), while all affected Purkinje cells, including those in the flocculonodular lobes show intense ATXN1 immunoreactivity. Analysis of labelling intensities suggest a binary distribution ATXN1 immunostaining in Purkinje cells of ATXN1[82Q] mice, being either very high or at the same

level of Purkinje cells in wild-type animals. Based on this analysis, we define Purkinje cells in ATXN1[82Q] mice as either transgene-positive or transgene-negative, although very low expression in negative cells, and subtle difference in expression in positive cells cannot be excluded. Systematic analysis of all cerebellar lobules shows that, in all instances, affected Purkinje cells show high levels of mutant protein expression, while all spared Purkinje cells are negative for the transgene (Figure 5).

Closer inspection of the flocculus and the nodulus indicate that despite relative preservation, many Purkinje cells do express the mutant protein and exhibit somatodendritic atrophy (Figure 5). In fact, somatodendritic atrophy to some extent was masked by calbindin staining of preserved Purkinje cells. Counting of the relative number of transgene-positive Purkinje cells revealed that ~45% of Purkinje cells express the transgene in the flocculus. For comparison ~98% of the Purkinje cells express the transgene in lobules II and III of the vermis. These data indicate that the regional sparing of Purkinje cells in the ATXN1[82Q] mouse correlates with incomplete expression of the ATXN1 mutant protein.

Relative sparing of vestibular functions in in ATXN1[82Q] mice despite locomotor deficits:

ATXN1[82Q] mice have previously been shown to display severe and progressive ataxia starting from 4-6 weeks of age (16,23). However, in view of the relative sparing of specific regions, we questioned whether this would allow for the relative preservation of specific cerebellar behaviors but not others. To this end, we performed four behavioral tests on ATXN1[82Q] mice between 6 and 24 weeks of age, consisting of a balance beam test and locomotor test that require intact spinocerebellar regions, largely consisting of lobules I-V and lobule VIII of the vermis (50,56,62), and two tests that are linked to relatively preserved areas of ATXN1[82Q] mice: a licking test associated with crus I (15), and compensatory eye movements tests that require normal function of the flocculus (7).

The performance of the ATXN1[82Q] mice on the balance beam confirmed the development of progressive ataxia starting before 6 weeks of age (Figure 6A-B). Their ability to walk along a 1 m wooden beam declined with age, with as little as 10% successful trials at 24 weeks of age. Deficits were already apparent at 7 weeks of age, as ATXN1[82Q] performed significantly worse than their wild type littermates ($p < 0.001$, Fisher's exact tests after Benjamini-Hochberg correction for multiple comparisons; Figure 6). Even if the ATXN1[82Q] mice were able to reach the other side of the

beam, their travel times were longer than those of the wild type littermates (p < 0.01, Mann-Whitney tests with Benjamini-Hochberg correction for multiple comparisons; Figure 6).

To further probe locomotor performance, we tested mice on the ErasmusLadder, a horizontal ladder with an alternating high/low pattern of rungs. C57BL6/J mice show a strong preference for walking on the upper rungs, skipping one higher rung and avoiding lower rung touches, while cerebellar mutants show more lower rung steps and in addition show shorter steps (93,94). However, FVB/N wildtype mice of the current study exhibited more lower rung touches than C57BL6/J mice do and the number of lower rung touches was not significantly different between wild-type and ATXN1[82Q] mice (p = 0.370, $F_{1,19}$ = 0.844, repeated measures ANOVA; Figure 6D). However, ATXN1[82Q] mice did make significantly fewer long steps (p = 0.004, $F_{1,19}$ = 10.689, repeated measures ANOVA; Figure 6D), an effect that was already apparent from 12 weeks on (p = 0.003, t_{18} = 3.482, t-test, significant after Benjamini-Hochberg correction for multiple testing). The number of small steps was not significantly increased until 19 weeks (p = 0.004, t_{18} = 3.361, t-test, significant after Benjamini-Hochberg correction for multiple testing; Figure 6D). The smaller steps made by the mutant mice could not be explained by a decrease in body weight, as they ATXN1[82Q] were on average even a bit heavier that their wild type littermates, although this difference did not reach statistical significance (e.g., at 18 weeks: WT: median weight = 21.3 g (interquartile range = 9.4 g), ATXN1[82Q]: median = 26.9 g (interquartile range = 6.9 g), p = 0.778, U = 50.5, Mann-Whitney test). In conclusion, spinocerebellum-dependent behaviors including performance on the balance beam and the ErasmusLadder deteriorated progressively during the course of the disease.

In view of relative sparing of crus I, we adopted a licking test that may require functional integrity of this lobule (15). Mice can lick at a sustained, high rate of up to 12 Hz (70), which can be affected by cerebellar damage (15). We measured the lick rates overnight in the home cages of ATXN1[82Q] mice and wildtype littermates. As we were interested in the licking speed, we focused on licking bouts with a maximal inter-lick interval of 150 ms (Figure 7). There was no significant deficit in the licking frequency of the ATXN1[82Q] mice compared to their wild type littermates at any age (WT: median frequency = 10.5 Hz (interquartile range = 0.4 Hz), ATXN1[82Q] = 10.1 Hz (0.4 Hz), p = 0.136, U = 29.5, Mann-Whitney test; Figure 7). However, at 12 and 24 weeks, licking was slightly but significant more irregular in ATXN1[82Q] mice as compared to wildtype littermates (12 weeks: WT: CV2 = 0.095 (interquartile range = 0.008), ATXN1[82Q] = 0.106 (0.012), p = 0.0208, U =

Region-specific preservation of Purkinje cell morphology and motor behavior in the ATXN1[82Q] mouse model of Spinocerebellar Ataxia 1

3.1

19, Mann-Whitney test; 24 weeks: WT: CV2 = 0.091 (0.009), ATXN1[82Q] = 0.100 (0.012), *p* = 0.0208, *U* = 19, Mann-Whitney test; Figure 7). Thus, we found only a mild impact of the ATXN1[82Q] mutation on the ability to lick rhythmically at a high speed, but no impact on frequency.

Finally, we examined the cerebellar behaviors associated with the flocculus. Compensatory eye movements include the optokinetic reflex (OKR), which is driven by movement of the visual field, and the vestibulo-ocular reflex (VOR), which is the response to head rotation or angular vestibular input, and require intact floccular lobules (2,11,14,69,82,99). Loss of floccular Purkinje cells results in a robust decrease in the gain of the OKR and VOR in the light (also referred to as visual or VVOR), both of which rely heavily on visual input. Instead, OKR and VVOR are largely intact in ATXN1[82Q] mice (Figure 8). There is no significant difference in OKR between ATXN1[82Q] mice and their control littermates at 6 weeks, 12 weeks or 18 weeks (Repeated Measures ANOVA: 6 weeks: p = 0.215, 12 weeks: p = 0.187; 18 weeks: p =0.142). While, the VVOR gain is marginally, yet significantly, different at 6 weeks and 18 weeks, but not at 12 weeks (Repeated Measures ANOVA; 6 weeks: p = 0.010, 12 weeks: p = 0.560, 18 weeks: p = 0.015)., there was no significant difference in phase of VVOR at any age (Two-way ANOVA; 6 weeks: p = 0.085, 12 weeks: p = 0.869, 18 weeks: p = 0.210). There was a more prominent effect on VOR gain at the last time point tested (Repeated Measures ANOVA; 6 weeks: p = 0.465, 12 weeks: p = 0.844, 18 weeks: p = 0.009). Importantly, VOR gain increase adaptation, typically even more sensitive to cerebellar deficits than eye movement performance (10,14,32), was not impaired at any of the ages tested (Repeated Measures ANOVA; 6 weeks: p = 0.116, 12 weeks: p = 0.187, 18 weeks: p = 0.237). In conclusion, unlike spinocerebellum-dependent behaviors, behaviors linked to crus I and the flocculus are relatively spared in ATXN1[82Q] mice.

Discussion

In this study, we aimed to further establish the causes and consequences of patterned Purkinje cell degeneration in the ATXN1[82Q] mouse model, a Purkinje cell degeneration mouse model designed to study disease mechanisms underlying SCA1. Based on previous studies of cerebellar patterned degeneration (79), our starting hypothesis was that AldoC-expressing Purkinje cells are relatively preserved, and that consequently cerebellar behaviors requiring AldoC-positive Purkinje cells are relatively intact, while behavior controlled by AldoC-negative Purkinje cells

are severely affected. Our behavioral analyses are indeed consistent with this idea. There is relative preservation of compensatory eye movements and rhythmic licking, behaviors linked to the flocculonodular lobes and crus I respectively, which are relatively preserved. In contrast, behaviors controlled by predominantly AldoC-negative, non-spared lobules are severely affected. However, our pathological analyses instead indicate that patterned Purkinje cell degeneration in ATXN1 mice does not correlate with differential AldoC expression in the same way that it does in other cerebellar degenerative models (79). Specifically, although we confirm that most preserved Purkinje cells are AldoC-positive, this preservation is actually linked to absent (or much lower) transgene expression especially in the flocculus, nodulus and crus I. Furthermore, we found that a large proportion of Purkinje cells that typically express AldoC, including those in caudal vermal lobules VII-IX and dorsal paraflocculus, exhibit the same pathology as AldoC-negative Purkinje cells in conjunction with complete loss of AldoC expression. This leads us to the conclusion that regional sparing in the ATXN1[82Q] mouse does not correlate with AldoC expression, but is based on an incomplete, region-specific transgene expression.

Our data place the ATXN1[82Q] mouse model in contrast to many rodent models of cerebellar disease which exhibit cell death or degeneration preferentially in AldoC-negative Purkinje cells (79), Such a patterned degeneration is most clearly illustrated in leaner mouse that carries a mutation in a CaV2.1 subunit, and shows preservation of AldoC-positive Purkinje cells (37). Other cerebellar models of patterned degeneration with relative preservation of AldoC-positive Purkinje cells, include other channelopathies (79,80,95), the lysosomal storage disorders Niemann-Pick disease type A/B and type C (58,78,79), and ischemia (96). The presence of similarly patterned atrophy/degeneration in these rodent models that lack any similarity in their pathogenic etiology, suggests that genetic heterogeneity Purkinje cells (22,59) protects subpopulations of Purkinje cells to conditions affecting ionic and metabolic homeostasis. The absence of evidence favoring patterned degeneration in ATXN1[82Q] mice indicate that mutant ATXN1 unlike other stressors is damaging to all Purkinje cells independent of their neurochemical identity. ATXN1 is a DNA-binding protein and the polyQ expansion of ATXN1 induces massive transcriptional dysregulation in Purkinje cells, resulting in reduced expression of key physiological genes (41,53). Consistent with our data showing disruption of patterned AldoC expression in ATXN1[82Q] mice, it has been found that many genes with patterned expression in Purkinje cells like AldoC, PLCB3, KCTD12 and TRPC3 show severely reduced expression in cerebellar cortex of ATXN1[82Q] and other ATXN1 mice

(41,53). These data raise the possibility that neurochemical heterogeneities between subpopulations of Purkinje cells may be lost in conditions impacting transcription as is suggested for SCA1 (41,53).

The ATXN1[82Q] mouse used in the current study has a long L7/Pcp2 promoter sequence predicted to result in expression in all Purkinje cells from an early postnatal age (16,66,92). Our finding that this promotor results in incomplete transgene expression in some lobes, contrast with many other studies using this promoter sequence to drive gene expression specifically in Purkinje cells from an early postnatal age (35,36,51,52,67,66,82,97). Of note, truncated or altered L7/Pcp2 promoter lengths or genome locations can confine marker expression to bands or modules of Purkinje cells and display different developmental progressions (68,66,92). This ability to drive expression in a banded pattern by altering the promoter length is demonstrable of the intrinsic organization and heterogeneity of Purkinje cells. Here we show that the long promoter sequence may lead to transgene expression in a subset of Purkinje cells, putatively linked to transgenic site or other factors influencing the differential regulation of genes in Purkinje cells.

The spared regions include the flocculus and nodulus, which are involved primarily in eye movement (42). Additionally, crus I is spared, which receives somatosensory input from the orofacial region (9,54,86). In rodents, Purkinje cells in crus I are also involved in the motor control of orofacial behaviors, such as licking, whisking and respiration (15,73,74). In humans, tongue movements seem to be more related to lobule VI (34), but crus I is activated during speech (26). The maintenance of behaviors related to these areas suggest that, even in the context of a severely degenerating neural population, selective sparing can result in differentiation in disease symptoms. Importantly, many Purkinje cells within the apparently spared regions express mutant ATXN1 are not in fact spared, but it has been documented that the number of Purkinje cells necessary for motor behavior to remain normal is low (60). So any relative sparing can result in differentiation of disease symptoms.

Although in this model, regional sparing is caused by incomplete transgene expression, patterned degeneration is frequently observed in human cerebellar patients. Patterned degeneration in the cerebellum could potentially explaining why some motor functions are affected earlier than others (55). SCAs are a group of neurodegenerative disorders that have a highly heterogeneous etiology as well as a broad spectrum of symptoms (49). Over fifty subtypes have been described, ranging from mutations in membrane channels to transcription factors (8,83,91). Of the most prevalent repeat expansion SCAs (SCA1, SCA2, SCA3 and SCA6), SCA1 has the fastest disease progress (29). At the end stage, there is widespread atrophy

of, among other brain regions, the cerebellum, the pons, the brainstem and the putamen, while the cerebral cortex is relatively spared (71). *Post mortem* studies demonstrate the partial loss of Purkinje cells in the cerebellum (77). There is some evidence for patterned degeneration and differential behavioral deficits in humans with cerebellar neurodegenerative disease. MRI results demonstrate unique degenerative signatures between different diseases (38). A Voxel-based morphometry study found predominant loss of gray matter volume in the anterior vermis of SCA1 patients (33). Preferential anterior deficits have also been found in SCA3 and SCA6 (65). *Post mortem* tissue analysis has revealed marked differences in the degree of atrophy between cerebellar regions, at least in a number of spinocerebellar ataxias, including SCA1 (43,44,71,72,84). Indeed, SCA1 appears to sometimes lead to specific degeneration of the vermis and preservation of the flocculonodular lobes in human patients (72). Several analyses of oculomotor behavior in SCA patients have revealed a relative lack of deficits in SCA1 patients compared with other SCAs (3,17,47). Although a variety of eye movement defects are present in SCA1 patients, they appear to manifest at later stages in disease progression (88) and to a lesser extent than other SCAs (64).

The modular organization of Purkinje cells based on molecular marker expression is conserved across species including humans (61,87). Our data show both that the expression pattern of mutated genes must be taken into account when analyzing differential susceptibility of Purkinje cells to specific disease but also that the sparing of specific regions of the cerebellar cortex will lead to sparing of specific behaviors even in the context of an otherwise unhealthy cerebellum. The maintenance of these behaviors indicates a mechanism for a functional reserve due to the anatomical organization of the cerebellum. Understanding the modular organization of the cerebellum will be relevant to therapeutic approaches and should thus be further explored in this and other human cerebellar diseases.

3.1

1   Ahn AH, Dziennis S, Hawkes R, Herrup K (1994) The cloning of zebrin II reveals its identity with aldolase C. *Development* **120**:2081–2090.

2   Aiba A, Kano M, Chen C, Stanton ME, Fox GD, Herrup K *et al.* (1994) Deficient cerebellar long-term depression and impaired motor learning in mGluR1 mutant mice. *Cell* **79**:377–388.

3   Anderson TJ, MacAskill MR (2013) Eye movements in patients with neurodegenerative disorders. *Nat Rev Neurol* **9**:74–85.

4   Anheim M, Tranchant C, Koenig M (2012) The autosomal recessive cerebellar ataxias. *N Engl J Med* **366**:636–646.

5   Apps R, Hawkes R (2009) Cerebellar cortical organization: a one-map hypothesis. *Nat Rev Neurosci* **10**:670–681.

6   Apps R, Hawkes R, Aoki S, Bengtsson F, Brown AM, Chen G *et al.* (2018) Cerebellar Modules and Their Role as Operational Cerebellar Processing Units. *The Cerebellum* doi:10.1007/s12311-018-0952-3.

7   Baarsma EA, Collewijn H (1974) Vestibulo□ocular and optokinetic reactions to rotation and their interaction in the rabbit. *J Physiol* **238**:603–625.

8   Becker EBE (2017) From Mice to Men: TRPC3 in Cerebellar Ataxia. *Cerebellum* **16**:877–879.

9   Bosman LWJ, Koekkoek SKE, Shapiro J, Rijken BFM, Zandstra F, van der Ende B *et al.* (2010) Encoding of whisker input by cerebellar Purkinje cells. *J Physiol* **588**:3757–3783.

10   Boyden ES, Katoh A, Pyle JL, Chatila TA, Tsien RW, Raymond JL (2006) Selective Engagement of Plasticity Mechanisms for Motor Memory Storage. *Neuron* **51**:823–834.

11   Boyden ES, Katoh A, Pyle JL, Chatila TA, Tsien RW, Raymond JL (2006) Selective Engagement of Plasticity Mechanisms for Motor Memory Storage. :823–834.

12   Brichta L, Greengard P (2014) Molecular determinants of selective dopaminergic vulnerability in Parkinson's disease: An update. *Front Neuroanat* **8**:1–16.

13   Brochu G, Maler L, Hawkes R (1990) Zebrin II: a polypeptide antigen expressed selectively by Purkinje cells reveals compartments in rat and fish cerebellum. *J Comp Neurol* **291**:538–52.

14   Bruinsma CF, Schonewille M, Gao Z, Aronica EMA, Judson MC, Philpot BD *et al.* (2015) Dissociation of locomotor and cerebellar deficits in a murine Angelman syndrome model. *J Clin Invest* **125**:4305–4315.

15   Bryant JL, Boughter JD, Gong S, Ledoux MS, Heck DH (2010) Cerebellar cortical output encodes temporal aspects of rhythmic licking movements and is necessary for normal licking frequency. *Eur J Neurosci* **32**:41–52.

16   Burright EN, Brent Clark H, Servadio A, Matilla T, Feddersen RM, Yunis WS *et al.* (1995) SCA1 transgenic mice: A model for neurodegeneration caused by an expanded CAG trinucleotide repeat. *Cell* **82**:937–948.

17   Buttner N, Geschwind D, Jen JC, Perlman S, Pulst SM, Baloh RW (1998) Oculomotor phenotypes in autosomal dominant ataxias. *Arch Neurol* **55**:1353–1357.

18   Cerminara NL, Lang EJ, Sillitoe R V, Apps R (2015) Redefining the cerebellar cortex as an assembly of non-uniform Purkinje cell microcircuits. *Nat Rev Neurosci* **16**:79–93.

19   Chopra R, Bushart DD, Cooper JP, Yellajoshyula D, Morrison LM, Huang H *et al.* (2020) Altered Capicua expression drives regional Purkinje neuron vulnerability through ion channel gene dysregulation in spinocerebellar ataxia type 1. *Hum Mol Genet* **29**:3249–3265.

20   Chopra R, Shakkottai VG (2014) Translating cerebellar Purkinje neuron physiology to progress in
      dominantly inherited ataxia. *Future Neurol* **9**:187–196.

21   Chuang C-S, Chang J-C, Soong B-W, Chuang S-F, Lin T-T, Cheng W-L *et al.* (2019) Treadmill
      training increases the motor activity and neuron survival of the cerebellum in a mouse model of
      spinocerebellar ataxia type 1. *Kaohsiung J Med Sci* :2–8.

22   Chung S-H, Calafiore M, Plane JM, Pleasure DE, Deng W (2011) Apoptosis Inducing Factor
      Deficiency Causes Reduced Mitofusion 1 Expression and Patterned Purkinje Cell Degeneration.
      Neurobiol Dis **41**:445–457.

23   Clark H, Burright E, Yunis W, Larson S, Wilcox C, Hartman B *et al.* (1997) Purkinje cell expression
      of a mutant allele of SCA1 in transgenic mice leads to disparate effects on motor behaviors,
      followed by a progressive cerebellar dysfunction and histological alterations. *J Neurosci* **17**:7385–
      7395.

24   Comley L, Allodi I, Nichterwitz S, Nizzardo M, Simone C, Corti S *et al.* (2015) Motor neurons
      with differential vulnerability to degeneration show distinct protein signatures in health and ALS.
      Neuroscience **291**:216–229.

25   Cook AA, Fields E, Watt AJ (2020) Losing the beat: contribution of Purkinje cell firing dysfunction
      to disease, and its reversal. *Neuroscience* doi:10.1016/j.neuroscience.2020.06.008.

26   Correia JM, Caballero-Gaudes C, Guediche S, Carreiras M (2020) Phonatory and articulatory
      representations of speech production in cortical and subcortical fMRI responses. *Sci Rep* **10**:1–14.

27   Dawson TM, Dawson VL (2003) Molecular Pathways of Neurodegeneration in Parkinson's
      Disease. *Science (80-)* **302**:819–822.

28   Dell'Orco JM, Wasserman AH, Chopra R, Ingram MAC, Hu Y-S, Singh V *et al.* (2015) Neuronal
      Atrophy Early in Degenerative Ataxia Is a Compensatory Mechanism to Regulate Membrane
      Excitability. *J Neurosci* **35**:11292–11307.

29   Diallo A, Jacobi H, Cook A, Labrum R, Durr A, Brice A *et al.* (2018) Survival in patients with
      spinocerebellar ataxia types 1, 2, 3, and 6 (EUROSCA): a longitudinal cohort study. *Lancet Neurol*
      17:327–334.

30   Fu H, Hardy J, Duff KE (2018) Selective vulnerability in neurodegenerative diseases. *Nat Neurosci*
      21:1350–1358.

31   Fujita H, Aoki H, Ajioka I, Yamazaki M, Abe M, Oh-Nishi A *et al.* (2014) Detailed expression pattern
      of Aldolase C (Aldoc) in the cerebellum, retina and other areas of the CNS studied in Aldoc-Venus
      knock-in mice. *PLoS One* **9**:22–27.

32   Galliano E, Potters J-W, Elgersma Y, Wisden W, Kushner S a, De Zeeuw CI *et al.* (2013) Synaptic
      transmission and plasticity at inputs to murine cerebellar Purkinje cells are largely dispensable for
      standard nonmotor tasks. *J Neurosci* **33**:12599–618.

33   Ginestroni A, Della Nave R, Tessa C, Giannelli M, De Grandis D, Plasmati R *et al.* (2008) Brain
      structural damage in spinocerebellar ataxia type 1 : A VBM study. *J Neurol* **255**:1153–1158.

34   Guell X, Gabrieli J DE, Schmahmann JD (2018) TRIPLE REPRESENTATION OF LANGUAGE,
      WORKING MEMORY, SOCIAL AND EMOTION PROCESSING IN THE CEREBELLUM:
      CONVERGENT EVIDENCE FROM TASK AND SEED-BASED RESTING-STATE FMRI
      ANALYSES IN A SINGLE LARGE COHORT. *Neuroimage2* **172**:437–449.

35   Guo C, Witter L, Rudolph S, Elliott HL, Ennis KA, Regehr WG (2016) Purkinje Cells Directly Inhibit
      Granule Cells in Specialized Regions of the Cerebellar Cortex. *Neuron* **91**:1330–1341.

36   Gutierrez-Castellanos N, Da Silva-Matos CM, Zhou K, Canto CB, Renner MC, Koene LMC *et al.*

3.1

(2017) Motor Learning Requires Purkinje Cell Synaptic Potentiation through Activation of AMPA-Receptor Subunit GluA3. *Neuron* **93**:409–424.

37   Heckroth JA, Abbott LC (1994) Purkinje cell loss from alternating sagittal zones in the cerebellum of leaner mutant mice. *Brain Res* **658**:93–104.

38   Hernandez-Castillo CR, King M, Diedrichsen J, Fernandez-Ruiz J (2018) Unique degeneration signatures in the cerebellar cortex for spinocerebellar ataxias 2, 3, and 7. *NeuroImage Clin* doi:10.1016/j.nicl.2018.09.026.

39   Holt GR, Softky WR, Koch C, Douglas RJ (1996) Comparison of discharge variability in vitro and in vivo in cat visual cortex neurons. *J Neurophysiol* **75**:1806–14.

40   Horn KM, Pong M, Gibson AR (2010) Functional relations of cerebellar modules of the cat. *J Neurosci* **30**:9411–9423.

41   Ingram M, Wozniak EAL, Duvick L, Yang R, Bergmann P, Carson R *et al.* (2016) Cerebellar Transcriptome Profiles of ATXN1 Transgenic Mice Reveal SCA1 Disease Progression and Protection Pathways. *Neuron* **89**:1194–1207.

42   Ito M (1982) Cerebellar control of the vestibulo-ocular reflex - around the flocculus hypothesis. *Annu Rev Neurosci* **5**:275–296.

43   Jacobi H, Hauser TK, Giunti P, Globas C, Bauer P, Schmitz-Hübsch T *et al.* (2012) Spinocerebellar ataxia types 1, 2, 3 and 6: The clinical spectrum of ataxia and morphometric brainstem and cerebellar findings. *Cerebellum* **11**:155–166.

44   Jung BC, Choi SI, Du AX, Cuzzocreo JL, Ying HS, Landman BA *et al.* (2012) MRI shows a region-specific pattern of atrophy in spinocerebellar ataxia type 2. *Cerebellum* **11**:272–279.

45   Kakei S, Ishikawa T, Lee J, Honda T, Hoffman DS (2018) Physiological and Morphological Principles Underpinning Recruitment of the Cerebellar Reserve. *CNS Neurol Disord - Drug Targets* **17**:184–192.

46   Katoh A, Kitazawa H, Itohara S, Nagao S, Thompson RF (1998) Dynamic characteristics and adaptability of mouse vestibulo-ocular and optokinetic response eye movements and the role of the flocculo-olivary system revealed by chemical lesions. *Neurobiology* **95**:7705–7710.

47   Kim JS, Kim JS, Youn J, Seo DW, Jeong Y, Kang JH *et al.* (2013) Ocular motor characteristics of different subtypes of spinocerebellar ataxia: Distinguishing features. *Mov Disord* **28**:1271–1277.

48   Klement IA, Skinner PJ, Kaytor MD, Yi H, Hersch SM, Clark HB *et al.* (1998) Ataxin-1 nuclear localization and aggregation: Role in polyglutarnine- induced disease in SCA1 transgenic mice. *Cell* **95**:41–53.

49   Klockgether T, Mariotti C, Paulson HL (2019) Spinocerebellar ataxia. *Nat Rev Dis Prim* doi:10.1016/B978-0-444-64189-2.00010-X.

50   Lackey EP, Sillitoe R V. (2020) Eph/ephrin Function Contributes to the Patterning of Spinocerebellar Mossy Fibers Into Parasagittal Zones. *Front Syst Neurosci* **14**:1–15.

51   Lee KH, Mathews PJ, Reeves AMB, Choe KY, Jami SA, Serrano RE *et al.* (2015) Circuit mechanisms underlying motor memory formation in the cerebellum. *Neuron* **86**:529–540.

52   Lewis PM, Gritli-Linde A, Smeyne R, Kottmann A, McMahon AP (2004) Sonic hedgehog signaling is required for expansion of granule neuron precursors and patterning of the mouse cerebellum. *Dev Biol* **270**:393–410.

53   Lin X, Antalffy B, Kang D, Orr HT, Zoghbi HY (2000) Polyglutamine expansion down-regulates specific neuronal genes before pathologic changes in SCA1. *Nat Neurosci* **3**:157–163.

54   Logan K, Robertson LT (1986) Somatosensory representation of the cerebellar climbing fiber system in the rat. *Brain Res* **372**:290–300.

55   Luo L, Wang J, Lo RY, Figueroa KP, Pulst SM, Kuo P-H *et al.* (2017) The Initial Symptom and Motor Progression in Spinocerebellar Ataxias. *Physiol Behav* **16**:615–622.

56   Luo Y, Patel RP, Sarpong GA, Sasamura K, Sugihara I (2018) Single axonal morphology and termination to cerebellar aldolase C stripes characterize distinct spinocerebellar projection systems originating from the thoracic spinal cord in the mouse. *J Comp Neurol* **526**:681–706.

57   Luong TN, Carlisle HJ, Southwell A, Patterson PH (2011) Assessment of Motor Balance and Coordination in Mice using the Balance Beam. :5–7.

58   Marques ARA, Aten J, Ottenhoff R, Van Roomen CPAA, Moro DH, Claessen N *et al.* (2015) Reducing GBA2 activity ameliorates neuropathology in niemann-pick type C mice. *PLoS One* **10**:1–18.

59   Martin KB, Williams IM, Cluzeau C V., Cougnoux A, Dale RK, Iben JR *et al.* (2020) Identification of novel pathways associated with patterned cerebellar purkinje neuron degeneration in niemann-pick disease, type C1. *Int J Mol Sci* **21**. doi:10.3390/ijms21010292.

60   Martin LA, Goldowitz D, Mittleman G (2003) The cerebellum and spatial ability: Dissection of motor and cognitive components with a mouse model system. *Eur J Neurosci* **18**:2002–2010.

61   Marzban H, Hawkes R (2011) On the architecture of the posterior zone of the cerebellum. *Cerebellum* **10**:422–434.

62   Matsushita M (2017) Projections from the lowest lumbar and sacral-caudal segments to the cerebellar cortex in the rat: An anterograde tracing study. *Neurosci Res* **114**:43–54.

63   Mattsson N, Schott JM, Hardy J, Turner MR, Zetterberg H (2016) Selective vulnerability in neurodegeneration: Insights from clinical variants of Alzheimer's disease. *J Neurol Neurosurg Psychiatry* **87**:1000–1004.

64   Moscovich M, Okun MS, Favilla C, Figueroa KP, Pulst SM, Perlman S *et al.* (2015) Clinical evaluation of eye movements in spinocerebellar ataxias: A prospective multicenter study. *J Neuro-Ophthalmology* **35**:16–21.

65   Nanri K, Koizumi K, Mitoma H, Taguchi T, Takeguchi M, Ishiko T *et al.* (2010) Classification of cerebellar atrophy using voxel-based morphometry and SPECT with an easy Z-score imaging system. *Intern Med* **49**:535–541.

66   Oberdick J, Smeyne RJ, Mann JR, Zackson S, Morgan JI (1990) A promoter that drives transgene expression in cerebellar Purkinje and retinal bipolar neurons. *Science* **248**:223–226.

67   Oberdick J, Levinthal F, Levinthal C (1988) A purkinje cell differentiation marker shows a partial DNA sequence homology to the cellular sis/PDGF2 gene. *Neuron* **1**:367–376.

68   Oberdick J, Schilling K, Smeyne RJ, Corbin JG, Bocchiaro C, Morgan JI (1993) Control of segment-like patterns of gene expression in the mouse cerebellum. *Neuron* **10**:1007–1018.

69   Peter S, Ten Brinke MM, Stedehouder J, Reinelt CM, Wu B, Zhou H *et al.* (2016) Dysfunctional cerebellar Purkinje cells contribute to autism-like behaviour in Shank2-deficient mice. *Nat Commun* **7**. doi:10.1038/ncomms12627.

70   Rahmati N, Owens CB, Bosman LWJ, Spanke JK, Lindeman S, Gong W *et al.* (2014) Cerebellar potentiation and learning a whisker-based object localization task with a time response window. *J Neurosci* **34**:1949–1962.

71   Reetz K, Costa AS, Mirzazade S, Lehmann A, Juzek A, Rakowicz M *et al.* (2013) Genotype-specific patterns of atrophy progression are more sensitive than clinical decline in SCA1, SCA3

3.1

and SCA6. *Brain* **136**:905–917.

72 Robitaille Y, Schut L, Kish SJ (1995) Structural and immunocytochemical features of olivopontocerebellar atrophy caused by the spinocerebellar ataxia type 1 (SCA-1) mutation define a unique phenotype. *Acta Neuropathol* **90**:572–581.

73 Romano V, de Propris L, Bosman LWJ, Warnaar P, Ten Brinke MM, Lindeman S *et al.* (2018) Potentiation of cerebellar purkinje cells facilitates whisker reflex adaptation through increased simple spike activity. *Elife* **7**:1–33.

74 Romano V, Reddington AL, Cazzanelli S, Mazza R, Ma Y, Strydis C *et al.* (2020) Functional Convergence of Autonomic and Sensorimotor Processing in the Lateral Cerebellum. *Cell Rep* **32**:107867.

75 Roselli F, Caroni P (2015) From intrinsic firing properties to selective neuronal vulnerability in neurodegenerative diseases. *Neuron* **85**:901–910.

76 Rossi M, Anheim M, Durr A, Klein C, Koenig M, Synofzik M *et al.* (2018) The genetic nomenclature of recessive cerebellar ataxias. *Mov Disord* **33**:1056–1076.

77 Rüb U, Schöls L, Paulson H, Auburger G, Kermer P, Jen JC *et al.* (2013) Clinical features, neurogenetics and neuropathology of the polyglutamine spinocerebellar ataxias type 1, 2, 3, 6 and 7. *Prog Neurobiol* **104**:38–66.

78 Sarna J, Miranda SRP, Schuchman EH, Hawkes R (2001) Patterned cerebellar Purkinje cell death in a transgenic mouse model of Niemann Pick type A/B disease. *Eur J Neurosci* **13**:1873–1880.

79 Sarna JR, Hawkes R (2003) *Patterned Purkinje cell death in the cerebellum*. 2003 doi:10.1016/S0301-0082(03)00114-X.

80 Sawada K, Azad AK, Sakata-Haga H, Lee NS, Jeong YG, Fukui Y (2009) Striking pattern of Purkinje cell loss in cerebellum of an ataxic mutant mouse, tottering. *Acta Neurobiol Exp (Wars)* **69**:138–145.

81 Saxena S, Caroni P (2011) Selective Neuronal Vulnerability in Neurodegenerative Diseases: From Stressor Thresholds to Degeneration. *Neuron* **71**:35–48.

82 Schonewille M, Belmeguenai A, Koekkoek SK, Houtman SH, Boele HJ, van Beugen BJ *et al.* (2010) Purkinje cell-specific knockout of the protein phosphatase PP2B impairs potentiation and cerebellar motor learning. *Neuron* **67**:618–628.

83 Schorge S, van de Leemput J, Singleton A, Houlden H, Hardy J (2010) Human ataxias: a genetic dissection of inositol triphosphate receptor (ITPR1)-dependent signaling. *Trends Neurosci* **33**:211–219.

84 Seidel K, Siswanto S, Brunt ERP, Den Dunnen W, Korf HW, Rüb U (2012) Brain pathology of spinocerebellar ataxias. *Acta Neuropathol* **124**:1–21.

85 Sen NE, Canet-Pons J, Halbach M V., Arsovic A, Pilatus U, Chae WH *et al.* (2019) Generation of an Atxn2-CAG100 knock-in mouse reveals N-acetylaspartate production deficit due to early Nat8l dysregulation. *Neurobiol Dis* **132**:104559.

86 Shambes GM, Gibson JM, Welker W (1978) Fractured somatotopy in granule cell tactile areas of rat cerebellar hemispheres revealed by micromapping. *Brain Behav Evol* **15**:94–140.

87 Sillitoe R V., Marzban H, Larouche M, Zahedi S, Affanni J, Hawkes R (2004) Conservation of the architecture of the anterior lobe vermis of the cerebellum across mammalian species. *Prog Brain Res* **148**:283–297.

88 Stephen CD, Schmahmann JD (2019) Eye Movement Abnormalities Are Ubiquitous in the Spinocerebellar Ataxias. *Cerebellum* **18**:1130–1136.

89   Sugihara I (2018) Crus I in the Rodent Cerebellum: Its Homology to Crus I and II in the Primate
      Cerebellum and Its Anatomical Uniqueness Among Neighboring Lobules. *Cerebellum* **17**:49–55.

90   Sugihara I, Quy PN (2007) Identification of Aldolase C Compartments in the Mouse Cerebellar
      Cortex by Olivocerebellar Labeling. *J Comp Neurol* **500**:1076–1092.

91   Sullivan R, Yau WY, O'Connor E, Houlden H (2019) Spinocerebellar ataxia: an update. *J Neurol*
      266:533–544.

92   Vandaele S, Nordquist DT, Feddersen RM, Tretjakoff I, Peterson AC, Orr HT (1991) Purkinje cell
      protein-2 regulatory regions and transgene expression in cerebellar compartments. *Genes Dev*
      5:1136–1148.

93   Vinueza Veloz MF, Buijsen RAM, Willemsen R, Cupido A, Bosman LWJ, Koekkoek SKE *et al.*
      (2012) The effect of an mGluR5 inhibitor on procedural memory and avoidance discrimination
      impairments in Fmr1 KO mice. *Genes, Brain Behav* **11**:325–331.

94   Vinueza Veloz MF, Zhou K, Bosman LWJ, Potters JW, Negrello M, Seepers RM *et al.* (2015)
      Cerebellar control of gait and interlimb coordination. *Brain Struct Funct* **220**:3513–3536.

95   Wassef M, Sotelo C, Cholley B, Brehier A, Thomasset M (1987) Cerebellar mutations affecting
      the postnatal survival of Purkinje cells in the mouse disclose a longitudinal pattern of differentially
      sensitive cells. *Dev Biol* **124**:379–389.

96   Welsh JP, Yuen G, Placantonakis DG, Vu TQ, Haiss F, O'Hearn E *et al.* (2002) Why do Purkinje
      cells die so easily after global brain ischemia? Aldolase C, EAAT4, and the cerebellar contribution
      to posthypoxic myoclonus. *Adv Neurol* **89**:331–359.

97   White JJ, Arancillo M, Stay TL, George-Jones NA, Levy SL, Heck DH *et al.* (2014) Cerebellar
      Zonal Patterning Relies on Purkinje Cell Neurotransmission. *J Neurosci* **34**:8231–8245.

98   White JJ, Sillitoe R V. (2013) Development of the cerebellum: From gene expression patterns to
      circuit maps. *Wiley Interdiscip Rev Dev Biol* **2**:149–164.

99   Wulff P, Schonewille M, Renzi M, Viltono L, Sassoè-Pognetto M, Badura A *et al.* (2009) Synaptic
      inhibition of Purkinje cells mediates consolidation of vestibulo-cerebellar motor learning. *Nat
      Neurosci* **12**:1042–1049.

100   Xiao J, Cerminara NL, Kotsurovskyy Y, Aoki H, Burroughs A, Wise AK *et al.* (2014) Systematic
      regional variations in Purkinje cell spiking patterns. *PLoS One* **9**. doi:10.1371/journal.
      pone.0105633.

101   De Zeeuw CI, Ten Brinke MM (2015) Motor learning and the cerebellum. *Cold Spring Harb
      Perspect Biol* **7**:1–20.

102   Zhou H, Lin Z, Voges K, Ju C, Gao Z, Bosman LWJ *et al.* (2014) Cerebellar modules operate at
      different frequencies. *Elife* **2014**:1–3.

103   Zhou H, Voges K, Lin Z, Ju C, Schonewille M (2015) Differential Purkinje cell simple spike activity
      and pausing behavior related to cerebellar modules. *J Neurophysiol* **113**:2524–36.

104   Zoghbi HY, Orr HT (2009) Pathogenic mechanisms of a polyglutamine-mediated
      neurodegenerative disease, Spinocerebellar ataxia type 1. *J Biol Chem* **284**:7425–7429.

105   Zu T, Duvick LA, Kaytor MD, Berlinger MS, Zoghbi HY, Clark HB *et al.* (2004) Recovery from
      Polyglutamine-Induced Neurodegeneration in Conditional SCA1 Transgenic Mice. *J Neurosci*
      24:8853–8861.

3.1
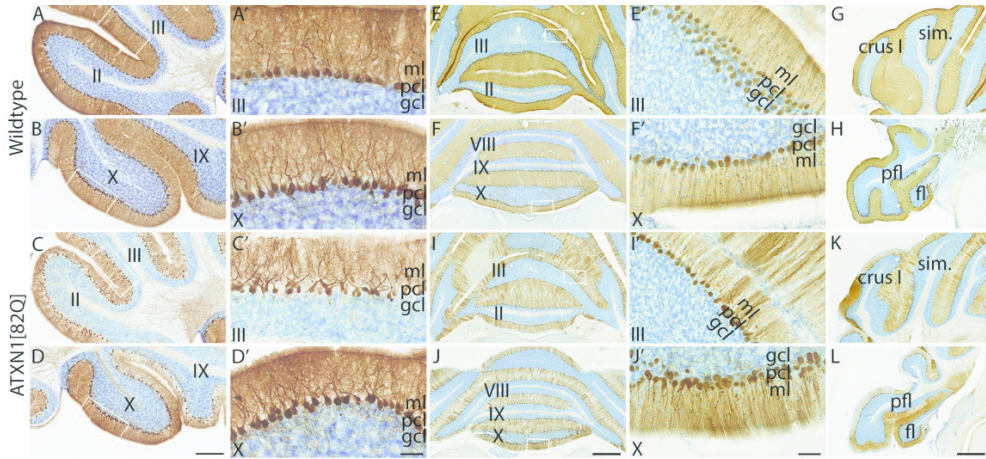
Figure 1: Purkinje cell degeneration is spared in a region-specific manner in 12 week ATXN1[82Q] mice.

Purkinje cells in wildtype littermates show consistent morphology and calbindin labeling throughout the cerebellar cortex (A,B,A',B',E,F,E',F',G,H). Purkinje cells in ATXN1[82Q] mice exhibit severe degeneration in lobules II and III (C,C',I,I') as compared with lobule X (D,D',J,J'), crus I (K) and the floccular complex (L). (Scale bars: A-D=250 μm, A'-D'=50 μm, E-L=500 μm, E'-L'=50 μm). Abbreviations: ml= molecular layer, pcl = Purkinje cell layer, gl = granular layer, sim. = lobulus simplex, pfl = paraflocculus, fl = flocculus.
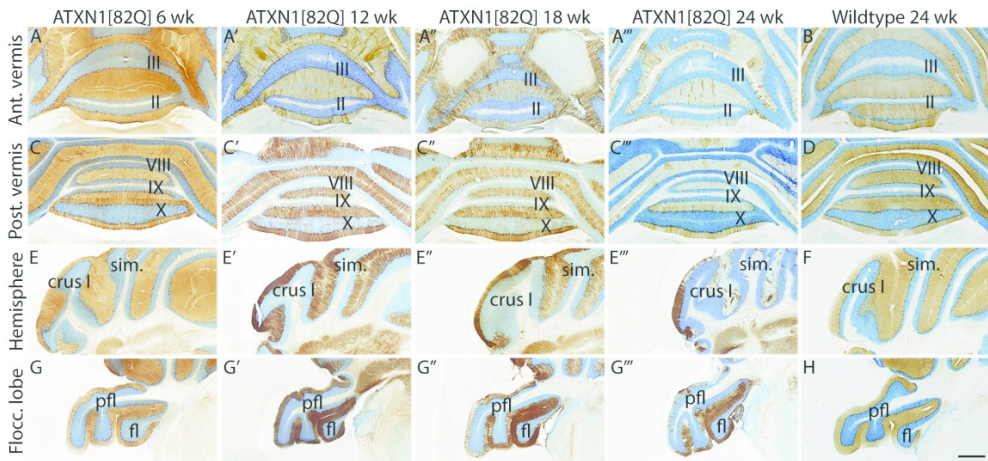
Figure 2: Purkinje cell degeneration is progressive in non-spared regions of the cerebellar cortex in ATXN1[82Q] mice.

Spared regions remain spared at all ages. Regions that feature spared Purkinje cell morphology are highlighted and apparent with consistent calbindin staining. The anterior vermis (Ant. vermis) features the most severely atrophied Purkinje cells as compared wildtype littermates (A-A''', B). The posterior vermis (Post.

Vermis) also features severe atrophy with the exception of lobule X (C-C''', D). Other preferentially spared regions are crus I in the hemisphere (E-E''', F) and the flocculus/ventral paraflocculus (G-G''', H). Scale bar = 500 µm. Abbreviations: wk, = week, Ant. = anterior, Post. = posterior, Flocc. = floccular, sim. = lobulus simplex, pfl = paraflocculus, fl = flocculus.
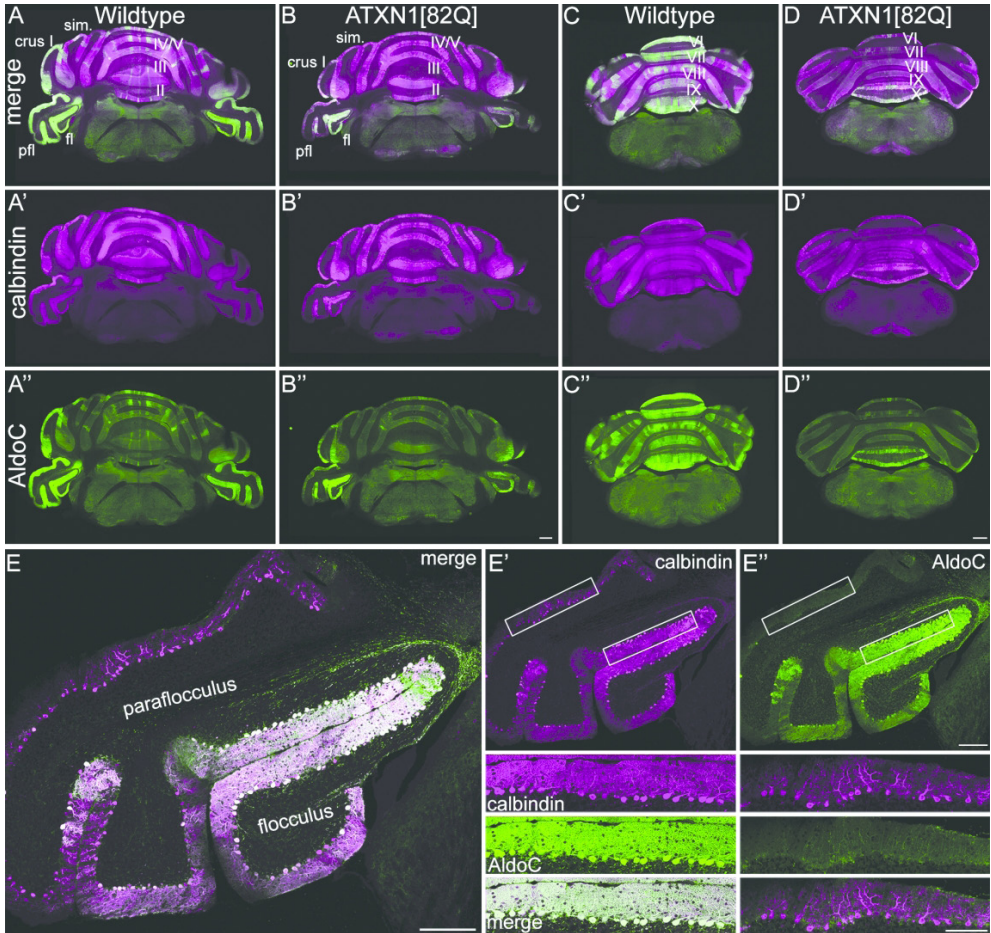
Figure 3: Lack of normal AldoC expression in Purkinje cells of 12 week ATXN1[82Q] mice is associated with degeneration.

Spared Purkinje cells maintain their AldoC expression. The normal AldoC pattern (A-A'',C-C'') is disrupted in ATXN1[82Q] mice (B-B'', D-D''). Typically AldoC-positive regions, such as the dorsal paraflocculus (E,E',E''), lose their AldoC identify and feature Purkinje cell atrophy. Scale bars = 500 µm (A-B''), 500 µm (C-D''), 200 µm (E), 200 µm (E',E''), 100 µm (E' and E'' insets). Abbreviations: sim. = lobulus simplex, pfl = paraflocculus, fl = flocculus.
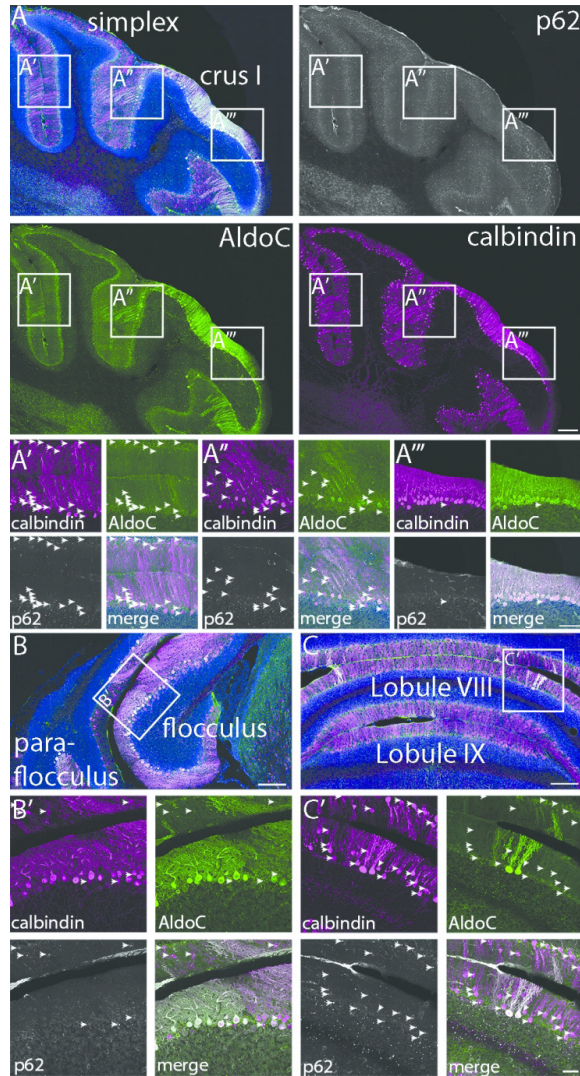
Figure 4: Purkinje cells that continue to express AldoC do not exhibit p62 inclusions.

Arrowheads indicate all Purkinje cells exhibiting a p62 inclusion. There is a negative correlation between expression of AldoC and expression of a p62 inclusion that is consistently present in areas that are predominantly spared, visualized by calbindin expression, like the flocculus and crus I as well as in areas that only have sporadic, spared Purkinje cells such as in the simplex and lobule VIII. Images are of sections from 12 week ATXN1[82Q] mice. Scale bars = 200 µm (A), 100 µm (A'-A'''), 200 µm (B), 200 µm (C), 50 µm (B',C').
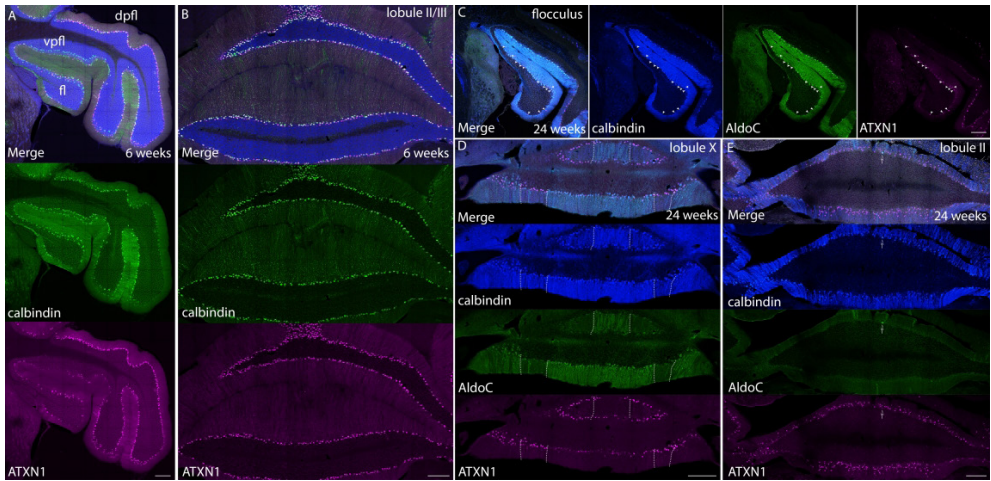
Figure 5: Purkinje cells in spared regions are less likely to express mutant ATXN1 in ATXN1[82Q] mice.

The flocculus and ventral paraflocculus of ATXN1[82Q] contain fewer Purkinje cells expressing ATXN1 than the dorsal paraflocculus (A) or lobules II/III (B) at 6 weeks of age. This relationship also exists at 24 weeks and is associated with AldoC expression. In the flocculus, the subpopulation of Purkinje cells that expresses mutant ATXN1 does not express AldoC (arrowheads in C). This same relationship exists in the nodulus (lobule X) which has a higher likelihood of mutant ATXN1 expression in AldoC-negative bands (borders indicated with dotted lines in D). The vast majority of Purkinje cells in lobule II are atrophied and express mutant ATXN1, except for very rare healthy Purkinje cells which express AldoC (arrow in E). Scale bars = 200 μm. Abbreviations: fl = flocculus, vpfl = ventral paraflocclus, dpfl = dorsal paraflocculus.

3.1
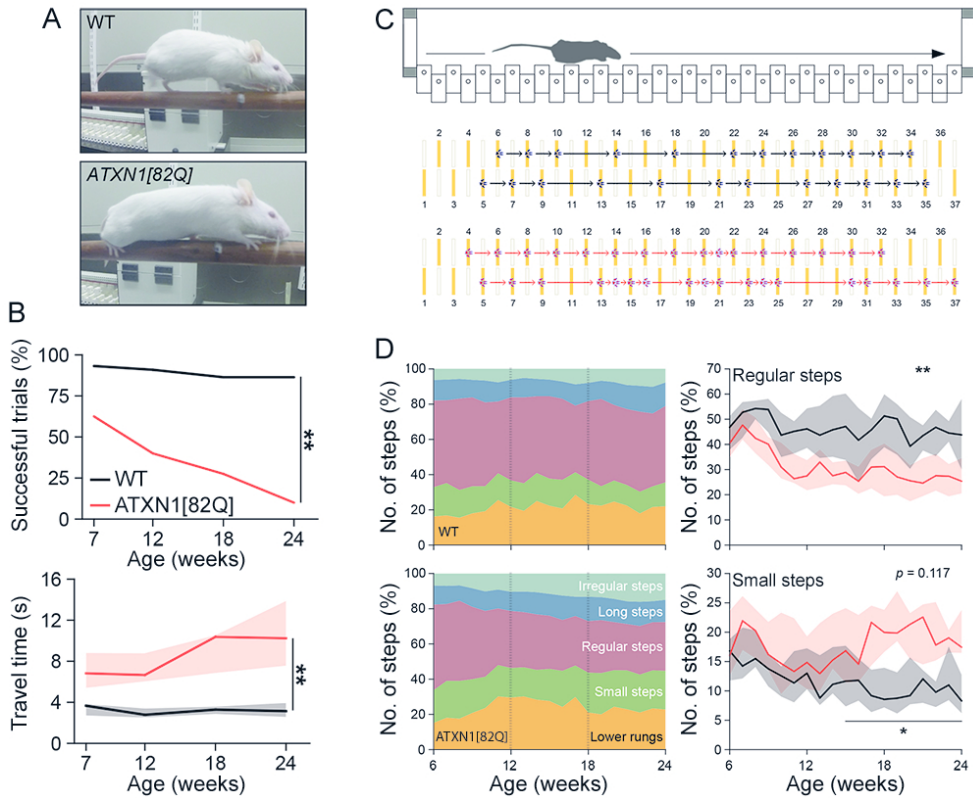
Figure 6: ATXN1[82Q] exhibit progressive deficit in motor coordination on both the balance beam and the ErasmusLadder.

Example images of an ATXN1[82Q] mouse and wildtype littermate demonstrate typical posture on the balance beam (A). Compared to wildtype littermates, ATXN1[82Q] mice exhibit progressively decreasing percentage of successful balance beam trials and increased time to cross the beam (B). Representative examples of ErasmusLadder performance demonstrate the propensity for ATXN1[82Q] mice to make short steps as compared with wildtype littermates (C). Performance on the ErasmusLadder progressively changed over time (D). However, significant differences between groups were evident later in the disease progression than observed on the balance beam.
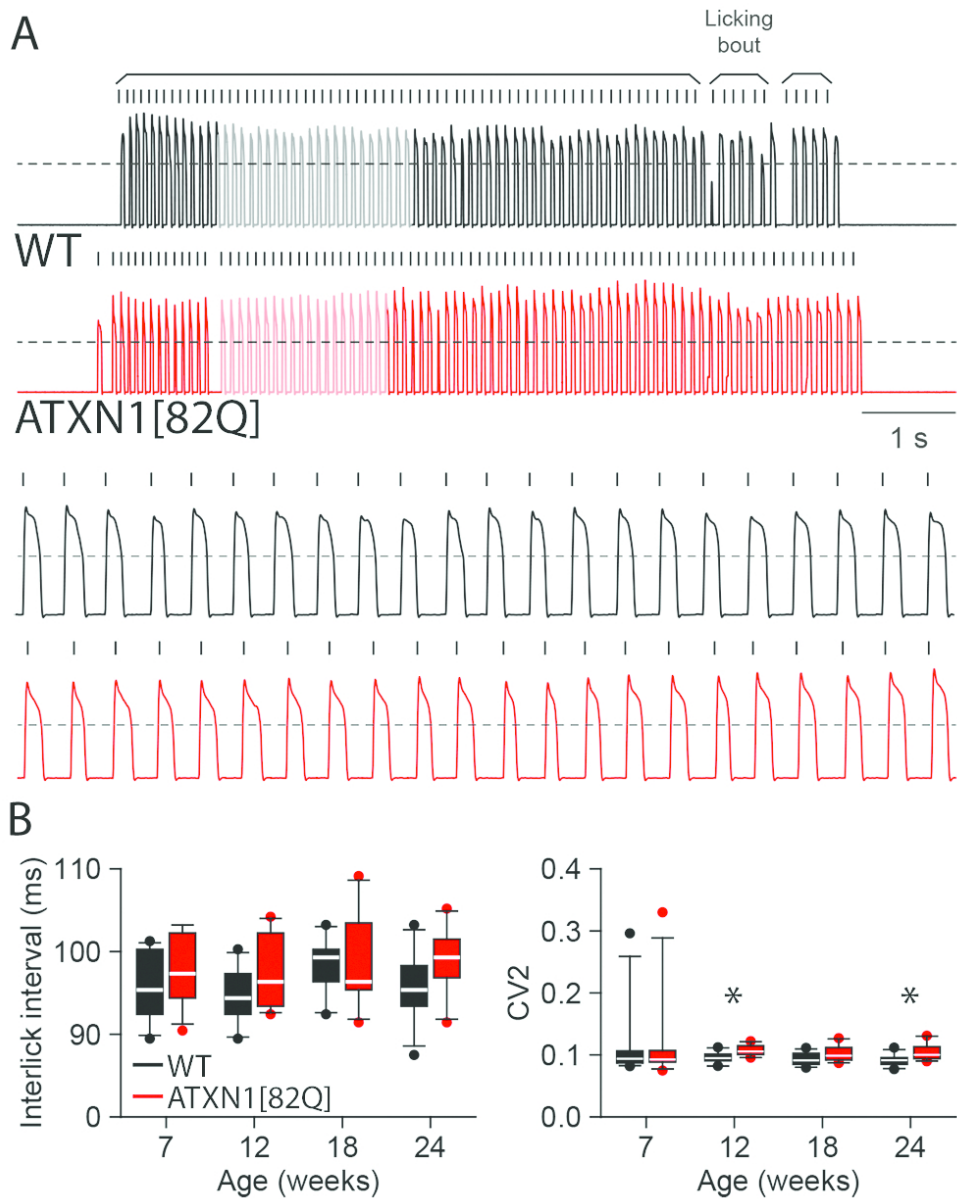
Figure 7: Licking behavior is largely conserved in ATXN1[82Q] mice.
Example licking traces for wildtype (WT) and ATXN1[82Q] mice demonstrate comparable behavior (A). There are no significant differences between groups in Interlick interval at any age. However, a mild but significant difference was found in CV2 at 12 and 24 weeks (p = 0.0208) (B).
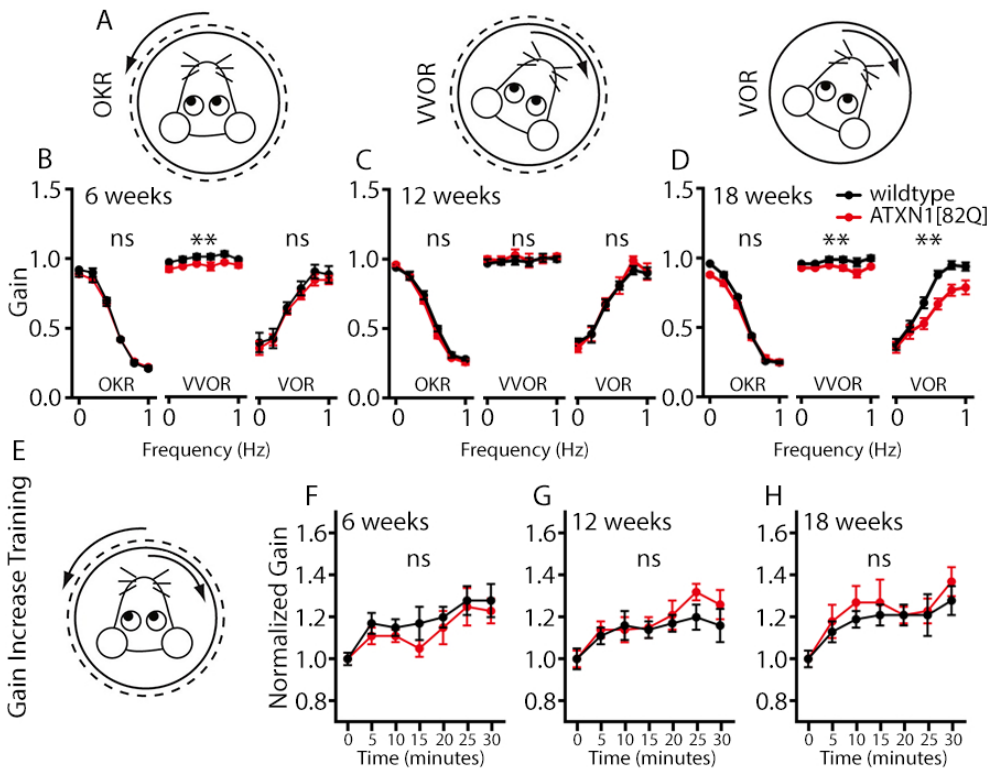
Figure 8: Compensatory eye movement behavior in ATXN1[82Q] mice is minimally affected at all ages tested.

Three baseline eye movement behaviors were tested: the optokinetic reflex (OKR), visual vestibulo-ocular reflex (VVOR) and vestibule-ocular reflex (VOR) (A). At 6 weeks of age there is no significant differences between OKR or VOR, but the VVOR gain is marginally affected (B). There is no significant difference in any baseline eye movement behavior at 12 weeks of age (C). VVOR and VOR behaviors are significantly but mildly impaired at 18 weeks (D). In order to test cerebellar-dependent learning, mice underwent gain increase training (E) using out of phase visual and vestibular input, aimed at increasing the gain of the VOR. All values were normalized to the value before training (t=0). There was no significant difference in gain increase training at any age tested (F, G, H). ** indicates p ~ 0.01.
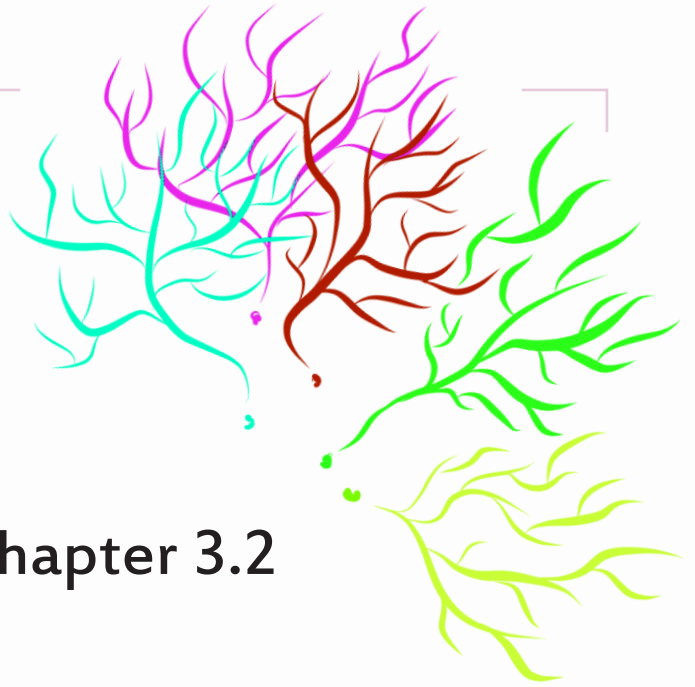
Chapter 3.2

Sphingolipid metabolism controls cerebellar Purkinje cell predisposition for patterned degeneration

François G.C. Blot, Wilhelmine H.J.J. Krijnen, Sandra Den Hoedt, Catarina Osório, Joshua J. White, Monique T. Mulder, Martijn Schonewille

Abstract

Patterned degeneration of cerebellar Purkinje cells (PCs) can be observed in a wide range of neuropathologies, but no mechanism has been confirmed to explain non-random cerebellar neurodegeneration as of yet. Sphingolipid metabolism dyshomeostasis typically leads to PC neurodegeneration, hence we questioned whether local sphingolipid balance underlie regional sensitivity to pathological insults. Here, we investigated the regional compartmentalization of sphingolipids and their related enzymes in the cerebellar cortex in healthy and pathological conditions. Western blot analysis in wild type animals revealed higher sphingosine kinase 1 (Sphk1) levels in the flocculo-nodular cerebellum, while HPLC-MS/MS analysis showed that sphingosine-1-phophate (S1P) and sphingosine levels were higher in the anterior cerebellum. Next, we investigated *Atxn1[82Q]/+* mice, a model for spino-cerebellar ataxia type I (SCA1), model in which PC degeneration is severe in the anterior cerebellum while the flocculo-nodular region is preserved. In *Atxn1[82Q]/+* mice, we found that levels of Sphk1 and 2 were region-specifically decreased and that S1P levels increased, particularly in the anterior cerebellum. Finally, to determine if there is a causal link between S1P levels and neurodegeneration, we deleted *Sphk1* gene in *Atxn1[82Q]/+* mice. Immunohistochemical analysis of *Atxn1[82Q]/+; Sphk1-/-* mice confirmed a neuroprotective effect, rescuing PCs in parasagittal domains that follow the modules defined by AldolaseC expression. Taken together, our results demonstrate for the first time that there are regional differences in sphingolipid metabolism and that this metabolism is directly involved in PC degeneration in *Atxn1[82Q]/+* mice. This finding suggests that sphingolipid homeostasis is an important factor in patterned degeneration in cerebellar pathologies.

Introduction

Purkinje cells (PCs) integrate all afferent sensorimotor information using their massive dendritic tree, and form the exclusive output source of the cerebellar cortex. Based on the highly structured and repetitive organization of the cerebellar cortex, PCs are often regarded as a homogeneous population of neurons. However, for several decades anatomical and immunohistochemical studies have emphasized that different subtypes of PCs can be identified in the cerebellar cortex, including: transverse zones, e.g. the anterior versus flocculo-nodular cerebellum, parasagittal modules,

e.g. AldolaseC-positive versus negative domains, and others such as apex versus sulcus or vermis versus hemispheres (1). Regional differences in PC density (2), dendritic arborization (3), morphology of organelles (4) and axonal thickness (5) can be observed across the cerebellar cortex. The most commonly studied pattern is defined by Aldolase C (also known as ZebrinII) expression, which divides PC subtypes in parasagittal bands with distinct molecular footprints (6–9), distinct electrophysiological intrinsic and synaptic properties (10–12), as well as input/output connectivity (13, 14). Cerebellar heterogeneity is also illustrated by the non-homogeneous and non-random PC degeneration across the cerebellar cortex observed in a broad spectrum of cerebellar pathologies. These cerebellar pathologies, displayed by patient or rodent models, can result from genetic mutations such as *leaner* (15), *Harlequin* (16), *sticky* (17), *Slc9a6*$^{-/-}$ (18), *Cav2.1*$^{-/-}$ (19), as well as brain ischemia (20), viral infections (21), prion diseases (22), and alcohol abuse such as alcohol-related cerebellar degeneration (23). As described by Sarna and Hawkes (24), not all patterned neurodegenerations are similar. Two main types of patterned degeneration have been observed: 1) pathologies in which the flocculo-nodular cerebellum is more resistant, leading to a clear separation regarding the progression of the neurodegeneration between anterior cerebellum and flocculo-nodular lobule; and 2) pathologies in which PC degeneration affects primarily AldolaseC-negative domains, leading to parasagittal compartmentalization of neurodegeneration. Thus far, mechanisms explaining the patterned neurodegeneration of Purkinje cells have not been revealed, though metabolic pathways have been suggested to be involved, such as the metabolism of sphingolipids (24).

Sphingolipids are essential bioactive sphingoid-based complex lipids that regulate physiological processes such as cell differentiation, neurogenesis, synaptic strengthening, and cell survival (25–28). Particularly, sphingosine-1-phophate (S1P) is a potent bioactive modulator, acting intracellularly, or in a autocrine/paracrine manner (29). S1P is the product of sphingosine (Sph) phosphorylation, which is catalyzed by sphingosine kinases, Sphk1 and 2, and can be reversed by dephosphorylation through sphingosine phosphate phosphatases, Sgpp1 and 2, or irreversibly degraded by S1P lyase (30). Both Sph and S1P are part of the ceramide metabolism, known to be a central mediator in programed cell death (31). The S1P/ceramide ratio, or rheostat, is decisive for cell fate in several tissues (32), and tight regional control has been correlated with local neuroprotective effects in CNS as well as PNS structures (33, 34).PCs are known to be sensitive to sphingolipid levels, as decreasing ceramide and sphingosine levels by blocking the *de novo* ceramide synthesis pathway through the

serine palmitoyltransferase (SPTLC1) inhibitor led to a decrease in survival rate of PCs in culture (35). Conversely, enrichment of culture media with ceramide, sphingosine, or dihydro-ceramide promoted PC survival. *In vivo*, PC degeneration was observed in mutant models targeting enzymes of the sphingolipid pathway, such as ceramide synthase CerS1 (36), Acid Ceramidase 3 (37), and Saposin D (38, 39). Typically, all those mutants show either preferential degeneration of the anterior cerebellum or AldolaseC-negative PCs, patterns which could appear similar but remain clearly distinct once properly scrutinized. In mouse models of Niemann-Pick disease types A and C, featuring loss of function of acid ceramidase or NPC1 respectively, patterned PC degeneration was clearly described (40). Although most of these data indicate an anti-apoptotic role of S1P in PC, accumulation of long-chain bases Sph and S1P have also been reported as pro-apoptotic *in vitro* (41) and *in vivo* (42, 43), and restoring long-chain base levels rescued the neurodegenerative phenotype in the CerS1 (44). Together, this suggests that subcellular origin of S1P defines its neuroprotective or neurotoxicity effect (41)and stresses the impact of the sphingolipid balance on PC fate. Based on the central role of sphingolipid homeostasis in cellular fate and its implication in several patterned neurodegeneration we investigated the impact of local sphingolipid metabolism on cerebellar neurodegeneration. Here we show that Sphk1 levels are higher in the flocculonodular region, while its lipid substrate Sph and product S1P levels are higher in the anterior region in adult wild type mice. In *Atxn1[82Q]/+* mice degeneration primarily affects the anterior region, as shown before (45–47), and we found that this preference correlates with increased S1P levels and region-specific decreases in Sphk1 and Sphk2 expression levels compared to control mice. To test the potential contribution of Sphk1 activity to neurodegeneration we crossed the *Atxn1[82Q]/+* mice with Sphk1 knockout mice (*Sphk1-/-*). Whereas *Sphk1-/-* mice did not exhibit cerebellar defects or significant changes in S1P levels, the deletion of Sphk1 in *Atxn1[82Q]/+* mice resulted in a neuroprotective effect on specific PC subpopulations, organized in parasagittal domains reminiscent AldolaseC-positive PC modules. Taken together, we show that S1P plays a major role in PC fate and present the sphingolipid pathway as a candidate pathway to explain patterned neurodegeneration.

Results

Sphk1, but not Sphk2, has region-dependent expression in the adult cerebellum:

Sphk1 and 2 are two protein isoforms responsible for the phosphorylation of Sph to produce S1P (Fig. 1A). Previous work showed a non-uniform expression of Sphk1 in cerebellar PCs (48). To determine if Sphk1 and 2 levels are region-specific, we quantified the relative protein levels in the anterior and the flocculo-nodular fraction in wild type mice (littermate controls of the *Atxn1[82Q]* mice). For both juvenile and adult the Sphk1 expression levels in the flocculo-nodular fraction were significantly higher than in the anterior fraction (juvenile: $p<0.05$, and adult: $p<0.005$, Fig. 1B, C; Suppl. Fig. 1). In contrast, the iso-enzyme Sphk2 was expressed at higher levels in the anterior than in the flocculo-nodular fractions in juvenile animals ($p<0.05$), with no difference in adult mice ($p=0.299$). When comparing juvenile and adult mice, Sphk1 expression levels did not change (anterior: $p=0.263$; flocculo-nodular: $p=0.146$), while Sphk2 expression levels increased from juvenile to adult (anterior: $p<0.001$; flocculo-nodular: $p<0.001$). Thus, both sphingosine kinases show signs of cerebellar region-specific differences in expression, with the higher levels of Sphk1 in the anterior fraction being the most pronounced and consistent difference across ages.

Progressive and region-specific atrophy in the anterior region of Atxn1[82Q]/+ mice:

The *Atxn1[82Q]/+* mouse (49) is a model of SCA1 featured by the overexpression of the expanded Ataxin1 protein with 82 glutamine (Q) repeats under the control of the PC-specific *Pcp2* promoter. This model has been shown to have relatively normal cerebellar development up to P25, with no apparent signs of morphological changes in PCs (47). The neuropathology is apparent from 5-6 weeks and characterised by PC atrophy, disorganisation of the PCs monolayer with ectopic PCs and reduction of calbindin (CaBP) expression. One feature of the *Atxn1[82Q]/+* mouse model, also identified in the human pathology, is that the neurodegenerative process unfolds more rapidly in the anterior region, leaving the flocculo-nodular region spared (47). Histological analysis in adult (P140) *Atxn1[82Q]/+* mice confirmed PC atrophy, disorganisation of the monolayer, and altered dendritic arborisation predominantly in the anterior cerebellum (Fig. 1D, E). The differential degeneration in adult mice was confirmed by western blot quantification that showed a decrease of CaBP expression levels in both fractions of the mutant

compared to wild type (*Atxn1[82Q]/-* vs. *Atxn1[82Q]/+* anterior: p<0.001; flocculo-nodular: p<0.001), but with higher expression levels in the flocculo-nodular fraction compared to the anterior fraction in the *Atxn1[82Q]/+* mice (p<0.005; Fig. 1C, D, E; Suppl. Fig.1). Analysis of CaBP expression levels at P21-23 (juvenile) showed no significant changes in both fractions of the mutant compared to the wild type (*Atxn1[82Q]/-* vs. *Atxn1[82Q]/+* anterior: p=0.364; flocculo-nodular: p=0.158). These data were in line with the time course and region-specificity of the pathology previously described for this
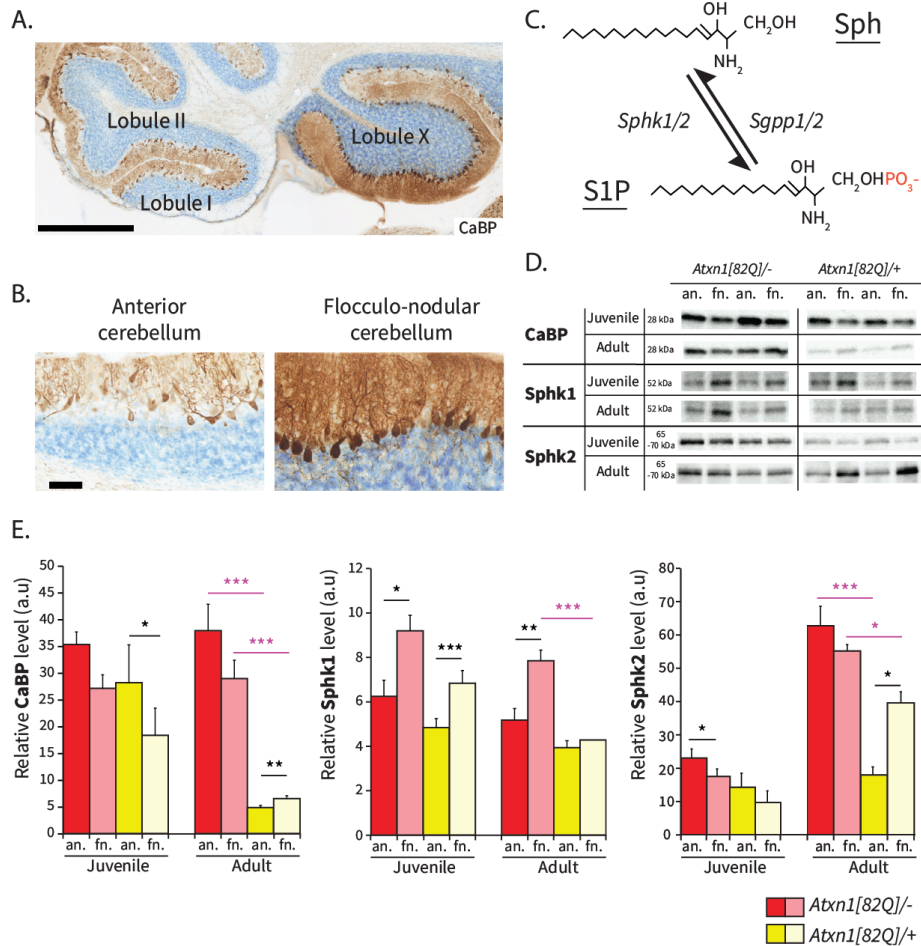
Fig. 1. Sphk1 and Sphk2 expression are region-dependent in wild type and Atxn1[82Q]/+ mice.

(A) Schematic representation of sphingosine (Sph) phosphorylation in sphingosine-1-phosphate (S1P) through addition of a phosphate group (red) by kinases Sphk1/2, and the reverse reaction driven by phosphatases Sgpp1/2. (B) Western blotting

images of CaBP, Sphingosine kinase 1 (Sphk1), and 2 (Sphk2) expression levels in anterior and flocculo-nodular regions of Atxn1[82Q]/+ and wild type littermates Atxn1[82Q]/-. (C) Bar plot of western blotting protein quantification for CaBP (n=5 per group), Sphk1 (n=5 per group), and Sphk2 (n=4 per group) expression levels. (D) Immunohistochemistry for Calbindin (CaBP) protein in P140 Atxn1[82Q]/+ sagittal cerebellar section; scale bar = 500µm. (E) High magnification of cerebellar cortex in anterior and flocculo-nodular regions. Data are shown as mean ± S.E.M. Juvenile= P21-23, Adult= P143-153; anterior (an.), flocculo-nodular (fn.). Black asterisks : significance for an. vs. fn.; purple: significance for Atxn1[82Q]/- vs. Atxn1[82Q]/+. *p<0.05, **p<0.005, ***p<0.001.

model (47). Based on these results, we selected this mouse model to test our hypothesis that there is a correlation between patterned degeneration and sphingolipids metabolism.

Region-specific changes in Sphk1 and 2 expression levels in Atxn1[82Q]/+ mice:

3.2

Correlation between sphingolipid metabolism and spino-cerebellar ataxia have been described previously (50), but have been largely focused on ceramide, sphingomyelin and ganglioside metabolism, instead of S1P synthesis. To investigate a potential involvement of this pathway in ataxia, we measured Sphk1 and 2 expression levels in cerebellar fractions of *Atxn1[82Q]/+* mice. In juvenile *Atxn1[82Q]/+* mice, Sphk1 expression levels did not significantly differ from wild type mice (all p>0.05), replicating the difference between anterior and flocculo-nodular fractions (p<0.001) (Fig. 1B, C; Suppl. Fig. 1). In the adult *Atxn1[82Q]/+* mice, unlike in the wild type mice, there was no significant difference in the expression of Sphk1 between the anterior and flocculo-nodular fractions (p=0.544). The loss of region-specific difference, is primarily caused by a robust decrease of Sphk1 in the flocculo-nodular fraction (*Atxn1[82Q]/-* vs. *Atxn1[82Q]/+*, p<0.001), as there is no significant decrease in the anterior fraction(*Atxn1[82Q]/-* vs. *Atxn1[82Q]/+*, p=0.074). Conversely, in adult *Atxn1[82Q]/+* mice the Sphk2 expression levels were more than halved in the anterior fraction compared to wild type mice (*Atxn1[82Q]/-* vs. *Atxn1[82Q]/+,* p<0.001) with a smaller decrease in the flocculo-nodular fractions (p<0.05), resulting in a significant difference between anterior and flocculo-nodular expression levels (p<0.05, Fig. 1D, E; Suppl. Fig. 1). Taken together, these data showed that cerebellar neurodegeneration following the expression of *Atxn1[82Q]* transgene in PCs correlates with a reduction of the expression levels of both Sphk1 and 2, but the magnitude of the changes is directly dependent on the cerebellar region.

S1P and Sph levels differ between fractions in wild type mice:

The differential Sphk1 expression levels between fractions in wild type mice suggest a tight regulation of sphingolipids levels in distinct regions of the cerebellum in healthy conditions. We used high-performance liquid chromatography with tandem mass spectrometry (HPLC-MS/MS) to measure the relative levels of S1P, Sph, ceramides, and sphingomyelins, in both the anterior and the flocculo-nodular fraction. All sphingolipids are composed of sphingosine, an 18 carbon chain with one double bound (d18:1), which for ceramides and sphingomyelins is associated with a fatty acid of variable length (d18:1/[fatty acid carbon number]:[fatty acid double bounds]). We found that S1P(d18:1) and Sph(d18:1) levels were significantly higher in the anterior fraction than the flocculo-nodular fraction (S1P(d18:1) p<0.001; Sph(d18:1) p<0.05; Fig 2A-B), in wild type adult mice. These differential levels emerged later in development as no significant differences were observed between fractions for S1P(d18:1) (p=0.124) and Sph(d18:1) (p=0.959) in juvenile mice. When we examined the levels of ceramides and sphingomyelin, other prominent lipids in the cascade, we found no significant differences between anterior and flocculo-nodular fractions, neither in juvenile, nor in adult wild type mice (all p>0.05; Fig.2A; Suppl. Fig. 2A). These data, together with the protein expression, highlight the tight and specific region-dependent control on S1P and Sph levels in wild type animals (Fig. 2B).

Increased levels of S1P in the anterior cerebellum of adult Atxn1[82Q]/+ mice:

Given that cerebellar regions exhibit differential vulnerability to neurodegeneration, we then investigated regional sphingolipid levels in the *Atxn1[82Q]/+* mouse. In adult mice we observed a robust increase of S1P(d18:1) levels in the anterior cerebellar fraction of *Atxn1[82Q]/+* adult mice when compared to wild type animals (*Atxn1[82Q]/-*: 11.5 ± 1.27 pmol/mg; *Atxn1[82Q]/+* : 20.76 ± 2.74 pmol/mg; *Atxn1[82Q]/-* vs. *Atxn1[82Q]/+* p<0.001) (Fig. 2A, C). A significant, but smaller increase of S1P(d18:1) levels was also observed in the flocculo-nodular fraction of the mutant (*Atxn1[82Q]/-*: 8.16 ± 1.46 pmol/mg; *Atxn1[82Q]/+* : 11.90 ± 1.68 pmol/mg; *Atxn1[82Q]/-* vs. *Atxn1[82Q]/+*, p<0.005). To determine whether the increases of S1P and Sph represent an overall increase of sphingolipid metabolism, we quantified several ceramides and sphingomyelins. Strikingly, all significant differences observed between wild type and mutant mice were restricted to the anterior fraction, as Cer(d18:1/16:0) (p<0.05), SM(d18:1/16:0) (p<0.001), SM(d18:1/18:0) (p<0.001), and SM(d18:1/18:1) (p<0.001) levels increased,

Fig. 2. S1P(d18:1) and Sph(d18:1) are differentially expressed between fractions in adult wild type Atxn1[82Q]/- and in Atxn1[82Q]/+ mice S1P, ceramide and sphingomyelin are affected in the anterior cerebellum.

(A) Bar plot of HP-LC MS/MS quantification of selected sphingolipid levels in wild type Atxn1[82Q]/- (FVB/N) and mutant Atxn1[82Q]/+ mice. Data are expressed as mean ± S.E.M. (N=10 per group); unit = pmol/mg of protein. Juvenile= P21-23, Adult= P143-153. Black asterisks: significance for anterior (an.) vs. flocculo-nodular (fn.); purple: significant statement for Atxn1[82Q]/- vs. Atxn1[82Q]/+. *p<0.05, **p<0.005, ***p<0.001. (B) Schematic of the sphingolipid metabolic pathway with representation of levels differences between anterior (red) and flocculo-nodular (pink) fractions. (C) Schematic of sagittal view of the Atxn1[82Q]/+ cerebellum with identification of the fractions, and annotation of the sphingolipid changes measured in the mutant in independent fractions.

while Cer(d18:1/20:0) (p<0.05), and Cer(d18:1/24:1) (p<0.05) levels decreased compared to wild type mice (Fig 2A, C). The course of change observed regarding sphingolipid levels suggest a complex mechanism with down and up-regulation of different enzymes and iso-enzymes in the pathway. Despite changes in both upstream and downstream metabolites, Sph(d18:1) levels were unaffected with no overall changes between wild type and mutant (anterior: *Atxn1[82Q]/-* vs. *Atxn1[82Q]/+*, p=0.59; flocculo-nodular: *Atxn1[82Q]/-* vs *Atxn1[82Q]/+*, p=0.97). In contrast to the anterior fraction, none of the ceramide or sphingomyelin levels were significantly changed in the flocculo-nodular fraction of mutant *Atxn1[82Q]/+* mice (all p>0.05; Fig 2A; Suppl. Fig. 2). Moreover, in juvenile *Atxn1[82Q]/+* mice that lack signs of neurodegeneration all sphingolipid levels did not differ significantly from wild type mice in both fractions (all p>0.05; Fig. 2A, Suppl. Fig. 2A). Our findings that sphingolipid levels change with the temporal and spatial progression of the neurodegeneration and that the increase in S1P is most prominent in the anterior region, which is most affected by the pathology, demonstrate a correlation between sphingolipid levels and neurodegeneration.

Sphk1 deletion has marginal effects on sphingolipid levels and cerebellum-dependent behavior:

To further investigate the role of S1P synthesis in PCs, we evaluated the consequences of *Sphk1* knockout on cerebellar sphingolipid levels, development and function. The deletion of the Sphk1 protein in *Sphk1-/-* mice was confirmed in both cerebellar fractions (Suppl. Fig. 3A). Sphingosine kinases convert Sph into S1P, thus, the deletion of *Sphk1* could have both a direct effect on S1P levels, and/or indirect repercussions upstream in the pathway. Surprisingly, the deletion of Sphk1 had no measurable effect on the levels of S1P(d18:1)(Fig. 3A). In contrast, the Sph(d18:1) levels were reduced (*Sphk1+/+*: 46.39 ± 6.61 pmol/mg, *Sphk1-/-*: 33.70 ± 7.14 pmol/mg; p<0.05) (Fig.3A, C), suggesting a possible compensatory change upstream in the pathway. However, the majority of ceramide and sphingomyelin levels are not significantly changed following *Sphk1* deletion (Fig. 3A, C, Suppl. Fig. 2B), arguing against a general decrement of the pathway. *Sphk1-/-* mice were previously described to have no major neurological impairments (51), however, the cerebellum and cerebellar functions have not been explicitly evaluated. Immunostaining for CaBP revealed no apparent developmental defects in lobulation, laminar organisation, or neuronal migration, or any degenerative processes, such as PC torpedoes or PC shrinkage at P140 (Suppl. Fig. 3B). To further investigate the effect of deleting *Sphk1* on
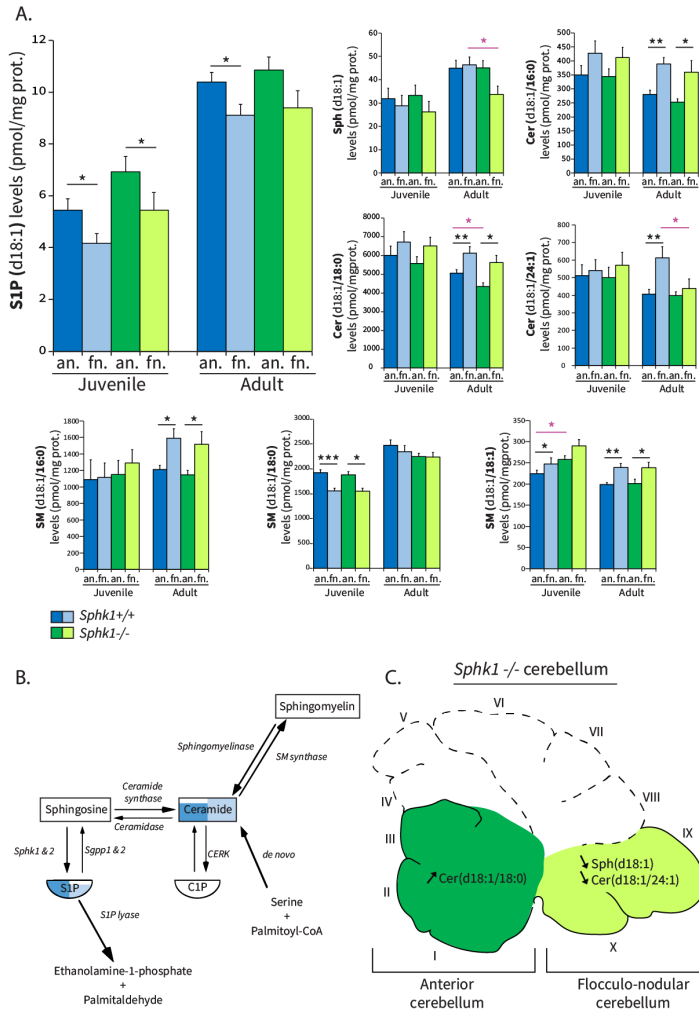
Fig. 3. Sphk1 deletion has marginal effects on sphingolipid levels in the cerebellum.

(A) Bar plot of HP-LC MS/MS quantification of selected sphingolipid levels in wild type Sphk1+/+ (C57BL/6J) and mutant Sphk1-/- mice. (B) Schematic of the sphingolipid metabolic pathway with representation of levels differences between anterior (dark blue) and flocculo-nodular (light blue) fractions. Difference between fractions for ceramides was based on total ceramide. (C) Schematic of sagittal view of the Sphk1--/- cerebellum, with identification of the fractions, and annotation of the sphingolipid changes measured in the adult (except SM(d18:1/18:0)) mutant in independent fractions. Data are expressed as mean ± S.E.M. (n=10 per group); unit = pmol/mg of protein. Juvenile= P21-23, Adult= P143-153. Black stars: significance for anterior (an.) vs. flocculo-nodular (fn.); purple: significant statement for Atxn1[82Q]/- vs. Atxn1[82Q]/+. *p<0.05, **p<0.005, ***p<0.001.

cerebellar development and function we subjected *Sphk1-/-* and wild type *Sphk1+/+* littermate mice to adaptive locomotor and balance-related tasks. There was no significant differences between wild type and mutant mice subjected to the balance beam task in the relative number of slips on the 12 mm (thick) or 6 mm (thin) beam at 6, 12 and 18 weeks, or in the time to cross the thick or thin beam at 6, 12 and 18 weeks (Suppl. Fig. 3C). In addition, locomotion behavior of these mice was examined longitudinally using the Erasmus Ladder (Suppl. Fig. 3D). In the training weeks, a significant increase of the ratio of long steps vs. short steps was found over time for both genotypes (p<0.001) and no differences were observed between *Sphk1+/+* and *Sphk1-/-* (p=0.208). Mouse performance in the following weeks did not improve over time (p=0.087) and did not differ between genotypes (p=0.460). Together these data indicate that deletion of Sphk1 shows marginal changes in measured sphingolipid levels without any effects on cerebellum-dependent behavior.

S1P and Sph levels show a significant multi-interaction effect of age, cerebellar fraction, and genotype:

The extended lipidomic dataset we obtained allowed for further investigation of possible multi-interaction effects for all genotypes, ages, and cerebellar fractions. To this end, we performed a linear mixed model analysis and considered all interaction effects involving the fraction as a fixed effect (fraction*age; fraction*genotype; fraction*age*genotype). Out of the 16 tested sphingolipids, only S1P(d18:1) (p<0.001) and Sph(d18:1) (p<0.05) had a significant multi-interaction effect for age*fraction*genotype. Together with the representation of the mean sphingolipid levels and the 95% confidence interval (Suppl. Fig.4) it showed that the considerable increase of S1P(d18:1) observed in the anterior fraction of adult *Atxn1[82Q]/+* mice, and the significant decrease of Sph(d18:1) observed in the flocculo-nodular fraction of adult *Sphk1-/-* mice were the result of multi-interaction effect of age*fraction*genotype. For all other ceramides or sphingomyelins no interaction effect of age*fraction*genotype was observed (all p>0.05). We observed that only SM(d18:1/18:0) exhibits an interaction effect for fraction*age (p<0.05), while the other sphingolipid levels did not show significance for either fraction*age or fraction*genotype interactions (all p>0.05). These data confirmed that the changes for S1P(d18:1) and Sph(d18:1) observed in the *Atxn1[82Q]/+* and *Sphk1-/-* mice compared to wild type mice, respectively, cannot be attributed to random effects.

Sphk1 deletion in the Atxn1[82Q]/+ rescues populations of PCs:

Based on our sphingolipids analysis and the central role of S1P, we hypothesized that the increase of S1P contributes to the pathogenicity in the *Atxn1[82Q]/+* mice. To investigate a potential benefit of reducing the sphingosine kinase activity, we deleted the *Sphk1* gene in *Atxn1[82Q]/+* mice and analysed the consequences on PC atrophy. We compared the pathology observed in the double mutant (*Atxn1[82Q]/+;Sphk1-/-*) with the PC degeneration observed in the single mutant (*Atxn1[82Q]/+;Sphk1+/+*) using CaBP expression as an indicator of abnormal physiology, morphology, and PC degeneration (52). In single mutant *Atxn1[82Q]/+;Sphk1+/+* mice we observed a decrease of CaBP expression throughout the cerebellum, compared to wild type littermates (*Atxn1[82Q]/-;Sphk1+/+*) (Fig. 4A). The reduction in CaBP was pronounced, as shown by the example plot profile of fluorescent intensity from lobule X and lobule III (Fig. 4B, yellow trace) compared to the expression in wild type mice (Fig. 4B red trace). A reduction in CaBP was also observed in the cerebellar nuclei, which are the target regions of PC axons (Fig. 4C). The single mutant littermates (*Atxn1[82Q]/+;Sphk1+/+* in FVB/N;C57BL/6-J) showed a degeneration similar to the original line (*Atxn1[82Q]/+;Sphk1+/+* in FVB/N), exhibiting a consistent decrease of CaBP expression levels (Suppl. Fig.5). In double mutant *Atxn1[82Q]/+;Sphk1-/-* mice, CaBP expression appeared considerably preserved, indicating a rescue of specific PCs (Fig. 4A; Suppl. Fig. 5). In the anterior cerebellum (lobule III), rescued PCs are distributed in domains illustrated by the peaks of high CaBP expression in the plot profile of fluorescent intensity (Fig. 4B bottom, pink trace). In the nodular cerebellum (lobule X), there was an overall increase of intensity (Fig. 4B top, pink trace). The phenotype of double mutant *Atxn1[82Q]/+;Sphk1-/-* mice was consistently observed in each biological replicate (n=3, Suppl. Fig. 5). We conclude that the deletion of *Sphk1* results in the rescue of subpopulations of PCs from the pathological effect of the *Atxn1[82Q]* transgene expression.

Deletion of Sphk1 in Atxn1[82Q]/+ mice rescues parasagittal domains of PCs:

In double mutant *Atxn1[82Q]/+; Sphk1-/-* mice, rescued PCs appear to be clustered in bands in the transversal plan along the cortex (Fig. 4A), reminiscent of the cerebellar modules. We used immunostaining for Aldolase C (AldoC) to identify the rescued sub-populations of PC distributed in parasagittal domains. Comparing the profile of CaBP expression with the AldoC pattern showed that rescued PC domains in the *Atxn1[82Q]/+; Sphk1-/-* double
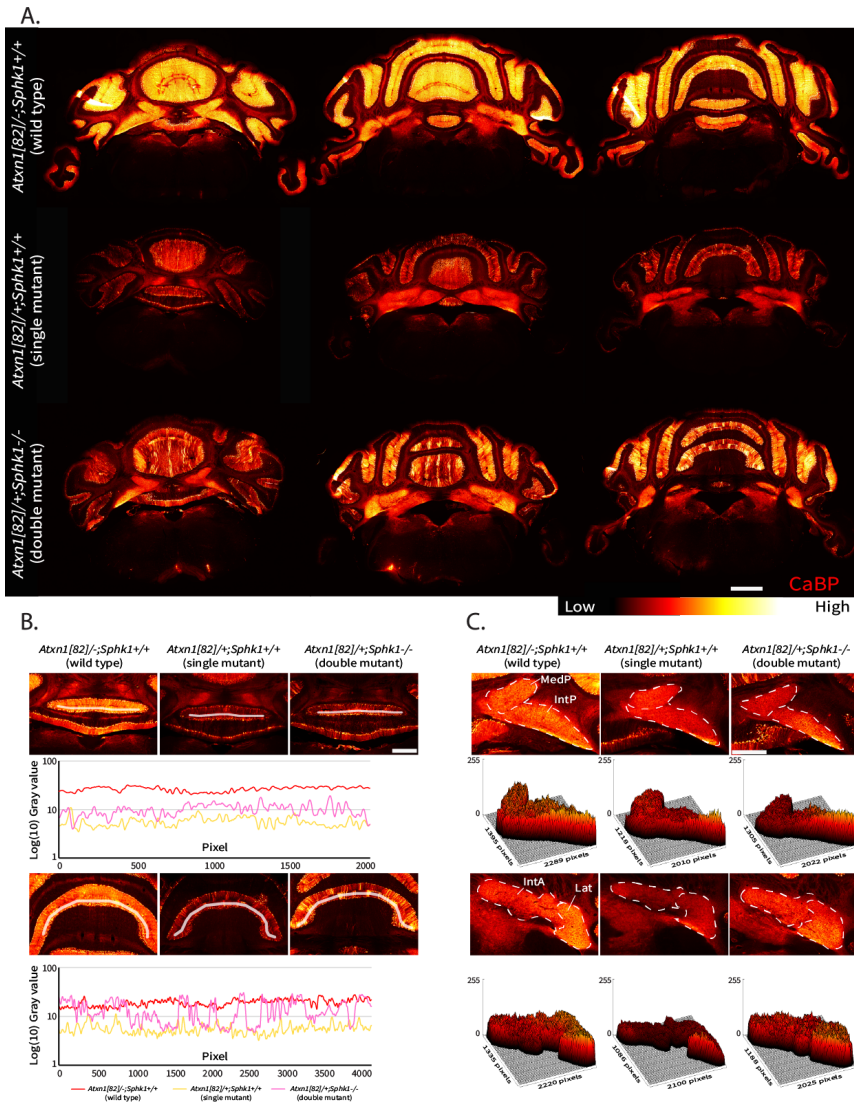
Fig. 4. Deletion of Sphk1 in Atxn1[82Q]/+ mice partially rescues PC degeneration.

(A) Overviews of the cerebellum immunostained for CaBP in wild type (Atxn1[82Q]/-; Sphk1+/+), single mutant (Atxn1[82Q]/+;Sphk1+/+), and double mutant (Atxn1[82Q]/+; Sphk1-/-) mice. CaBP expression levels represented by heat map, from low (red) to high expression levels (white). Scale bar = 1 mm. (B) Plot profile of CaBP immunofluorescent intensity in wild type (red), single mutant (yellow) and double mutant (pink) mice. Measures were done in lobule X (upper panel) and lobule III (lower panel). Scale bar = 500 μm. (C) Surface plot profile of CaBP immunofluorescent intensity in the cerebellar nuclei. MedP: medial posterior, IntP: interposed posterior, IntA: interposed anterior, Lat: lateral. Scale bar = 500 μm

mutant partially match with the AldoC-positive bands observed in the wild type *Atxn1[82Q]/-; Sphk1+/+* mice (Fig. 5A, C, Suppl. Fig.6). For example, in the vermis of the double mutant we observed that rescued regions, identified by CaBP expression, correspond to the parasagittal domains 1+/2+/3+ as defined by the AldoC immunostaining in the wild type (Fig. 5A; Suppl. Fig. 6). However, PC rescue was not limited to the AldoC-positive domains, as the domain 3- also exhibited high levels of CaBP expression. The pattern of rescue was consistent in all biological replicates (Suppl. Fig. 5). In single mutant *Atxn1[82Q]/+; Sphk1+/+* mice we observed that the AldoC expression was mostly disrupted (Fig. 5A-B) across the cerebellum and only lobule X, CrusI and Flocculus conserved an expression relatively identical to the wild type animals (data not shown). In contrast, double mutant *Atxn1[82Q]/+; Sphk1-/-* mice partially recovered AldoC expression, primarily in the anterior
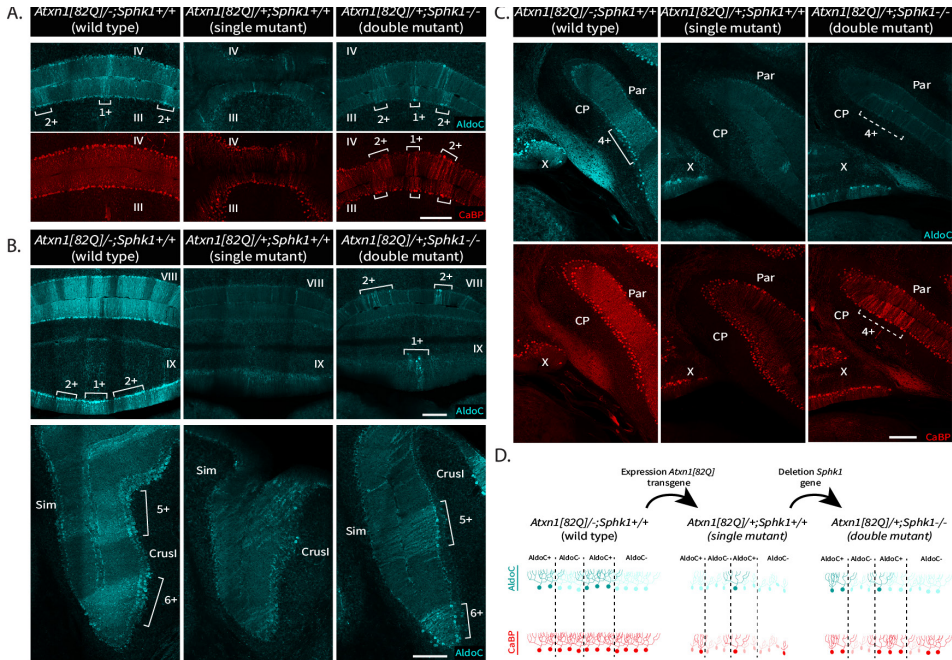
Fig. 5. Rescued PC population in double mutant correlate with cerebellar modules defined by the AldoC pattern.

(A-B-C) Co-Immunostaining for AldoC protein and CaBP in wild type (Atxn1[82Q]/-; Sphk1+/+), single mutant (Atxn1[82Q]/+; Sphk1+/+) and double mutant (Atxn1[82Q]/+; Sphk1-/-) mice. 1+/2+/3+/4+/5+/6+=domains of high AldoC expression as defined by Sugihara and Quy (2007). Dashed line=putative AldoC-positive domain. Cyan=AldoC; Red=CaBP. CP=Copula Pyramidis, Par=Paramedian lobule, Sim=Simplex lobule. Scale bar = 200µm

cerebellum (Fig. 5A, B lower panel). In the posterior cerebellum (lobules VII/VIII/IX) despite signs of AldoC expression recovery the pattern remained heavily disrupted (Fig. 5B upper panel). Interestingly, while we observed that CaBP expression recovery, a sign of rescue, appeared predominantly in putative AldoC-positive domains, AldoC expression is not systematically recovered (Fig. 5C). This indicates that AldoC expression is not a sine qua non condition to PC rescue. These results demonstrate that *Sphk1* deletion in the *Atxn1[82Q]/+* leads to survival of PCs preferentially but not exclusively in AldoC-positive domains, and that AldoC expression is partly recovered but is not an absolute requirement for PC survival.

Discussion

In the present study we provide the first comprehensive analysis of region-specific differences in sphingolipid metabolism in the cerebellar cortex, its alterations in a mouse model for spino-cerebellar ataxia type 1, and its implication in PC fate and patterned degeneration. In healthy cerebella we found differential levels of Sphk1, as well as S1P and Sph between anterior and flocculo-nodular region. We showed that while expression of both enzymes decreases in the *Atxn1[82Q]/+* mice, S1P levels increase significantly and predominantly in the anterior region, where neurodegeneration is prevalent. Finally, we showed that *Sphk1* deletion rescues PCs in the *Atxn1[82Q]/+* mice, supporting a causal role for sphingolipid metabolism in PC degeneration in *Atxn1[82Q]/+* model (Fig. 5D).

In healthy cerebella Sphk1 expression levels were higher in the flocculo-nodular than in the anterior region, confirming previous report (48), while Sphk2 expression levels were comparable between cerebellar regions. Although S1P is the product of the enzymatic reaction catalysed by Sphk1, and Sphk1 levels were lower in the anterior region, the S1P levels were higher in the anterior region of adult animals compared to the flocculo-nodular region. This difference was observed in both wild type FVB/N and C57BL/6-J control lines, indicating this is a consistent feature of cerebellar lipid homeostasis in mice. We also observed that *Sphk1* gene deletion had no significant impact on regional S1P levels. This suggests that regional S1P levels are controlled by different Sphk2 activity and/or other enzymes in this pathway expressed differentially in the cerebellar cortex, and are not only the result of Sphk1 differential expression. A recently published high spatial resolution single cell RNA sequencing study (53) listed 669 genes with non-homogeneous expression in the PC layer, highlighting different patterns of expression in

the cerebellar cortex. Among the reported genes were ceramide kinase (Cerk), ceramide synthase 4 (CerS4), sphingomyelin phosphodiesterase 1 (Smpd1) and Sphk1 interactor (Sphkap). Taken together, this highlights the existence of regional molecular mechanisms to maintain the adequate level of sphingolipids, resulting in a local tight control of S1P metabolism in healthy physiological condition. As an essential driver of cellular fate, S1P physiological levels are responsible for different vulnerabilities to neuropathological insults, which do not exclude other potential mechanisms behind the regional sensitivity observed in multiple cerebellar diseases (24).

Previous studies showed correlations between sphingolipid dyshomeostasis and cerebellar ataxia pathologies, in mouse (37–39, 43, 54, 55) and human (50). In this work, we investigate for the first time sphingolipid metabolism in a mouse model for spinocerebellar ataxia type 1. In *Atxn1[82Q]/+* mice, a model for SCA type 1, we found that sphingolipid levels correlate with the progression of the neurodegeneration. In this model, no discernible signs of neurodegeneration can be observed in juvenile animals (47), while adult mice exhibit severe neurodegeneration, predominantly in the anterior cerebellum. In juvenile *Atxn1[82Q]/+* mice sphingolipids and the two kinases, Sphk1 and 2, were not significantly changed, in line with the absence of a neurodegenerative phenotype. In adult mutant mice, Sphk1 expression levels decreased in the flocculo-nodular region while Sphk2 expression levels decreased in both anterior and flocculo-nodular regions, with a predominant decrease in the anterior cerebellum. In parallel, we observed that S1P levels increased in both regions with a predominant change in the anterior cerebellum. As the mutation in *Atxn1[82Q]/+* mice is under a PC-specific promotor, the observed changes are putatively intrinsic to PCs. In addition to S1P, some ceramide and sphingomyelin levels change in the *Atxn1[82Q]/+* mice, all specifically in the anterior region which is primarily compromised by neurodegeneration. The balance between ceramide and S1P controls cellular apoptosis, as defined by the "sphingolipid rheostat" concept (32, 56). However, in the cerebellum accumulation of long-chain bases correlates with neurodegeneration (34, 44), independently from the ceramide levels, and S1P can act as pro-apoptotic mediator (41). The cellular fate driven by S1P is thought to be dependent on the kinase in play, and therefore its sub-cellular localisation(41). Hence, the overall increase of S1P that we found in the cerebellum of *Atxn1[82Q]/+* mice could be interpreted either as a cause, or as a response to the neurodegeneration. Is S1P an efficient pro-apoptotic mediator or an ineffective neuroprotective agent? As the region primarily affected by the pathology (anterior cerebellum) exhibits higher S1P levels compared to the region preserved from the neuropathology (flocculo-

nodular cerebellum), our working hypothesis was that in *Atxn1[82Q]/+* mice the increase of S1P has a pro-apoptotic effect. Indeed, we found that deletion of Sphk1 in *Atxn1[82Q]/+* mutant mice improves the survival rate of PC. In Allende *et al.* 2004 (51), the authors found that in *Sphk1-/-* mice the kinase activity and S1P synthesis in brain homogenate were maintained at normal physiological levels, and suggested this was due to compensatory activity of Sphk2, a redundancy that could explain why we did not observed a change in S1P in the *Sphk1-/-* mice. In double mutant *Atxn1[82Q]/+;Sphk1-/-* mice our data do not allow to establish whether PC rescue resulted from a different subcellular location of S1P, via Sphk2 activity, or an overall change of S1P levels. Yet, we confirmed that sphingosine kinases, an therefore S1P metabolism, contributes to PC degeneration in *Atxn1[82Q]/+* mice.

PC rescue in double mutant Atxn1[82Q]/+;Sphk1-/- mice occurs predominantly in the anterior cerebellum, with rescued PCs forming parasagittal bands reminiscent of the known AldoC-positive domains. This preferred rescue of AldoC-positive domains was expected, as Sphk1 expression is relatively higher in this sub-population (48). The idea that AldoC expression is a determinant factor for PC survival has been addressed for many pathologies (24). However, here survival is not only restricted to AldoC-positive PCs domains as we also observed some AldoC-negative PCs being rescued in the double mutant, and PCs rescued in putative AldoC-positive domain do not systematically recover a proper AldoC expression. This suggest that AldoC is not the direct cause of preferential survival as it has been suggested (ref). PC sub-populations cannot be defined solely based on the expression of AldoC, as several markers such as Hsp25 (57) and Trpc3 (11) showed expression patterns that are not strictly identical to the AldoC pattern. While Sphk1 was described as exhibiting a pattern of expression that is strictly identical, it would not be surprising that other proteins in the pathway are expressed differently, which would explain the complex pattern of rescue we observed.

We conclude that 1) sphingolipid metabolism is controlled locally, depending on the molecular identity of PCs, 2) sphingosine kinases and related lipid levels are affected in a common mouse model for cerebellar neurodegeneration and 3) deletion of a main sphingosine kinase is able to rescue part of the degeneration and change the pattern of degeneration. These data establish sphingolipid metabolism as central actor in the neurodegenerative process and support the therapeutic perspectives that sphingolipid pathway modulators could offer (58–60).

Materials and methods

Animals:

Atxn1[82Q]/+ mice are taken from the transgenic line B05, originally created by Burright *et al.* (49) and were a gift of Harry T. Orr. The line was maintained in FVB/N background. *Sphk1-/-* mice (51) were purchased from The Jackson Laboratory (Sacramento, CA) and were maintained in a C57BL/6-J background. *Atxn1[82Q]/+* and *Sphk1-/-* lines were crossed to obtain *Atxn1[82Q]/-;Sphk1-/+* and *Atxn1[82Q]/+;Sphk1-/+* mice (=F1). *Atxn1[82Q]/+;Sphk1-/+* mice were then inbred to obtain *Atxn1[82Q]/-;Sphk1+/+* (wild type)*, Atxn1[82Q]/+;Sphk1+/+* (single mutant)*, and Atxn1[82Q]/+;Sphk1-/-* (double mutant) mice (=F2). Mice were randomly housed together with two to four siblings of the same gender, both mutants and controls. Male and female *Atxn1[82Q]/+*, *Sphk1-/-*, and their wild type littermates were tested between age postnatal (P) 21 and P23 (juvenile), or P143 to P153 (adult). All experiment protocols were approved by the institutional welfare committee of the Erasmus Medical Centre.

Western Blotting:

The animals were anesthetised with 0.2 ml pentobarbital (60mg/ml) and perfused using sodium chloride to rinse out the blood. Cerebella were removed and isolated into the anterior fraction composed of vermal lobule I, II, III, and the flocculo-nodular fraction composed of vermal lobule IX, X, Paraflocculus and Flocculus. All tissues were frozen at -80ºC avoiding freeze-thaw cycles. Cerebellar tissue was homogenised in lysis buffer (50 mM Tris-HCl, pH 8.0, 150 mM NaCl, 0.5% sodium deoxycholate, 1% NP-40, 0.1% SDS, 1 mM sodium orthovanadate and protease inhibitor cocktail). Protein concentrations were measured using Pierce BCA protein assay kit (Thermo Fisher). Samples were centrifuged at 12,000 rpm at 4°C for 10 min and the supernatant was denatured for 10 min at 95°C. Proteins were separated on SDS-PAGE (Criterion™ TGX Stain-Free™ Gels, Bio-Rad) and transferred onto a nitrocellulose membrane with the Trans-Blot® Turbo™ Blotting System (Bio-Rad). Before transfer, gels were activated and imaged as a protein loading control using the Gel Doc EZ Imager (Bio-Rad). Membranes were blocked with 5% BSA (Sigma-Aldrich) in TBST (20mM Tris-HCl pH7.5, 150mM NaCl and 0.1%, Tween20) for 1 h and incubated with either anti-Sphk1 (mouse monoclonal, SC-365401, Santa Cruz Biotechnology), anti-Calbindin (rabbit polyclonal, CB-38a, Swant) or anti-Sphk2 (rabbit polyclonal,

3.2

17096-1-AP, proteintech) primary antibody diluted 1:1000 in 5% BSA in TBST overnight at 4°C. Protein levels were detected using either HRP conjugated goat anti-mouse antibody (Dako;P0447, 1:5000), goat anti-rabbit antibody(Dako;P0448, 1:10000).

High Performance Liquid Chromatography-Mass Spectrometry:

We quantified selected sphingolipid levels using HPLC-MS/MS. Cerebella were obtained from juvenile (n =10 per group) and adult (n = 10 per group) and extracted as previously described. In each sample Sphingolipids were extracted as previously described by Hoogendoorn *et al.* (61). Frozen cerebellar samples were homogenized in cold Millipore water (MQ, 18.2 MΩ cm) from a Milli-Q® PF Plus system (Millipore B.V., Amsterdam, the Netherlands). To 10 µL cerebellum homogenates, the internal standards Cer(d18:1/17:0), Cer(d17:0/24:1), and S1P(d18:1)-D7 were added (10 µL of 2, 2, and 0.2 µg/mL in methanol, respectively; IS: Avanti Polar Lipids, Alabaster, AL, USA; methanol: Merck Millipore B.V.). After addition of 10 µL of 10% TEA solution (triethylamine (10/90, v/v) in methanol/dichloromethane (DCM) (50/50, v/v); TEA: Merck Millipore B.V., DCM: Merck Millipore B.V.) lipids were extracted with 450 µL methanol/DCM (50/50, v/v). Samples were vortexed and incubated under constant agitation for 30 min at 4 °C followed by centrifugation at 18500 g for 20 min at 4 °C (Hettich mikro 200R, Geldermalsen, the Netherlands). Supernatants were transferred to glass vials, freeze dried and reconstituted in 100 µL methanol before liquid chromatography-tandem mass spectrometry (LC-MSMS). LC-MSMS analysis was performed as previously described (61) on a Sciex Qtrap 5500 quadruple mass spectrometer (AB Sciex Inc., Thornhill, Ontario, Canada). S1P, sphingosine, and the seven most abundant ceramide species for which standards were commercially available were analysed. Nine-point calibration curves were constructed by plotting analyte to internal standard peak area ratios for Cer(d18:1/14:0), Cer(d18:1/16:0), Cer(d18:1/18:0), Cer(d18:1/20:0), Cer(d18:1/22:0), Cer(d18:1/24:1), Cer(d18:1/24:0), sphingosine and S1P(d18:1) (all Avanti polar lipids). Instrument control and quantification of spectral data was performed using MultiQuant software (AB Sciex Inc.). Cerebellum sphingolipid levels were normalized to protein content obtained by bichonic acid assay.

Histology:

Animals were deeply anesthetized through intraperitoneal administration of sodium pentobarbital (60mg/ml), directly followed by transcardial perfusion with 4% paraformaldehyde (PFA) in 0.12M phosphate buffer (PB), pH=7.6. Brains were postfixed for 1 h in 4% PFA at room temperature (rT), transferred to 10% sucrose solution overnight at 4°C. The cerebella were embedded in a 10% gelatine (FUJIFILM Wako Pure Chemicals) 10% sucrose mix, gelatin blocks were incubated in 30% sucrose/10% formaldehyde for 2h at rT and incubated overnight in 30% sucrose at 4°C. Subsequently, coronal sections were cut at a 40 µm thickness with freezing microtome. Free-floating sections were rinsed with 0.1M PB and incubated in 10mM sodium citrate (pH6) at 80°C for 2h, for antigen retrieval. For immuno-fluorescence, sections were rinsed with 0.1M PB, followed by 3 washes of 10 min in Phosphate Buffered saline (PBS). Then, sections were incubated 90 min at rT in a solution of PBS/0.5%Triton-X100/10% normal horse serum to block nonspecific protein-binding sites, and incubated 48h at 4°C in a solution of PBS/0.4% Triton-X100/2% normal horse serum (NHS), with primary antibodies diluted as follows: Calbindin 1:14000 (rabbit polyclonal, CB-38a, Swant), AldolaseC 1:500 (goat polyclonal, SC-12065, Santa Cruz Biotechnology). After rinsing in PBS, sections were incubated for 2h at rT in PBS/0.4% Triton-X100/2% NHS solution with secondary antibodies coupled with Alexa488, Cy3 or Cy5 (1:200, Jackson ImmunoResearch). Sections were mounted on coverslip in a solution of gelatin/chrome alum and covered with Mowiol (Polysciences Inc.). For light microscopy sections were pre-treated for endogenous peroxidase activity blocking with 3%H_2O_2 in PBS, then rinsed for 30 min in PBS, incubated 90 min in a solution of PBS/0.5%Triton-X100/10% NHS, followed by the primary antibody incubation as described before. After 48h, sections were rinsed in PBS and incubated 2h at rT in PBS/0.4% Triton-X100/10% normal horse serum solution with HRP coupled secondary antibodies (1:1000, Jackson ImmunoResearch). Sections were rinsed with 0.1M PB and incubated in diaminobenzidine (DAB, 75 mg/100ml) for 10 min. Sections were mounted on glasses in a solution of gelatin/chrome alum, counterstained with Thionin dehydrated with successive ethanol steps (2x 96%, 3x 100%), incubated in Xylene and covered with Permount mounting medium (Fisher Chemical).

Imaging acquisition and analysis:

Images were acquired with an upright Imager M2 (Zeiss) equipped with a 10x lens, for fluorescence microscopy, a confocal microscope LSM700 (Zeiss)

with upright 20x lenses, and Hamamatsu Nanozoomer 2 whole slide imager equipped with 40x lenses for light microscopy. Images were treated with a Photoshop routine to perfect overall brightness and signal level homogeneously on the pictures, all treatment being equally applied on the entire images. Calbindin intensity measurements were performed with FIJI software. In order to compare wild type, single mutant and double mutant mice we performed identical immunostaining process (antibody concentration, incubation time), identical image acquisition (gain, exposure time, resolution), and identical image adjustment for analysis (brightness and contrast values), all performed in parallel in a single session for the three genotypes with four animals per group.

Behavioral tests:

Balance Beam tests were performed using a thick (12 mm) and a thin (6mm) beam, both with 80 cm of length, placed between an attachment pole and a cage 50 cm above the table top. Time to cross the beam and number of slips were quantified. A video camera was attached to the pole to record each measurement session. Mice were measured at 6, 12 and 18 weeks of age. Each test consisted of one training session and two measurement sessions. Mice were placed on the beam and the time was register when the front paw crossed the starting stripe and stopped when the front paw crossed the end stripe. Mice had to travel each beam twice without falling off and these successful runs were averaged. Video recordings were used to analyse the slips and time to cross the beam (62).

The Erasmus Ladder consists of an horizontal ladder composed of 37 rods, distributed between high and low position, equipped with individual pressure sensors. Animals are trained to cross at a constant speed to reach either ends of the ladder. We analysed short steps and long steps along the ladder. In the paradigm we used, each mouse underwent a daily session for five consecutive days at 6 to 7 weeks old. Hereafter, they performed one session every week for the following twelve weeks. Every session consisted of 42 trials, non-perturbed, in which the mice had to walk from one box to the next after a light stimulus. First, mice had to wait between 8 and 12 seconds before the light cue. If mice leave the box early an air cue from the opposite box will drive them back and the trial would start from the beginning. If the light cue does not induce a run, an air cue will be given 3 seconds later to spur them on. Upon entering the goal box, the next trial would start. The first five sessions served to create a baseline. The definition of the steps concurs with the description made by Vinueza Veloz *et al.* (63). All behavioural experiments were performed by a blinded investigator.

Statistical analysis:

Statistical analysis for WB protein quantification and LC-MS/MS lipids quantification were performed using Student t-test, defined as paired for anterior and flocculo-nodular fractions comparisons (black stars) , and as unpaired when comparing fractions from different groups (purple stars). The linear mixed model is a classic mixed effects ANOVA with a random intercepts on which we fitted separate error variance per subgroup. Three covariates were defined: genotypes (Atxn1[82Q] -/-, Atxn1[82Q] -/+, Sphk1+/+ and Sphk1-/-), fractions (anterior and flocculo-nodular) , and age groups (juvenile and adult), for a total of sixteen subgroups (4 genotypes x 2 fractions x 2 age groups). Animal number was established as a random effect to resolve the non-independency resulting from the extraction of both fractions from a single subject.

3.2

1. N. L. Cerminara, E. J. Lang, R. V. Sillitoe, R. Apps, Redefining the cerebellar cortex as an assembly of non-uniform Purkinje cell microcircuits. *Nat. Rev. Neurosci.* (2015) https:/doi.org/10.1038/nrn3886.
2. D. M. Armstrong, R. F. Schild, A quantitative study of the purkinje cells in the cerebellum of the albino rat. *J. Comp. Neurol.* (1970) https:/doi.org/10.1002/cne.901390405.
3. H. Nedelescu, M. Abdelhack, Comparative morphology of dendritic arbors in populations of purkinje cells in mouse sulcus and apex. *Neural Plast.* (2013) https:/doi.org/10.1155/2013/948587.
4. U. Müller, H. Heinsen, Regional differences in the ultrastructure of Purkinje cells of the rat. *Cell Tissue Res.* (1984) https:/doi.org/10.1007/BF00213728.
5. J. Voogd, Cerebellar zones: A personal history. *Cerebellum* (2011) https:/doi.org/10.1007/s12311-010-0221-6.
6. G. Brochu, L. Maler, R. Hawkes, Zebrin II: A polypeptide antigen expressed selectively by purkinje cells reveals compartments in rat and fish cerebellum. *J. Comp. Neurol.* (1990) https:/doi.org/10.1002/cne.902910405.
7. Y. Dehnes, *et al.*, The glutamate transporter EAAT4 in rat cerebellar Purkinje cells: A glutamate-gated chloride channel concentrated near the synapse in parts of the dendritic membrane facing astroglia. *J. Neurosci.* (1998) https:/doi.org/10.1523/jneurosci.18-10-03606.1998.
8. J. R. Sarna, H. Marzban, M. Watanabe, R. Hawkes, Complementary stripes of phospholipase Cβ3 and Cβ4 expression by Purkinje cell subsets in the mouse cerebellum. *J. Comp. Neurol.* (2006) https:/doi.org/10.1002/cne.20912.
9. I. Sugihara, P. N. Quy, Identification of aldolase C compartments in the mouse cerebellar cortex by olivocerebellar labeling. *J. Comp. Neurol.* (2007) https:/doi.org/10.1002/cne.21219.
10. H. Zhou, *et al.*, Cerebellar modules operate at different frequencies. *Elife* (2014) https:/doi.org/10.7554/eLife.02536.
11. B. Wu, *et al.*, TRPC3 is a major contributor to functional heterogeneity of cerebellar Purkinje cells. *Elife* (2019) https:/doi.org/10.7554/eLife.45590.
12. J. I. Wadiche, C. E. Jahr, Patterned expression of Purkinje cell glutamate transporters controls synaptic plasticity. *Nat. Neurosci.* (2005) https:/doi.org/10.1038/nn1539.
13. S. A. Gebre, S. L. Reeber, R. V. Sillitoe, Parasagittal compartmentation of cerebellar mossy fibers as revealed by the patterned expression of vesicular glutamate transporters VGLUT1 and VGLUT2. *Brain Struct. Funct.* (2012) https:/doi.org/10.1007/s00429-011-0339-4.
14. J. Voogd, T. J. H. Ruigrok, The organization of the corticonuclear and olivocerebellar climbing fiber projections to the rat cerebellar vermis: The congruence of projection zones and the zebrin pattern. *J. Neurocytol.* (2004) https:/doi.org/10.1023/B:NEUR.0000029645.72074.2b.
15. J. A. Heckroth, L. C. Abbott, Purkinje cell loss from alternating sagittal zones in the cerebellum of leaner mutant mice. *Brain Res.* (1994) https:/doi.org/10.1016/S0006-8993(09)90014-2.
16. S. H. Chung, M. Calafiore, J. M. Plane, D. E. Pleasure, W. Deng, Apoptosis inducing factor deficiency causes reduced mitofusion 1 expression and patterned Purkinje cell degeneration. *Neurobiol. Dis.* (2011) https:/doi.org/10.1016/j.nbd.2010.10.016.
17. J. R. Sarna, R. Hawkes, Patterned Purkinje cell loss in the ataxic sticky mouse. *Eur. J. Neurosci.* (2011) https:/doi.org/10.1111/j.1460-9568.2011.07725.x.
18. P. Strømme, *et al.*, X-linked Angelman-like syndrome caused by Slc9a6 knockout in mice exhibits evidence of endosomal-lysosomal dysfunction. *Brain* (2011) https:/doi.org/10.1093/brain/awr250.
19. T. Miyazaki, *et al.*, Ca v2.1 in cerebellar Purkinje cells regulates competitive excitatory synaptic wiring, cell survival, and cerebellar biochemical compartmentalization. *J. Neurosci.* (2012) https:/doi.org/10.1523/JNEUROSCI.2755-11.2012.
20. J. P. Welsh, *et al.*, Why do Purkinje cells die so easily after global brain ischemia? Aldolase C, EAAT4, and the cerebellar contribution to posthypoxic myoclonus. *Adv. Neurol.* (2002).
21. B. L. Williams, K. Yaddanapudi, M. Hornig, W. I. Lipkin, Spatiotemporal Analysis of Purkinje Cell Degeneration Relative to Parasagittal Expression Domains in a Model of Neonatal Viral Infection. *J. Virol.* (2007) https:/doi.org/10.1128/jvi.02245-06.
22. A. Ragagnin, *et al.*, Cerebellar compartmentation of prion pathogenesis. *Brain Pathol.* (2018) https:/doi.org/10.1111/bpa.12503.
23. J. H. Lee, S. H. Heo, D. Il Chang, Early-stage alcoholic cerebellar degeneration: Diagnostic imaging clues. *J. Korean Med. Sci.* (2015) https:/doi.org/10.3346/jkms.2015.30.11.1539.
24. J. R. Sarna, R. Hawkes, Patterned Purkinje cell death in the cerebellum. *Prog. Neurobiol.* (2003) https:/doi.org/10.1016/S0301-0082(03)00114-X.
25. I. Ishii, N. Fukushima, X. Ye, J. Chun, Lysophospholipid Receptors: Signaling and Biology. *Annu.*

Rev. Biochem. (2004) https:/doi.org/10.1146/annurev.biochem.73.011303.073731.

26. A. Olivera, *et al.*, Sphingosine kinase expression increases intracellular sphingosine-1- phosphate and promotes cell growth and survival. *J. Cell Biol.* (1999) https:/doi.org/10.1083/jcb.147.3.545.

27. K. Mizugishi, *et al.*, Essential Role for Sphingosine Kinases in Neural and Vascular Development. *Mol. Cell. Biol.* (2005) https:/doi.org/10.1128/mcb.25.24.11113-11121.2005.

28. T. Kanno, *et al.*, Regulation of synaptic strength by sphingosine 1-phosphate in the hippocampus. *Neuroscience* (2010) https:/doi.org/10.1016/j.neuroscience.2010.10.021.

29. J. Chun, *et al.*, International Union of Pharmacology. XXXIV. Lysophospholipid receptor nomenclature. *Pharmacol. Rev.* (2002) https:/doi.org/10.1124/pr.54.2.265.

30. A. Kihara, S. Mitsutake, Y. Mizutani, Y. Igarashi, Metabolism and biological functions of two phosphorylated sphingolipids, sphingosine 1-phosphate and ceramide 1-phosphate. *Prog. Lipid Res.* (2007) https:/doi.org/10.1016/j.plipres.2007.03.001.

31. T. A. Taha, T. D. Mullen, L. M. Obeid, A house divided: Ceramide, sphingosine, and sphingosine-1-phosphate in programmed cell death. *Biochim. Biophys. Acta - Biomembr.* (2006) https:/doi.org/10.1016/j.bbamem.2006.10.018.

32. J. Newton, S. Lima, M. Maceyka, S. Spiegel, Revisiting the sphingolipid rheostat: Evolving concepts in cancer therapy. *Exp. Cell Res.* (2015) https:/doi.org/10.1016/j.yexcr.2015.02.025.

33. S. Rashad, *et al.*, Intracellular S1P Levels Dictate Fate of Different Regions of the Hippocampus following Transient Global Cerebral Ischemia. *Neuroscience* (2018) https:/doi.org/10.1016/j.neuroscience.2018.05.015.

34. C. S. Petit, *et al.*, Inhibition of sphingolipid synthesis improves outcomes and survival in GARP mutant wobbler mice, a model of motor neuron degeneration. *Proc. Natl. Acad. Sci. U. S. A.* (2020) https:/doi.org/10.1073/pnas.1913956117.

35. S. Furuya, J. Mitoma, A. Makino, Y. Hirabayashi, Ceramide and Its Interconvertible Metabolite Sphingosine Function as Indispensable Lipid Factors Involved in Survival and Dendritic Differentiation of Cerebellar Purkinje Cells. *J. Neurochem.* (2002) https:/doi.org/10.1046/j.1471-4159.1998.71010366.x.

36. C. Ginkel, *et al.*, Ablation of neuronal ceramide synthase 1 in mice decreases ganglioside levels and expression of myelin-associated glycoprotein in oligodendrocytes. *J. Biol. Chem.* (2012) https:/doi.org/10.1074/jbc.M112.413500.

37. K. Wang, *et al.*, Alkaline Ceramidase 3 Deficiency Results in Purkinje Cell Degeneration and Cerebellar Ataxia Due to Dyshomeostasis of Sphingolipids in the Brain. *PLoS Genet.* (2015) https:/doi.org/10.1371/journal.pgen.1005591.

38. J. Matsuda, *et al.*, Mutation in saposin D domain of sphingolipid activator protein gene causes urinary system defects and cerebellar Purkinje cell degeneration with accumulation of hydroxy fatty acid-containing ceramide in mouse. *Hum. Mol. Genet.* (2004) https:/doi.org/10.1093/hmg/ddh281.

39. J. Matsuda, A. Yoneshige, K. Suzuki, The function of sphingolipids in the nervous system: lessons learnt from mouse models of specific sphingolipid activator protein deficiencies. *J. Neurochem.* (2007) https:/doi.org/10.1111/j.1471-4159.2007.04709.x.

40. J. R. Sarna, *et al.*, Patterned Purkinje cell degeneration in mouse models of Niemann-Pick type C disease. *J. Comp. Neurol.* (2003) https:/doi.org/10.1002/cne.10522.

41. N. Hagen, *et al.*, Subcellular origin of sphingosine 1-phosphate is essential for its toxic effect in lyase-deficient neurons. *J. Biol. Chem.* (2009) https:/doi.org/10.1074/jbc.M807336200.

42. N. Hagen, M. Hans, D. Hartmann, D. Swandulla, G. Van Echten-Deckert, Sphingosine-1-phosphate links glycosphingolipid metabolism to neurodegeneration via a calpain-mediated mechanism. *Cell Death Differ.* (2011) https:/doi.org/10.1038/cdd.2011.7.

43. L. Zhao, *et al.*, A deficiency of ceramide biosynthesis causes cerebellar purkinje cell neurodegeneration and lipofuscin accumulation. *PLoS Genet.* (2011) https:/doi.org/10.1371/journal.pgen.1002063.

44. S. D. Spassieva, *et al.*, Ectopic expression of ceramide synthase 2 in neurons suppresses neurodegeneration induced by ceramide synthase 1 deficiency. *Proc. Natl. Acad. Sci. U. S. A.* (2016) https:/doi.org/10.1073/pnas.1522071113.

45. Y. Robitaille, L. Schut, S. J. Kish, Structural and immunocytochemical features of olivopontocerebellar atrophy caused by the spinocerebellar ataxia type 1 (SCA-1) mutation define a unique phenotype. *Acta Neuropathol.* (1995) https:/doi.org/10.1007/BF00318569.

46. S. Gilman, The spinocerebellar ataxias. *Clin. Neuropharmacol.* (2000) https:/doi.org/10.1097/00002826-200011000-00002.

47. H. B. Clark, *et al.*, Purkinje cell expression of a mutant allele of SCA1 in transgenic mice leads to disparate effects on motor behaviors, followed by a progressive cerebellar dysfunction and

3.2

histological alterations. *J. Neurosci.* (1997) https:/doi.org/10.1523/jneurosci.17-19-07385.1997.

48. N. Terada, *et al.*, Compartmention of the Mouse Cerebellar Cortex by Sphingosine Kinase. *J. Comp. Neurol.* (2004) https:/doi.org/10.1002/cne.11002.

49. E. N. Burright, *et al.*, SCA1 transgenic mice: A model for neurodegeneration caused by an expanded CAG trinucleotide repeat. *Cell* (1995) https:/doi.org/10.1016/0092-8674(95)90273-2.

50. N. E. Sen, *et al.*, In human and mouse spino-cerebellar tissue, ataxin-2 expansion affects ceramide-sphingomyelin metabolism. *Int. J. Mol. Sci.* (2019) https:/doi.org/10.3390/ijms20235854.

51. M. L. Allende, *et al.*, Mice deficient in sphingosine kinase 1 are rendered lymphopenic by FTY720. *J. Biol. Chem.* (2004) https:/doi.org/10.1074/jbc.M406512200.

52. K. Ishikawa, *et al.*, Calbindin-D 28k immunoreactivity in the cerebellum of spinocerebellar degeneration. *J. Neurol. Sci.* (1995) https:/doi.org/10.1016/0022-510X(94)00279-W.

53. S. Rodrigues, *et al.*, Slide-seq: A Scalable Technology for Measuring Genome-Wide Expression at High Spatial Resolution. *Slide-seq A Scalable Technol. Meas. Genome-Wide Expr. High Spat. Resolut.* (2019) https:/doi.org/10.1101/563395.

54. Y. Sun, *et al.*, Combined saposin C and D deficiencies in mice lead to a neuronopathic phenotype, glucosylceramide and α-hydroxy ceramide accumulation, and altered prosaposin trafficking. *Hum. Mol. Genet.* (2007) https:/doi.org/10.1093/hmg/ddm040.

55. H. E. Kong, *et al.*, Metabolic pathways modulate the neuronal toxicity associated with fragile X-associated tremor/ataxia syndrome. *Hum. Mol. Genet.* (2019) https:/doi.org/10.1093/hmg/ddy410.

56. O. Cuvillier, *et al.*, Suppression of ceramide-mediated programmed cell death by sphingosine-1-phosphate. *Nature* (1996) https:/doi.org/10.1038/381800a0.

57. C. L. Armstrong, A. M. Krueger-Naug, R. W. Currie, R. Hawkes, Constitutive expression of the 25-kda heat shock protein Hsp25 reveals novel parasagittal bands of Purkinje cells in the adult mouse cerebellar cortex. *J. Comp. Neurol.* (2000) https:/doi.org/10.1002/(SICI)1096-9861(20000117)416:3<383::AID-CNE9>3.0.CO;2-M.

58. A. Lucaciu, R. Brunkhorst, J. Pfeilschifter, W. Pfeilschifter, J. Subburayalu, The S1P–S1PR Axis in Neurological Disorders—Insights into Current and Future Therapeutic Perspectives. *Cells* (2020) https:/doi.org/10.3390/cells9061515.

59. M. Pitteri, R. Magliozzi, A. Bajrami, V. Camera, M. Calabrese, Potential neuroprotective effect of Fingolimod in multiple sclerosis and its association with clinical variables. *Expert Opin. Pharmacother.* (2018) https:/doi.org/10.1080/14656566.2018.1434143.

60. M. Bigaud, D. Guerini, A. Billich, F. Bassilana, V. Brinkmann, Second generation S1P pathway modulators: Research strategies and clinical developments. *Biochim. Biophys. Acta - Mol. Cell Biol. Lipids* (2014) https:/doi.org/10.1016/j.bbalip.2013.11.001.

61. A. Hoogendoorn, *et al.*, Variation in Coronary Atherosclerosis Severity Related to a Distinct LDL (Low-Density Lipoprotein) Profile: Findings From a Familial Hypercholesterolemia Pig Model. *Arterioscler. Thromb. Vasc. Biol.* (2019) https:/doi.org/10.1161/ATVBAHA.119.313246.

62. T. N. Luong, H. J. Carlisle, A. Southwell, P. H. Patterson, Assessment of motor balance and coordination in mice using the balance beam. *J. Vis. Exp.* (2011) https:/doi.org/10.3791/2376.

63. M. F. Vinueza Veloz, *et al.*, Cerebellar control of gait and interlimb coordination. *Brain Struct. Funct.* (2015) https:/doi.org/10.1007/s00429-014-0870-1.
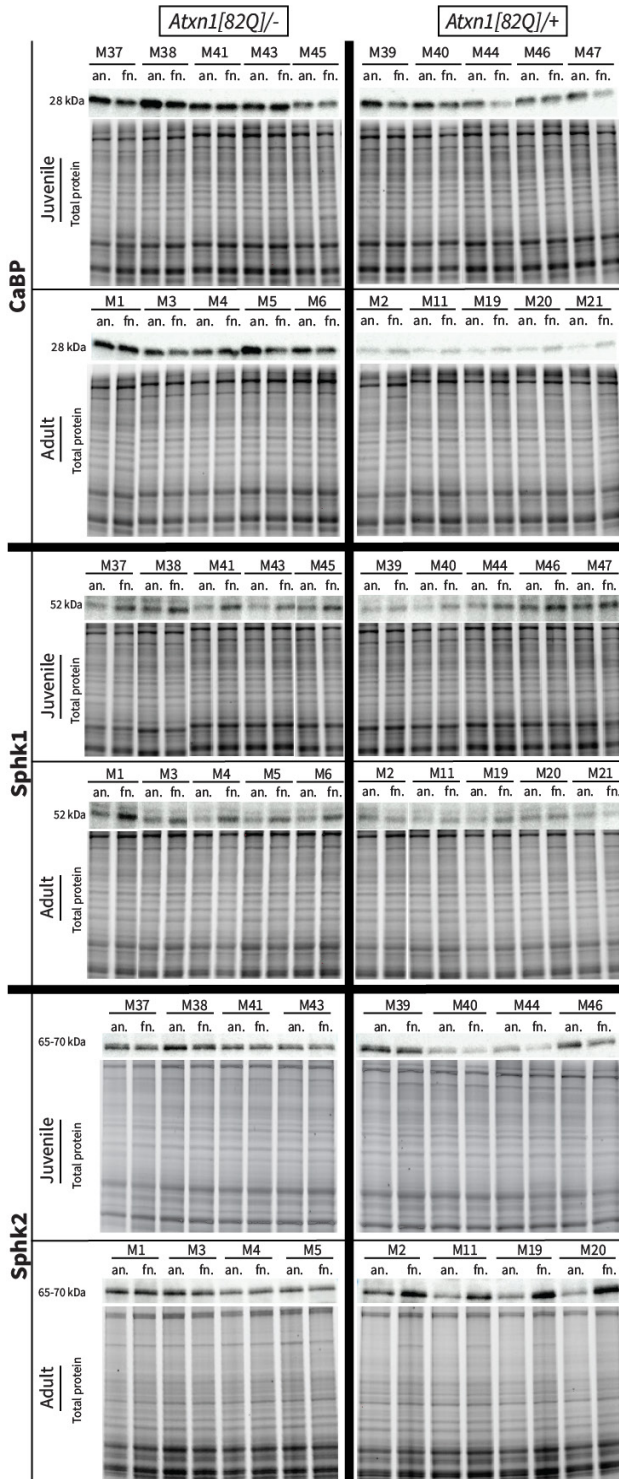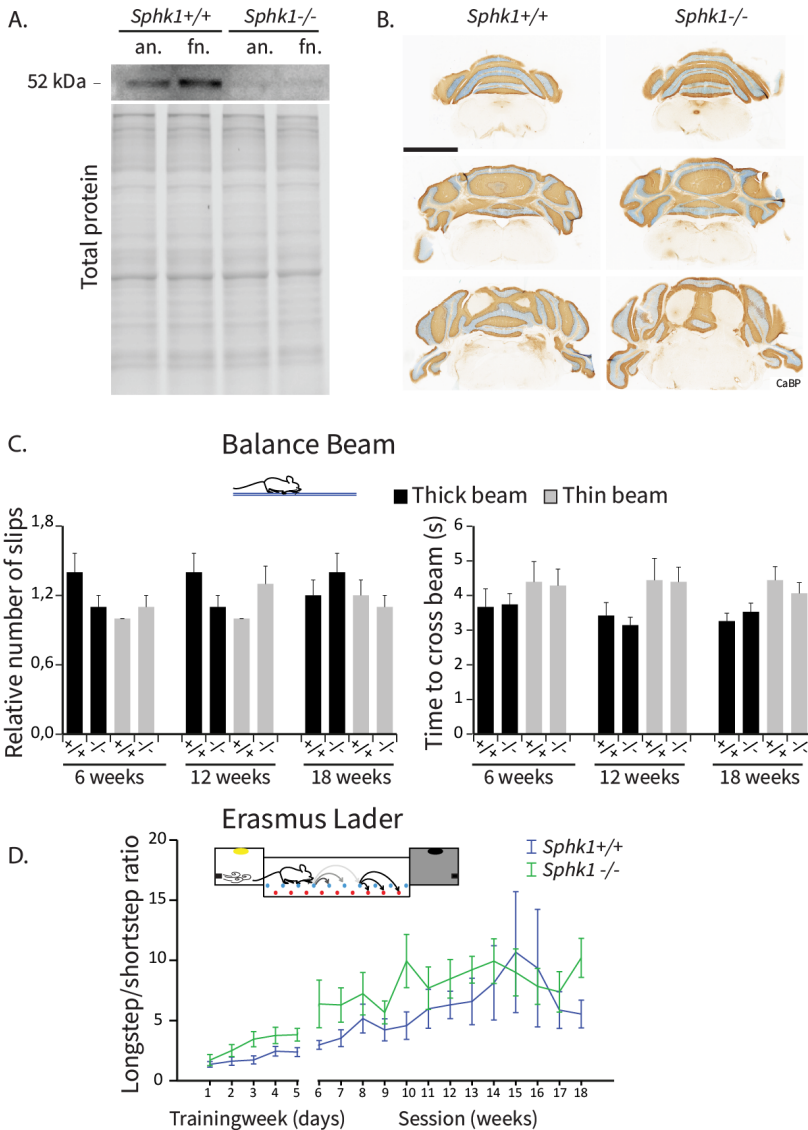
Suppl. Fig 1. Western blotting for CaBP, Sphk1 and Sphk2 proteins.

Western blotting gels for all biological replicates for CaBP (28kDa), Sphk1 (52kDa) and Sphk2 (65-70kDa) proteins, together with total protein migration used for normalization. Four to five mouse (M) were used as biological replicates (M[number]) per age group, per genotype. Atxn1[82Q]/-=wild type (M/38/41/43 for juvenile and M 1/3/4/5/6 for adult); Atxn1[82Q]/+=transgenic mutant (M39/40/44/46/47 for juvenile and M2/11/19/20/21 for adult). Juvenile= P21-23, Adult= P143-153; anterior (an.), flocculo-nodular (fn.).

3.2
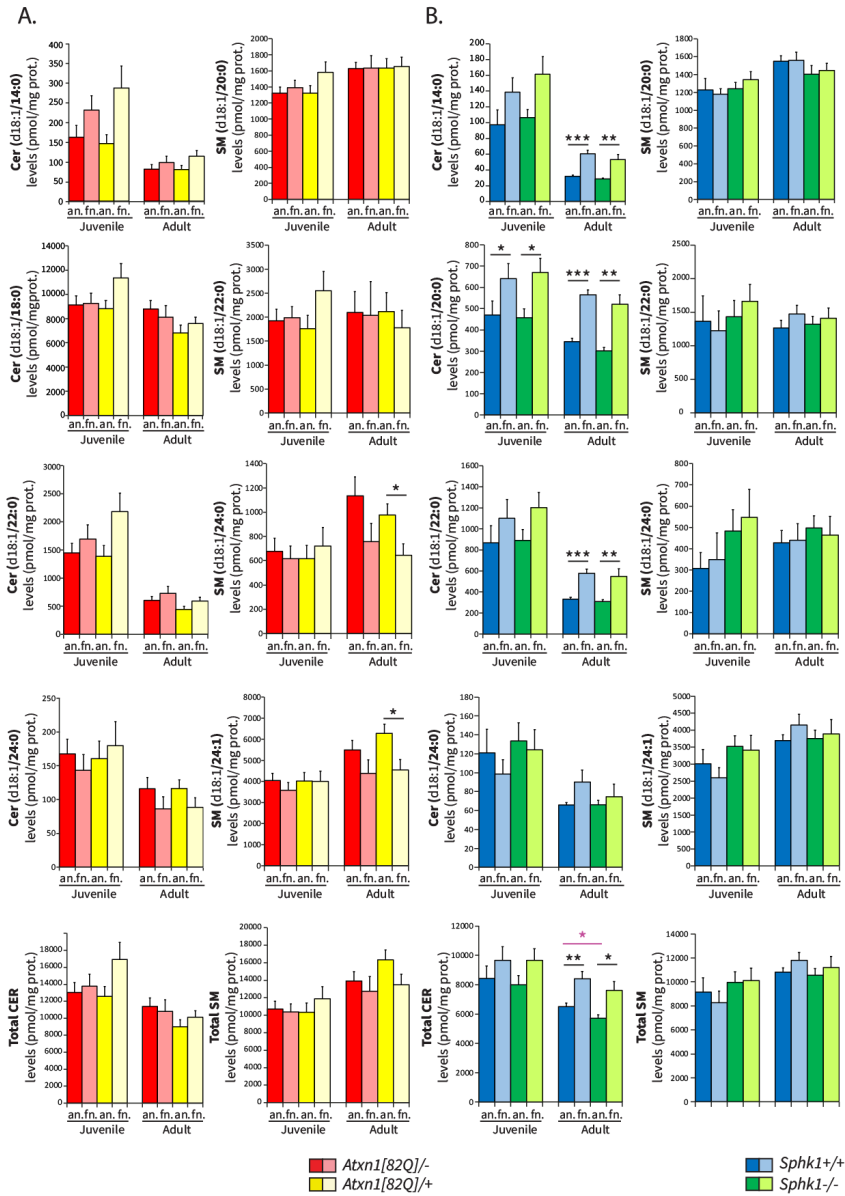
Suppl. Fig 2. Extended list of sphingolipids measured in all experiments.

Bar plot of HP-LC MS/MS quantification of supplementary selected sphingolipid levels in (A) wild type Atxn1[82Q]/- (FVB/N) and mutant Atxn1[82Q]/+ and in (B) wild type Sphk1+/+ (C57BL/6J) and mutant Sphk1-/- . Data are expressed as mean ± S.E.M. (N=10 per group); unit = pmol/mg of protein. Juvenile= P21-23, Adult= P143-153. Black asterisks: significance for anterior (an.) vs. flocculo-nodular (fn.); purple: significant statement for Atxn1[82Q]/- vs. Atxn1[82Q]/+. *p<0.05, **p<0.005, ***p<0.001.

Suppl. Fig. 3. Sphk1-/- mice show normal anatomy and cerebellar function

(A) Western blotting identification of Sphk1 protein in wild type Sphk1+/+ and mutant Sphk1-/- mice, together with total protein migration. (B) CaBP (brown) immunostaining in the adult wild type Sphk1+/+ mice (left panel) and the mutant Sphk1-/- mice (right panel). (C) Balance beam test for both wild type and mutant to measure relative number of slips (left panel) and time to cross the beams (right panel0, for both thin (=6mm, grey) and thick beam (=12mm, black). (D) Erasmus ladder test to evaluate the long-step/short-step ration, for both genotypes. Data are expressed as mean ± S.E.M. *p<0.05, **p<0.005, ***p<0.001.
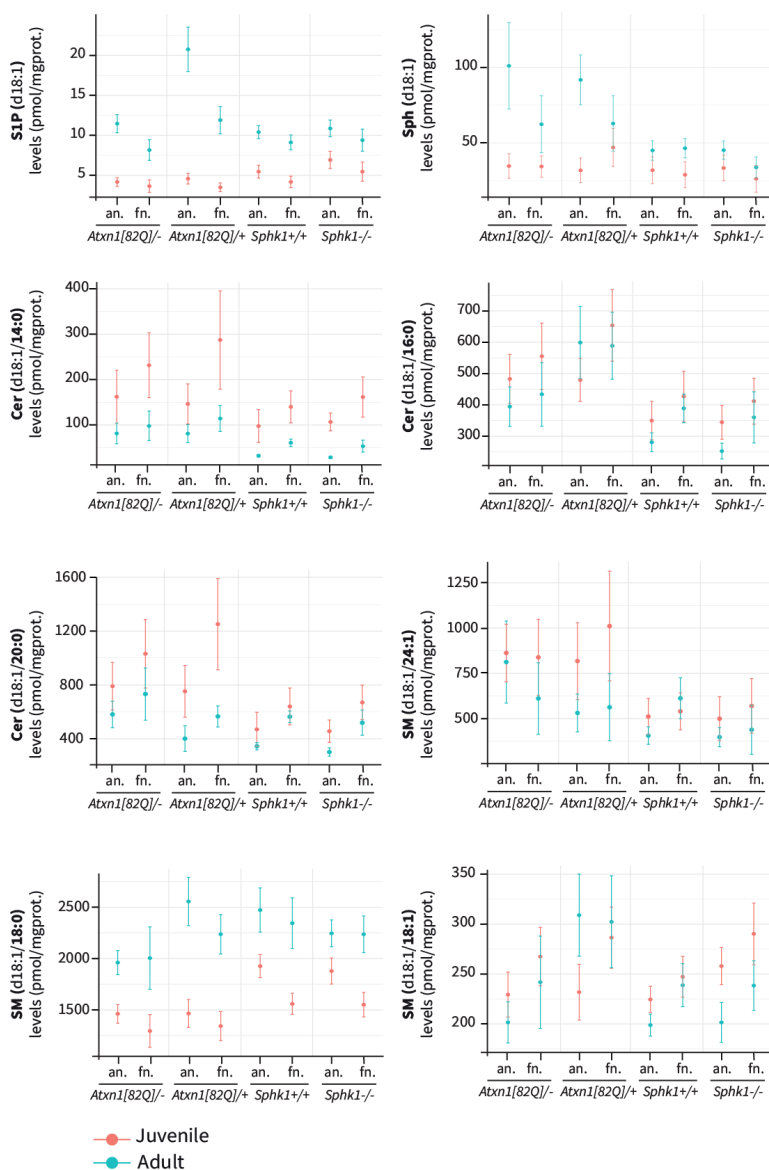
Suppl. Fig. 4. S1P(d18:1) and Sph(d18:1) are the only sphingolipids presenting a multi interaction effect of age*fraction*genotype.

Plot of HP-LC MS/MS quantification of selected sphingolipid levels in all genotypes : wild type Atxn1[82Q]/- and mutant Atxn1[82Q]/+ (in FVB/N background); wild type Sphk1+/+ and mutant Sphk1-/- (in C57BL/6J background). Data are expressed as mean with 95% confidence interval (± 2*S.E.M.) (n=10 per group). Unit = pmol/mg of protein; Juvenile= P21-23 (orange), Adult= P143-153 (blue); anterior (an.), flocculo-nodular (fn.).
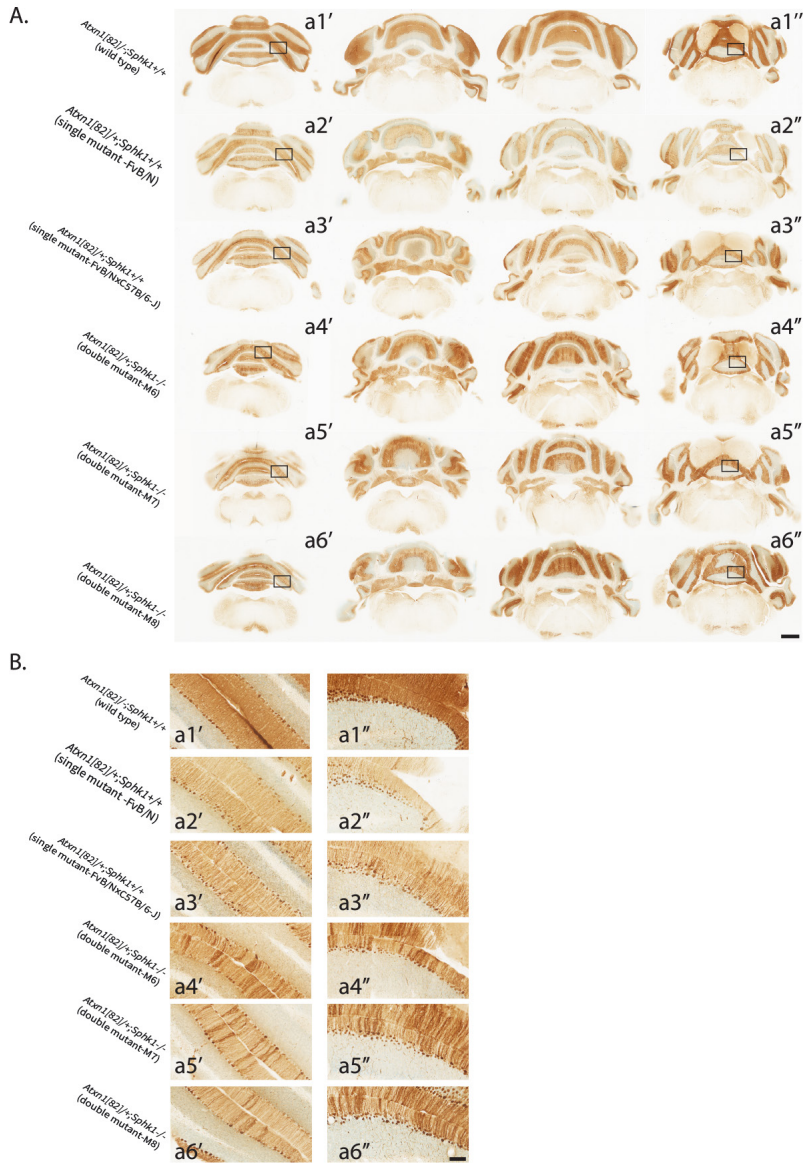
Suppl. Fig5. Sphk1 deletion in the Atxn1[82Q]/+ mice partially rescues PC degeneration

(A) CaBP immunostaining in a wild type Atxn1[82Q]/-;Sphk1+/+ and a single mutant Atxn1[82Q]/+;Sphk1+/+ mouse in the original FVB/N background, a single mutant Atxn1[82Q]/+;Sphk1+/+ mouse, (result of the crossbreeding (FVB/N;C57B/6-J)) and three Atxn1[82Q]/+;Sphk1-/- double mutant mice to show biological replication (#1/2/3) at P140. Scale bar = 1 mm (B) High magnification of dorsal lobule VIII-ventral lobule VII (a1', a2', a3', a4', a5', a6') and dorsal lobule II (a1'', a2'', a3'', a4'', a5'', a6''). Scale bar = 100 μm
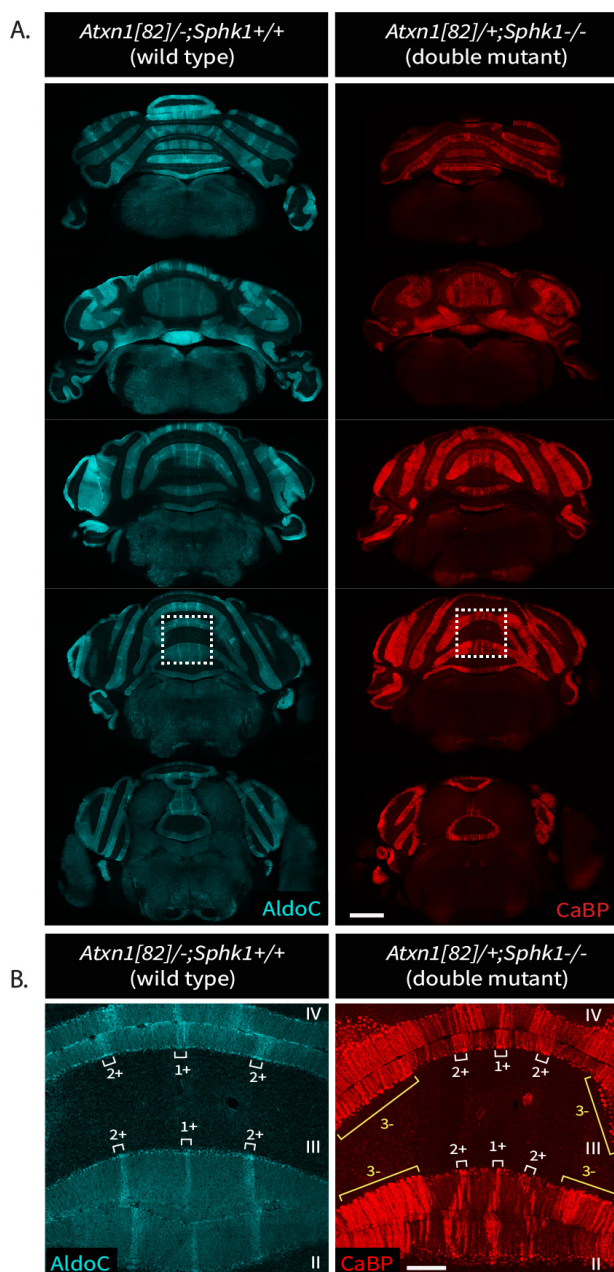
Suppl. Fig 6. Distribution of rescued PC in the double mutant Atxn1[82Q]/+;Sphk1-/- mice partially correlates with AldoC expression pattern. *(A) AldoC (cyan) immunostaining in wild type Atxn1[82Q]/-;Sphk1+/+ mice (left), and CaBP (red) immunostaining in double mutant Atxn1[82Q]/+;Sphk1-/- mice (right), at P140. Scale bar = 1 mm (B) High magnification of vermal lobule II-III-IV. Scale bar = 200 μm.*

Chapter 4

Multi-modular control of the eye movement

François G.C. Blot, Joshua J. White, Amy van Hattem, Vaishnavi Balaji, Licia Scotti, Martijn Schonewille

in preparation

Abstract

The vestibulo-ocular reflex (VOR) has been essential to establish cerebellar and more generally brain processing models. Regarded as a relatively simple system, the diversity of neuronal subtypes and discrete circuitry hidden in the anatomical route of the oculo-motor control are largely underestimated. We investigated the recently identified 9+ and 9- Purkinje cell domains of the flocculus, the cerebellar structure responsible for the learning of VOR adaptation. This novel partition based on the molecular subtypes of the principal neuron of the cerebellum challenge the current models. We demonstrated that 9+ and 9- PCs present distinct molecular and electrophysiological profiles which define PC subtypes has a continuum of variability in gene expression and intrinsic properties. We showed with high cellular specificity that both domains integrate in distinct circuitries established by both afferent and efferent long range projections. Along this study we identified two mutant models that allow targeting of specific PC subtypes which offer new perspectives of anatomical and functional characterization of cerebellar modules.

Introduction

Neuronal types are commonly defined based on morphology, lineage, connections or location within the brain. More recently, the major classes of neurons have been further broken down in subpopulations, as we gained new insight into their molecular identity, electrophysiological properties and refined connectivity (1–4). However, the full representation of the neuronal diversity, and the biological meaning behind the brain's heterogeneity has yet to be elucidated. The cerebellum offers an ideal ground to study the impact of neuronal diversity as local specificities can be directly associated with a motor output. In the cerebellar cortex, aldolase C (AldoC), originally named zebrinII, was one of the first molecular markers found to highlight Purkinje cell (PC) neuronal diversity (5). It currently defines the known PC sub-populations as AldoC-positive and AldoC-negative PCs. A large palette of molecular markers has since been identified to highlight PC sub-populations either identical (EAAT4 (6), PLCB3 (7), Sphk1 (8)), or complementary (PLCB4 (7), mGlur1b (9)), to AldoC defined domains. The two AldoC subpopulations have different firing properties (10), synaptic properties (11), developmental origins (12), and local microcircuitry (13, 14). However, it is important to note that AldoC expression in the mouse cerebellum is not purely binary (15). Several cerebellar modules, including e.g., 3+, 3b+, e1-, e1+, e2+

parasagittal domains, present what can be defined as an intermediate level of AldoC expression. Other molecular markers such as Nfh (16), Hsp25 (17)and TrpC3 (11) further support and expand the idea of higher level of diversity as their expression patterns only partially match the AldoC domains. This leads to the question whether such intermediate populations also differ in the properties mentioned above.

The flocculus is the control centre of two major eye movement reflexes, the vestibulo-ocular (VOR) and the optokinetic reflex (OKR). Assumed to be fully described in its anatomy and function, the flocculus has been essential to theoretical models of cerebellar processing (18–20). In the mouse, the flocculus was found to be organised into five functional micro-zones define by preferred complex spike modulation in response to either optokinetic stimulation along the horizontal axis (zone 1 and 3), stimulation along the vertical axis (zone 2 and 4), or the absence of response to either stimulations (zone C2) (21). They are analogous to the micro-zones described in rat and rabbit, and to a certain extent, the ones described in cat (presenting three more subdivisions) and monkeys (reviewed in (22)). The distinct modulations observed in those micro-zones was attributed to different afferent (olivo-cerebellar) and efferent (cortico-vestibular) projections. Despite the functional and anatomical evidence for the compartmentalisation of the flocculus, the existence of potential PC subpopulations within the flocculus is still debated. The original description of AldoC compartments from Hawkes in 1995 (5), and the first extensive map of Sugihara in 2007 (15), classified floccular PCs as "entirely" AldoC-positive. However, using an AldoC-Venus knock-in mouse line Fujita *et al.* (23) questioned these original descriptions and provided evidence for two micro-domains: the AldoC-positive caudal aspect (9+), and AldoC-negative rostral aspect (9-). As current cerebellar models are based on the uniformity of the floccular cortex, it is essential to understand the extent of the cortical heterogeneity, and its functional relevance.

In this study, we redefine the flocculus as a non-homogeneous structure from the molecular, anatomical and physiological point of view. We identified molecular markers such as the Potassium Channel Tetramerization Domain Containing 12 (KCTD12) and Protein Kinase C And Casein Kinase Substrate In Neurons 2 (Pacsin2), which present an expression profile confirming the existence of the floccular micro-domains recently described, 9+ and 9-. We identified and characterised two mutant Cre lines which allowed gene-based targeting of either 9+ or 9- PCs. We show that these subtypes of PCs present distinct electrophysiological properties and form distinct microcircuits by their afferent and efferent projections.

Material and Methods

Animals:

Sst$^{tm2.1(cre)Zjh}$/J (SST-Cre, Stock #013044), B6.Cg-Tg(Camk2a-cre)T29-1Stl/J (Camk2a$^{Cre/T29}$, Stock #005359, (24)), and B6.129(SJL)-Kcng4$^{tm1.1(cre)Jrs}$/J (Kcng4^{Cre}, Stock #029414, (25)) were purchased from the Jackson Laboratory. As knock-in/knock-out model, we tested the potential effect of reduced Kcng4 expression on cerebellar functions. Tested for rotarod and balance beam test, homozygous carrier of the Kcng4^{Cre} allele (full Knock-out) did not show motor impairments, suggesting no deficits in cerebellar connectivity or physiology. All mice lines were maintained and used as heterozygous line.

Histology:

Animals were deeply anesthetized through intraperitoneal administration of sodium pentobarbital (60mg/ml), directly followed by transcardial perfusion with 4% paraformaldehyde (PFA) in 0.12M phosphate buffer (PB), pH=7.6. Brains were postfixed for 1 hour in 4% PFA at room temperature (rT), transferred to 10% sucrose solution overnight at 4°C. The cerebella were embedded in a 10% gelatine (FUJIFILM Wako Pure Chemicals) 10% sucrose mix, gelatin blocks were incubated in 30% sucrose/10% formaldehyde for 2h at rT and incubated overnight in 30% sucrose at 4°C. Subsequently, coronal or sagittal sections were cut at a 40 μm thickness with freezing microtome. Free-floating sections were rinsed with 0.1M PB and incubated in 10mM sodium citrate (pH6) at 80°C for 2h, for antigen retrieval. Sections were rinsed with 0.1M PB, followed by 3 washes of 10 minutes in Phosphate Buffered saline (PBS). Then, sections were incubated 90 minutes at rT in a solution of PBS/0.5%Triton-X100/10% normal horse serum to block nonspecific protein-binding sites, and incubated 48h at 4°C in a solution of PBS/0.4% Triton-X100/2% normal horse serum (NHS), with primary antibodies diluted as follows: KCTD12 1:500 (rabbit polyclonal, 15523-1-AP, ProteinTech), KCTD12 1:200 (mouse monoclonal, sc-271855, SantaCruz Biotech.), Pacsin2 (mouse monoclonal, sc-390136, SantaCruz Biotech.), AldolaseC 1:500 (goat polyclonal, SC-12065, Santa Cruz Biotech.), PLCB4 1:1000 (rabbit polyclonal, SC-20760, Santa Cruz Biotech.), Hsp25 1:1000 (rabbit polyclonal, SPA-801, Stressgen), Nfh (), SST 1:500 (chicken polyclonal, 366006, Synaptic Systems), NECAB1 1:1000 (rabbit polyclonal, HPA023629, Atlas Antibodies), GFP 1:1000 (chicken

polyclonal, GFP-1020, Aves), RFP 1:1000 (guinea-pig polyclonal, 390005, Synaptic Systems), Parvalbumine 1:7000 (rabbit polyclonal, PV-25, Swant), VGluT2 1:2000 (guinea-pig polyclonal, AB2251-I, Millipore), VGluT1 1:2000 (guinea-pig polyclonal, AB5905, Millipore). After rinsing in PBS, sections were incubated for 2h at rT in PBS/0.4% Triton-X100/2% NHS solution with secondary antibodies coupled with Alexa488, Cy3 or Cy5 (1:200, Jackson ImmunoResearch). Sections were mounted on coverslip in a solution of gelatin/chrome alum and covered with Mowiol (Polysciences Inc.).

<u>Imaging acquisition and processing:</u>

Images were acquired with an upright Imager M2 (Zeiss) equipped with a 10x and 20x lenses, for fluorescent microscopy, and a confocal microscope LSM700 (Zeiss) with upright 20x, 40x and 63x lenses. Images were treated with a Photoshop routine to perfect overall brightness and signal level homogeneously on the pictures, all treatment being equally applied on the entire images. For serial reconstruction we performed identical immunostaining process (fixation, incubation time), identical image acquisition (gain, exposure time, resolution), and identical image adjustment for analysis (brightness and contrast values) per marker, all performed in parallel in a single session for all marker tested.

<u>In vitro slice physiology:</u>

For in vitro recordings, a total of 18 C57BL/6J mice from 30 to 60 days were deeply anesthetized with isoflurane and decapitated. As previously described (Beekhof *et al.*, 2021), the brain was quickly extracted and placed in ice-cold slice solution continuously carbogenated with 95% O_2 and 5% CO_2 containing the following (in mM): 240 Sucrose, 2.5 KCl, 1.25 NaH_2PO_4, 2 $MgSO_4$, 1 $CaCl_2$, 26 $NaHCO_3$, 10 D-glucose. 250-µm-thick coronal cerebellar slices were cut in ice-cold slice solution using a vibratome (VT1000S, Leica Biosystems, Wetzlar, Germany) with a ceramic blade (Campden Instruments Ltd, Manchester, United Kingdom). Slices were transferred to a recovery bath and incubated in continuously carbogenated artificial cerebrospinal fluid (ACSF) containing (in mM): 124 NaCl, 5 KCl, 1.25 Na_2HPO_4, 2 $MgSO_4$, 2 $CaCl_2$, 26 $NaHCO_3$, 20 D-glucose and maintained at 34°C for one hour before being transferred to room temperature. For recording, individual slices were transferred to a recording chamber and maintained at 34±1°C with a feedback temperature controller (Scientifica, Uckfield, United Kingdom) under continuous perfusion with the carbogenated

ACSF. Slices were bathed with ACSF supplemented with synaptic receptor blockers, NMDA receptor antagonist D-AP5 (50 μM, Hellobio, Bristol, UK), selective and competitive AMPA receptor antagonist NBQX (10 μM, Hellobio, Bristol, UK), non-competitive GABAA receptor antagonist and glycine receptor inhibitor Picrotoxin (100 μM, Hellobio, Bristol, UK). PCs were visualized with SliceScope Pro 3000, a CCD camera, a trinocular eyepiece (Scientifica, Uckfield, UK) and Ocular (Teledyne Qimaging, Surrey, Canada). Whole-cell and cell attached recordings were obtained using borosilicate pipettes (Harvard apparatus, Holliston, MA, USA) with a resistance of 4-6 MΩ, filled with internal solution containing (in mM): 9 KCl, 3.48 $MgCl_2$, 4 NaCl, 120 K+-Gluconate, 10 HEPES, 28.5 Sucrose, 4 Na_2ATP, 0.4 Na_3GTP in total pH 7.25-7.35, osmolarity 290-300 mOsmol/Kg (Sigma-Aldrich, Merck KGaA, Darmstadt, Germany) and 1 mg/ml biocytin. Recordings were performed using an ECP-10 amplifier (HEKA Electronics, Lambrecht, Germany) and digitized at 20 kHz. Acquisition was done in Patchmaster (HEKA Electronics, Lambrecht, Germany) and ABF Utility (Synaptosoft, Fort Lee, NJ, USA) was used to convert the Patchmaster files for analysis. Clampfit 10 (Molecular Devices, LLC, San Jose, USA) was used to analyze spikes and a custom-build MATLAB code (Mathworks, Natick, MA, USA) using inter spike properties was used to analyze spike variables. After recording, slices were transferred to 4% paraformaldehyde for at least 24h followed by successive washes of 0.1M PB before going through standard immunohistological protocol.

Stereotaxic injections:

For stereotaxic injections of Adeno-Associated Virus (AAVs) in the mouse flocculus, animals were anesthetized with a mixture of isoflurane/oxygen (5% for induction, 1.5–2.0% for maintenance), while carprofen (Rimadyl Cattle i.p. 5 mg/kg), buprenorphine (Temgesic, i.p. 0.05 mg/kg), lidocaine (s.c. 0.4 mg/ml) and bupivacaïne (s.c. 0.1 mg/ml) were applied to reduce perisurgical pain. Ophthalmic ointment was applied to the eyes to prevent corneal drying and damage. Body temperature was monitored and kept constant at 37 °C throughout the entire surgical procedure. Mice were positioned on a custom-made mouse stereotaxic frame with a mouse gas anesthesia head holder (David Kopf Instruments, model 933-B). After removal of the scalp a craniotomy (diameter ~1.5 mm) was made onto the interparietal bone. A micromanipulator was used to direct a glass pipette (Hirschmann® microcapillary pipette, Z611239) of 20-30 μm internal tip diameter, based on coordinates established from the Paxinos mouse brain atlas (Paxinos & Franklin, 2001), as following: 5.2mm from Bregma, 39° angle from the vertical axe at the midline, going 4.6

and 4.8mm deep. One injection of 50 to 60 nL was performed at each depth with mechanical pressure (~10 nl/s). After each injection, the pipette was left in place for >10 min before being slowly withdrawn. Anterograde tracing was performed using AAV1-CAG-Flex-TdTomato (lot #AV5328A2) and rAAV5-CAG-ChR2-GFP (lot #AV4597D) at a ratio 1:1, purchased from University of North Carolina (UNC) Vector Core. Retrograde tracing was performed with pAAV-CAG-FLEX-rc [Jaws-KGC-GFP-ER2] (Addgene, Catalog No. 84445-AAVrg). Post-injection survival times for injected mice were 2–3 weeks.

Results

Identification of novel markers to discriminate 9+and 9- domains of the flocculus:

The commonly described AldoC compartments in the flocculus have been recently questioned (23). In order to bring precision on the nature of 9+ and 9- domains, we aimed to elaborate on their respective molecular profiles. In our hands, immunostaining for AldoC or PLCB4 proteins do not clearly and systematically reveal 9+ and 9- domains. We then screened for molecular markers drawing similar compartments in the flocculus giving high reproducibility and accuracy. Using the Allen Brain Atlas *in situ* hybridization data base, we identified candidate markers such as Potassium Channel Tetramerization Domain Containing 12 (KCTD12), Calcium Binding Protein 7 (Cabp7), and Carbonic Anhydrase 7 (Car7), all markers with higher mRNA levels in PCs located in the caudal half of the flocculus, possibly demarcating the 9+ domain (Fig. 1A-C). In contrast, Protein Kinase C And Casein Kinase Substrate In Neurons 2 (Pacsin2), Semaphorin-3A (Sema3A), and Fatty Acyl-CoA Reductase 2 (Far2), showed a complementary pattern, with higher mRNA levels in the PCs located in the rostral half of the flocculus, potential 9- domain (Fig. 1E-G). Immunolabelling of KCTD12 and Pacsin2 proteins validated the *in situ* hybridisation data and showed the existence of two complementary PC subpopulations in the flocculus, with a caudal KCTD12-positive/Pacsin2-negative PC group (Fig. 1D$_{1-2}$ and H$_{1-2}$), and a rostral KCTD12-negative/Pacsin2-positive PC group (Fig. 1D$_{3-4}$ and H$_{3-4}$). As the subpopulations are allocated along the rostro-caudal axes, the demarcation between groups is easily identifiable in the sagittal orientation. Sagittal serial sections confirmed the presence of two domains in the flocculus, a caudal KCTD12-positive (KCTD12+) domain, and a rostral KCTD12-negative (KCTD12-) domain (Fig. 2A). The flocculus extends latero-caudally and as a result of this complex 3D structure, the most lateral aspect of the flocculus, or apex, is the most caudal part, while the medi-

al aspect, or base, is the most rostral. The most lateral part of the flocculus is mainly populated by KCTD12+ PCs (Fig. 2A$_1$), while the most medial aspect is predominantly populated by KCTD12- PCs (Fig. 2A$_6$). To investigate how these domains relate to the previously described 9+ and 9- domains, we compared this pattern of expression with markers previously used to define cerebellar domains: AldoC and PLCB4. In the lateral aspect of the flocculus, AldoC did not show a clear delineation of PC domains (Fig. 2B$_{1-3}$, purple arrows indicate the expected borders based on KCTD12 expression), while in the medial aspect the contrast in immunoreactivity allowed for the discrimination of the two domains (Fig. 2B$_{4-6}$), with a relatively higher level of AldoC expression in the caudal part of the flocculus compared to the rostral part (white arrows indicate borders defined by AldoC matching with KCTD12 borders). To confirm this, we immunolabelled PLCB4 protein and showed that floccular compartments drawn by PLCB4 perfectly complement KCTD12 compartments, defining a PLCB4+/ KCTD12- rostral domain and a PLCB4-/KCTD12+ caudal domain (Fig. 2C$_{1-6}$, white arrows). The similar borders drawn by KCTD12, AldoC and PLCB4 expression support the conclusion that KCTD12 compartments correspond to 9+ (KCTD12+) and 9- (KCTD12-) domains as described by Fujita *et al.* (23). Whereas the contrast in the delineation of 9+ and 9- with AldoC or PLCB4 immunostaining was very sensitive to the quality of the immunohistological preparation (perfusion, antigen retrieval, quality of antibody) in our hands, KCTD12 immunolabelling offered a more reliable method to discriminate 9+ and 9-. It was previously shown that AldoC or PLCB4 do not depict the full extent of PC molecular diversity as proteins like Hsp25 or Nfh are also expressed in distinct cerebellar compartments. Hsp25 was shown to be expressed in a subset of AldoC+ PCs, making it the first molecular marker to discriminate PC subpopulations in the flocculus (17, 26). While in the medial aspect of the flocculus Hsp25 immunoreactive PCs match the KCTD12 expression pattern (Fig. 2A$_6$, B$_6$, D$_6$; white arrows), the domains defined by Hsp25 and KCTD12 are clearly distinct more laterally, toward the apex of the flocculus (Fig. 2A$_{1-5}$-D$_{1-5}$, purple arrows). Thus, Hsp25+ PCs in the flocculus represent a subpopulation of KCTD12+ PCs. Nfh expression pattern in PCs was showed to be complementary to AldoC expression in the anterior (lobules I-V) and posterior (lobules VIII and anterior IX) cerebellum, while being complementary to Hsp25 expression in the central (lobules VI-VII) and nodular (lobules posterior IX-X) cerebellum (27, 28). In the flocculus, we observed that Nfh expression pattern perfectly overlaps with PLCB4 expression (Fig. 2E$_{1-6}$). Thus, Nfh expression is complementary to KCTD12 expression, not complementary to Hsp25 expression, exclusively labelling the 9- domain. Overall, known markers for cerebellar differentiation are expressed in patterns that match the subdivision of the floc-

culus 9+ and 9- domains (Fig. 2F). However, where Fujita and colleagues describe 9- domain as AldoC-, our results indicate that 9- domain express an intermediate level of AldoC. We compared the relative changes in AldoC expression between the lobule IX (1+/2+/3+ versus 1-/2- domains) and the flocculus (9+ versus 9- domains) based on fluorescent intensities. The sharp contrast of relative fluorescent changes observed in lobule IX between juxtaposed positive and negative domains was less pronounced in the flocculus (Fig. 2G, red curves). In comparison, KCTD12 immunostaining has identical contrast between juxtaposed positive and negative domains of the lobule IX, and the flocculus. This low contrast of AldoC expression between 9+ and 9- in the flocculus not only explained the complexity in identifying these domains, but also questions if 9- domain should classified as an AldoC- domain simi-
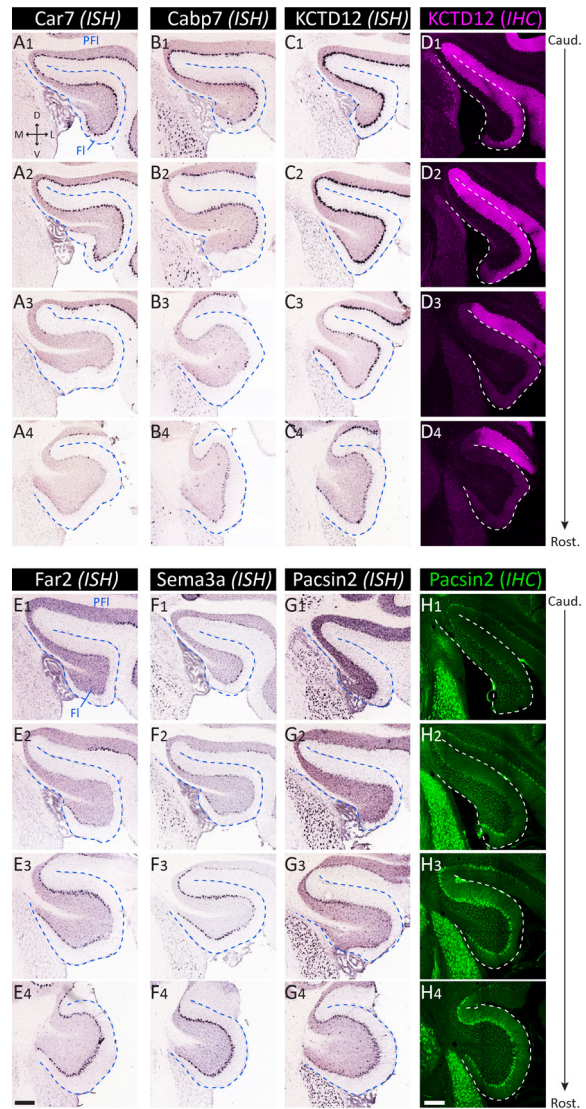
Fig. 1 Identification of domains in the flocculus based on PC molecular identity.

(A-C & E-G) Serial images of in situ hybridization (ISH) on coronal sections of the flocculus (blue dashed line) from the Allen Brain Institute for Car7 (Exp. #74511736), Cabp7 (Exp. #73930835), KCTD12 (Exp. #73520993), Far2 (Exp. #71358652), Sema3a (Exp. #79591337), and Pacsin2 (Exp. #74047920). Section go from caudal (Caud.) to rostral (Rost.) (1→4). Scale Bar = 210µm. (D & H) Serial images of maximum intensity projections of confocal images of the flocculus (white dashed line) following immunohistochemistry (IHC) with anti-KCTD12 (D) or anti-Pacsin2 (H) antibodies. Scale Bar = 200µm. Thickness = 40 µm PFl=paraflocculus; Fl=flocculus; D=dorsal; V=ventral; M=medial; L=lateral

lar to 1- or 2-, or corresponds to a domain of intermediate expression such as 3b+, e1-, e1+, e2+ parasagittal domains (15).

9+ and 9- PCs manifest distinct intrinsic physiological properties:

We next aimed to further investigate the properties of PCs with an intermediate expression of AldoC in the 9- domain of the flocculus. Based on work demonstrating physiological differences between AldoC+ and AldoC-
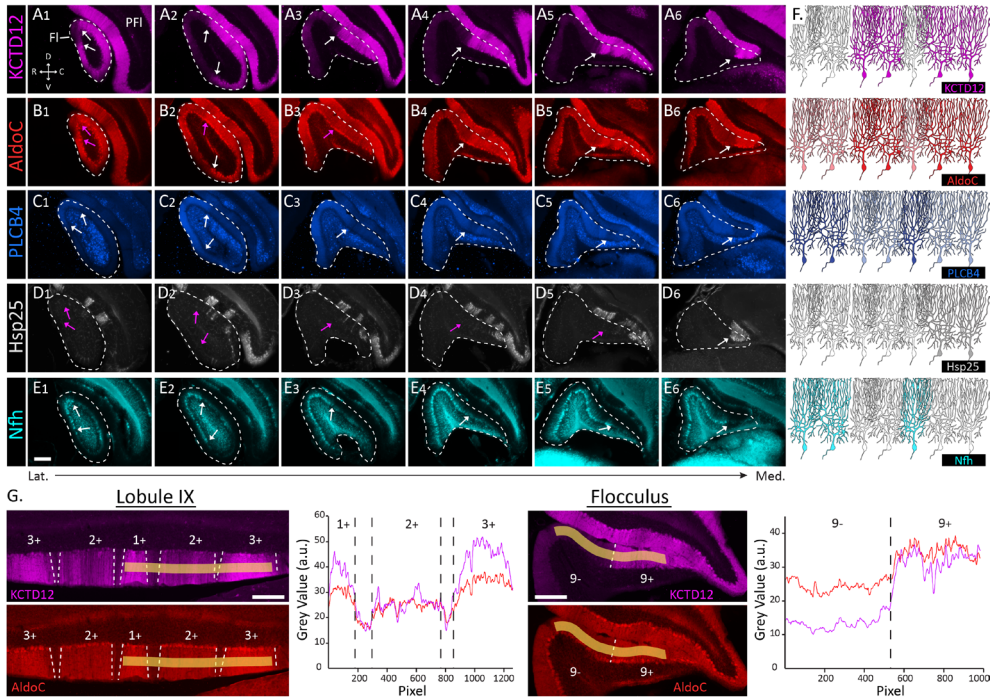
Fig. 2 Comparison of KCTD12 defined domains with known patterning markers.

(A-E) Serial sagittal sections of the flocculus (white dashed line) with KCTD12 (A), AldoC (B), PLCB4 (C), Hsp25 (D), or Nfh (E) immunolabeling. KCTD12 and AldoC were co-immunolabeled while all other proteins were immunolabeled on independent brain series from the same animal. White arrows point at defined boundaries identified in KCTD12 immunostaining and observed with other markers. Purple arrows point at defined boundaries identified in KCTD12 immunostaining but not observed with other markers. Lateral (Lat.) to medial (Med.) (1-6). Scale Bar = 200µm. (F) Schematic representation of differential protein expression among PC subpopulations. (G) Relative signal intensity of KCTD12 (purple curve) and AldoC (red curve) expression along a region of interest (yellow trace) in the molecular layer of lobule IX (coronal) and the flocculus (sagittal). Scale Bar = 200µm. Thickness = 40µm. PFl=paraflocculus; Fl=flocculus; C=caudal; R=rostral; D=dorsal; V=ventral.

domains in the cerebellum as a whole (10, 29, 30), we examined if there are intrinsic firing differences between the highly expressing AldoC+ PCs of the flocculus and the intermediate AldoC PCs. We used ex vivo slice physiology to compare PCs from these two regions of the flocculus, using KCTD12 as the identifying marker (Fig. 3A). Additionally, to contextualize the physiological characteristics, we recorded PCs from the anterior vermis and lobule X, which have been used in previous studies as proxies for AldoC- and AldoC+ populations, respectively. We first recorded spontaneous firing of PCs in the cell-attached configuration in acute cerebellar slices with synaptic transmission blocked. These recordings demonstrated that indeed there are differences in PC activity between these regions of the flocculus identified by KCTD12 labelling and anatomical location (Fig. 3B-C). These distinctions were observable irrespective of the presence of synaptic blockers. Specifically, KCTD12- PCs fire at a higher rate with a lower regularity that KCTD12+ floccular PCs (61.95 ± 3.03 vs 43.38 ± 3.79; p = 0.0005) but with the same regularity. This relationship is reminiscent of the relationship between AldoC- and AldoC+ PCs reported in previous studies (10). Comparing the floccular recordings to recordings we attained in lobules III and X of the vermis, we found that the flocculus as a whole had lower firing rate and was more regular than the anterior vermis, despite the intrafloccular differences (Fig. 3C). This suggests that there is a correlative relationship between these firing characteristics and AldoC expression levels, i.e. intermediate expression of AldoC correlates with intermediate firing frequency and regularity. This same relationship was confirmed by whole cell recordings where spiking was driven with current injection steps. KCTD12- PCs are more excitable than KCTD12+ but not as excitable as PCs in the anterior vermis (Fig. 3D-E). These intrinsic physiological properties combined with the anatomical evidence presented above strongly suggest an intermediate zone within the flocculus, at midway between the commonly described AldoC+ and AldoC-. We next asked to what extent these zones are discretely connected to afferent and efferent extracerebellar nuclei.

9+ domain receives a unique SST28+mossy fiber input from the Pr and MVeMC:

Cortical compartments defined by PC sub-populations are known to correlate with topographical distribution of mossy fiber (MF) afferents identified through anatomical tracing (16, 31–33) as well as molecular markers (SST28 (34), CRF (35), Enkephalin (36), Calrt (37), VGluT1/2 (38)). In the vermis, the SST28 peptide was described to be expressed in a restricted subset of MFs primarily distributed in the cortical domains defined by HSP25 immuno-reactive PCs. Co- and serial immunostaining showed that in the
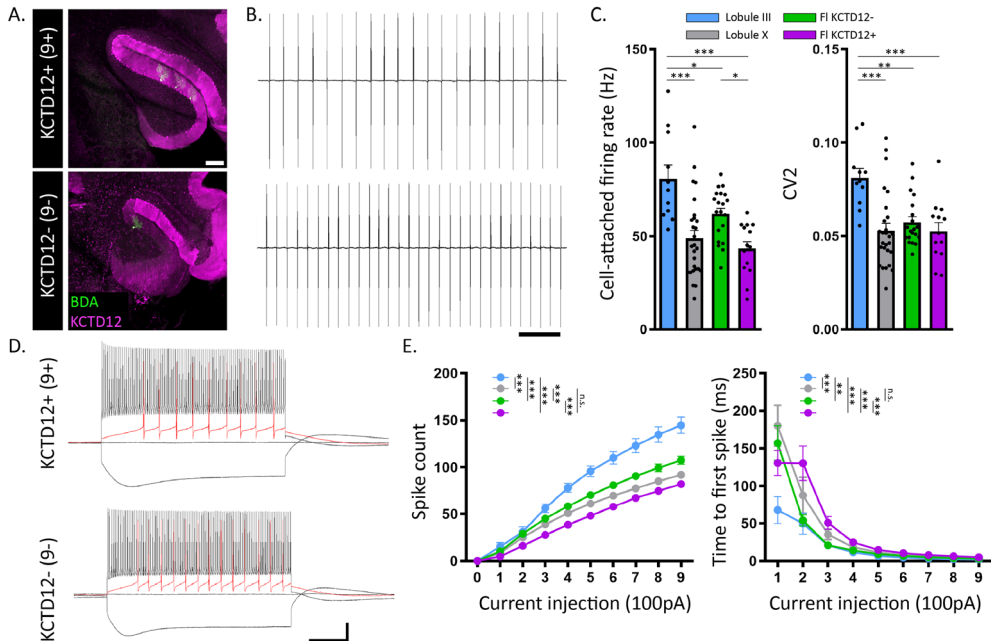
Fig. 3 Intrinsic physiological properties of 9+ and 9- domains.

*(A) Example biotin-filled Purkinje cells in different regions of the flocculus. KCTD12 border indicated with white arrow. Scale bar = 200 μm. (B) Example cell-attached recordings from KCTD12- (top) and KCTD12+ (bottom) Purkinje cells. Scale bar= 100ms. (C) Summary data of firing rate and CV2 from Purkinje cells from Lobule III, Lobule X, KCTD12- flocculus and KCTD12+ flocculus. (D) Example traces from current injections steps. Black traces indicate -600 (bottom) and +900 (top) pA current injections around holding current. Red trace indicates +100 pA current injection. Scale bar= 100ms/20mV (E) Summary data of current injection steps from Purkinje cells from Lobule III, Lobule X, KCTD12- flocculus and KCTD12+ flocculus. Left graph displays the average number of spikes in response to a 500 ms current pulse from +100 to +900 pA. Right graph displays the average time to the first spike at each of the current injection steps. PFl = paraflocculus, Fl = flocculus, Bs = brainstem. ***: p < 0.001, **: p < 0.01; *: p < 0.05..*

flocculus the SST28+ MF territory extends throughout KCTD12+ domain (Fig. 4A, purple and white arrows), while being more densely present in the HSP25+ domain (Fig. 4A, white arrows). At the transition from 9+ to 9- domain, SST28+ MFs were sparse (Fig. 4A green arrow), and become absent towards the rostral aspect of the flocculus. To investigate the origin(s) of these afferent projections, we screened pre-cortical nuclei for SST28+ somata and found positive neurons in the white matter of the flocculus, in the nucleus Prepositus Hypoglossi (Pr), the parvicellular medial vestibular nucle-
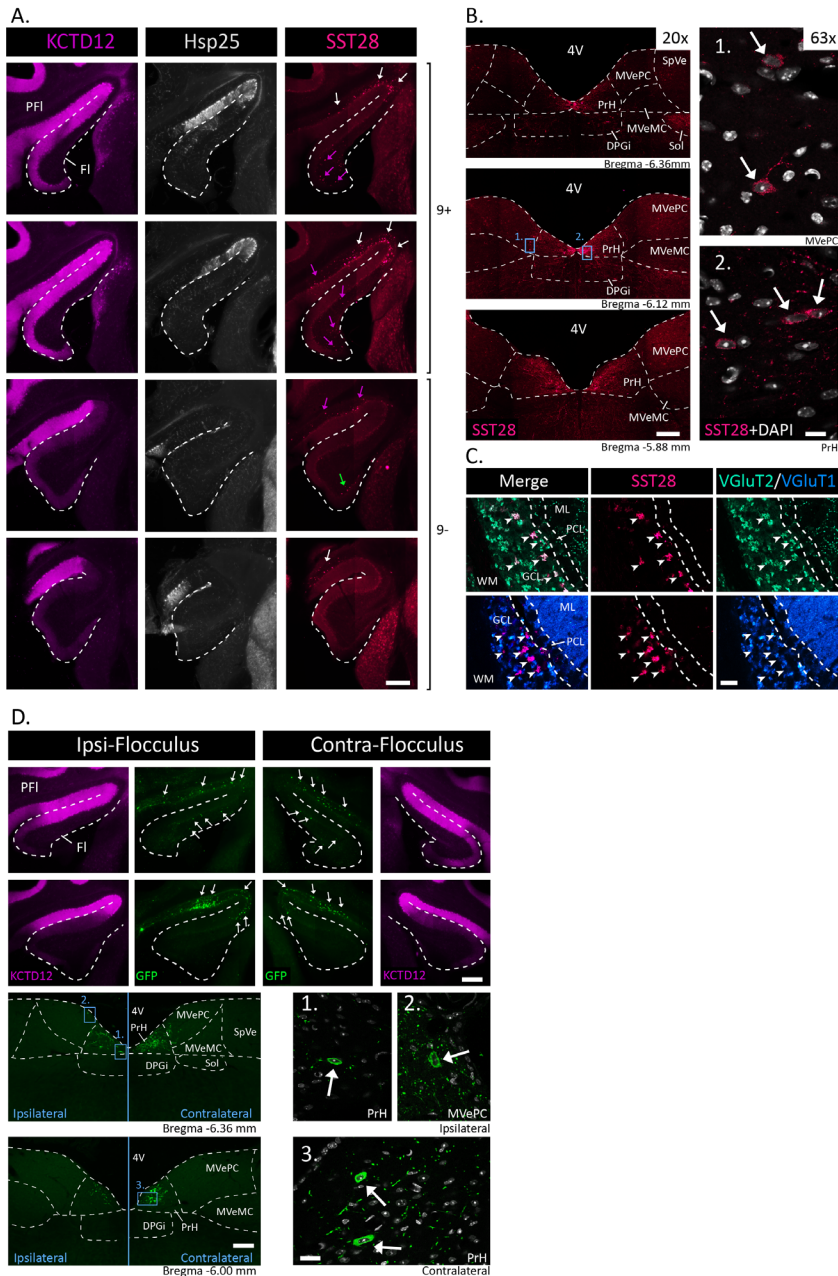
Fig. 4 SST28+ MFs define a circuit restricted to 9+ domain.

(A) Serial transverse sections of the flocculus (white dashed line) with KCTD12, Hsp25, and SST28 immunolabeling. SST28+ MFs are present in Hsp25+ domain (white arrows), KCTD12+ domain (white + purple arrows) and KCTD12- domain (green arrow). Scale Bar = 200μm. (B) SST28 immunoreactivity in the dorsal brainstem, with

SST28+ cells in the MVePC (1.) and the Pr (2.). Scale Bar 20x = 200μm. Scale Bar 63x = 10μm. (C) Characterization of SST28+ MFs molecular identity with co-labeling with VGluT1 or VGluT2 vesicular transporters. Scale Bar = 20μm. (D) Unilateral injection of retrograde AAV (pAAV-CAG-FLEX-rc [Jaws-KGC-GFP-ER2]) in the flocculus of SST^Cre mice showed labelled MFs restricted to the KCTD12+ domain in both ipsi- and contralateral flocculus, and retrogradelly labeled neurons in ipsi- and contralateral Pr (1. And 3.) and MVePC (2.). Scale Bar Flocculus= 200μm; Scale Bar Brain Stem 20x= 200μm; Scale Bar Brain Stem 63x= 20μm. PFl=paraflocculus; Fl=flocculus; PrH=nucleus prepositus hypoglossi; MVePC=medial vestibular parvicellular; MVeMC=medial vestibular magnocellular; SpVe=spinal vestibular; DPGi=dorsal paragigantocellular nucleus of the reticular formation; Sol=solitary nucleus; 4V=fourth ventricle; ML=molecular layer; PCL=Purkinje cell layer; GCL= granular cell layer; C=caudal; R=rostral; D=dorsal; V=ventral

us (MVePC), the spinal vestibular nucleus (SpVe), and the dorsal paragigan-tocellular reticular nucleus (DPGi) (Fig. 4B). Co-immunostaining for SST28 and NECAB1 showed that SST28+ somata in the floccular white matter cor-respond to neurons of the Basal Interstitial Nucleus of the cerebellum (BIN) (39), a population of inhibitory neurons projecting to the floccular GCL. In that same study we also found that the flocculus does not receive afferent input from the DPGi. SST28+ MFs are exclusively VGluT2+/VGluT1- (Fig. 4C), which is in accordance with the known expression of the glutamate transport-ers in Pr, SPVe and MvePC neurons (40), suggesting that SST28+ MFs orig-inate from either one or several of these nuclei. To validate our hypothesis, we injected a retrograde AAV carrier of an inversed GFP sequence flanked with loxP sites, pAAV-CAG-FLEX-rc [Jaws-KGC-GFP-ER2] unilaterally into the flocculus of an SST-Cre transgenic mouse line, to exclusively label the SST28+ MFs terminals present in the flocculus (n=2). We observed GFP-la-belled MFs distributed in a pattern identical to SST28 immunoreactive MFs in both the injected flocculus and the contra-lateral non-injected flocculus (Fig. 4D). We identified GFP+ somata in throughout the Pr and the dorsal aspect of MVePC, both ipsi- and contralaterally, with no other GFP labelled cells observed in the the SpVe or any other brain region. These data showed that SST28+ population of neurons in the PrH and MVePC project specifically and bilaterally to the 9+ domain of the flocculus.

Identification and characterisation of two transgenic lines to genetically tar-get 9+ and 9- domains:

Studies of cerebellar microcircuitry have so far been limited by the spa-tial resolution needed to target restricted subpopulations of PCs. Transgenic Cre

lines have been proven to be the most precise and reliable tool to target individual cellular populations. However, there is, to our knowledge, no transgenic Cre line identified that allows to specifically target subsets of PCs. We have used open access data-bases to identify candidate transgenic Cre lines that would allow for the genetic targeting of PC subsets. The manual screening included the databases of the Allen Brain institute, the Gene Expression Nervous System Atlas (GenSat) project of the Rockefeller University, and the Mouse Genome Informatics (MGI) of Jackson Laboratory. Based on these datasets, we selected two mouse lines: CaMKIIα$^{Cre/T29}$, a transgenic model of Cre recombinase expression under the control of the calcium/calmodulin-dependent protein kinase II alpha promoter (CaMKIIα, (24)), and Kcng4^{Cre} , a knock-in/knock-out model of Cre recombinase expression under the control of the endogenous promoter of the potassium voltage-gated channel modifier subfamily G member 4 (Kv6.4, (25)). To test the spatial expression pattern of Cre, both lines were crossed with the Ai14 mouse line, in which Cre recombinase activity drives the expression of the reporter protein TdTomato. In the cerebellum of the CaMKIIα$^{Cre/T29}$xAi14 mice, TdTomato expression revealed organised clusters of PCs in lobule VI, ventral lobule IX and lobule X, lobule simplex, anterior Crus1, ventral Paraflocculus, and Flocculus (Fig. 5A$_{1-6}$). Previous immunohistological studies on CaMKIIα expression in the cerebellum reported an homogeneous expression of the protein in all PCs (41, 42). However, the CaMKIIα-GFP reporter line presented by Wang *et al.* (43) shows an uneven distribution of GFP+ PCs which predominantly populate the posterior cerebellum (lobules IX and X), but are essentially absent in the anterior lobules. These diverging results question possible artefactual expression in transgenic lines due to the transgene construct, insertion and/or copy number. Nevertheless, the Cre-expression pattern appeared identical in all biological replicates (n=4), and match with the images in the GenSat database, demonstrating a stable and reproducible targeting of specific PC clusters. To assess if these clusters represent biologically relevant subpopulations of PCs, we performed co- and serial-immunostainings with anti-Hsp25 or anti-KCTD12 antibodies on CaMKIIα$^{Cre/T29}$xAi14 brain sections. In ventral lobule IX and lobule X TdTomato+ PC clusters match with the Hsp25-immunoreactive PCs and high KCTD12-immunoreactive domains (Fig. 5A$_{1-4}$, B$_{1-4}$ and C$_{1-4}$). In the paraflocculus, Cre-expression correlates with Hsp25+ domains but not KCTD12+ defined domains (Fig. 5A$_{4-5}$, B$_{4-5}$ and C$_{4-5}$). In lobule simplex and anterior Crus1, TdTomato+ PC clusters did not correspond to either Hsp25+ or KCTD12+ domains (Fig. 5A$_{5-6}$, B$_{5-6}$ and C$_{5-6}$). Finally, in the flocculus we observed that TdTomato+ PCs overlap with the KCTD12+ domain, which represent a larger PCs group than the Hsp25+ PCs (Fig. 5A$_5$, B$_5$, C$_5$ and 6A). Besides these clusters, we observed in the CaMKIIα$^{Cre/T29}$xAi14 a sparse and random distribution of TdTomato+ PCs

all over the cerebellum which did not match with any known PC subpopulation markers, and occasionally labelled Golgi or other interneurons. In the cerebellum of the Kcng4[Cre]xAi14 mice, we observed expression of TdTomato in a large group of PCs. The distribution of TdTomato+ PCs revealed clusters primarily complementing the AldoC expression pattern (Fig. 5E$_1$ and F$_1$). However, we observed in lobule X that TdTomato expression complemented KCTD12 expression and not AldoC expression, as KCTD12 labelling and Td-Tomato expression revealed parasagittal domains in the dorsal lobule X not observed with AldoC immunostaining (Fig. 5C$_3$, E$_3$ and F$_3$). Same observation was done in the ventral lobule IX at the 2+ domain, appearing AldoC+ while being essentially Kctd12- and TdTomato+ (Fig. 5C$_2$, E$_2$ and F$_2$). In the flocculus, we observed a differential expression of TdTomato between the caudal and rostral aspects, matching 9+ (TdTomato-) and 9- (TdTomato+) domains (Fig. 5E$_{5-6}$ and 6A). The observed expression profile may more reliably reflect the expression of Kcng4 protein as the model is a knock-in, and the patterned expression of kcng4 was previously suggested in Rodriques *et al.* (44). In addition to the expression in PCs, a population of small TdTomato+ neurons was found in the molecular layer, which we identified as a subset of molecular layer interneurons (MLI) based on their immunoreactivity for Parvalbumine (Parv) (Suppl. Fig. 1; white arrows). TdTomato+/Parv+ neurons were distributed homogeneously along the cortex in the lower half of the ML. The upper half presented TdTomato-/Parv+ interneurons (Suppl. Fig. 1A; red arrow heads), suggesting that TdTomato+/Par+ interneurons are predominantly Basket cells (45). In line with this hypothesis, we found TdTomato+ pinceau-like structures enwrapping all PC somata (Suppl. Fig. 3B), which leaded us to conclude that Kcng4[Cre] drives TdTomato expression in AldoC- PCs, and Basket cells (Suppl. Fig. 3C). In conclusion, the expression patterns observed in the CaMKIIα[Cre/T29] and the Kcng4[Cre] mice allow to genetically target distinct PC sub-populations (Fig. 5D and G).

9+ and 9- PCs project to distinct brain stem nuclei:

The strict complementary Cre expression of CaMKIIα[Cre/T29] and Kcng-4[Cre] mice observed specifically in the flocculus (Fig. 5D and G, 6A) allowed us to target the 9+ and 9- PC domains, respectively (Fig. 6B). We traced PCs of each domain using a viral strategy based on the co-injection of two AAVs: a Cre recombinase-dependent reporter expression (AAV1-CAG-Flex-TdTomato) to label specific PC subsets, and a constitutive reporter expression (AAV5-CAG-ChR2-GFP) to control for the volume of the flocculus injected (Fig. 6B). Injections in both CaMKIIα[Cre/T29] (n=2) and Kcng4[Cre] (n=4) mice resulted in labelled terminals in the Spinal (SpVe), Medial (MVe), Superior

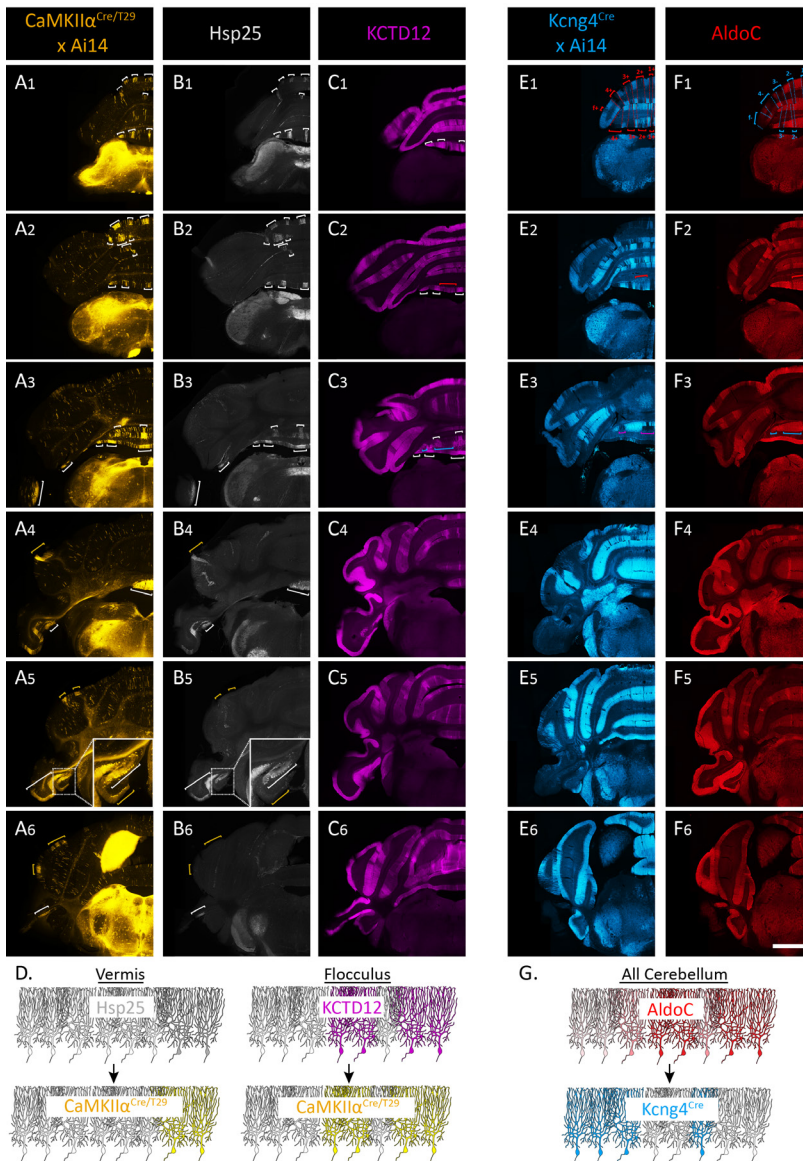**Fig. 5 Characterization of CaMKIIα$^{Cre/T29}$ (transgenic) and Kcng4^{Cre} (knock-in/ knock-out) mouse models.**

(A-C and E-F) Serial transverse sections of the cerebellum of CaMKIIα$^{Cre/T29}$ xAi14 (A) and Kcng4^{Cre}xAi14 (E) mouse with Hsp25 (B), KCTD12 (C), and AldoC (F) immunolabeling. White brackets indicate the Hsp25 domains (B) and the corresponding TdTomato+ domains in the CaMKIIα$^{Cre/T29}$ xAi14 (A), as well as KCTD12+ domains (C). Yellow brackets indicate the TdTomato+ domains from the CaMKIIα$^{Cre/T29}$ xAi14 which do not correspond to any Hsp25+ domains, with a

zoom on the flocculus (A_5 and B_5). Blue and red brackets and dotted lines show the complementation of TdTomato+, from the Kcng4^{Cre}xAi14, and the AldoC+ populations (E_1 and F_1). The 2+ band in the ventral lobule IX appears AldoC+ and TdTomato+ (Kcng4^{Cre}xAi14), but KCTD12- (C_2, E_2 and F_2). In the dorsal lobule X, KCTD12 and TdTomato (Kcng4^{Cre}xAi14) reveal complementary domains virtually absent from the AldoC immunostaining (C_3, E_3 and F_3). (D) Schematic representation of Cre expression in the CaMKIIα$^{Cre/T29}$ relative to Hsp25 and KCTD12 expression profiles. (G) Schematic representation of Cre expression in the Kcng4^{Cre} relative to AldoC expression profile. Scale bar = 1mm.

(SuVe), and Lateral (LVe) vestibular nuclei and the Pr nucleus. In the CaM-KIIα$^{Cre/T29}$ a large density of terminals was found in the dorsal PrH and MVe-PC, primarily along the floor of the fourth ventricle and at the transition zone from PrH to MVePC (Fig. 6C$_{1-3}$), in the caudal aspect of these nuclei. Clusters of labelled terminals were also observed in the dorsal aspect of the SuVe (Fig. 6C$_{4-5}$). In the MVeMC, SpVe and LVe labelled terminals were extremely scarce despite passing fibers. Injections performed in the Kcng4^{Cre} mice strongly contrast as we observed almost no labelled terminals in the Pr (Fig. 6D$_5$). In the MVePC majority of the terminals were in the rostro-ventral aspect, at the border with the MVeMC, while the magnocellular region was rich in PC terminals (Fig. 6D$_{3-4}$). The SuVe and LVe appeared to be the primary target of the labelled PCs as we observed a large plexus of axon terminals in the ventral SuVe and dorsal LVe (Fig. 6D$_{4-5}$). Based on these two transgenic lines, we conclude that 9+ PCs project primarily to the Pr and dorsal MVePC while the 9- PCs project largely to the MVeMC, SuVe and LVe.

Discussion

In this study we showed that minor nuances in PCs molecular identity reflect physiological and anatomical distinctions. AldoC protein is currently the molecular marker of reference to study PC sub-populations. However, thirty years after the first characterisation of AldoC expression pattern in the cerebellum (46), the exact compartmentalisation of PC subtypes is still questioned and redrawn (15, 23). Here, we introduce new markers and genetic tools that support a further differentiation of cerebellar compartments and allow for specific examination of anatomical connectivity. We have applied these new tools to confirm the recently established sub-division of the flocculus and detail the features of 9+ and 9- domains.

In immunohistochemistry, pattern recognition can become subjective as the biological variance get closer to the sensitivity limit of the method.

Fig. 6 Anterograde tracing from 9+ and 9- domains.

(A) Serial transverse sections of the flocculus of CaMKIIα^{Cre/T29} xAi14 (yellow) and Kcng4^{Cre}xAi14 (blue) mouse with KCTD12 (purple) immunolabeling. Scale bar= 200 μm. (B) Scheme of the stereotaxic injection of AAV1-CAG-Flex-TdTomato/AAV5-CAG-ChR2-GFP in the flocculus with the expected location of Cre expressing PCs in either CaMKIIα^{Cre/T29} (yellow dots) or Kcng4^{Cre} (blue dots) mouse. Example of injected flocculus in both models. Scale bar = 200 μm. (C and D) TdTomato (cre-dependent) labelled fibers in the vestibular structure following injection of AAV1-CAG-Flex-TdTomato in the flocculus of CaMKIIα^{Cre/T29} (yellow) or Kcng4^{Cre} (blue)

animals. Scale bars = 200µm. Thickness = 40µm. PFl=paraflocculus; Fl=flocculus; PrH=prepositus hypoglossi; SuVe=superior vestibular nucleus; LVe=lateral vestibular nucleus; MVePC=medial vestibular parvicellular nucleus; MVeMC=medial vestibular magnocellular nucleus; SpVe=spinal vestibular nucleus; Lat=lateral cerebellar nucleus; IntP= nucleus interpositus posterior; IntA=nucleus interposituc anterior; DPGi=dorsal paragigantocellular nucleus of the reticular formation; Sol=solitary nucleus; 4V=fourth ventricle.

We observed that AldoC and PLCB4 immunostainings are not optimal ways to delineate the newly identified 9+ and 9- domains of the flocculus (23). Despite our standardized perfusion and immunohistological processes, we noticed variability in staining intensity and contrast between domains, from sample to sample. Among others, we identified KCTD12 protein as a more suitable marker to delineate 9+ and 9- domains. KCTD12 immunoreactivity was previously described as a zebrin-like marker in the cerebellum (44, 47). However, we show that KCTD12 expression delineate compartments hard-ly distinguishable or absent from AldoC expression map. We have tested two anti-AldoC (goat polyclonal, SC-12065; mouse monoclonal) and two an-ti-KCTD12 (rabbit polyclonal, 15523-1-AP; mouse monoclonal, sc-271855) antibodies. The immunoreactivities varied from one antibody to another, but KCTD12 immunoreactivity consistently demonstrated more contrast be-tween floccular domains than the AldoC immunoreactivity. The high contrast of KCTD12 expression reveals the meaningful nuances of AldoC expression, and to question the nature of the 9- domain.

Previous work of our group showed that AldoC- and AldoC+ PCs operate at distinct simple spike and complex spike frequencies (10). While this study focused on the high and low ends of AldoC expression range, the physiology of PC subtypes presenting intermediate AldoC levels, such as b+/3+/3b+/f+/e1+/e1- and e2+ (15), was not established. The 9- domain was described by Fujita *et al.* (23)as AldoC-. Indeed 9- domain shows the com-mon traits of AldoC- PCs being PLCB4+/Nfh+/KCTD12-/Hsp25-. However, our comparative analysis of AldoC expression between lobule IX and the flocculus indicates that the 9- domain is an intermediate AldoC expression domain. This nuance is not trivial with respect to the intrinsic electrophysi-ological properties of 9- PCs, as we observed that they differ from AldoC+ (lobule X) but also from AldoC- PCs (lobule I-II-III). All electrophysiological properties tested demonstrated that 9- PCs are approximately halfway be-tween AldoC+ and AldoC-. The study of PCs in the 9- domain suggest that there is a linear correlation between AldoC levels and firing properties of PCs. The co-variance of protein expression and electrophysiological proper-

ties within neuronal types has been recently described in the cortex, striatum and hippocampus (2, 4, 48). Using novel Patch-seq approaches, these studies demonstrated that neuronal types are continua of physiological, morphological and molecular variations. All together they question the current clustering methodology. Our data raised the same point and question the current bimodal (AldoC- vs. AldoC+) view of PC subpopulations (19).

Immunohistochemical based methodologies have a lower sensitivity than the RNA single-cell sequencing technics discussed above, but it allows for integration of anatomical and connectomic data with the physiological and molecular characterisation (49). We show in this study that 9+ and 9- domains integrate in distinct circuitries. In regard to the afferent projections, we circled out a cluster of MFs originating from the PrH and the MVeMC, projecting specifically to the 9+ territory. SST28 expression pattern demonstrates that cerebellar afferents defined by a unique molecular signature are organised in discrete pathways that may originate from distinct pre-cerebellar nuclei but converge to the same cerebellar domains. The tracing of the efferent pathway showed that PCs in the 9+ and 9- domains have distinct long range projections. PCs from 9+ domain principally project to the PrH and the dorsal MVePC. From our data we were not able to determine if the 9+ PCs project back onto the SST28+ neurons in these regions. The highest density of terminals appeared at the junction of both nuclei which might correspond to the "marginal zone" (MZ) described in the macaque and the cat (50). The MZ was shown to project to both contra- and ipsilateral abducens nucleus, suggesting that 9+ is preferentially involved in the horizontal eye movement circuitry (51, 52). Transsynaptic retrograde rabies tracing from the lateral and medial rectus appears to predominantly label neurons in the PrH, MZ and dorsal MVePC (53). Surprisingly, transynaptically labelled PCs are essentially located in the rostral aspect of the flocculus in this same study. Our data would have predicted labelled PCs in the caudal (9+) domain. The very limited number of studies on retrograde transsynaptic tracing from the ocular muscle do not allow us to conclude if 9+ and 9- control distinct set of muscles. However, it is for us unlikely that 9+ and 9- are solely confined to the control of either horizontal or vertical eye movements. First, the heterogeneity of the vestibular nuclei and PrH neurons and the intertwined projections to the oculomotor and abducens nuclei (54, 55) do not allow to determine the downstream pathways solely based on the terminal field of floccular projections. The molecular identification of 9+ and 9- targets in the PrH and VN would allow to precisely determine the anatomical routes toward the eye muscles. Second, the overlay of our anatomical map and the detailed functional map of the flocculus previously established (21, Fig.7), predicts that

9+ domain encompass zone 1 (HA) and 2 (VA), while 9- domain encompass zone 3 (HA) and 4 (VA). This contradicts previous inferences (23), but is supported by the map of the flocculus with the new markers and the neuronal tracing known from HA and VA zones (21). Based on this assessment, zone 1 and 3 are respectively HA-KCTD12+ and HA-KCTD12- PCs projecting predominantly to the SuVe, while zone 2 and 4 are respectively VA-KCTD12+ and VA-KCTD12- PCs projecting to the MVe, LVe and PrH (only for zone 2). Each domain defined by PC molecular expression would then act on both horizontal and vertical eye movement modalities. This concept is reminiscent of the compartmentalisation of the vestibulocerebellum observed in the pigeon (56). While in the pigeon a functional zone (e.g., HA) encompass two molecular domains (AldoC+ and AldoC-), in mouse a molecular domain (e.g., KCTD12+) encompass two functional zones (HA and VA). Slightly distinct, these two topographies result in a similar distribution of PCs sensitivity for HA and VA stimulations among the distinct molecular subpopulations.

To decipher the downstream network it is necessary to combine connectomic approaches with specific molecular subtypes targeting. Methods such as transsynaptic modified rabies tracing or the recently described spectral connectomics (49) offer such tools for high specificity of anatomical studies. In regards to the functional output of each subpopulations we suggest the use the newly characterized CaMKIIα$^{Cre/T29}$ and the Kcng4^{Cre} for optogenetic stimulation. Simultaneous optogenetic stimulation of all floccular PCs with a *pcp2*^{Cre} results of an eye movement in both horizontal and vertical plan (57). The lines we characterised allow to individually stimulate 9+ or 9- domains. Both models have limitations to take account for, nevertheless, they remain to our knowledge the only mutant models described to specifically target PCs subpopulations. Integrated with the anatomical, physiological and lesion studies from the literature, the optogenetic manipulation of floccular compartments would represent a considerable step forward in the construction of cerebellar models.
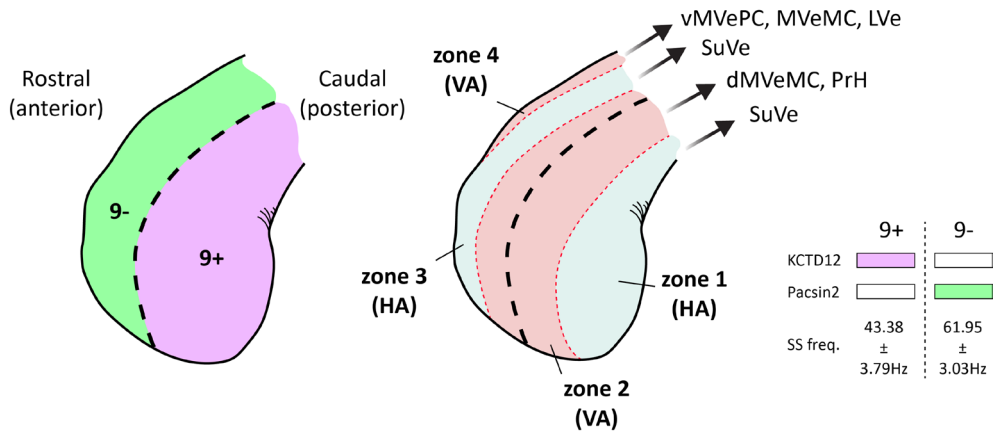
Fig. 7 Molecular and functional domains of the flocculus.

Scheme of floccular domains based on PC molecular subtypes (left) and functional zones described by Schonewille et al. (right). PrH=prepositus hypoglossi; SuVe=superior vestibular nucleus; LVe=lateral vestibular nucleus; d/vMVePC=dorsal/ventral medial vestibular parvicellular nucleus; MVeMC=medial vestibular magnocellular nucleus; SS freq.=simple spike firing frequency.

1. N. W. Gouwens, *et al.*, Integrated Morphoelectric and Transcriptomic Classification of Cortical GABAergic Cells. *Cell* (2020) https:/doi.org/10.1016/j.cell.2020.09.057.

2. F. Scala, *et al.*, Phenotypic variation within and across transcriptomic cell types in mouse motor cortex. *bioRxiv* (2020) https:/doi.org/10.1101/2020.02.03.929158.

3. C. M. Houston, *et al.*, Exploring the significance of morphological diversity for cerebellar granule cell excitability. *Sci. Rep.* (2017) https:/doi.org/10.1038/srep46147.

4. A. B. Muñoz-Manchado, *et al.*, Diversity of Interneurons in the Dorsal Striatum Revealed by Single-Cell RNA Sequencing and PatchSeq. *Cell Rep.* (2018) https:/doi.org/10.1016/j.celrep.2018.07.053.

5. R. Hawkes, K. Herrup, Aldolase C/zebrin II and the regionalization of the cerebellum. *J. Mol. Neurosci.* (1995) https:/doi.org/10.1007/BF02736761.

6. M. Paukert, Y. H. Huang, K. Tanaka, J. D. Rothstein, D. E. Bergles, Zones of enhanced glutamate release from climbing fibers in the mammalian cerebellum. *J. Neurosci.* (2010) https:/doi.org/10.1523/JNEUROSCI.5118-09.2010.

7. J. R. Sarna, H. Marzban, M. Watanabe, R. Hawkes, Complementary stripes of phospholipase Cβ3 and Cβ4 expression by Purkinje cell subsets in the mouse cerebellum. *J. Comp. Neurol.* (2006) https:/doi.org/10.1002/cne.20912.

8. N. Terada, *et al.*, Compartmentation of the Mouse Cerebellar Cortex by Sphingosine Kinase. *J. Comp. Neurol.* (2004) https:/doi.org/10.1002/cne.11002.

9. J. M. Mateos, *et al.*, Parasagittal compartmentalization of the metabotropic glutamate receptor mGluR1b in the cerebellar cortex. *Eur. J. Anat.* (2001).

10. H. Zhou, *et al.*, Cerebellar modules operate at different frequencies. *Elife* (2014) https:/doi.org/10.7554/eLife.02536.

11. B. Wu, *et al.*, TRPC3 is a major contributor to functional heterogeneity of cerebellar Purkinje cells. *Elife* (2019) https:/doi.org/10.7554/eLife.45590.

12. K. Tran-Anh, *et al.*, Common origin of the cerebellar dual somatotopic areas revealed by tracking embryonic purkinje cell clusters with birthdate tagging. *eNeuro* (2020) https:/doi.org/10.1523/ENEURO.0251-20.2020.

13. A. M. Valera, *et al.*, Stereotyped spatial patterns of functional synaptic connectivity in the cerebellar cortex. *Elife* (2016) https:/doi.org/10.7554/eLife.09862.

14. W. Gao, G. Chen, K. C. Reinert, T. J. Ebner, Cerebellar cortical molecular layer inhibition is organized in parasagittal zones. *J. Neurosci.* (2006) https:/doi.org/10.1523/JNEUROSCI.2434-06.2006.

15. I. Sugihara, P. N. Quy, Identification of aldolase C compartments in the mouse cerebellar cortex by olivocerebellar labeling. *J. Comp. Neurol.* (2007) https:/doi.org/10.1002/cne.21219.

16. R. V. Sillitoe, D. Stephen, Z. Lao, A. L. Joyner, Engrailed homeobox genes determine the organization of Purkinje cell sagittal stripe gene expression in the adult cerebellum. *J. Neurosci.* (2008) https:/doi.org/10.1523/JNEUROSCI.2059-08.2008.

17. C. A. Duffin, R. McFarland, J. R. Sarna, M. W. Vogel, C. L. Armstrong, Heat shock protein 25 expression and preferential purkinje cell survival in the lurcher mutant mouse cerebellum. *J. Comp. Neurol.* (2010) https:/doi.org/10.1002/cne.22309.

18. C. I. De Zeeuw, M. M. Ten Brinke, Motor learning and the cerebellum. *Cold Spring Harb. Perspect. Biol.* (2015) https:/doi.org/10.1101/cshperspect.a021683.

19. C. I. De Zeeuw, Bidirectional learning in upbound and downbound microzones of the cerebellum. *Nat. Rev. Neurosci.* (2020) https:/doi.org/10.1038/s41583-020-00392-x.

20. J. Porrill, P. Dean, S. R. Anderson, Adaptive filters and internal models: Multilevel description of cerebellar function. *Neural Networks* (2013) https:/doi.org/10.1016/j.neunet.2012.12.005.

21. M. Schonewille, *et al.*, Zonal organization of the mouse flocculus: Physiology, input, and output. *J. Comp. Neurol.* (2006) https:/doi.org/10.1002/cne.21036.

22. T. J. H. Ruigrok, Organization of the vestibulocerebellum in *Annals of the New York Academy of Sciences*, (1996) https:/doi.org/10.1111/j.1749-6632.1996.tb15728.x.

23. H. Fujita, *et al.*, Detailed expression pattern of Aldolase C (Aldoc) in the cerebellum, retina and other areas of the CNS studied in Aldoc-Venus knock-in mice. *PLoS One* (2014) https:/doi.org/10.1371/journal.pone.0086679.

24. J. Z. Tsien, *et al.*, Subregion- and cell type-restricted gene knockout in mouse brain. *Cell* (1996) https:/doi.org/10.1016/S0092-8674(00)81826-7.

25. X. Duan, A. Krishnaswamy, I. De La Huerta, J. R. Sanes, Type II cadherins guide assembly of a direction-selective retinal circuit. *Cell* (2014) https:/doi.org/10.1016/j.cell.2014.06.047.

26. C. L. Armstrong, A. M. Krueger-Naug, R. W. Currie, R. Hawkes, Constitutive expression of the 25-kda heat shock protein Hsp25 reveals novel parasagittal bands of Purkinje cells in the adult mouse cerebellar cortex. *J. Comp. Neurol.* (2000) https:/doi.org/10.1002/(SICI)1096-9861(20000117)416:3<383::AID-CNE9>3.0.CO;2-M.

27. A. Demilly, S. L. Reeber, S. A. Gebre, R. V. Sillitoe, Neurofilament heavy chain expression reveals a unique parasagittal stripe topography in the mouse cerebellum. *Cerebellum* (2011) https:/doi.org/10.1007/s12311-010-0156-y.

28. J. J. White, *et al.*, Cerebellar zonal patterning relies on purkinje cell neurotransmission. *J. Neurosci.* (2014) https:/doi.org/10.1523/JNEUROSCI.0122-14.2014.

29. J. Xiao, *et al.*, Systematic regional variations in Purkinje cell spiking patterns. *PLoS One* (2014) https://doi.org/10.1371/journal.pone.0105633.

30. E. M. Perkins, *et al.*, Loss of cerebellar glutamate transporters EAAT4 and GLAST differentially affects the spontaneous firing pattern and survival of Purkinje cells. *Hum. Mol. Genet.* (2018) https://doi.org/10.1093/hmg/ddy169.

31. A. Pijpers, R. Apps, J. Pardoe, J. Voogd, T. J. H. Ruigrok, Precise spatial relationships between mossy fibers and climbing fibers in rat cerebellar cortical zones. *J. Neurosci.* (2006) https:/doi.org/10.1523/JNEUROSCI.2905-06.2006.

32. Y. Luo, R. P. Patel, G. A. Sarpong, K. Sasamura, I. Sugihara, Single axonal morphology and termination to cerebellar aldolase C stripes characterize distinct spinocerebellar projection systems originating from the thoracic spinal cord in the mouse. *J. Comp. Neurol.* (2018) https:/doi.org/10.1002/cne.24360.

33. E. P. Lackey, R. V. Sillitoe, Eph/ephrin Function Contributes to the Patterning of Spinocerebellar Mossy Fibers Into Parasagittal Zones. *Front. Syst. Neurosci.* (2020) https://doi.org/10.3389/fnsys.2020.00007.

34. C. L. Armstrong, *et al.*, A novel somatostatin-immunoreactive mossy fiber pathway associated with HSP25-immunoreactive Purkinje cell stripes in the mouse cerebellum. *J. Comp. Neurol.* (2009) https:/doi.org/10.1002/cne.22167.

35. P. Errico, N. H. Barmack, Origins of cerebellar mossy and climbing fibers immunoreactive for corticotropin☐releasing factor in the rabbit. *J. Comp. Neurol.* (1993) https:/doi.org/10.1002/

cne.903360211.

36. J. A. Schulman, T. E. Finger, N. C. Brecha, H. J. Karten, Enkephalin immunoreactivity in Golgi cells and mossy fibres of mammalian, avian, amphibian and teleost cerebellum. *Neuroscience* (1981) https:/doi.org/10.1016/0306-4522(81)90026-9.

37. M. R. Diño, F. H. Willard, E. Mugnaini, Distribution of unipolar brush cells and other calretinin immunoreactive components in the mammalian cerebellar cortex. *J. Neurocytol.* (1999) https:/doi.org/10.1023/A:1007072105919.

38. S. A. Gebre, S. L. Reeber, R. V. Sillitoe, Parasagittal compartmentation of cerebellar mossy fibers as revealed by the patterned expression of vesicular glutamate transporters VGLUT1 and VGLUT2. *Brain Struct. Funct.* (2012) https:/doi.org/10.1007/s00429-011-0339-4.

39. D. Jaarsma, *et al.*, The basal interstitial nucleus (BIN) of the cerebellum provides diffuse ascending inhibitory input to the floccular granule cell layer. *J. Comp. Neurol.* (2018) https:/doi.org/10.1002/cne.24479.

40. S. Hisano, *et al.*, Expression of inorganic phosphate/vesicular glutamate transporters (BNPI/VGLUT1 and DNPI/VGLUT2) in the cerebellum and precerebellar nuclei of the rat. *Mol. Brain Res.* (2002) https:/doi.org/10.1016/S0169-328X(02)00442-4.

41. C. Hansel, *et al.*, αCaMKII Is Essential for Cerebellar LTD and Motor Learning. *Neuron* (2006) https:/doi.org/10.1016/j.neuron.2006.08.013.

42. T. Ichikawa, S. ichi Sekihara, S. Ohsako, Y. Hirata, T. Yamauchi, Ca2+/calmodulin-dependent protein kinase II in the rat cerebellum: An immunohistochemical study with monoclonal antibodies specific to either α or β subunit. *J. Chem. Neuroanat.* (1992) https:/doi.org/10.1016/0891-0618(92)90054-T.

43. X. Wang, C. Zhang, G. Szábo, Q. Q. Sun, Distribution of CaMKIIα expression in the brain in vivo, studied by CaMKIIα-GFP mice. *Brain Res.* (2013) https:/doi.org/10.1016/j.brainres.2013.04.042.

44. S. Rodriques, *et al.*, Slide-seq: A Scalable Technology for Measuring Genome-Wide Expression at High Spatial Resolution. *Slide-seq A Scalable Technol. Meas. Genome-Wide Expr. High Spat. Resolut.* (2019) https:/doi.org/10.1101/563395.

45. S. L. Palay, V. Chan-Palay, *Cerebellar Cortex* (1974) https:/doi.org/10.1007/978-3-642-65581-4.

46. G. Brochu, L. Maler, R. Hawkes, Zebrin II: A polypeptide antigen expressed selectively by purkinje cells reveals compartments in rat and fish cerebellum. *J. Comp. Neurol.* (1990) https:/doi.org/10.1002/cne.902910405.

47. M. Metz, M. Gassmann, B. Fakler, N. Schaeren-Wiemers, B. Bettler, Distribution of the auxiliary GABAB receptor subunits KCTD8, 12, 12b, and 16 in the mouse brain. *J. Comp. Neurol.* (2011) https:/doi.org/10.1002/cne.22610.

48. K. D. Harris, *et al.*, Classes and continua of hippocampal CA1 inhibitory neurons revealed by single-cell transcriptomics. *PLoS Biol.* (2018) https:/doi.org/10.1371/journal.pbio.2006387.

49. F. Y. Shen, *et al.*, Light microscopy based approach for mapping connectivity with molecular specificity. *Nat. Commun.* (2020) https:/doi.org/10.1038/s41467-020-18422-8.

50. T. Langer, C. R. S. Kaneko, C. A. Scudder, A. F. Fuchs, Afferents to the abducens nucleus in the monkey and cat. *J. Comp. Neurol.* (1986) https:/doi.org/10.1002/cne.902450307.

51. R. F. Spencer, R. J. Wenthold, R. Baker, Evidence for glycine as an inhibitory neurotransmitter of vestibular, reticular, and prepositus hypoglossi neurons that project to the cat abducens nucleus. *J. Neurosci.* (1989) https:/doi.org/10.1523/jneurosci.09-08-02718.1989.

52. D. B. Belknap, R. A. McCrea, Anatomical connections of the prepositus and abducens nuclei in the

squirrel monkey. *J. Comp. Neurol.* (1988) https:/doi.org/10.1002/cne.902680103.

53. I. Billig, C. D. Balaban, Zonal organization of the vestibulo-cerebellum in the control of horizontal extraocular muscles using pseudorabies virus: I. Flocculus/ventral paraflocculus. *Neuroscience* (2004) https:/doi.org/10.1016/j.neuroscience.2004.01.051.

54. M. Shin, *et al.*, Multiple types of cerebellar target neurons and their circuitry in the vestibule-ocular reflex. *J. Neurosci.* (2011) https:/doi.org/10.1523/JNEUROSCI.0768-11.2011.

55. H. Matsuno, *et al.*, Distribution and structure of synapses on medial vestibular nuclear neurons targeted by cerebellar flocculus purkinje cells and vestibular nerve in mice: Light and electron microscopy studies. *PLoS One* (2016) https:/doi.org/10.1371/journal.pone.0164037.

56. I. Craciun, C. Gutiérrez-Ibáñez, J. R. Corfield, P. L. Hurd, D. R. Wylie, Topographic organization of inferior olive projections to the zebrin II stripes in the pigeon cerebellar uvula. *Front. Neuroanat.* (2018) https:/doi.org/10.3389/fnana.2018.00018.

57. K. Voges, B. Wu, L. Post, M. Schonewille, C. I. De Zeeuw, Mechanisms underlying vestibulo-cerebellar motor learning in mice depend on movement direction. *J. Physiol.* (2017) https:/doi.org/10.1113/JP274346.
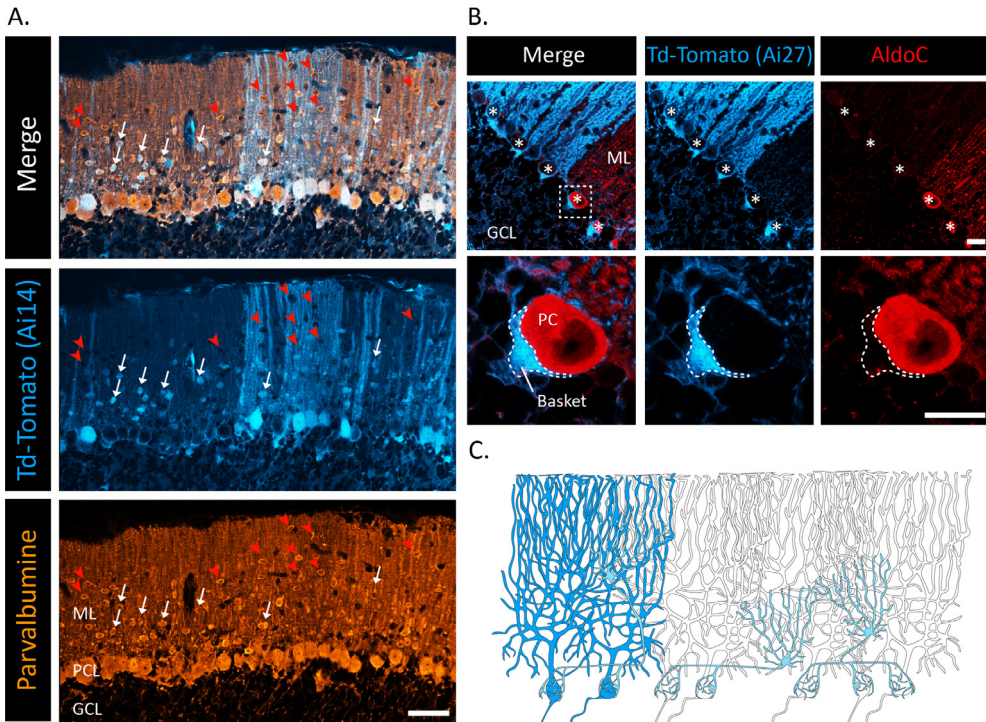
Suppl. Fig. 1 . Labelling of molecular layer interneurons in the Kcng4^{Cre} mouse.

(A) Transverse section of the cerebellum of a Kcng4^{Cre}xAi14 mouse with parvalbumin (Parv) immunolabeling. TdTomato expression under cre recombinase activity reveals labelled PCs and small circular cell bodies, Parv+, in the lower third of the molecular layer (white arrows). Parv+/TdTomato- interneurons localize essentially in the upper part of the molecular layer (red arrow heads). Scale bar=50µm. (B) Transverse section of the cerebellum of a Kcng4^{Cre}xAi27 mouse with aldoC immunolabeling. The membrane bound localization of TdTomato of the Ai27 reveals a basket-like structure around all PCs. Scale bars=20µm. (C) Scheme of cell type specific expression of cre recombinase in the Kcng4^{Cre}. ML=molecular layer; PCL=Purkinje cell layer; GCL= granular cell layer.
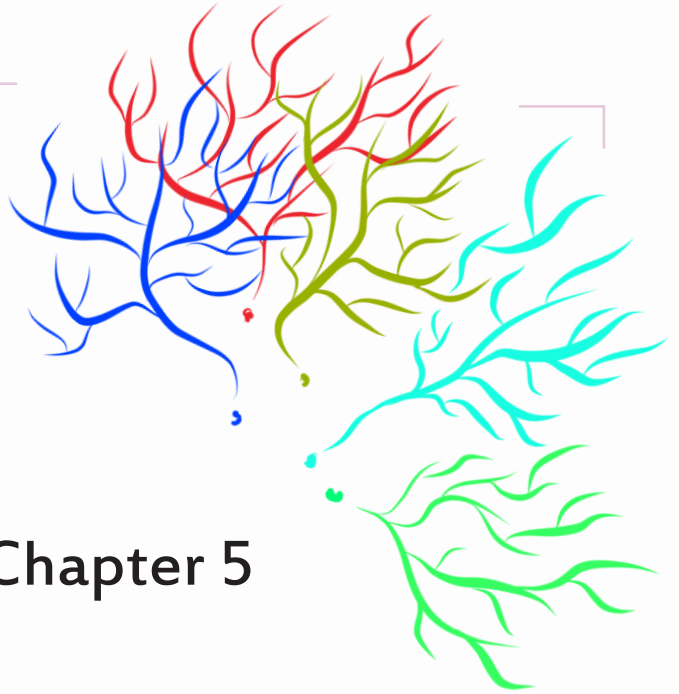
Chapter 5

TRPC3 is a major contributor to functional heterogeneity of cerebellar Purkinje cells

Bin Wu, François G.C. Blot, Aaron Benson Wong, Catarina Osório, Youri Adolfs, Jeroen Pasterkamp, Jana Hartmann, Esther BE Becker, Henk-Jan Boele, Chris I De Zeeuw, Martijn Schonewille

Abstract

Despite the canonical homogeneous character of its organization, the cerebellum plays differential computational roles in distinct sensorimotor behaviors. Previously, we showed that Purkinje cell (PC) activity differs between zebrin-negative (Z–) and zebrin-positive (Z+) modules(Zhou *et al.*, 2014). Here, using gain-of-function and loss-of-function mouse models, we show thattransient receptor potential cation channel C3 (TRPC3) controls the simple spike activity of Z–, butnot Z+ PCs. In addition, TRPC3 regulates complex spike rate and their interaction with simple spikes, exclusively in Z– PCs. At the behavioral level, TRPC3 loss-of-function mice show impaired eyeblink conditioning, which is related to Z– modules, whereas compensatory eye movement adaptation, linked to Z+ modules, is intact. Together, our results indicate that TRPC3 is a major contributor to the cellular heterogeneity that introduces distinct physiological properties in PCs,conjuring functional heterogeneity in cerebellar sensorimotor integration.
DOI: https://doi.org/10.7554/eLife.45590.001

Introduction

Maintaining correct sensorimotor integration relies on rapid modifications of activity. The cerebellum is instrumental herein, evidenced by the fact that disruptions of cerebellar functioning, for example through stroke or neurodegenerative disorders, affect coordination and adaptation of many types of behaviors such as gait, eye movements and speech (Ackermann *et al.*, 1992; Bodranghien *et al.*,2016). The palette of behavioral parameters controlled by the cerebellum is also broad and includes features like timing (Raymond *et al.*, 1996; De Zeeuw and Yeo, 2005; Yang and Lisberger, 2014), strength (Hirata and Highstein, 2000; Witter *et al.*, 2013), as well as coordination of muscle activity (Thach *et al.*, 1992; Vinueza Veloz *et al.*, 2015). However, the pluriformity of behavioral features does not match with the homogeneity of the structure and cyto-architecture of the cerebellar cortex.

Recently, it has been uncovered that the sole output neurons of the cerebellar cortex, the Purkinje cells (PCs), can be divided into two main groups with a distinct firing behavior (Xiao *et al.*,2014; Zhou *et al.*, 2014). One group, consisting of PCs that are positive for the glycolytic enzymealdolase C, also referred to as zebrin II (Brochu *et al.*, 1990; Ahn *et al.*, 1994), shows relatively low simple spike firing rates, whereas the PCs in the other group that form zebrin-negative zones, fire at higher rates (Zhou *et al.*, 2014). Zebrin

II demarcates olivocerebellar modules, anatomically defined operational units each consisting of a closed loop between the inferior olive, parasagittal bands of the cerebellar cortex and the cerebellar nuclei (Sugihara and Quy, 2007; Ruigrok, 2011). Given that different motor domains are controlled by specific olivocerebellar modules (Horn *et al.*, 2010; Ruigrok, 2011; Graham and Wylie, 2012), the differential intrinsic firing frequencies may be tuned to the specific neuronal demands downstream of the cerebellum (De Zeeuw and Ten Brinke, 2015). Thus, dependent on the specific behavior controlled by the module involved, the PCs engaged may show low or high intrinsic firing as well as related plasticity rules to adjust these behaviors (Apps *et al.*, 2018).

Cellular heterogeneity can drive differentiation in the activity and plasticity of individual cells that operate within a larger ensemble (Altschuler and Wu, 2010). The molecular and cellular determinants of differential electrophysiological processing in the cerebellar PC modules are just starting to be identified (Cerminara *et al.*, 2015; Apps *et al.*, 2018). For example, while the impact of zebrin II itself is still unclear (Zhou *et al.*, 2014), excitatory amino acid transporter 4 (EAAT4) and GLAST/EAAT1 may selectively modulate simple spike activity of zebrin-positive PCs as well as plasticity of their parallel fiber (PF) inputs (Wadiche and Jahr, 2005; Perkins *et al.*, 2018). Likewise, the distributions of particular subcategories of receptors that may be relevant for firing properties are linked to the same modular organization. For example, whereas g-aminobutyric acid type B ($GABA_B$) receptors occur in both zebrin-positive and zebrin-negative PCs (Tian and Zhu, 2018), the $GABA_{B2}$ receptor is selectively expressed in a pattern similar to that of zebrin II (Chung *et al.*, 2008). Or, whereas the alpha isoform of mGluR1 (mGluR1a) is uniformly expressed in all PCs (Ohtani *et al.*, 2014) the mGluR1b receptor is expressed in a pattern complementary to that of zebrin II (Mateos *et al.*, 2001). Interestingly, the modular distributions of most of these receptors point towards a critical role of transient receptor potential cation channel subfamily C member 3 (TRPC3) in regulating electrophysiological properties of PCs. For example, while the mGluR1b receptor interacts with TRPC3 to drive mGluR1-dependent currents (Hartmann *et al.*, 2008), the $GABA_B$ receptors modulate mGluR1-triggered TRPC3-mediated currents (Tian and Zhu, 2018). However, where and how TRPC3 operates in cerebellar PCs is still largely unknown (Zhou *et al.*, 2014).

Here, we set out to test the hypothesis that TRPC3 is a key player in the molecular machinery responsible for differential control over the activity and function of Z+ and Z– PCs. We demonstrate that TRPC3 in the brain has particularly high expression levels in the cerebellum, in a pattern largely, but

not precisely, complementary to zebrin. We examined the impact of TRPC3 gain-of-function and loss-of-function mutations and found effects on the spiking rate of Z– but not Z+ PCs in vitro. In vivo recordings during quiet wakefulness in the same mutants revealed that the level of TRPC3 influences both simple spike and complex spike rates, and the interaction between the two, also selectively in Z– modules. Finally, we show that adaptation of compensatory eye movements, which is controlled by Z+ modules in the vestibulocerebellum (Sanchez *et al.*, 2002; Zhou *et al.*, 2014), is not affected by the loss of TRPC3 function, whereas the learning rate during eyeblink conditioning, which is linked to the Z– modules (Hesslow, 1994; Mostofi *et al.*, 2010), is decreased after PC-specific ablation of TRPC3, highlighting the behavioral relevance of firing rate modulation by TRPC3.

Results

Specific expression pattern and subcellular localization of TRPC3 in the mouse brain:

        As the expression of TRPC3 in the adult mammalian brain is still unclear, we first set out to examine the immunohistochemistry of TRPC3 using a novel TRPC3-specific antibody (Cell signaling, #77934). We found that in the normal mouse brain TRPC3 is most prominently expressed in the olivocerebellar circuit (Figure 1A), specifically in PCs and unipolar brush cells (UBCs) (Figure 1B). This is in line with previous immunostainings and in situ data (Allen Brain Atlas, http://mouse.brain-map.org/). Upon further scrutiny it is clear that, although expressed in all PCs, endogenous TRPC3 was not distributed homogeneously. The TRPC3 levels in the anterior cerebellum, where the PCs are predominantly Z–, were higher than those in the posterior PCs, which are primarily Z+ (Figure 1A, Figure 1—figure supplement 1). To further visualize the relationship between TRPC3 and Zebrin II, labeled as Aldolase C (Ahn *et al.*, 1994), we quantified their relative levels in several subregions (Figure 1C–D and Figure 1—figure supplement 2). This analysis confirmed that TRPC3 expression is complementary to that of Zebrin in the vermis, while in the hemispheres the TRPC3 expression varies between homogeneous expression and expression complementary to Zebrin II. To visualize this pattern in a more comprehensive manner, we also employed whole-mount brain light sheet imaging following iDISCO-based clearing (Figure 1-video 1). The antibody staining appears to be of better quality in the iDISCO protocol, resulting for instance in a clearer picture of the expression
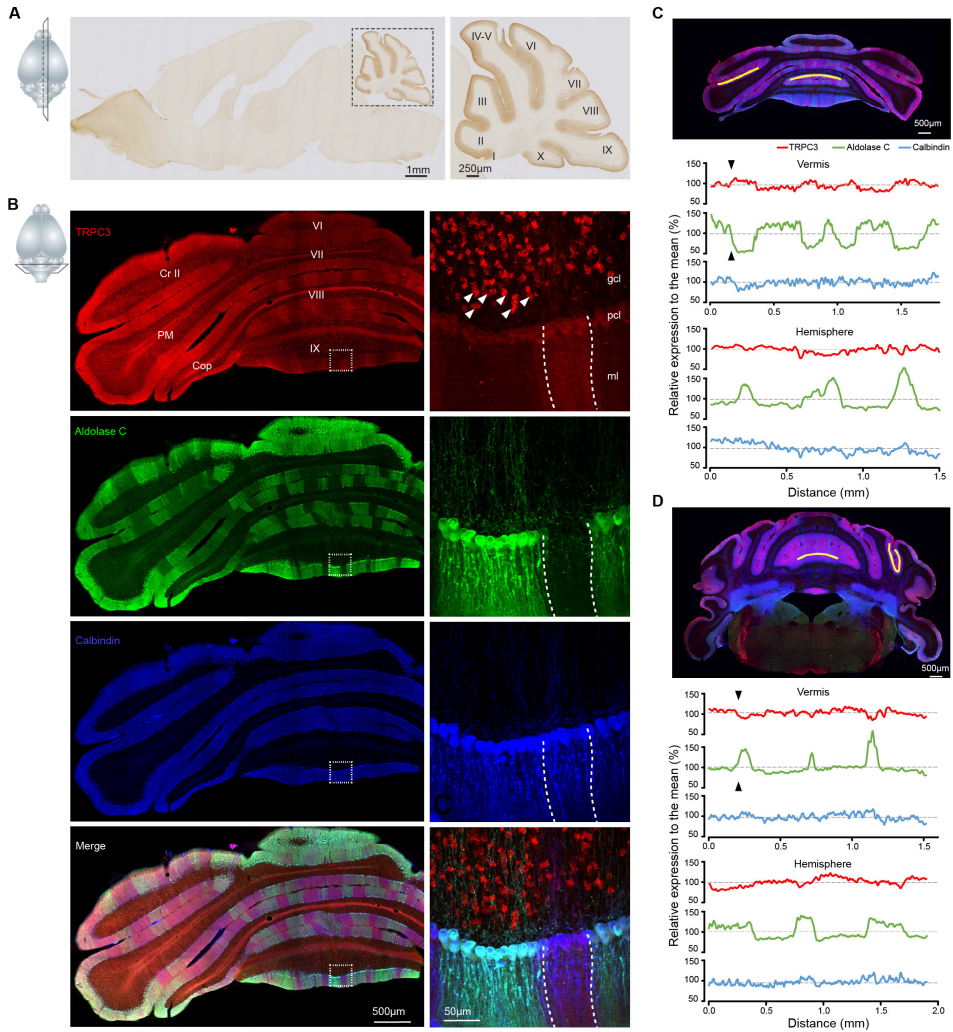
Figure 1. *TRPC3 is predominantly expressed in the cerebellum in a zebrin-related pattern. (A) Representative image and magnification (right) of sagittal cryosection of an adult mouse brain stained with anti-TRPC3. Inset, plane of section. (B) Coronal immunofluorescence images with anti-TRPC3 (red), anti-Zebrin II/Aldolase C (green) and anti-calbindin (blue) staining of the cerebellar cortex (left), with magnifications (right). TRPC3 is expressed in the cerebellar PCs and UBCs (triangles), in a pattern that in the vermis complements that of zebrin and appears more uniform in the hemispheres. Inset, plane of section. (C) Posterior coronal section of the cerebellar cortex (top) used to performed a quantification of the relative intensity of immunofluorescence staining of TRPC3, Zebrin II/Aldolase C and calbindin for PCs in the vermis (ventral lob. VIII, middle) and the hemisphere (ventral PM, bottom) (values normalized to the respective means). (D) Similar analysis of dorsal lob. III (middle) and sulcus of Sim to Crus I (bottom) in anterior section (top). TRPC3*

expression is largely complementary to Zebrin II in the vermis and parts of the hemispheres (black arrow heads), but more uniform in other hemispheric areas. In general, TRPC3 expression demonstrates a weaker differentiation between low and high levels than Zebrin II. I-X, cerebellar lobules I-X; Sim, Simplex lobule; Cr II, Crus II; PM, paramedian lobule; Cop, Copula Pyramidis; gcl, granule cell layer; pcl, Purkinje cell layer; ml, molecular layer; D, dorsal; V, ventral; M, medial; L, lateral.
DOI: https://doi.org/10.7554/eLife.45590.002The following video and figure supplements are available for figure 1:

Figure supplement 1*. Overview and local patterns of TRPC3 expression.*
DOI: https://doi.org/10.7554/eLife.45590.003

Figure supplement 2. *Quantification of TRPC3 expression compared to Zebrin II and calbindin.*
DOI: https://doi.org/10.7554/eLife.45590.004

Figure supplement 3. *Western blot and immunostaining of pcp2Cre;TRPC3fl/fl mice.*
DOI: https://doi.org/10.7554/eLife.45590.005

Figure 1— video 1. *Light sheet imaging reconstruction of whole-mount immunolabeling for TRPC3 (white signal), cleared with iDISCO protocol and scanned in the horizontal plane of an adult mouse brain from dorsal to ventral (see Materials and methods).*
DOI: https://doi.org/10.7554/eLife.45590.006

of TRPC3 in the inferior olive (most ventral, Figure 1-video 1). The anterior/ posterior differences in the protein amount were confirmed by western blot analysis (Figure 1—figure supplement 3A–B).

Our immunohistochemical imaging reveals that TRPC3 is present in the soma and dendritic arborof PCs (Figure 1B and Figure 1—figure supplement 1B–E). To further examine the subcellular localization of TRPC3 in the cerebellum, we performed immunoblots of isolated fractions following a synaptic protein extraction procedure (Figure 1—figure supplement 3C). As expected, TRPC3, a channel protein, is abundantly present in the membrane and almost completely absent in the cytosol (Figure 1—figure supplement 3D). Moreover, TRPC3 is enriched in synapstosomes (Figure 1—figure supplement 3D), in line with the common conception of mGluR1b-dependent activation ofTRPC3 (Hartmann *et al.*, 2008; Ohtani *et al.*, 2014). Together, these results indicate that, within the brain, high TRPC3 expression levels are restricted to the olivocerebellar circuit, where it is present in all PCs and UBCs, but at particularly high levels in Z– PCs.
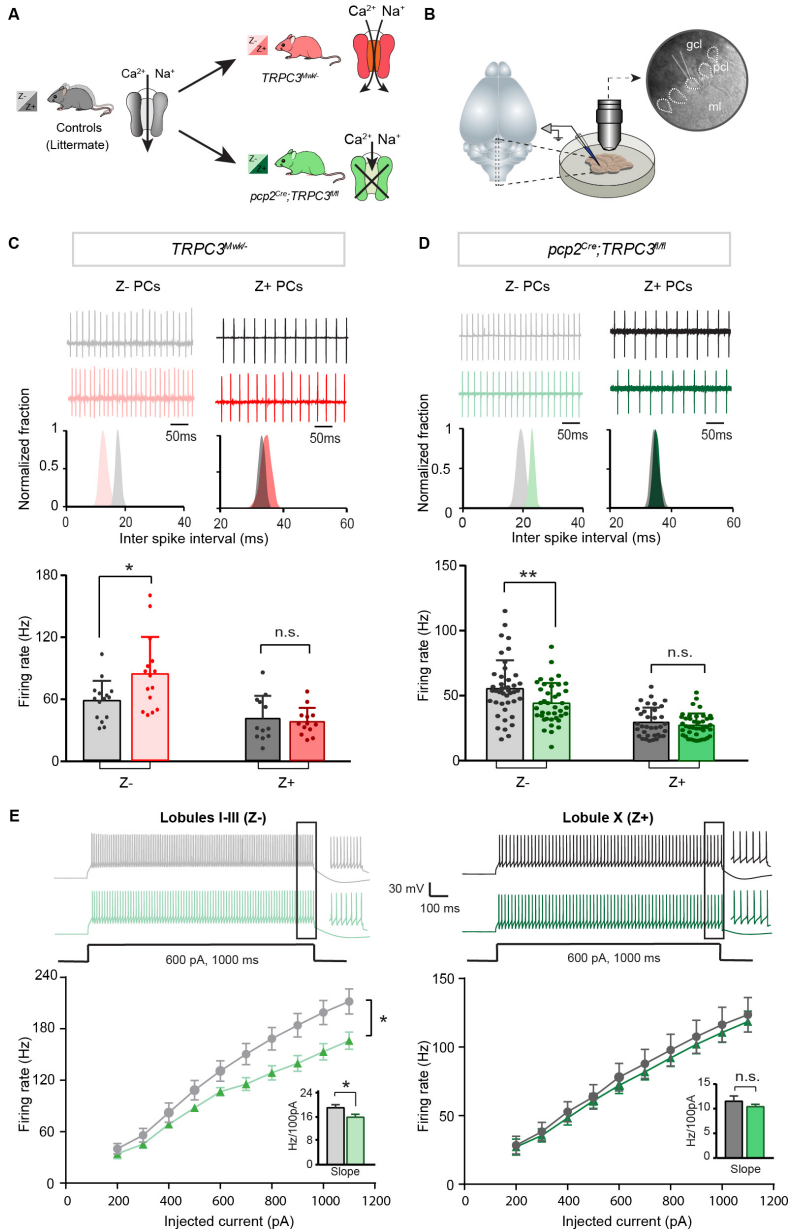
Figure 2. *Differential controls of PC firing properties by TRPC3 in vitro. (A) Schematic
drawing of TRPC3 channel function in control (black), gain-of-function (TRPC3$^{Mwk/-}$,
red) and loss-of-function (pcp2^{Cre};TRPC3$^{fl/fl}$, green) mice. (B) Schematic approach
illustrating of PCs (right circle, dashed lines) recording in vitro, in acute sagittal slices.
(C, D) Representative traces of cell-attached PC recordings (top) and corresponding
inter spike interval (ISI) distributions (middle) in a Z– PC (left) and a Z+ PC (right) of
TRPC3$^{Mwk/-}$ (C) and pcp2^{Cre};TRPC3$^{fl/fl}$ (D) mice. Z– PCs were affected in TRPC3$^{Mwk/-}$*

*(C), light-red, n = 15 cells/N = 4 mutant mice vs. n = 15 cells/N = 4 littermate controls, t_{28} = −2.47, p=0.020 and in pcp2^{Cre};TRPC3$^{fl/fl}$ mice (D), light-green, n = 40/N = 6 mutants vs. n = 43/N = 5 controls, t_{81} = 2.69, p=0.009). No differences in the firing rate of Z+ PCs in TRPC3$^{Mwk/-}$ (C), dark-red, n = 13/N = 4 mutants vs. n = 12/N = 4 controls, t_{18} = 0.419, p=0.680) and pcp2^{Cre};TRPC3$^{fl/fl}$ mice (D), dark-green, n = 36/N = 10 mutants vs. n = 35/N = 4 controls, t_{64} = 0.937, p=0.352). (E) Whole-cell patch-clamp recordings in slice from PCs of pcp2^{Cre};TRPC3$^{fl/fl}$ and control mice were used to test intrinsic excitability, by keeping cells at a holding potential of −65 mV and evoking action potentials by current steps of 100 pA (example, top). Top, exemplary traces evoked by current injection at 600 pA. Bottom, Input-output curves from whole-cell recordings of pcp2^{Cre};TRPC3$^{fl/fl}$ mice of Z– PCs (left, n = 17/N = 5 mutants vs n = 17/N = 5 controls, t_{32} = −2.20, p=0.035) and Z+ PCs (right, n = 12/N = 5 mutants vs n = 12/N = 4 controls, t22 = −0.95, p=0.354). gcl, granule cell layer; pcl, Purkinje cell layer; ml, molecular layer. (C–D), data are represented as mean ± s.d.; (E), data are represented as mean ± s.e.m., * means p<0.05 and **p<0.01. For values see Source data.*
DOI: https://doi.org/10.7554/eLife.45590.007The following source data and figure supplement are available for figure 2:
Source data 1. Source data for Figure 2 and supplement.
DOI: https://doi.org/10.7554/eLife.45590.009
Figure supplement 1. PC firing activity in TRPC3 mutants in vitro.
DOI: https://doi.org/10.7554/eLife.45590.008

<u>TRPC3 differentially controls the physiological properties of PCs in vitro:</u>

Next, we investigated the contribution of TRPC3 to cerebellar function in Z+ and Z– PCs using both gain-of-function and loss-of-function mouse models (Figure 2A). TRPC3-Moonwalker (*TRPC3$^{Mwk/-}$*) mice harbor a point mutation resulting in TRPC3 gain-of-function through increased Ca^{2+} influx upon activation (Becker *et al.*, 2009). These mice are featured by neurodegeneration, first of UBCs and later also of PCs, and as a consequence display early onset ataxia (Sekerková *et al.*, 2013). Inversely, we generated a PC-specific loss-of-function mouse model for TRPC3 (pcp2^{Cre};TRPC3$^{fl/fl}$) by crossing mice carrying loxP-flanked TRPC3 alleles (Hartmann *et al.*, 2008) with L7-Cre (Pcp2-Cre) (Barski *et al.*, 2000) mice. These pcp2^{Cre};TRPC3$^{fl/fl}$ mice exhibited no overt signs of ataxia or other movement deficits upon visual inspection. Western blotting and immunostaining of the anterior (Z–) and the posterior (Z+) cerebellar cortex of pcp2^{Cre};TRPC3$^{fl/fl}$ mice confirmed that TRPC3 protein levels are reduced, without disrupting the typical zebrin staining pattern (WB, anterior: t_{19}=2.63, p=0.034; posterior: t_{19} = 2.67, p=0.028) (Figure 1—figure supplement 3A–B,E–F). The loss of TRPC3 was specific for

cerebellar PCs, as TRPC3 expression in UBCs was not affected (Figure 1—figure supplement 3F, white arrow heads).

PCs are intrinsically active pace-making neurons, which fire regular action potentials even when deprived of synaptic inputs (Raman and Bean, 1999; Womack and Khodakhah, 2002). To FIG 2 determine the contribution of TRPC3 to the activity of Z+ and Z– PCs, we performed in vitro electrophysiological recordings on sagittal sections of adult mice of both mutants (Figure 2B), taking lobules X and I-III as proxies for Z+ and Z– PC modules, respectively (see Brochu et $al.$, 1990; Sugihara and Quy, 2007; Zhou et $al.$, 2014). In littermate controls, the intrinsic firing rate of Z– PCs is higher than that of Z+ PCs, confirming previous results (Zhou et $al.$, 2014). Gain-of-function TRPC3$^{Mwk/-}$ mice showed an increase in PC simple spike firing rate selectively in Z– PCs (84.5 ± 36.2 Hz vs. 58.4 ± 19.6 Hz for mutants vs. controls; t_{19} = -2.47, p=0.020), without affecting Z+ PCs (36.7 ± 13.0 Hz vs. 39.7 ± 21.5 Hz for mutants vs. controls t_{21}=0.419, p=0.680) (Figure 2C). Inversely, ablating TRPC3 from PCs caused a decrease in firing rate in Z– PCs (44.1 ± 15.6 Hz vs. 55.4 ± 21.8 Hz, mut. vs. ctrl, t_{81}=2.69, p=0.009), again without affecting Z+ PCs (28.5 ± 9.3 Hz vs. 30.8 ± 11.7 Hz, mut. vs. ctrl, t_{64}=0.937, p=0.352) (Figure 2D). However, in the absence of TRPC3 the firing rate of Z– PCs does not drop to the levels of Z+ PCs, suggesting that TRPC3 provides a major, but not exclusive, contribution to the difference. We also assessed the regularity of firing activities by measuring the coefficient of variation (CV) and the coefficient of variation of adjacent intervals (CV2) of ISI. Both the CV and CV2 of Z– PCs in lobules I-III declined significantly in $pcp2^{Cre}$;TRPC3$^{fl/fl}$ mice, while remaining unchanged in $TRPC3^{Mwk/-}$ mice; in contrast, in Z+ lobule X, none of these parameters were altered in either $TRPC3^{Mwk/-}$ or $pcp2^{Cre}$;TRPC3$^{fl/fl}$ mice (Figure 2—figure supplement 1A–B).

To verify the effect of TRPC3 deletion on other cell physiological properties of PCs, we performed whole-cell patch-clamp recordings in a subset of PCs. Injections of current steps into PCs evoked increasing numbers of action potential, in the presence of blockers for both excitatory and inhibitory synaptic inputs. In line with the cell-attached recordings, in loss-of-function $pcp2^{Cre}$;TRPC3$^{fl/fl}$ mice, PC intrinsic excitability, quantified by the slope of firing rate versus current injection curve, was significantly reduced in lobules I-III (16.0 ± 1.0 Hz/100 pA vs. 19.2 ± 1.1 Hz/100 pA, mut. vs. ctrl, t_{32}=-2.20, p=0.035), but unchanged in lobule X, compared with those of littermate controls (10.4 ± 0.5 Hz/100 pA vs. 11.5 ± 1.1 Hz/100 pA, mut. vs. ctrl, t_{22}=-0.95, p=0.354) (Figure 2E). Other physiological parameters in terms of holding current, amplitudes, half-widths and after-hyperpolarization amplitudes (AHPs), were not significantly affected in either lobules I-III or lobule X (Figure 2—figure supplement 1C).

Together, our in vitro recordings from gain- and loss-of-function mutants indicate that TRPC3selectively controls the activity in Z– PCs, without affecting other cell intrinsic properties. Thus, at least in vitro, TRPC3 contributes to the difference in intrinsic firing activity between Z+ and Z– PCs,by directly controlling the intrinsic excitability of Z– PCs.

<u>TRPC3 regulates the activity of simple spikes selectively in Z– PCs in vivo:</u>

To examine the role of TRPC3 in the closed loop, intact cerebellar module, we next performed PC recordings in vivo in adult mice during quiet wakefulness (Figure 3A). PCs could be identified during extracellular recordings by the presence of complex spikes, while the consistent presence of a pause in simple spikes following each complex spike confirmed that the recording was obtained from a single unit (De Zeeuw *et al.*, 2011). PC recording locations in either Z– lobules I-III or Z+ lobule X were confirmed with iontophoretic injections of biotinylated dextran amine (BDA), which could be identified by immunostaining (Figure 3B). As we showed before (Zhou *et al.*, 2014; Zhou *et al.*, 2015), PCs in Z– modules fired simple spikes at a higher rate than those in Z+ modules (Figure 3D and F).

In vivo, in the presence of physiological inputs the PCs in Z– lobules I-III of *TRPC3$^{Mwk/-}$* mutants showed an increased simple spike firing rate (110.0 ± 22.6 Hz vs. 89.1 ± 15.3 Hz, mut. vs. ctrl, t_{60}=- 4.58, p<0.001), whereas the Z+ PCs were unaffected (50.6 ± 13.6 Hz vs. 45.3 ± 10.4 Hz, mut. vs. ctrl, t_{42}=-1.47, p=0.148). Conversely, Z– PCs in *pcp2^{Cre};TRPC3$^{fl/fl}$* mutants featured a decreased simple spike firing rate (74.4 ± 18.6 Hz vs. 88.5 ± 17.4 Hz, mut. vs. ctrl, t_{54}=2.88, p=0.006), but again without changes in PCs of the Z+ lobule X (50.2 ± 15.5 Hz vs. 50.0 ± 12.9 Hz, mut. vs. ctrl, t_{54}=-0.053, p=0.958), all compared to those of their littermate controls (*Figure 3C–F*). Thus, here too, the ablation of TRPC3 did not decrease simple spike firing rate in the Z– PCs completely to levels of Z+ PCs (74.4 Hz vs. 50.0 Hz in Z– vs. Z+ of *pcp2^{Cre};TRPC3$^{fl/fl}$*, respectively). Unlike in vitro, PCs in the *pcp2^{Cre};TRPC3$^{fl/fl}$* mice showed comparable CV and CV2 to controls for both Z– and Z+ modules (Figure 3—figure supplement 1C–D). The CV of simple spike ISI was, however, prominently elevated in both Z– and Z+ modules in *TRPC3$^{Mwk/-}$* mutants (Figure 3—figure supplement 1A), while the CV2 did not differ (Figure 3—figure supplement 1B). It should be noted that PC regularity in vivo is largely determined by external inputs (compare Figure 2—figure supplement 1 to Figure 3—figure supplement 1), which thereby can offset those intrinsic variations induced by the mutation of TRPC3. The irregular firing activity of PCs in *TRPC3$^{Mwk/-}$* mutants, at least for Z+ PCs,

may be attributed to impaired function or degeneration of UBCs, while the physiological synaptic input in vivo in *pcp2^Cre^;TRPC3^fl/fl^* mice could obscure the regularity changes observed in vitro in these mice.

In short, even in vivo, in the presence of all physiological inputs both gain-of-function and loss-of-function mutations of TRPC3 exclusively affects Z– PCs, with the most pronounced, persistent effect being the mutation-selective influence on simple spike firing rate.

<u>TRPC3-related effects correlate with zebrin expression and are independent of development:</u>

Our results so far have identified selective TRPC3-related effects by comparing lobules I-III and X, as proxies for Z– and Z+ modules. Immunohistochemical analysis indicated that the TRPC3 expression differs substantially between these lobules (Figure 1—figure supplements 1–2 and Figure 1—video 1), suggesting that the effects of gain- and loss-of-function mutations could be directly related to protein levels. Alternatively, other differences in molecular machinery could underlie or further enhance this cellular differentiation, for instance through mGluR1b-related effects. As the difference in TRPC3 expression is minimal or absent in the more lateral parts of the cerebellum (Figure 1—figure supplements 1–2), recording the activity of adjacent Z– and Z+ PCs there would solve this question (Wu and Schonewille, 2018). To this end, we crossed *pcp2^Cre^;TRPC3^fl/fl^* mice with EAAT4^GFP^ mice that express GFP in Z+ PCs to generate *pcp2^Cre^;TRPC3^fl/fl^;EAAT4^GFP/-^* mice. Using two-photon microscopy, we identified Z+ and Z– modules on the dorsal surface (lobules IV-VI and simplex) of the cerebellum and recorded PC activity (Figure 4A–B). Here, the absence of TRPC3 attenuated the firing rate (36.5 ± 23.2 Hz vs. 72.7 ± 26.5 Hz, mut. vs. ctrl, $t_{28}=3.99$, $p<0.001$) and enhanced the irregularity (e.g. CV: 0.55 ± 0.16 vs. 0.44 ± 0.10, mut. vs. ctrl, $t_{28}=-2.27$, $p=0.031$) of Z– PCs even more robustly, without an effect on Z+ PCs (rate: 36.6 ± 19.5 Hz vs. 33.0 ± 9.8 Hz, mut. vs. ctrl, $t_{21}=-0.550$, $p=0.588$; CV: 0.47 ± 0.22 vs. 0.56 ± 0.26, mut. vs. ctrl, $t_{21}=0.853$, $p=0.393$) (Figure 4C–D, Figure 4—figure supplement 1A–B, cf Figure 3F). The similar firing rates of Z– and Z+ PCs lacking TRPC3 inthese targeted recordings supports the possibility that in some areas TRPC3 is solely responsible for the difference and that further differentiation divides the zebrin-based populations into smaller subpopulations (Armstrong *et al.*, 2001). It also fits with the finding that other proteins, for example mGluR1b, influence TRPC3 activity and thereby differentially determine the spikingFIG 3FIG 4activity of PCs in areas where TRPC3 expression is more homogeneous. As stated above, the
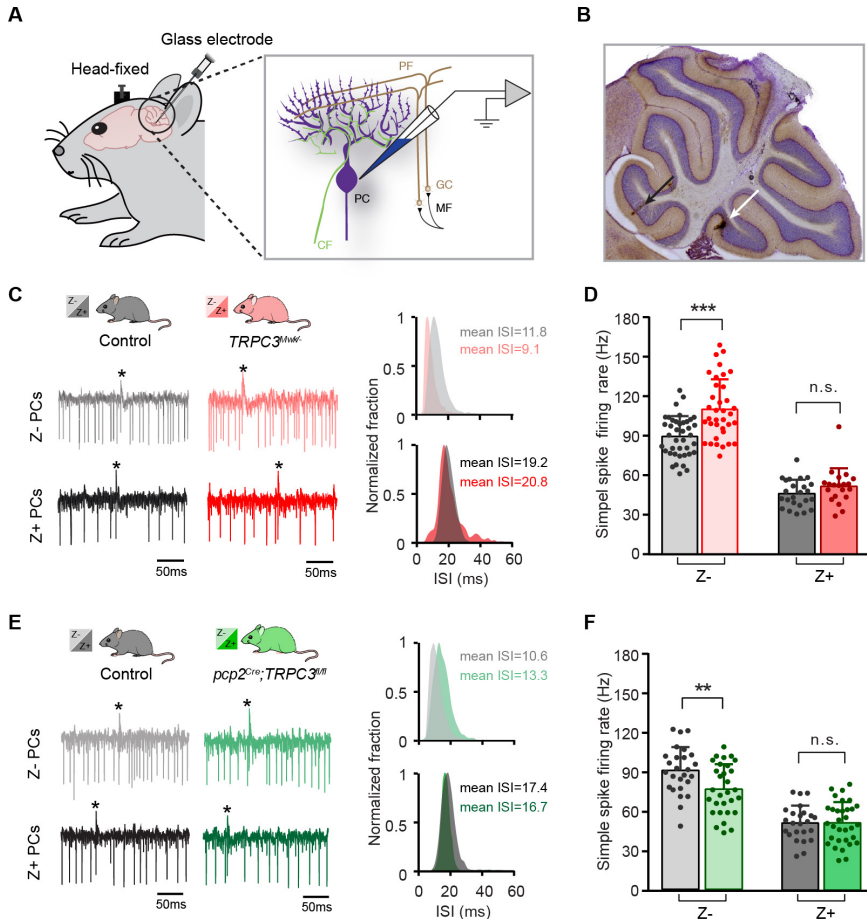
Figure 3. TRPC3 contributes to the in vivo simple spike firing rate of Z–, but not Z+ PCs. (A) Schematic illustration of extracellular recording configuration in vivo. PF, parallel fiber; CF, climbing fiber; MF, mossy fiber; GC, granule cell. (B) Representative sagittal cerebellar section with recording sites labeled by BDA injection, in lobule II (black arrow) and X (white arrow). (C) Representative example traces (left) and ISI distributions (right) of a Z– PC (top) and a Z+ PC (bottom) in gain-of-function TRPC3$^{Mwk/-}$ mice. (D) PC simple spike firing rate recorded in vivo in TRPC3$^{Mwk/-}$ mice compared to control littermates, for the Z–lobules I-III (light-red, n = 36/N = 7 mutants vs. n = 40/N = 6 controls, t_{60} = −4.58, p<0.001) and the Z+ lobule X (dark-red, n = 20/N = 6 mutants vs. n = 24/N = 5 controls, t_{42}=-1.47, p=0.148). (E) Representative example traces (left) and ISI distributions (right) in a Z– PC (top) and a Z+ PC (bottom) of loss-of-function pcp2^{Cre};TRPC3$^{fl/fl}$ mice. (F) PC simple spike firing rate of pcp2Cre;TRPC3fl/fl mice compared to controls, for Z– lobules I-III (light-green, n = 30/N = 7 mutants vs. n = 26/N = 8 controls, t_{54}=2.88, p=0.006) and in Z+ lobule X (dark-green, n = 32/N = 8 mutants vs. n = 24/N = 6 controls, t_{54} = −0.053, p=0.958). Data are represented as mean ± s.d., for values see Source data, ** means p<0.01 and ***p<0.001.

experiments in loss-of-function *pcp2^{Cre};TRPC3$^{fl/fl}$* mice suggest that TRPC3 cannot account for the entire difference between Z+ and Z– PCs. As the L7 promotor turns on early in development (postnatal week 1–2; Barski *et al.*, 2000), it could be that the ablation of TRPC3 early in development provokes compensatory mechanisms that limit the decrease in simple spike rate in Z– PCs in adult mice. Alternatively, developmental changes in the activity in the olivocerebellar loop could be partially responsible for the lower firing rate. To test the possibility that developmental effects influenced PC activity in the adult mice, we crossed the *loxP*-flanked TRPC3 mice with tamoxifen-dependent *pcp2^{CreERT2}* to generate *pcp2^{CreERT2};TRPC3$^{fl/fl}$* mice (Figure 4E). Four weeks after tamoxifen treatment, *pcp2^{CreERT2};TRPC3$^{fl/fl}$* mice showed a virtually complete ablation of TRPC3 in PCs (Figure 4F). If the absence of TRPC3 early in development drives compensatory mechanisms or contributes to the low simple spike firing rate in adult Z– PCs, we should observe a larger or smaller effect, respectively, in *pcp2^{CreERT2};TRPC3$^{fl/fl}$* adult mice after tamoxifen injections (injected after maturation). In vivo recordings revealed that, again, simple spike firing rates were affected in Z– (from lobules I-III, 72.9 ± 9.1 Hz vs. 86.5 ± 10.9 Hz, mut. vs. ctrl, t_{53} = 5.05, p<0.001), but not Z+ PCs (lobule X, rate: 47.0 ± 11.6 Hz vs. 51.6 ± 13.4 Hz, mut. vs. ctrl, t_{44}=1.21, p=0.234) of tamoxifen injected adult *pcp2^{CreERT2};TRPC3$^{fl/fl}$* mice (Figure 4G–H and Figure 4—figure supplement 1C–D), in a manner similar to that in *pcp2^{Cre};TRPC3$^{fl/fl}$* mice. To verify the efficiency and selectivity of the inducible PC-specific Cre expression line, these mice were also crossed with Cre-dependent tdTomato expressing (Ai14) mice and injected with tamoxifen in the same manner. Confocal images confirm that labeling is virtually exclusively found in PCs (Figure 4—figure supplement 1E).

Taken together and combined with *pcp2^{Cre};TRPC3$^{fl/fl}$* data, these results indicate that the TRPC3-dependent effects in zebrin-identified PCs are independent of cerebellar development or develop-mental compensation. Moreover, the larger effect of TRPC3 ablation on Z– PCs in areas where its expression is similar to that in Z+ PCs points towards a further subdivision based on other proteins that might contribute to the simple spike rate in Z– PCs.
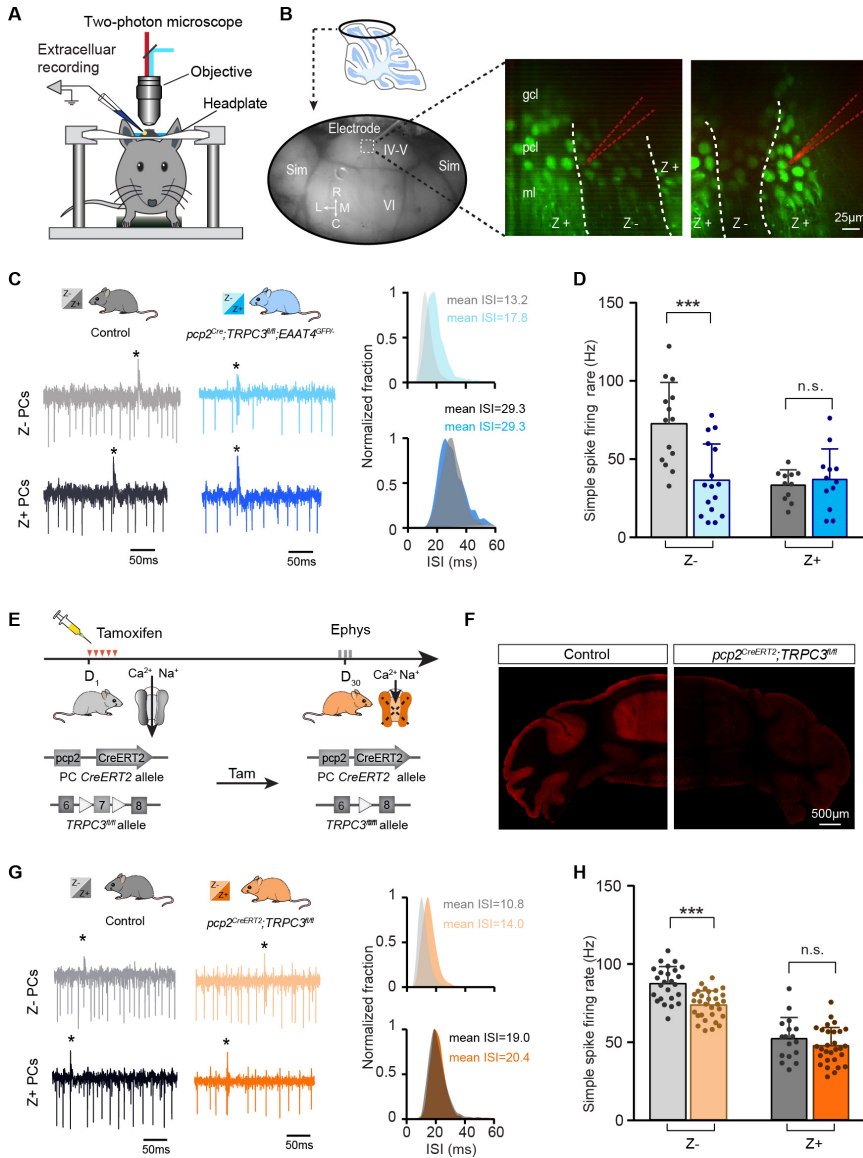
Figure 4. *The contribution of TRPC3 to firing rate is dependent on zebrin-identity and independent of developmental changes. (A) Schematic experimental setup for two-photon imaging-based targeted PC recordings, in vivo. (B) Sagittal view of cerebellum (schematic, top) indicating the recording region in the ellipse (bottom). Representative images (right) show the visualization of Z+ bands (dark green) in an awake pcp2^Cre;TRPC3^fl/fl; EAAT4^GFP/- mouse, with recording electrodes (red) positioned in Z– (left) and Z+ (right) bands. (C) Representative firing traces (left) and ISI distributions (right) in a Z– PC (top) and a Z+ PC (bottom) of loss-of-function pcp2^Cre;TRPC3^fl/fl;EAAT4^GFP/- mice (blue) and control littermates (no*

Cre; gray). (D) Average simple spike firing rate of PCs recorded from adjacent modules of pcp2^{Cre};TRPC3$^{fl/fl}$;EAAT4$^{GFP/-}$ mice and those in controls. Comparison for Z– PCs (light-blue, n = 16/N = 3 mutants vs. n = 14/N = 2 controls, t$_{28}$ = 3.99, p<0.001), and Z+ PCs (dark-blue, n = 12/N = 3 mutants vs. n = 12/N = 2 controls, t$_{21}$ = −0.550, p=0.588). (E–F) Intraperitoneal tamoxifen injections for five days (D1-5) to trigger TRPC3 gene ablation solely in PCs in adult pcp2^{CreERT2};TRPC3$^{fl/fl}$ mice. Open triangles indicate loxP sites. PC in vivo extracellular activity was recorded four weeks later (D29-31) in pcp2^{CreERT2};TRPC3$^{f/fl}$ mice (orange). TRPC3 deletion was confirmed post-mortem by confocal imaging following anti-TRPC3 staining (F). (G) Representative firing traces (left) and ISI distributions (right) in a Z– PC (top) and a Z+ PC (bottom) of pcp2^{CreERT2};TRPC3$^{fl/fl}$ mice. (H) Simple spike firing rate in vivo in pcp2^{CreERT2};TRPC3$^{fl/fl}$ and control mice (no Cre) recorded in lobules I-III (Z–) and lobule X (Z+) PCs. Comparison for Z– PCs (light-orange, n = 30/N = 4 mutants vs. n = 25/N = 4 controls, t$_{53}$ = 5.05, p<0.001), and Z+ PCs (dark orange, n = 29/N = 4 mutants vs. n = 17/N = 3 controls, t$_{44}$ = 1.21, p=0.234). Sim, simplex lobule; IV-VI, lobules IV-VI, R, rostral, C, caudal; L, lateral, M, medial. Data are represented as mean ± s.d., for values see Source data, *** means p<0.001.

DOI: https://doi.org/10.7554/eLife.45590.013The following source data and figure supplement are available for figure 4:

Source data 1. *Source data for Figure 4 and supplement.*
DOI: https://doi.org/10.7554/eLife.45590.015

Figure supplement 1. *In vivo extracellular recordings of PC simple spike activity in pcp2^{Cre};TRPC3$^{fl/fl}$;EAAT4$^{GFP/-}$ and pcp2^{CreERT2};TRPC3$^{fl/fl}$ mice.*
DOI: https://doi.org/10.7554/eLife.45590.014

TRPC3 mutations selectively affect the activity in Z– olivocerebellar modules:

PCs in the cerebellar cortex, form a closed loop with the cerebellar nuclei neurons they innervate by their axon output and the olivary neurons from which they receive their climbing fiber input (Ruigrok, 2011). If TRPC3 contributes to the output of this loop, one could hypothesize that other elements in the loop should be affected by the mutations (Chaumont *et al.*, 2013; Witter *et al.*, 2013). To test this hypothesis, we examined complex spikes activity in PCs, as the complex spike directly reflects the activity of the climbing fiber and thereby that of the inferior olivary neuron it originates from Chaumont *et al.* (2013). We identified complex spikes based on their characteristic shape in our in vivo recordings from Z– lobules I-III or Z+ lobule X (Figure 5A). Complex spike firing rates were, similar to simple spike rates, higher in Z– than in Z+ PCs (*Figure 5B*), as shown previously (Zhou *et al.*, 2014). Chronic manipulations of TRPC3 activity, gain- and loss-of-function, in PCs predominantly affected complex spike firing rate in Z– (*TRPC3$^{Mwk/-}$*: t$_{68}$=2.68, p=0.009; *pcp2^{Cre};TRPC3$^{fl/fl}$*: t$_{54}$=2.50, p=0.016; *pcp2^{Cre};TRPC3$^{fl/}$*

fl;EAAT4$^{GFP/-}$: t$_{28}$=3.49, p=0.002), but not Z+ PCs (*TRPC3$^{Mwk/-}$*: t$_{42}$=1.56, p=0.126; *pcp2^{Cre};TRPC3$^{fl/fl}$*: t54=1.41, p=0.164), except for that in *pcp2^{Cre}*;FIG 5*TRPC3$^{fl/fl}$;EAAT4$^{GFP/-}$* mice (t$_{20}$ = 3.03, p=0.007) (Figure 5B). Intriguingly, acute ablation of TRPC3 in *pcp2^{CreERT2};TRPC3$^{fl/fl}$* mice did not affect complex spike activity in terms of firing rate, CV, CV2 or pause in simple spikes following climbing fiber activation (CF-pause) in Z– PCs (rate: t$_{53}$=-0.940, p=0.352) (Figure 5B bottom panel, Figure 5—figure supplement 1J–L). In line with the lower simple spike firing rates in loss-of-function TRPC3 mutants, the CF-pause of *pcp2^{Cre};TRPC3$^{fl/fl}$* and *pcp2^{Cre};TRPC3$^{fl/fl}$;EAAT4$^{GFP/-}$* mice were longer, selectively in Z– PCs (Figure 5—figure supplement 1F and I). Except for the CV value, other complex spike parameter changes in *TRPC3$^{Mwk/-}$* mice were not affected (Figure 5—figure supplement 1A–C, see also discussion). In *pcp2^{Cre};TRPC3$^{fl/fl}$* mice, the CV and CV2 of complex spike in both Z– and Z+ PCs do not differ from littermate controls (Figure 5—figure supplement 1D–E), however, in *pcp2^{Cre};TRPC3$^{fl/fl}$;EAAT4$^{GFP/-}$* mice, they were significantly increased for Z– PCs, not Z+ PCs, compared to those of littermate controls (Figure 5—figure supplement 1G–H). Together, in vivo experiments indicate that TRPC3 also selectively affects the activity in the inferior olive in that the Z– modules are most prominently affected, and this effect is only present when TRPC3 is deleted early in development.

Complex spikes are known to have a direct influence on simple spike activity (CS-SS) (Simpson *et al.*, 1996; Zhou *et al.*, 2014). Based on the peri-complex spike time histograms, we could categorize four different types of simple spike responses following the CF-pause (see also Zhou *et al.*, 2014), including no change in rate (normal), increased simple spike activity (facilitation), decreased simple spike activity (suppression), and a superimposed oscillatory pattern (oscillation) (Figure 5C). Our data confirmed our previous finding that the CS-SS interaction pattern among the Z+ and Z– PCs is different in that the facilitation prevails in the Z– PCs, whereas the suppression and oscillation types occur predominantly in the Z+ PCs (Figure 5D), with oscillations seen virtually exclusively in PCs with firing rates < 50 Hz and CV <0.3 (Zhou *et al.*, 2014). In addition, we found that manipulation of TRPC3 activity changed the types of CS-SS responses most frequently in Z– PCs (Figure 5D). Interestingly, Z– PCs exhibited much more suppression in gain-of-function *TRPC3$^{Mwk/-}$* mutants and vice versa more facilitation in loss-of-function *pcp2^{Cre};TRPC3$^{fl/fl}$;EAAT4$^{GFP/-}$* mice, compared to those in their littermate controls (Figure 5D), suggesting that Z– PCs partly compensate for the effects of TRPC3 manipulation.

Together, these results indicate that TRPC3 controls not only the activity of PCs, but also that of the inferior olivary neurons, another element
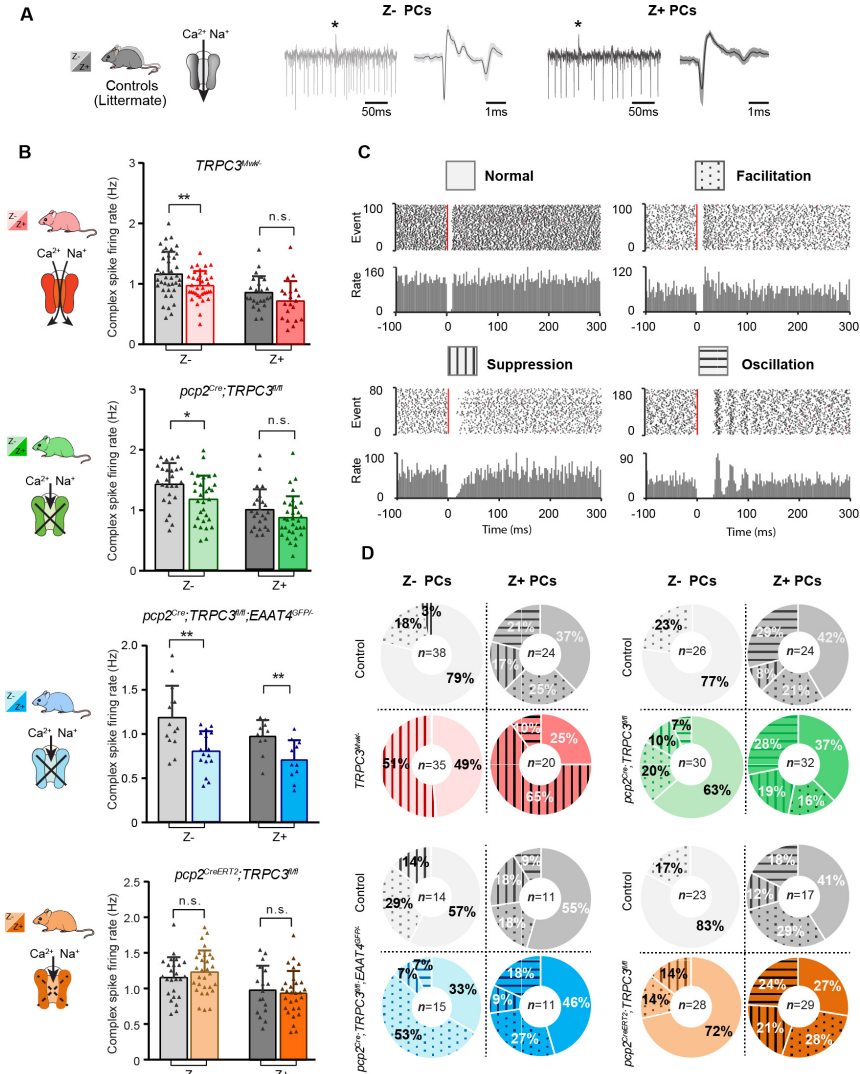
Figure 5. *Complex spikes and complex spike - simple spike interaction are affected by TRPC3 mutations. (A) Representative PC recording traces and complex spikes shape of Z– (light black) and Z+ (dark black) PCs in the control mice. (B) Top half, comparison of complex spike firing rates in TRPC3$^{Mwk/-}$ (red) and pcp2^{Cre};TRPC3$^{fl/fl}$ (green) mice versus their respective littermate controls for Z– PCs (TRPC3$^{Mwk/-}$: t_{68}=2.68, p=0.009; pcp2^{Cre}; TRPC3$^{fl/fl}$: t_{54}=2.50, p=0.016) and Z+ PCs (TRPC3$^{Mwk/-}$: t_{42}=1.56, p=0.126; pcp2^{Cre};TRPC3$^{fl/fl}$: t_{54}=1.41, p=0.164). Bottom half, comparison of complex spike firing rates in pcp2^{Cre};TRPC3$^{fl/fl}$;EAAT4$^{GFP/-}$ (blue) and pcp2^{CreERT2};TRPC3$^{fl/fl}$ (orange) mice versus their respective controls for Z– PCs (pcp2^{Cre}; TRPC3$^{fl/fl}$;EAAT4$^{GFP/-}$: t_{28}=3.49, p=0.002; pcp2^{CreERT2};TRPC3$^{fl/fl}$: t_{53}=-0.940, p=0.352) and Z+ PCs (pcp2^{Cre};TRPC3$^{fl/fl}$;EAAT4$^{GFP/-}$: t_{20}=3.03, p=0.007; pcp2^{CreERT2};TRPC3$^{fl/fl}$: t_{44}=0.448, p=0.656). (C)*

Raster plots of simple spike activity around the occurrence of each complex spike (−100 to +300 ms). These peri-complex splike time histograms can, based on post-complex spike activity, be divided into one of four types: normal (no change), facilitation, suppression and oscillation. (D) The distribution of post-complex spike response types for Z− and Z+ PCs, in TRPC3$^{Mwk/-}$, pcp2^{Cre};TRPC3$^{fl/fl}$, pcp2^{Cre};TRPC3$^{fl/fl}$;EAAT4$^{GFP/-}$ and pcp2^{CreERT2};TRPC3$^{fl/fl}$ mice. Data are represented as mean ± s.d., for values see Source data, * means p<0.05 and **p<0.01.

in the olivocerebellar loop. Moreover, manipulation ofTRPC3 activity alters the interaction between complex spikes and simple spikes.

Functional heterogeneity of TRPC3 is reflected in differential effects on motor behaviors:

The ultimate question is: does cellular heterogeneity of PCs also differentially affect their contribution to specific cerebellar functions? As the *TRPC3$^{Mwk/-}$* mutation is not cell-specific and affects for instance also UBCs (Sekerková *et al.*, 2013), we focused on the behavioral effects in *pcp2^{Cre};TRPC3$^{fl/fl}$* mice. *pcp2^{Cre};TRPC3$^{fl/fl}$* mice did not show any overt signs of changes in development or weight, changes in module anatomy or connectivity or signs of any type of locomotion deficit. Before testing specific functions, we first evaluated the consequences of the manipulations of TRPC3 on locomotion, a type of behavior that by nature requires the entire body and as such can be linked to many sub-regions of the cerebellar cortex, ranging from the Z+ vestibular zones to the Z− anterior lobules. We investigated whether these mutant mice showed any obvious deficits in locomotion using the Erasmus Ladder (Vinueza Veloz *et al.*, 2015) (Figure 6—figure supplement 1A). *pcp2^{Cre};TRPC3$^{fl/fl}$* mice could not be discriminated from control littermates by the percentage of different types of steps, including lower steps, also known as missteps (Figure 6—figure supplement 1B–C). The apparent discrepancy with earlier evidence in stride width in the global TRPC3 knockout (Hartmann *et al.*, 2008) could be due to the different methods or the fact that UBCs, particularly important in

the vestibular zone, are also affected in that mouse model (Sekerková´ *et al.*, 2013).

Next, we subjected *pcp2^{Cre};TRPC3$^{fl/fl}$* mice to two specific, but intrinsically distinct types of cerebellum-dependent learning tasks, that is, vestibulo-ocular reflex (VOR) adaptation and eyeblink conditioning. VOR adaptation is the adjustment of the amplitude and/or direction of compensatory eye movements controlled by the vestibulocerebellum (Figure 6A–C), which is predominantly Z+ (Figure 6—figure supplement 2A–B). Eyeblink conditioning requires the animal to generate a well-timed movement following a previously unrelated sensory input and is linked to more anterior regions that are largely Z– (Figure 7A and Figure 6—figure supplement 2A–B). Note that the difference in zebrin labeling is pronounced between the two related regions; while the difference in TRPC3 staining is less clear (Figure 6—figure supplement 2A–B). Nonetheless, given the electrophysiological changes described above, we hypothesized that altered TRPC3 function should impair Z– linked eyeblink conditioning, whereas VOR adaptation would be unaffected.

Before examining adaptation, we first tested whether the basal eye movement reflexes, the optokinetic reflex driven by visual input (OKR) and the vestibular input-driven VOR (in the dark) and visually-enhanced VOR (VVOR, in the light), were affected. Neither the gain (the ratio of eye movement to stimulus amplitude), nor the phase (timing of the response relative to input), differed significantly between *pcp2^{Cre};TRPC3$^{fl/fl}$* mutants and littermate controls (all p>0.25) (Figure 6—figure supplement 2C). Next, using mismatched visual and vestibular stimulation, we tested the ability of mutant mice to adapt their compensatory eye movements. When *pcp2^{Cre};TRPC3$^{fl/fl}$* mice were subjected to both out-of-phase and in-phase training paradigms, we did not observe any significant deficit in the VOR gain increase and VOR gain decrease, respectively (VOR increase, F = 0.012, p=0.913; VOR decrease, F = 0.252, p=0.621) (Figure 6D–E). To evaluate the ability of the mice to perform a long-term, more demanding adaptation, we subjected the mice for four more days, following the gain decrease training, to a training stimulus aimed at reversing the direction of their VOR, referred to as VOR phase reversal (Figure 6G). Again, no difference was found between *pcp2^{Cre};TRPC3$^{fl/fl}$* and control littermate mice: neither in the VOR phase over the training (Figure 6H), nor in the increase OKR gain following the phase reversal training (VOR phase reversal, F = 0.006, p=0.942; OKR increase, F = 0.922, p=0.922)(Figure 6F, compare to Figure 6—figure supplement 2C).

To determine whether the differential activity of TRPC3 ultimately also affects the behavior of the animal, we subjected mice to a task linked to

Z– modules, that is delay eyeblink conditioning. Mice were trained using a light pulse with 250 ms duration as the conditioned stimulus (CS) and a puff to the cornea as a short unconditioned stimulus (US) at the end of the CS, which over the period of several days evoked conditioned responses (CR, preventative eyelid closure) in the absence of the US (Figure 7B). In contrast to VOR adaptation, the L7-TPRC3[KO] mice showed significant deficits in eyeblink conditioning during the first week of training (Figure 7C). However, when we subjected them to longer periods, they reached similar CR percentages, amplitudes and timing (Figure 7D and Figure 7—figure supplement 1A–B). The delayed appearance of evoked conditioned responses could neither be explained by a deficit in the ability to close the eyelid, as the timing of the unconditioned response (UR) did not differ between mutant and control mice (Figure 7—figure supplement 1C), nor by a lower level of locomotor activity (Figure 6—figure supplement 1), which has previously been shown to impair eyeblink conditioning (Albergaria *et al.*, 2018).

Thus, although TRPC3 is expressed in both regions underlying the cerebellum-dependent behavioral experiments tested here, TRPC3 activity is selectively required to optimize the cerebellum-dependent learning behavior that is processed in a Z– module (De Zeeuw and Ten Brinke, 2015). This indicates that the cellular heterogeneity and consequential differentiation in cellular activity also affects the behavior of the animals.

Discussion

The cerebellum offers a rich repertoire of electrophysiological properties that allows us to coordinate a wide variety of sensorimotor and cognitive behaviors. We recently uncovered that there are at least two main types of cerebellar modules with different intrinsic profiles (Zhou *et al.*, 2014) and plasticity rules (Wadiche and Jahr, 2005; Suvrathan *et al.*, 2016; Voges *et al.*, 2017). This organization is highly preserved throughout phylogeny and characterized by a series of molecular markers FIG 6 such as zebrin that are distributed in a complementary fashion across the cerebellar cortex (Apps and Hawkes, 2009; Marzban and Hawkes, 2011; Graham and Wylie, 2012). Here, we demonstrated that zebrin-negative PCs show a relatively high expression of TRPC3, which has a dominant impact on its electrophysiological features (Figure 8). Indeed, gain-of-function and loss-of-function mutations in the gene encoding for TRPC3 selectively affected activity in the zebrin-negative modules and the motor behavior that is controlled by these modules.

Our results confirm previous work indicating that TRPC3 is expressed in all PCs, yet for the first time reveal that its expression is non-uniform and largely complementary to that of well-known marker of cerebellar modules, Zebrin II. Notably, the ablation of TRPC3 decreased the firing rate of Z– PCs to that of Z+ PCs in the superficial areas that were targeted by imaging approaches, but did not completely delete the difference in lobules I-III. Hence, TRPC3 is at least a major contributor to the increased firing rate of Z– PCs, but other factors putatively contribute as well. Although TRPC3 is present in all PCs, loss- and gain-of-function mutations selectively affected Z– PCs, suggesting that other proteins in the pathway leading to TRPC3 activation may be involved. TRPC channels, which are calcium-permeable upon activation by phospholipase C or diacylglycerol, are widely expressed in the brain and critically involved in the development and maintenance of synaptic transmission (Hartmann *et al.*, 2008; Hartmann *et al.*, 2011; Becker, 2014; Sun *et al.*, 2014). TRPC1 and TRPC3 are both prominently expressed in the cerebellum, but in PCs TRPC3 is most abundant (Hartmann *et al.*, 2008). In addition to its contribution to intrinsic activity, TRPC3 currents also mediate the slow excitatory postsynaptic potential following activation of mGluR1b, which is expressed in a pattern complementary to that of zebrin (Mateos *et al.*, 2001; Hartmann *et al.*, 2011; Ohtani *et al.*, 2014). Our results indicate that TRPC3 can be detected in all PCs in a pattern that is largely, but not completely, complementary to that of Zebrin II, while the effects of TRPC3 ablation are restricted to zebrin-negative PCs. Taken together, this suggests that it is in fact the 'molecular machinery' involving mGluR1b activation combined with TRPC3 expression patterns, that drive the differential TRPC3 function.

In contrast to mGluR1b, mGluR1a is expressed by all PCs (estimated ratio 2:1 to mGluR1b)(Mateos *et al.*, 2001). The metabotropic receptor mGluR1a is important for IP3-mediated calciumrelease, climbing fiber elimination as well as PF-PC LTD (Ohtani *et al.*, 2014). Intriguingly, and in line with the concept of modular differentiation, mGluR1-dependent processes are hampered in zebrin-positive PCs by the expression of EAAT4 (Wadiche and Jahr, 2005), whereas zebrin-negative PCs selectively express PLCb4 that works in concert with mGluR1a (Ohtani *et al.*, 2014). The differences in expression patterns may enhance the probability of PF-PC LTD in zebrin-negative PCs over FIG 7 that in zebrin-positive PCs, which is supported by experiments performed in P21 mice (Wadiche and Jahr, 2005). The consequences of EAAT4 or PLCb4 deletion on PC physiology have been evaluated in vitro in several studies (*Hashimoto et al., 2001;* Miyata *et al.*, 2001; Wadiche and Jahr, 2005; Perkins *et al.*, 2018), but what the consequences in vivo on circuit physiology and on the behaviors tested here are, is unclear.
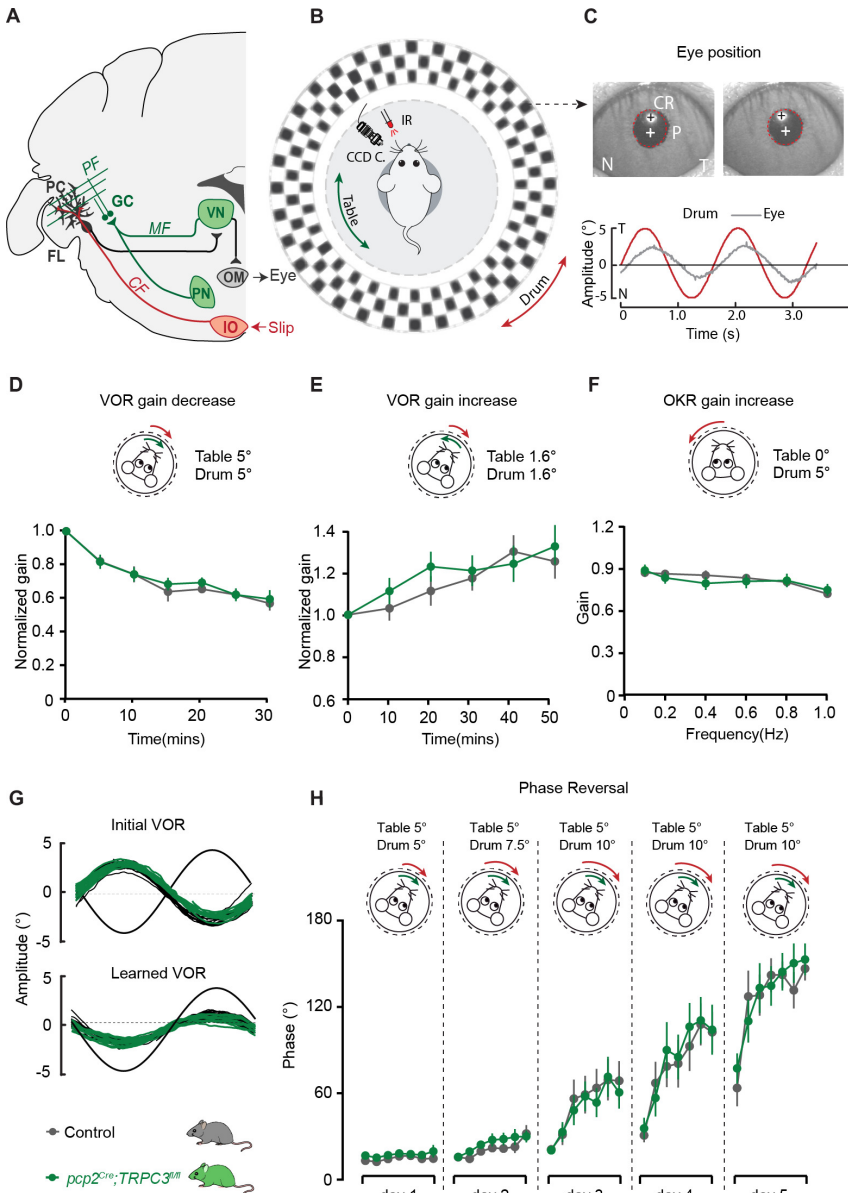
Figure 6. PC-specific deletion of TRPC3 does not affect Z+-dependent VOR adaptation. (A) Cerebellar circuitry controlling compensatory eye movements and their adaptation. PCs in the flocculus (FL) receive vestibular and visual input via the mossy fiber (MF) - parallel fiber (PF) system (green) and climbing fiber input (CF, red) from the inferior olive (IO), indicating retinal slip. These two inputs converge on PCs, which influence eye movements via the vestibular nuclei (VN) and the oculomotor (OM) neurons. PN, pontine nuclei; GC, granule cell. (B) Schematic illustration of eye movement recording setup. Mice are head-fixed in the center of a turntable for

vestibular stimulation and surrounded by a random dotted pattern ('drum') for visual stimulation. A CCD camera was used for infrared (IR) video-tracking of the left eye. (C) Top, examples of nasal (N) and temporal (T) eye positions. Red circles, pupil fit; black cross, corneal reflection (CR); white cross, pupil center. Bottom, example trace of eye position (gray) with drum position (red), during stimulation at an amplitude of 5° and frequency of 0.6 Hz. (D) $pcp2^{Cre}$;$TRPC3^{fl/fl}$ and control mice were subjected to six 5 min training sessions with mismatched in-phase visual and vestibular stimulation (in light, see insets), aimed at decreasing the VOR gain (probed in the dark before, between and after sessions). (E) Similar, but now mice were trained with out-of-phase stimulation, aimed at increasing VOR gain. (F) Re-recording of OKR gain following the VOR phase reversal training (see G–H) to test OKR gain increase (compare to Figure 6—figure supplement 2C, left). (G) Multiple-day training using in-phase mismatch stimulation (see inset in H) aimed at reversing the direction of the VOR (quantified as a reversal of the phase). Representative eye position recordings of VOR before (top) and after (bottom) training. (H) Results of five days of VOR phase reversal training, probed by recording VOR (in the dark before, between and after sessions) with mice kept in the dark in overnight. Data are represented as mean ± s.e.m., N = 11 mutants versus N = 13 controls, all p>0.05, ANOVA for repeated measurements. See Source data for values.
DOI: https://doi.org/10.7554/eLife.45590.019The following source data and figure supplements are available for figure 6:
Source data 1. *Source data for Figure 6 and supplements.*
DOI: https://doi.org/10.7554/eLife.45590.022
Figure supplement 1. *$pcp2^{Cre}$;$TRPC3^{fl/fl}$ mice show normal Erasmus ladder performance.*
DOI: https://doi.org/10.7554/eLife.45590.020
Figure supplement 2. *Compensatory eye movements and eyeblink conditioning in $pcp2^{Cre}$;$TRPC3^{fl/fl}$ mice.*
DOI: https://doi.org/10.7554/eLife.45590.021

Our results here demonstrate that changes that occur at the cell physiological level, that is reduced simple spike rate and altered CS-SS interaction, lead to a more complex pattern of changes in the intact system. The additional effects are particularly striking in the *$pcp2^{Cre}$*;FIG 8*$TRPC3^{fl/fl}$* mice, where the reduced simple spike rate in zebrin-negative PCs leads to a lower complex spike rate. In principle, this could have been a direct olivocerebellar loop effect, as lower simple spike rate results in reduced inhibition of the also inhibitory projection from the cerebellar nuclei to the inferior olive (Chaumont *et al.*, 2013; Witter *et al.*, 2013). In contrast, *$TRPC3^{Mwk/-}$* mice exhibit a higher PC simple spike rate, but also a lower complex spike rate. This seems to argue against a direct olivocerebellar loop effect, but the gain-of-function mutation is present in all neurons of this mouse line and thus cell intrinsic

processing probably plays a -currently unknown- role herein. The unaltered complex spike rate of *pcp2^{CreERT2};TRPC3$^{fl/fl}$* mice suggests that there is a developmental component to the relationship between complex spikes and simple spikes (Badura *et al.*, 2013; White and Sillitoe, 2017).

It should be noted that in some experiments we found that also the Z+ PCs were affected byTRPC3 mutations. In *TRPC3$^{Mwk/-}$* mice the regularity of simple spikes and complex spikes was higher compared to controls. TRPC3 is expressed in UBCs and inferior olivary neurons (see also Figure 1 and Figure 1—figure supplements 1–2). UBCs are neurons that fire action potential with high regularity (Ruigrok *et al.*, 2011) and provide mossy fiber input in lobule X, which -indirectly- drives PC simple spike activity (Nunzi *et al.*, 2001), whereas inferior olivary neurons directly control the rate and regularity of complex spikes (De Zeeuw *et al.*, 2011). UBCs degenerate early in development in *TRPC3$^{Mwk/-}$*, while the effects of the mutation on inferior olivary neurons have not been described yet. Thus, the global nature of this mutation could drive changes in other cell types that explain the effects observed in the regularity of simple and complex spikes. In addition, it should be noted that the complex spike rate of Z+ PCs in *pcp2^{Cre};TRPC3$^{fl/fl}$* mice as observed with the use of 2-photon imaging, was also lower, for which we at current do not have an explanation. In general, in all conditions the complex spikes rate in Z– and Z+ appear to be significantly or trending towards lower values in mutant mice, except for those in inducible mice where the mutation occurred after development. This has two potential implications: 1) TRPC3 mutations, through direct effects on inferior olivary neurons and/or indirect effects through the olivocerebellar loop, have an inhibiting effect on complex spike rates, and 2) these effects are absent when the mutation is induced later in life.

To test the functional consequences of the loss of TRPC3 and the modular specificity of these effects, we tested the impact on behavioral experiments that can be linked to specific modules. Eyeblink conditioning and VOR adaptation are controlled by different modules in the cerebellum and they are distinctly different by nature. Eyeblink conditioning requires a novel, well-timed eyelid movement to a previously unrelated, neutral stimulus, and has been linked to largely or completely zebrin-negative modules in the anterior cerebellum (Hesslow, 1994; Mostofi *et al.*, 2010). The activity of the putative zebrin-negative PCs in this area is relatively high at rest, in line with their zebrin identity, and a decrease in this high firing rate correlates to the eyeblink response (Jirenhed *et al.*, 2007; Johansson *et al.*, 2014; ten Brinke *et al.*, 2015). Conversely, VOR adaptation adjusts the amplitude of an existing reflex to optimize sensory processing using visual feedback and
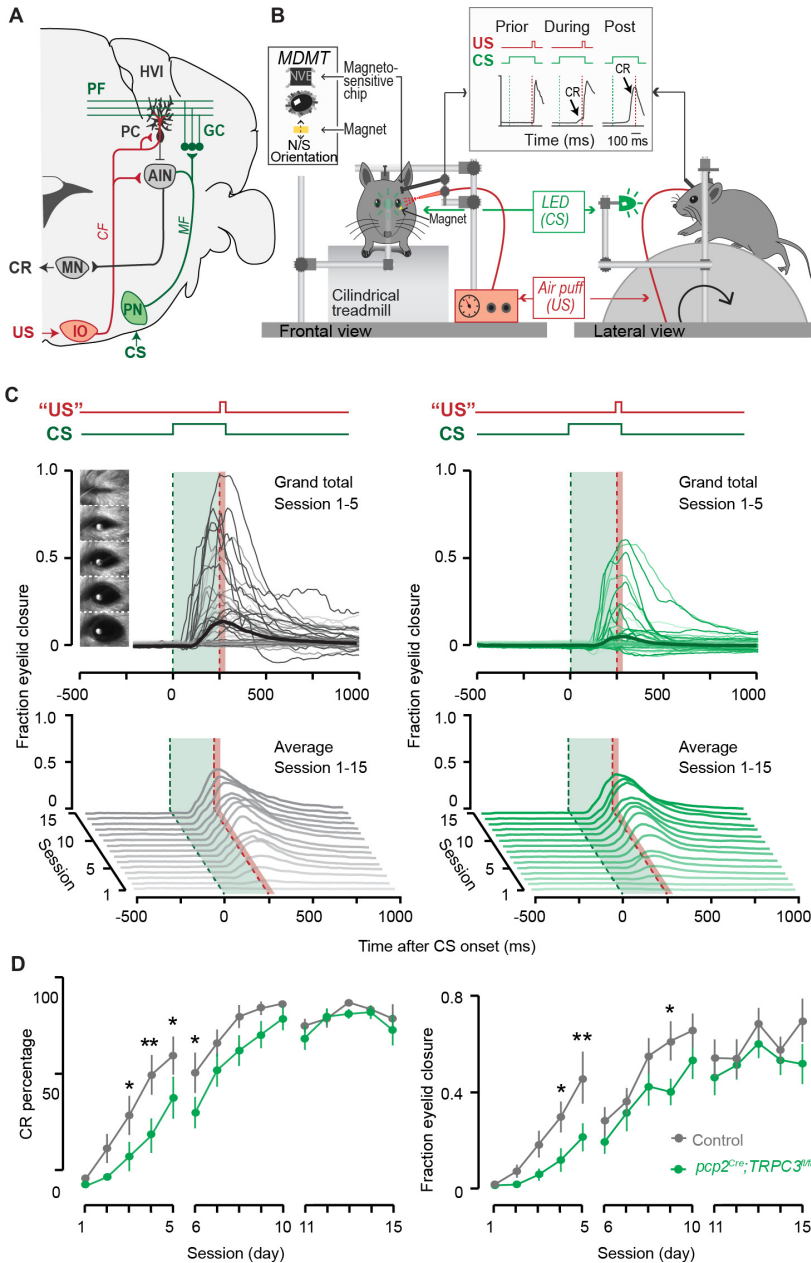
Figure 7. Eyeblink conditioning, linked to Z– modules is delayed in pcp2^{Cre};TRPC3$^{fl/fl}$
mice. (A) Cerebellar circuitry controlling eyeblink conditioning. PCs in the paravermal
region around the primary fissure receive inputs carrying sensory information from
for example the pontine nucleus (PN) through the MF-PF pathway and the error
signal from the inferior olive (IO) through the climbing fibers (CF). These PCs in
turn influence eyelid muscles via the anterior interposed nucleus (AIN) and motor

*nuclei (MN). (B) Schematic illustration of eyeblink conditioning setup. Head fixed mice on a freely moving treadmill, are presented a green LED light (conditional stimulus, CS) followed several hundred milliseconds later by a weak air-puff on the eye (unconditional stimulus, US). As a result of repeated CS-US pairings, mice will eventually learn to close their eye in response to the CS, which is called the conditioned response (CR). Eyelid movements were recorded with the magnetic distance measurement technique (MDMT). (C) Comparison of fraction of eyelid closure between controls (left) and pcp2^{Cre};TRPC3$^{fl/fl}$ mice (right). Top, session averages (thin-lines) per mouse and overall average (thick-lines) for the first 5 days (color intensity increasing from day 1 to 5). Insets: mouse eye video captures show eyelid closure ranging from 0 (fully-open) to 1 (fully-closed). Bottom, waterfall plot of the averaged eyeblink trace during CS-only trials for the 15 daily sessions. (D) The CR percentage and CR amplitude for pcp2^{Cre};TRPC3$^{fl/fl}$ mice initially have a significantly slower acquisition but eventually reach the same levels as control littermates. Data are represented as mean ± s.e.m., N = 15 mutants versus N = 15 controls, P values were all FDR corrected for multiple comparisons, see Source data for values and statistics, * means p<0.05 and **p<0.01.*

is controlled by the vestibulocerebellum, the flocculus in particular, which is classically considered to be zebrin-positive (Sanchez *et al.*, 2002; Zhou *et al.*, 2014; cf Sugihara and Quy, 2007; Fujita *et al.*, 2014). There are several variations in VOR adaptation aimed at different changes in temporal and/or spatial parameters (see e.g. Voges *et al.*, 2017). In unidirectional VOR gain increase, we recently found that the change correlating with the adapted eye movement consisted of a potentiation, an increase, of the -at rest- lower PC firing rate (Voges *et al.*, 2017). Although our current study has its main focus on the differential contribution of TRPC3 at the cell and systems physiological level, it is tempting to speculate how the loss of TRPC3 in PCs results in an eyeblink conditioning phenotype without affecting VOR adaptation. The reduction in firing rate of zebrin-negative PCs may directly contribute to the impaired conditioning. The suppression of simple spike firing that generally correlates with the conditioned response (ten Brinke *et al.*, 2015) might be occluded by the lower resting rate in *pcp2^{Cre};TRPC3$^{fl/fl}$* mice. Alternatively, PF-PC LTD could play a role as it is in line with the simple spike suppression and blocking TRPC3 function completely abolishes this form of LTD (Kim, 2013). However, genetically ablating PF-PC LTD did not affect the ability to

Zebrin-negative PCs										
Mouse line	In vitro				In vivo					
	Cell-attach			Cur-inj	Simple spike			Complex spike			CF-pause
	FF	CV	CV2	FF	FF	CV	CV2	FF	CV	CV2	
Gain-of-function TRPC3$^{Mwk/-}$	↑	—	—	N/A	↑	↑	—	↓	↑	—	—
Loss-of-function pcp2^{Cre};TRPC3$^{fl/fl}$	↓	↓	↓	↓	↓	—	—	↓	—	—	↑
Loss-of-function pcp2^{Cre};TRPC3$^{fl/fl}$;EAAT4$^{GFP/-}$	N/A				↓	↑	↑	↓	↑	↑	↑
loss-of-function pcp2^{CreERT2};TRPC3$^{fl/fl}$	N/A				↓	—	—	—	—	—	—
Zebrin-positive PCs											
Mouse line	In vitro				In vivo					
	Cell-attach			Cur-inj	Simple spike			Complex spike			CF-pause
	FF	CV	CV2	FF	FF	CV	CV2	FF	CV	CV2	
Gain-of-function TRPC3$^{Mwk/-}$	—	—	—	N/A	—	↑	—	—	↑	—	—
Loss-of-function pcp2^{Cre};TRPC3$^{fl/fl}$	—	—	—	—	—	—	—	—	—	—	—
Loss-of-function pcp2^{Cre};TRPC3$^{fl/fl}$;EAAT4$^{GFP/-}$	N/A				—	—	—	↓	—	—	—
loss-of-function pcp2^{CreERT2};TRPC3$^{fl/fl}$	N/A				—	—	—	—	—	—	—

Figure 8. *Summary of the electrophysiological changes in the gain- and loss-of-function TRPC3 mutants.*
DOI: https://doi.org/10.7554/eLife.45590.026

perform eyeblink conditioning successfully (Schonewille *et al.*, 2011), arguing against an exclusive role for this form of plasticity. Schreurs and colleagues demonstrated that intrinsic excitability is increased after eyeblink conditioning (Schreurs *et al.*, 1997). A third option could be that TRPC3 also affects the adaptive increase of excitability, intrinsic plasticity, which is calcium-activated potassium channel function dependent (Ohtsuki *et al.*, 2012), and thereby delays the expression of a conditioned blink response. All three options would not necessarily affect VOR adaptation and could contribute to the deficits in eyeblink conditioning, but given the relatively mild phenotype, one or two could be sufficient. Future experiments will have to unravel the cellular changes underlying eyeblink conditioning and VOR adaptation and the specific role of TRPC3 in the former.

In this study we aimed to gain insight in the mechanisms that convert

molecular heterogeneity into differentiation of cell physiology and function. This mechanistic question goes hand in hand with the more conceptual question: why are there, at least, two different types of PCs? An appealing hypothesis is that zebrin-negative and zebrin-positive bands control two muscles with opposing functions, for example a flexor and an extensor. Trans-synaptic retrograde tracing using rabies virus from antagonist muscles demonstrated that there is no robust division in zebrin-negative and zebrin-positive strips, but that a partial segregation could not be excluded (Ruigrok *et al.*, 2008). A second possibility would be that individual muscles are controlled by either only zebrin-negative or zebrin-positive strips, or a combination of both, when needed. In the vestibulocerebellum of the pigeon, each movement direction is controlled by a set of zebrin-negative and zebrin-positive bands (Graham and Wylie, 2012). In this configuration each PC within the set, or separately, would then serve a distinct function, for which it is optimized by gene expression patterns. This dissociation of function could entail for example timing versus coordination (Diedrichsen *et al.*, 2007) or moving versus holding still (Shadmehr, 2017), although none of these distinctions have been linked to specific zebrin-identified modules. Alternatively, it may be the net polarity of the connectivity down-stream of the cerebellar nuclei up to the motor neurons or the cerebral cortical neurons that determines the demand(s) of the module(s) involved (De Zeeuw and Ten Brinke, 2015). Module-specific driver lines would greatly aid to answer these questions, but are currently not available.

To summarize, our results support the hypothesis that cerebellar modules control distinct behaviors based on cellular heterogeneity, with differential molecular configurations. We present the first evidence for a non-uniform expression pattern of TRPC3 in PCs, complementary to that of zebrin in the vermis but more homogeneous in the hemispheres. Nonetheless, TRPC3 effects are directly coupled to zebrin, a specificity that putatively requires mGluR1b (Ohtani *et al.*, 2014), the activator of TRPC3 that is expressed in a pattern perfectly complementary to zebrin (Mateos *et al.*, 2001).

Since the discovery of protein expression patterns in the cerebellar cortex (Brochu *et al.*, 1990),numerous other proteins with patterned expression have been identified (Cerminara *et al.*, 2015).These patterns have been linked to circuit organizations of modules (Apps and Hawkes, 2009), to disease and degeneration (Cerminara *et al.*, 2015), and more recently to electrophysiological differences (Wadiche and Jahr, 2005; Zhou *et al.*, 2014). Most expression patterns follow or complement that of zebrin II, but alternative patterns have been observed (Armstrong *et al.*, 2001). These patterns commonly further subdivided one of the two populations studied here and thus potentially underlie the remaining variation and differences between

lobules (Apps *et al.*, 2018). Altogether, this work demonstrates that proper cerebellar function is based on the presence of (at least) two modi operandi that have distinct molecular machineries, with TRPC3 as one of the major contributing factors, so as to differentially control sensorimotor integration in downstream circuitries that require control with opposite polarity.

Materials and methods

Key resources table

Reagent type (species) or resource	Designation	Source or reference	Identifiers	Additional information
Species *Mus musculus*	C57BL/6J mice	Charles Rivers	IMSR_JAX:000664	
Species *Mus musculus*	TRPC3$^{Mwk/-}$	*Becker et al., 2009*	MGI:3689326	F1 of (original) C3H/HeH and C57BL/6J background
Species *Mus musculus*	TRPC3$^{fl/fl}$	*Hartmann et al., 2008*	MGI:5451202	C57BL/6J background
Species *Mus musculus*	pcp2^{Cre}	*Barski et al., 2000*	MGI:2137515	C57BL/6Jbackground
Species *Mus musculus*	pcp2^{CreERT2}	The Institut Clinique de la Souris, www.ics-mci.fr		C57BL/6Jbackground
Species *Mus musculus*	EAAT4$^{GFP/-}$	*Gincel et al., 2007*		C57BL/6Jbackground
Species *Mus musculus*	Ai14	https://www. jax.org/strain/007908	MGI:3809524	C57BL/6J background
Antibody	Rabbit anti-TRPC3	Cell Signaling	Cat.#: 77934	IHC (1:500), WB (1:1000)
Antibody	Mouse anti-actin	Millipore	Cat.#: MAB1501	WB (1:1000)
Antibody	Goat anti-Zebrin II/ Aldolase C	Santa Cruz Biotechnology	Cat.#: SC-12065	IHC (1:500)
Antibody	Mouse anti-calbindin	Sigma	Cat.#: C9848	IHC (1:7000)
Antibody	Rabbit anti-GFP	Abcam	Cat. # 290	IHC (1:1000)
Chemical compound, drug	Dextran, Biotin, 3000 MW, Lysine Fixable (BDA-3000)	Thermo Fisher Scientific	D7135	
Software, algorithm	MATLAB v2014a	Mathworks	RRID: SCR_001622	
Software, algorithm	Clampfit 10	Molecular Devices	RRID: BDSC_14352	
Software, algorithm	Patchmaster software (for in vitro recording analysis)	HEKA Electronics		
Software, algorithm	Spiketrain software (for in vivo recording analysis)	Used under Neurasmus license, currently: kai. voges@nus.edu.sg		
Software, algorithm	Erasmus Ladder 2.0 analysis	Noldus, Wageningen, Netherlands		
Software, algorithm	Patchmaster software (for in vitro recording analysis)	HEKA Electronics		

(table continued on next page)

Software, algorithm	Spiketrain software (for in vivo recording analysis)	Used under Neurasmus license, currently: kai. voges@nus.edu.sg	
Software, algorithm	Erasmus Ladder 2.0 analysis	Noldus, Wageningen, Netherlands	
Software, algorithm	Compensatory eye movements analysis	https://github. com/MSchonewille/ iMove	
Software, algorithm	Eyeblink conditioning analysis	Neurasmus BV, Rotterdam, Netherlands	
Software, algorithm	GraphPad Prism 6	GraphPad	RRID: SCR_002798
Software, algorithm	SPSS 20.0	IBM SPSS	RRID: SCR_002865

Animals:

For all experiments, we used adult male and female mice with a C57Bl/6 background that were,unless stated otherwise, individually housed, had food ab libitum and were on a 12:12 light/dark cycle. In all experiments the experimenters were blind to mouse genotypes. All experiments were approved by the Dutch Ethical Committee for animal experiments and were in accordance with the Institutional Animal Care and Use Committee.

The generation of $TRPC3^{Mwk/-}$ mice has been described previously (Becker *et al.*, 2009). Briefly,male BALB/cAnN mice carrying the *Mwk* mutation which was generated in a large-scale ENU mutagenesis program were subjected to cross with normal C3H/HeH females, and the first filial generation (F_1) progeny were screened for a variety of defects. The *Mwk* colony was maintained by repeated backcrossing to C3H/HeH. Experimental mice were generated by crossing C3H/HeH mice heterozygous for the *Mwk* mutation with C57Bl/6 mice. Offspring with the *Mwk* mutation on one allele were classified as gain-of-function TRPC3 Moonwalker mutant (referred to as $TRPC3^{Mwk/-}$) and littermate mice lacking the *Mwk* mutation were used as controls. Note that, the $TRPC3^{Mwk/-}$ mutants present evident ataxic phenotype from a very early age, concomitant with progressive degeneration of UBCs and PCs (Sekerková *et al.*, 2013).

Mice in which exon 7 of the *Trpc3* gene was flanked by *loxP* sites ($TRPC3^{fl/fl}$ mice) were bred with mice that express Cre under the *Pcp2* promoter ($L7^{Cre/-}$ mice) (Barski *et al.*, 2000). The resulting offspring was genotyped using PCR of genomic DNA extracted from tail or toe by standard procedures. The F_1 was crossed again with the $TRPC3^{fl/fl}$ mice. Among the second filial generation (F_2), mice homozygous for the *loxP* sites and one Cre allele were classified as PC-specific TRPC3 knock-out ($L7^{Cre/-};TRPC3^{fl/fl}$, here referred to as $pcp2^{Cre};TRPC3^{fl/fl}$) mice and as controls when Cre was

absent (*pcp2$^{-/-}$;TRPC3$^{fl/fl}$*, here 'littermate controls').

pcp2^{Cre};TRPC3$^{fl/fl}$;EAAT4$^{GFP/-}$ mice were generated by crossing *pcp2$^{Cre/-}$;TRPC3$^{fl/fl}$* mice with heterozygous *EAAT$^{GFP/-}$* mice which express enhanced green fluorescent protein (GFP) under control of *Eaat4* promotor. The F$_2$ offspring those who expressed *TRPC3$^{fl/-}$*, *pcp2$^{Cre/-}$* and *EAAT$^{GFP/-}$* were crossed again with the *TRPC3$^{fl/fl}$* mice. Among the F$_3$, mice with a homozygous expression of *floxed-TRPC3*, one *Cre* allele and one *EAAT^{GFP}* allele (*pcp2$^{Cre/-}$;TRPC3$^{fl/fl}$;EAAT4$^{GFP/-}$*), were used and referred to as *pcp2^{Cre};TRPC3$^{fl/fl}$;EAAT4$^{GFP/-}$* mutant mice and as controls when Cre was absent (*pcp2$^{-/-}$;TRPC3$^{fl/fl}$;EAAT4$^{GFP/-}$*).

Inducible PC-specific TRPC3 knockouts (*pcp2^{CreERT2};TRPC3$^{fl/fl}$*) were generated by crossbreeding mice carrying the floxed *TRPC3* with mice expressing the tamoxifen-sensitive Cre recombinase *Cre-ERT2* under the control of the *pcp2* promoter (obtained from the Institut Clinique de la Souris, www.ics-mci.fr) (experimental mice: *pcp2$^{Cre-ERT2/-}$;TRPC3fl/fl*). Tamoxifen was dissolved in corn oil to obtain a 20 mg/ml solution, and intraperitoneally injected into all subjects for consecutive 5 days, four weeks prior to electrophysiological recordings. Injections were performed in adults between 12–31 weeks of age. Efficiency and selectivity of the *pcp2$^{Cre-ERT2/-}$* line was verified by crossing mice with Cre-dependent tdTomato expressing (Ai14) mice, injection offspring carrying both alleles with Tamoxifen in a similar manner and analyzing the resulting tdTomato expression. Experimental cohorts were always injected at the same time. Mice without *pcp2$^{Cre-ERT2}$* expression were used as controls in this study (experimental mice: *pcp2^{CreERT2};TRPC3$^{fl/fl}$*).

Immunohistochemistry

Anesthetized mice were perfused with 4% paraformaldehyde in 0.12M phosphate buffer (PB). Brains were taken out and post-fixed for 1 hr in 4% PFA at room temperature, then transferred in 10% sucrose overnight at 4°C. The next day, the solution was changed for 30% sucrose and left overnight at 4°C. Non-embedded brains were sectioned either sagittally or transversally at 40 mm thickness with freezing microtome. Free-floating sections were rinsed with 0.1M PB and incubated 2 hr in 10 mM sodium citrate at 80°C for 2 hr, for antigen retrieval. For immuno-fluorescence, sections were rinsed with 0.1M PB, followed by 30 min in Phosphate Buffered saline (PBS). Sections were incubated 90 min at room temperature in a solution of PBS/0.5%Triton-X100/10% normal horse serum to block nonspecific protein-binding sites, and incubated 48 hr at 4°C in a solution of PBS/0.4% Triton-X100/2% normal horse serum,

with primary antibodies as follows: Aldolase C (1:500, goat poly-clonal, SC-12065), Calbindin (1:7000, mouse monoclonal, Sigma, #C9848), and TRPC3 (1:500, rabbit polyclonal, Cell Signaling, #77934). The TRPC3 antibody was validated by comparing results to previous immunostainings and in situ hybridization data (Allen Brain Atlas) and by the selective absence of staining in PCs of PC-specific knockout mice (Figure 1—figure supplement 3E–F). After rinsing in PBS, sections were incubated 2 hr at room temperature in PBS/0.4% Triton-X100/2% normal horse serum solution with secondary antibodies coupled with Alexa488, Cy3 or Cy5 (Jackson ImmunoResearch), at a concentration of 1:200. Sections were mounted on coverslip in chrome alum (gelatin/chromate) and covered with Mowiol (Polysciences Inc). For Light Microscopy section were pre-treated for endogenous peroxidase activity blocking with 3%H2O2 in PBS, then rinsed for 30 min in PBS, incubated 90 min in a solution of PBS/0.5%Triton-X100/10% normal horse serum to block non-specific protein-binding sites, followed by the primary antibody incubation as described before. After 48 hr, sections were rinsed in PBS and incubated 2 hr at room temperature in PBS/0.4% Triton-X100/10% normal horse serum solution with HRP coupled secondary antibodies (Jackson ImmunoResearch), at a concentration of 1:200. Sections were rinsed with 0.1M PB and incubated in diamino-benzidine (DAB, 75 mg/100 ml) for 10 min. Sections were mounted on glasses in chrome alum (gelatin/chromate), dried with successive Ethanol steps, incubated in Xylene and covered with Permount mounting medium (Fisher Chemical). Images were acquired with an upright LSM 700 confocal microscope (Zeiss) for fluorescent microscopy, and Nanozoomer (Hamamatsu) for light microscopy. Fluorescence intensity along the regions of interest were assessed using the 'plot profile' function of Image J.

iDISCO and light sheet imaging:

This protocol has been adapted from a previous study (Renier *et al.*, 2014). After normal perfusionand post-fixation, brains were washed successively in PBS (1.5 hr), 20% methanol/H_2O (1 hr), 50% methanol/H_2O (1 hr), 80% methanol/H_2O (1 hr), and 100% methanol (1 hr) twice. To increase clearance, samples were treated with a solution of dichloromethane (DCM) and 100% methanol (2:1) for another hour. Brains were then bleached with 5% H_2O_2 in 90% methanol (ice cold) at 4°C overnight. After bleaching, samples successively washed in 80% methanol/H_2O, 50% methanol/H_2O, 40% methanol/PBS, and 20% methanol/PBS, for 1 hr each, and finally in PBS/0.2% Triton X-100 for 1 hr twice. After rehydration, samples were pre-treated in a solution of PBS/0.2% Triton X-100/20% DMSO/0.3M glycine at 37°C for 36 hr,

then blocked in a mixture of PBS/0.2% Triton X-100/10% DMSO/6% donkey serum at 37°C for 48 hr. Brains were incubated in primary antibody in PTwH solution (PBS/0.2% Tween-20/5% DMSO/3% donkey serum with 10 mg/ml heparin) for 7 days at 37°C with primary antibody: TRPC3 rabbit polyclonal, 1:500 (Cell Signaling, #77934). Amphotericin was added once every two days at 1 mg/ml to avoid bacterial growth. Samples were then washed in 24 hr in PTwH for six times (1 hr for each, after the fourth wash, leave it at room temperature overnight), followed by the second round of 7 day incubation with primary antibody. Brains were then washed in PTwH, 6 washes in 24 hr, as described before, then incubated in secondary antibody in PTwH/3% donkey serum at 37°C for 7 days with secondary anti-Rabbit Cy3 (Jackson ImmunoResearch) at 1:750. Brains were then washed in PTwH, 6 washes in 24 hr, again, followed by successive washes in 20% methanol/H_2O, 40% methanol/H_2O, 60% methanol/H_2O, 80% methanol/H_2O, and 100% methanol twice, for 1 hr each, and finally incubation overnight in a solution of DCM and100% methanol. For tissue clearing, brains were incubated 20 mins in DCM, twice, and conserved in Benzyl ether at room temperature.

Ready samples were imaged in horizontal orientation with an UltraMicroscope II (LaVision BioTec)light sheet microscope equipped with Imspector (version 5.0285.0) software (LaVision BioTec). Images were taken with a Neo sCMOS camera (Andor) (2560 2160 pixels. Pixel size: 6.5 6.5mm2). Samples were scanned with double-sided illumination, a sheet NA of 0.148348 (resuls in a 5mm thick sheet) and a step-size of 2.5 mm using the horizontal focusing light sheet scanning method with the optimal amount of steps and using the contrast blending algorithm. The effective magnification for all images was 1.36x (zoombody*objective + dipping lens = 0.63x*2.152x). Following laser filter combinations were used: Coherent OBIS 488–50 LX Laser with 525/50 nm filter, Coherent OBIS 561–100 LS Laser with 615/40 filter, Coherent OBIS 647–120 LX with 676/29 filter.

Western blot and fractionation:

Cerebellar tissue from $pcp2^{Cre}$;$TRPC3^{fl/fl}$ and control mice was dissected and immediately frozen in liquid nitrogen. Samples were homogenized with a Dounce homogenizer in lysis buffer containing 50 mM Tris-HCl pH 8, 150 mM NaCl, 1% Triton X-100, 0.5% sodium deoxycholate, 0.1% SDS and protease inhibitor cocktail. Protein concentrations were measured using Pierce BCA protein assay kit (Thermo Fisher). Samples were denatured and proteins were separated by SDS-PAGE in Criterion TGX Stain-Free Gels (Bio-Rad), and transferred onto nitrocellulose membranes with the Trans-Blot Turbo

Blotting System (Bio-Rad). Membranes were blocked with 5% BSA (Sigma-Aldrich) in TBST (20mM Tris-HCl pH7.5, 150 mM NaCl and 0.1%, Tween20) for 1 hr and probed with the following primary antibodies: rabbit anti-TRPC3 (Cell Signaling Technology, #77934; 1:1000) and mouse anti-actin (Millipore, MAB1501; 1:1000). Secondary antibodies used were IRDye 800CW Donkey anti-Rabbit IgG (LI-COR Biosciences, Cat # 925–32213; 1:20000) and IRDye 680RD Donkey anti-Mouse IgG (LI-COR Biosciences, Cat # 925–68072; 1:20000). Membranes were scanned by Odyssey Imager (LI-COR Biosciences) and quantified using Image Studio Lite (LI-COR Biosciences). For quantification, densitometry of protein bands of interest was normalized to that of actin. For fractionation experiments, cerebellar tissues from C57/BL6 were collected and the synaptosomes were isolated using Syn-PER Synaptic Protein Extraction Reagent (ThermoScientific, #87793) according to the manufacturer's instructions.

In vivo extracellular recordings and analysis:

We performed in vivo extracellular recordings in adult $TRPC3^{Mwk/-}$ (aged 15–47 weeks, ages roughly matched), $pcp2^{Cre};TRPC3^{fl/fl}$ (aged 22–43 weeks, ages roughly matched), $pcp2^{CreERT2};TRPC3^{fl/fl}$ (aged 17–28 weeks) mice, respectively, as previously described (Zhou et $al.$, 2014). Briefly, an immobilizing pedestal consisting of a brass holder with a neodymium magnet (4 × 4×2 mm) was fixed on the skull, overlying the frontal and parietal bones, and then a craniotomy (Ø3 mm) was made in the interparietal or occipital bone under general anesthesia with isoflurane/O_2 (4% induction, 1.5–2% maintenance). After over 24 hr of recovery, mice were head-fixed and body restrained for recordings. PCs were recorded from vermal lobules I-III and X, using a glass pipette (OD 1.5 mm, ID 0.86mm, borosilicate, Sutter Instruments, USA; 1–2 μm tips, 4–8 MΩ) with a downward pitch angle of 40° and 65° respectively. The pipettes were filled with 2 M NaCl-solution and mounted on a digital 3-axis drive (SM-5, Luigs Neumann, Germany). After recording, BDA was iontophoretically injected to confirm that the recordings were from Lobules I-III or X. PCs were identified by the presence of simple and complex spikes, and determined to be from a single unit by confirming that each complex spike was followed by a climbing fiber pause. All in vivo recordings were analyzed offline using Spiketrain (used under Neurasmus license, currently: kai.voges@nus.edu.sg), running under MatLab (Mathworks, MA, USA). For each cell, the firing rate, CV and mean CV2 were determined for simple and complex spikes, as well as the climbing fiber pause. The CV is calculated by dividing the standard deviation, SD, by

the mean of ISI_s, whereas CV2 is calculated as $2 \times |ISI_{n+1} - ISI_n| / (ISI_{n+1} + ISI_n)$. Both are measures for the regularity of the firing, with CV reflecting that of the entire recording and mean CV2 that of adjacent intervals, making the latter a measure of regularity on small timescales. The climbing fiber pause is determined as the duration between a complex spike and the fist following simple spike. To extend this analysis, we also plotted histograms of simple spike activity time locked on the complex spike, and labeled the shape of this time histogram as normal, facilitation, suppression, or oscillation.

<u>In vivo two-photon-targeted electrophysiology:</u>

Details on targeted electrophysiological recordings in vivo in the mouse cerebellum were describedpreviously (Wu and Schonewille, 2018). PCs in lobules IV-VI were recorded in adult *pcp2^{Cre};TRPC3$^{fl/fl}$;EAAT4$^{GFP/-}$* mice (aged 14–49 weeks, ages roughly matched) under two-photon microscope guidance. A custom-made head plate was fixed to the cleaned skull of each animal, under isoflurane anesthesia, with dental adhesive (Optibond; Kerr Corporation, West Collins, USA) and secured with dental acrylic. A craniotomy was made above the cerebellum, exposing lobules IV-VI. The craniotomy was sealed with biocompatible silicone (Kwik-Cast; World Precision Instruments) and the animal was allowed to recover from surgery before recording. The silicone seal was removed prior to recording. To keep the brain surface moist, Ringer solution containing (in mM): NaCl 135, KCl 5.4, $MgCl_2$ 1, $CaCl_2$ 1.8, HEPES 5 (pH 7.2 with NaOH; Merck, Darmstadt, Germany) was applied. Glass micropipettes with tip size of ~1µm (resistance: 6–9 MΩ) were advanced from the dorsal surface under a 25° angle into the cerebellum, allowing concurrent two-photon imaging with a long working distance objective (LUMPlanFI/IR 40×/0.8; Olympus) on a custom-built two-photon microscope. Pipettes were filled with the same Ringer solution with an additional 40 µM AlexaFluor 594 hydrazide (Sigma-Aldrich, Steinheim, Germany) for visualization. GFP and AlexaFluor 594 were simultaneously excited by a MaiTai laser (Spectra Physics Lasers, Mountain View, CA, USA) operated at 860 nm. Green (GFP) and red (AlexaFluor 594) fluorescence were separated by a dichroic mirror at 560 nm and emission filters centered at 510 nm (Brightline Fluorescence Filter 510/84; Semrock) and 630 nm (D630/60; Chroma), respectively. The brain surface was stabilized with agarose (2% in Ringer; Sigma–Aldrich) and pipette pressure was initially kept at 3 kPa while entering the brain tissue. It was then removed for cell approach and the actual recording. Extracellular potentials were acquired with a MultiClamp 700A amplifier (Molecular Devices, Sunnyvale, CA, USA)

in current-clamp mode. Signals were low-pass filtered at 10 kHz (four-pole Bessel filter) and digitized at 25 kHz (Digidata 1322A). Data were recorded with pCLAMP 9.2 (Molecular Devices). Z+ and Z– cells were identified by comparing the relative intensity of GFP fluorescence. Whenever possible, cells of both types were recording alternatingly between adjacent bands Purkinje neurons with high and low GFP fluorescence.

<u>In vitro electrophysiology and analysis:</u>

We performed in vitro electrophysiological recordings on *TRPC3*[Mwk/-] (aged 9–21 weeks, ages roughly matched) and *pcp2*[Cre]*;TRPC3*^{fl/fl} (aged 20–60 weeks, ages roughly matched). As described previously (Peter *et al.*, 2016), acute sagittal slices (250 µm thick) were prepared from the cerebellar vermis and put into ice-cold slicing medium which contained (in mM) 240 sucrose, 2.5 KCl, 1.25 Na_2HPO_4, 2 $MgSO_4$, 1 $CaCl_2$, 26 $NaHCO_3$ and 10 D-Glucose, carbogenated continuously with 95% O_2 and 5% CO_2. After cutting using a vibrotome (VT1200S, Leica), slices were incubated in artificial cerebrospinal fluid (ACSF) containing (in mM): 124 NaCl, 5 KCl, 1.25 Na_2HPO_4, 2 $MgSO_4$, 2 $CaCl_2$, 26 $NaHCO_3$ and 15 D-Glucose, equilibrated with 95% O_2 and 5% CO_2 at 33.0 ± 1.0°C for 30 min, and then at room temperature. NBQX (10 µM), DL-AP5 (50 µM), and picrotoxin (100 µM) were bath-applied to block AMPA-, NMDA-, and GABA subtype A ($GABA_A$)-receptors, respectively. PCs were identified using visual guidance by DIC video microscopy and water-immersion 40X objective (Axioskop 2 FS plus; Carl Zeiss, Jena, Germany). Recording electrodes (3–5 µW, 1.65 mm outside diameter and 1.11 mm interior diameter (World Precision Instruments, Sarasota, FL, USA) were prepared using a P-97 micropipette puller (Sutter Instruments, Novato, CA, USA), and filled with ACSF for cell-attached recordings, or with an intracellular solution containing (in mM): 120 K-Gluconate, 9 KCl, 10 KOH, 4 NaCl, 10 HEPES, 28.5 Sucrose, 4 Na_2ATP, 0.4 Na_3GTP (pH 7.25–7.35 with an osmolality of 295) for whole-cell recordings. We measured spontaneous firing activity of PCs in cell-attached mode (0 pA injection) and intrinsic excitability in whole-cell current-clamp mode by injection of brief(1 s) depolarizing current pulses (ranging from –100 to 1100 pA with 100 pA increments) from a membrane holding potential of –65 mV at 33.0 ± 1.0°C. The spike count of evoked action potential was taken as a measure of excitability. AP properties including peak amplitude, AHP and half-width were evaluated using the first action potential generated by each PC. AHP indicates the amplitude of undershoot relative to the resting membrane potential. Half-width indicates the width of the signal at 50% of the maximum amplitude. PCs that required > –800 pA to maintain

the holding potential at –65 mV or fired action potentials at this holding
potential were discarded. The average spiking rate measured over the entire
current pulse was used to construct current-frequency plots. For whole-cell
Recordings, cells were excluded if the series (Rs) or input resistances (Ri)
changed by >15% during the experiment, which was determined using a
hyperpolarizing voltage step relative to the –65 mV holding potential. All
electrophysiological recordings were acquired in lobules I-III and lobule X
of the vermal cerebellum using EPC9 and EPC10-USB amplifiers (HEKA
Electronics, Lambrecht, Germany) and Patchmaster software (HEKA
Electronics). Data were analyzed afterwards using Clampfit (Molecular
Devices).

Compensatory eye movement recordings:

We subjected alert *pcp2^{Cre};TRPC3^{fl/fl}* mice (aged 12–39 weeks,
ages roughly matched) to compensatory eye movement recordings which
were described in detail previously (Schonewille *et al.*, 2010). In short, mice
were equipped with a pedestal under general anesthesia with isoflurane/O_2.
After a 2–3 days of recovery, mice were head-fixed with the body loosely
restrained in a custom-made restrainer and placed in the center of a turntable
(diameter: 63 cm) in the experimental set-up. A round screen (diameter 60
cm) with a random dotted pattern ('drum') surrounded the mouse during the
experiment. Compensatory eye movements were induced by sinusoidal
rotation of the drum in light (OKR), rotation of the table in the dark (VOR)
or the rotation of the table in the light (visually enhanced VOR, VVOR) with
an amplitude of 5° at 0.1–1 Hz. Motor performance in response to these
stimulations was evaluated by calculating the gain (eye velocity/stimulus
velocity) and phase (eye to stimulus in degrees) of the response. Motor
learning was studied by subjecting mice to mismatched visual and vestibular
input. Rotating the drum (visual) and table (vestibular) simultaneously, in
phase at 0.6 Hz (both with an amplitude of 5°, 5 10 min) in the light will
induce an increase of the gain of the VOR (in the dark). Subsequently, VOR
Phase reversal was tested by continuing the next days (day 2–5, keeping
mice in the dark in between experiments) with in phase stimulation, but now
with drum amplitudes of 7.5° (days 2) and 10° (days 3, 4, and 5), while the
amplitude of the turntable remained 5°. This resulted, over days of training,
in the reversal of the VOR direction, from a normal compensatory rightward
eye movement (in the dark), when the head turns left, to a reversed response
with a leftward eye movement, when the head moves left. At the end of the
VOR phase reversal training the OKR was probed again and compared to

the OKR before training, to examine OKR gain increase. VOR gain increase was evoked by subjecting mice to out of phase drum and table stimulation at 1.0 Hz (both with an amplitude of 1.6°). A CCD camera was fixed to the turntable in order to monitor the eyes of the mice. Eye movements were recorded with eye-tracking software (ETL-200, ISCAN systems, Burlington, NA, USA). For eye illumination during the experiments, two infrared emitters (output 600 mW, dispersion angle 7°, peak wavelength 880 nm) were fixed to the table and a third emitter, which produced the tracked corneal reflection, was mounted to the camera and aligned horizontally with the optical axis of the camera. Eye movements were calibrated by moving the camera left-right (peak-to-peak 20°) during periods that the eye did not move (Stahl, 2004). Gain and phase values of eye movements were calculated using custom-made Matlab routines (MathWorks, https://github.com/MSchonewille/iMove) (Schonewille, 2019).

Eyeblink conditioning:

For all procedures on eyeblink conditioning we refer to the study done previously (Boele *et al.*,2018). *pcp2^{Cre};TRPC3$^{fl/fl}$* mice, aged 16–25 weeks (ages roughly matched), were anesthetized with an isoflurane/oxygen mixture and surgically placed a so-called pedestal on the skull. After a 2–3 days' recovery, mice were head-fixed and suspended over a foam cylindrical treadmill on which they were allowed to walk freely. Before each session starting, a minuscule magnet (1.5 x 0.7 x 0.5 mm) was placed on the left lower eyelid with superglue (cyanoacrylate) and an NVE GMR magnetometer was positioned above the left upper eyelid. With this magnetic distance measurement technique (MDMT), we measured the exact positions of each individual mouse eyelid by analyzing the range from optimal closure to complete aperture. The CS was a green LED light (CS duration 280 ms, LED diameter 5 mm) placed 10 cm in front of the mouse's head. The US consisted of a weak air-puff applied to the eye (30 psi, 30 ms duration), which was controlled by an API MPPI-3 pressure injector, and delivered via a 27.5-gauge needle that was perpendicularly positioned at 0.5–1 cm from the center of the left cornea. The training consisted of 3 daily habituation sessions, one baseline measurement, 3 blocks of 5 daily acquisition sessions (each block was separated by 2 days of rest). During the habituation sessions, mice were placed in the setup for 30–45 min, during which the air puff needle (for US delivery) and green LED (for CS delivery) were positioned properly but no stimuli were presented. On the day of acquisition session 1, each animal first received 20 CS-only trials as a baseline measure, to establish that the

CS did not elicit any reflexive eyelid closure. During each daily acquisition session, every animal received in total 200 paired CS-US trials, 20 US only trials, and 20 CS only trials. These trials were presented in 20 blocks, each block consisted of 1 US only trial, 10 paired CS-US trials, and 1 CS only trial. Trials within the block were randomly distributed, but the CS only trial was always preceded by at least two paired CS-US trials. The interval between the onset of CS and that of US was set at 250 ms. All experiments were performed at approximately the same time of day by the same experimenter. Individual eyeblink traces were analyzed with Blink 2.0 software (Neurasmus, www.neurasmus.nl, Rotterdam, Netherlands). Trials with significant activity in the 500 ms pre-CS period (>7*IQR) were regarded as invalid for further analysis. Valid trials were further normalized by aligning the 500 ms pre-CS baselines and calibrating the signal so that the size of a full blink was 1. In valid normalized trials, all eyelid movements larger than 0.1 and with a latency to CR onset between 50–250 ms and a latency to CR peak of 100–250 ms (both relative to CS onset)were considered as conditioned responses (CRs). For CS only trials in the probe session we used the exact same criteria except that the latency to CR peak time was set at 100–500 ms after CS onset.

Erasmus ladder:

Mice aged 11–16 weeks were subjected to the Erasmus Ladder (Noldus, Wageningen, Netherlands). As described previously (Vinueza Veloz *et al.*, 2015), the Erasmus Ladder is a fully automated system consisting of a horizontal ladder between two shelter boxes. The ladder has 2 x 37 rungs for the left and right side. Rungs are placed 15 mm apart, with alternate rungs in a descended position, so as to create an alternating stepping pattern with 30 mm gaps. All rungs are equipped with touch sensors, which are activated when subject to a pressure corresponding to more than four grams. The sensors are continuously monitored to record the position and the walking pattern of the mouse. A single crossing of the Erasmus Ladder is recorded as a trial. In this study, each mouse underwent a daily session consisting of 42 trials, for five consecutive days. Motor performance was measured by counting step durations and percentages during a trial, including short steps (steps from one high rung to the next high rung), long steps (skipping one high rung), jumps (skipping two high rungs), lower steps (a step forward steps, but the paw is placed on a low rung), back steps (a step backward steps from one high rung to the previous high rung). All data were collected and processed by ErasmusLadder 2.0 software (Noldus, Wageningen, Netherlands).

Statistical analysis

All values are shown as mean ± s.d., unless stated otherwise. To determine means, variance and perform statistical analysis, in the electrophysiological experiments the number of cells and in the behavioral experiment the number of mice were taken as the number of replicates. Apart from the requirements for inclusion in the final datasets as stated in the separate sections for each experimental technique above, data was excluded only when the signal to noise ratio was insufficient to warrant reliable analysis. For behavioral experiments group sizes were estimated a priori using sample size calculations based on minimal relevant differences and expected variation in control cells or mice. To study compensatory eye movements the numbers are based on the VOR phase reversal. A power analysis based on repeated measures ANOVA with α = 0.05, β = 0.20, minimal effect size f of 0.50 (Δ = 30°, SD 30°, seven measurements), indicated a minimum of 11 mice per group, which were obtained (n = 11/13 for controls/mutants). For eyeblink conditioning, these numbers are based on the percentage of conditioned responses and were: α = 0.05, β = 0.20, minimal effect size f of 0.42 (Δ = 25%, SD 30%. 15 repeats), resulting in a minimum of 14 mice per group, which were obtained (n = 15/15 for controls/mutants). For electrophysiological recordings the power analysis was based on previous experiments (Zhou *et al.*, 2014), which gave a minimum group size of 10 PCs per group (α = 0.05, β = 0.20, Δ = 18.1 Hz, SD 14.0 Hz, based on Student's t-test) for in vitro experiments and 6 PCs per group (a = 0.05, b = 0.20, D = 35.3 Hz, SD 17.8 Hz) for in vivo experiments, which were obtained in all experiments (all n ≥ 10 for in vitro, all n ≥ 12 for in vivo). Inter-group comparisons were done by two-tailed Student's t-test. ANOVA for repeated measures was used to analyze eye movement and Erasmus ladder behavioral data; linear mixed-effect model analysis (Boele *et al.*, 2018) (established in R version 1.1.442) was used to analyze eyeblink conditioning data. All statistical analyses were performed using SPSS 20.0 software. Data was considered statistically significant if p<0.05.

Acknowledgements

Additional Information

Author contributions:

Bin Wu, Conceptualization, Formal analysis, Supervision, Funding
acquisition, Validation,Visualization, Methodology, Writing—original draft,
Writing—review and editing; Francois GC Blot,Formal analysis, Visualization,
Methodology, Writing—review and editing; Aaron Benson Wong, Data curation,
Formal analysis, Visualization, Methodology, Writing—review and editing;
Catarina Oso´rio, Formal analysis, Validation, Visualization, Methodology;
Youri Adolfs, Data curation, Formal analysis, Visualization, Methodology;
R Jeroen Pasterkamp, Resources, Data curation, Software, Supervision,
Methodology; Jana Hartmann, Esther BE Becker, Resources, Methodology,
Writing—review and editing; Henk-Jan Boele, Data curation, Software,
Formal analysis, Supervision, Visualization, Methodology, Writing—review
and editing; Chris I De Zeeuw, Conceptualization, Resources, Software,
Funding acquisition, Writing—review and editing; Martijn Schonewille,
Conceptualization, Software, Supervision, Funding acquisition, Investigation,
Methodology, Writing—original draft, Project administration, Writing—review
and editing

5

Author ORCIDs:

Bin Wu https://orcid.org/0000-0003-4198-1661
Aaron Benson Wong http://orcid.org/0000-0003-1650-2710
R Jeroen Pasterkamp http://orcid.org/0000-0003-1631-6440
Esther BE Becker https://orcid.org/0000-0002-5238-4902
Chris I De Zeeuw http://orcid.org/0000-0001-5628-8187
Martijn Schonewille https://orcid.org/0000-0002-2675-1393

Ethics:

Animal experimentation: This study was performed under and all of the animals were handled according to a project license approved by the Dutch Central Committee for Animal Experiments(CCD, AVD #101002015273). Each experiment was separately verified and approved by the Animal Welfare Body (IvD/AWB, various numbers). All surgery was performed under isoflurane anesthesia combined with local anesthetics and analgesics in an effort to minimize suffering.

Decision letter and Author response:

Decision letter https://doi.org/10.7554/eLife.45590.031
Author response https://doi.org/10.7554/eLife.45590.032

Additional files

Supplementary files:
Supplementary file 1. Summary of the electrophysiological changes in gain- and loss-of-functionTRPC3 mutants.
DOI: https://doi.org/10.7554/eLife.45590.027.
Transparent reporting form
DOI: https://doi.org/10.7554/eLife.45590.028
Data availability:

All electrophysiology and behavioral data are included in the manuscript and supporting files.Source data files have been provided for Figures 2 to 7 and Figure 2—figure supplement 1, Figure3—figure supplement 1, Figure 4—figure supplement 1, Figure 5—figure supplement 1, Figure 6—figure supplement 1–2 and Figure 7—figure supplement 1.

5

Ackermann H, Vogel M, Petersen D, Poremba M. 1992. Speech deficits in ischaemic cerebellar lesions. Journalof Neurology 239:223–227. DOI: https://doi.org/10.1007/BF00839144, PMID: 1597689

Ahn AH, Dziennis S, Hawkes R, Herrup K. 1994. The cloning of zebrin II reveals its identity with aldolase C.Development 120:2081–2090. PMID: 7925012

Albergaria C, Silva NT, Pritchett DL, Carey MR. 2018. Locomotor activity modulates associative learning in mouse cerebellum. Nature Neuroscience 21:725–735. DOI: https://doi.org/10.1038/s41593-018-0129-x,PMID: 29662214

Altschuler SJ, Wu LF. 2010. Cellular heterogeneity: do differences make a difference? Cell 141:559–563.DOI: https://doi.org/10.1016/j.cell.2010.04.033, PMID: 20478246

Apps R, Hawkes R, Aoki S, Bengtsson F, Brown AM, Chen G, Ebner TJ, Isope P, Jörntell H, Lackey EP, LawrensonC, Lumb B, Schonewille M, Sillitoe RV, Spaeth L, Sugihara I, Valera A, Voogd J, Wylie DR, Ruigrok TJH. 2018.Cerebellar modules and their role as operational cerebellar processing units. The Cerebellum 17:654–682.DOI: https://doi.org/10.1007/s12311-018-0952-3

Apps R, Hawkes R. 2009. Cerebellar cortical organization: a one-map hypothesis. Nature Reviews Neuroscience10:670–681. DOI: https://doi.org/10.1038/nrn2698, PMID: 19693030

Armstrong CL, Krueger-Naug AM, Currie RW, Hawkes R. 2001. Expression of heat-shock protein Hsp25 in mouse purkinje cells during development reveals novel features of cerebellar compartmentation. The Journal of Comparative Neurology 429:7–21. DOI: https://doi.org/10.1002/1096-9861(20000101)429:1<7::AID-CNE2>3.0.CO;2-Q, PMID: 11086286

Badura A, Schonewille M, Voges K, Galliano E, Renier N, Gao Z, Witter L, Hoebeek FE, Chédotal A, De Zeeuw CI. 2013. Climbing fiber input shapes reciprocity of purkinje cell firing. Neuron 78:700–713. DOI: https://doi.org/10.1016/j.neuron.2013.03.018, PMID: 23643935

Barski JJ, Dethleffsen K, Meyer M. 2000. Cre recombinase expression in cerebellar purkinje cells. Genesis 28:93–98. DOI: https://doi.org/10.1002/1526-968X(200011/12)28:3/4<93::AID-GENE10>3.0.CO;2-W, PMID: 11105049

Becker EB, Oliver PL, Glitsch MD, Banks GT, Achilli F, Hardy A, Nolan PM, Fisher EM, Davies KE. 2009. A point mutation in TRPC3 causes abnormal purkinje cell development and cerebellar ataxia in moonwalker mice.PNAS 106:6706–6711. DOI: https://doi.org/10.1073/pnas.0810599106, PMID: 19351902

Becker EB. 2014. The moonwalker mouse: new insights into TRPC3 function, cerebellar development, and ataxia. The Cerebellum 13:628–636. DOI: https://doi.org/10.1007/s12311-014-0564-5, PMID: 24797279

Bodranghien F, Bastian A, Casali C, Hallett M, Louis ED, Manto M, Mariën P, Nowak DA, Schmahmann JD, Serrao M, Steiner KM, Strupp M, Tilikete C, Timmann D, van Dun K. 2016. Consensus paper: revisiting the symptoms and signs of cerebellar syndrome. The Cerebellum 15:369–391. DOI: https://doi.org/10.1007/s12311-015-0687-3, PMID: 26105056

Boele HJ, Peter S, Ten Brinke MM, Verdonschot L, IJpelaar ACH, Rizopoulos D, Gao Z, Koekkoek SKE, De ZeeuwCI. 2018. Impact of parallel fiber to purkinje cell long-term depression is unmasked in absence of inhibitory input. Science Advances 4:eaas9426. DOI: https://doi.org/10.1126/sciadv.aas9426, PMID: 30306129

Brochu G, Maler L, Hawkes R. 1990. Zebrin II: a polypeptide antigen expressed selectively by purkinje cells reveals compartments in rat and fish cerebellum. The Journal of Comparative Neurology 291:538–552.DOI: https://doi.org/10.1002/cne.902910405, PMID: 2329190

Cerminara NL, Lang EJ, Sillitoe RV, Apps R. 2015. Redefining the cerebellar cortex as an assembly of non-uniform purkinje cell microcircuits. Nature Reviews Neuroscience 16:79–93. DOI: https://doi.org/10.1038/nrn3886, PMID: 25601779

Chaumont J, Guyon N, Valera AM, Dugué GP, Popa D, Marcaggi P, Gautheron V, Reibel-Foisset S, Dieudonné S,Stephan A, Barrot M, Cassel JC, Dupont JL, Doussau F, Poulain B, Selimi F, Léna C, Isope P. 2013. Clusters of cerebellar purkinje cells control their afferent climbing fiber discharge. PNAS 110:16223–16228. DOI: https://doi.org/10.1073/pnas.1302310110, PMID: 24046366

Chung SH, Kim CT, Hawkes R. 2008. Compartmentation of GABA B receptor2 expression in the mousecerebellar cortex. The Cerebellum 7:295–303. DOI: https://doi.org/10.1007/s12311-008-0030-3, PMID: 18418671

De Zeeuw CI, Hoebeek FE, Bosman LW, Schonewille M, Witter L, Koekkoek SK. 2011. Spatiotemporal firing patterns in the cerebellum. Nature Reviews Neuroscience 12:327–344. DOI: https://doi.org/10.1038/nrn3011,PMID: 21544091

De Zeeuw CI, Ten Brinke MM. 2015. Motor learning and the cerebellum. Cold Spring Harbor Perspectives in Biology 7:a021683. DOI: https://doi.org/10.1101/cshperspect.a021683, PMID:

26330521

De Zeeuw CI, Yeo CH. 2005. Time and tide in cerebellar memory formation. Current Opinion in Neurobiology 15:667–674. DOI: https://doi.org/10.1016/j.conb.2005.10.008, PMID: 16271462

Diedrichsen J, Criscimagna-Hemminger SE, Shadmehr R. 2007. Dissociating timing and coordination as functions of the cerebellum. Journal of Neuroscience 27:6291–6301. DOI: https://doi.org/10.1523/JNEUROSCI.0061-07.2007, PMID: 17554003

Fujita H, Aoki H, Ajioka I, Yamazaki M, Abe M, Oh-Nishi A, Sakimura K, Sugihara I. 2014. Detailed expression pattern of aldolase C (Aldoc) in the cerebellum, retina and other Areas of the CNS studied in Aldoc-Venus knock-in mice. PLOS ONE 9:e86679. DOI: https://doi.org/10.1371/journal.pone.0086679, PMID: 24475166

Gincel D, Regan MR, Jin L, Watkins AM, Bergles DE, Rothstein JD. 2007. Analysis of cerebellar purkinje cells using EAAT4 glutamate transporter promoter reporter in mice generated via bacterial artificial chromosome-mediated transgenesis. Experimental Neurology 203:205–212. DOI: https://doi.org/10.1016/j.expneurol.2006.08.016, PMID: 17022974

Graham DJ, Wylie DR. 2012. Zebrin-immunopositive and -immunonegative stripe pairs represent functional units in the pigeon vestibulocerebellum. Journal of Neuroscience 32:12769–12779. DOI: https://doi.org/10.1523/JNEUROSCI.0197-12.2012, PMID: 22973000

Hartmann J, Dragicevic E, Adelsberger H, Henning HA, Sumser M, Abramowitz J, Blum R, Dietrich A, Freichel M, Flockerzi V, Birnbaumer L, Konnerth A. 2008. TRPC3 channels are required for synaptic transmission and motor coordination. Neuron 59:392–398. DOI: https://doi.org/10.1016/j.neuron.2008.06.009, PMID: 18701065

Hartmann J, Henning HA, Konnerth A. 2011. mGluR1/TRPC3-mediated synaptic transmission and calcium signaling in mammalian central neurons. Cold Spring Harbor Perspectives in Biology 3:a006726. DOI: https://doi.org/10.1101/cshperspect.a006726

Hashimoto K, Miyata M, Watanabe M, Kano M. 2001. Roles of phospholipase Cbeta4 in synapse elimination and plasticity in developing and mature cerebellum. Molecular Neurobiology 23:69–82. DOI: https://doi.org/10.1385/MN:23:1:69, PMID: 11642544

Hesslow G. 1994. Inhibition of classically conditioned eyeblink responses by stimulation of the cerebellar cortexin the decerebrate cat. The Journal of Physiology 476:245–256. DOI: https://doi.org/10.1113/jphysiol.1994.sp020127, PMID: 8046641

Hirata Y, Highstein SM. 2000. Analysis of the discharge pattern of floccular purkinje cells in relation to vertical head and eye movement in the squirrel monkey. Progress in Brain Research 124:221–232. DOI: https://doi.org/10.1016/S0079-6123(00)24019-3, PMID: 10943128

Horn KM, Pong M, Gibson AR. 2010. Functional relations of cerebellar modules of the cat. Journal of Neuroscience 30:9411–9423. DOI: https://doi.org/10.1523/JNEUROSCI.0440-10.2010, PMID: 20631170

Jirenhed DA, Bengtsson F, Hesslow G. 2007. Acquisition, extinction, and reacquisition of a cerebellar cortical memory trace. Journal of Neuroscience 27:2493–2502. DOI: https://doi.org/10.1523/JNEUROSCI.4202-06.2007, PMID: 17344387

Johansson F, Jirenhed DA, Rasmussen A, Zucca R, Hesslow G. 2014. Memory trace and timing mechanism localized to cerebellar purkinje cells. PNAS 111:14930–14934. DOI: https://doi.org/10.1073/pnas.1415371111,PMID: 25267641

Kim SJ. 2013. TRPC3 channel underlies cerebellar long-term depression. The Cerebellum 12:334–337. DOI: https://doi.org/10.1007/s12311-013-0455-1, PMID: 23408143

Marzban H, Hawkes R. 2011. On the architecture of the posterior zone of the cerebellum. The Cerebellum 10:422–434. DOI: https://doi.org/10.1007/s12311-010-0208-3, PMID: 20838950

Mateos JM, Osorio A, Azkue JJ, Benítez R, Elezgarai I, Bilbao A, Díez J, Puente N, Kuhn R, Knöpfel T, Hawkes R, Doñate-Oliver F, Grandes P. 2001. Parasagittal compartmentalization of the metabotropic glutamate receptor mGluR1b in the cerebellar cortex. European Journal of Anatomy 5:15–21.

Miyata M, Kim HT, Hashimoto K, Lee TK, Cho SY, Jiang H, Wu Y, Jun K, Wu D, Kano M, Shin HS. 2001. Deficient long-term synaptic depression in the rostral cerebellum correlated with impaired motor learning in phospholipase C beta4 mutant mice. European Journal of Neuroscience 13:1945–1954. DOI: https://doi.org/10.1046/j.0953-816x.2001.01570.x, PMID: 11403688

Mostofi A, Holtzman T, Grout AS, Yeo CH, Edgley SA. 2010. Electrophysiological localization of eyeblink-related microzones in rabbit cerebellar cortex. Journal of Neuroscience 30:8920–8934. DOI: https://doi.org/10.1523/JNEUROSCI.6117-09.2010, PMID: 20592214

Nunzi MG, Birnstiel S, Bhattacharyya BJ, Slater NT, Mugnaini E. 2001. Unipolar brush cells form a

5

glutamatergic projection system within the mouse cerebellar cortex. The Journal of Comparative Neurology 434:329–341.DOI: https://doi.org/10.1002/cne.1180, PMID: 11331532

Ohtani Y, Miyata M, Hashimoto K, Tabata T, Kishimoto Y, Fukaya M, Kase D, Kassai H, Nakao K, Hirata T, Watanabe M, Kano M, Aiba A. 2014. The synaptic targeting of mGluR1 by its carboxyl-terminal domain is crucial for cerebellar function. Journal of Neuroscience 34:2702–2712. DOI: https://doi.org/10.1523/JNEUROSCI.3542-13.2014, PMID: 24523559

Ohtsuki G, Piochon C, Adelman JP, Hansel C. 2012. SK2 channel modulation contributes to compartment-specific dendritic plasticity in cerebellar purkinje cells. Neuron 75:108–120. DOI: https://doi.org/10.1016/j.neuron.2012.05.025, PMID: 22794265

Perkins EM, Clarkson YL, Suminaite D, Lyndon AR, Tanaka K, Rothstein JD, Skehel P, Wyllie DJA, Jackson M.2018. Loss of cerebellar glutamate transporters EAAT4 and GLAST differentially affects the spontaneous firing pattern and survival of purkinje cells. Human Molecular Genetics: 2614–2627. DOI: https://doi.org/10.1093/hmg/ddy169, PMID: 29741614

Peter S, ten Brinke MM, Stedehouder J, Reinelt CM, Wu B, Zhou H, Zhou K, Boele H-J, Kushner SA, Lee MG, Schmeisser MJ, Boeckers TM, Schonewille M, Hoebeek FE, De Zeeuw CI. 2016. Dysfunctional cerebellar purkinje cells contribute to autism-like behaviour in Shank2-deficient mice. Nature Communications 7:e12627.DOI: https://doi.org/10.1038/ncomms12627

Raman IM, Bean BP. 1999. Ionic currents underlying spontaneous action potentials in isolated cerebellar purkinje neurons. The Journal of Neuroscience 19:1663–1674. DOI: https://doi.org/10.1523/JNEUROSCI.19-05-01663.1999, PMID: 10024353

Raymond JL, Lisberger SG, Mauk MD. 1996. The cerebellum: a neuronal learning machine? Science 272:1126–1131. DOI: https://doi.org/10.1126/science.272.5265.1126, PMID: 8638157

Renier N, Wu Z, Simon DJ, Yang J, Ariel P, Tessier-Lavigne M. 2014. iDISCO: a simple, rapid method to immunolabel large tissue samples for volume imaging. Cell 159:896–910. DOI: https://doi.org/10.1016/j.cell.2014.10.010, PMID: 25417164

Ruigrok TJ, Pijpers A, Goedknegt-Sabel E, Coulon P. 2008. Multiple cerebellar zones are involved in the controlof individual muscles: a retrograde transneuronal tracing study with Rabies virus in the rat. European Journal of Neuroscience 28:181–200. DOI: https://doi.org/10.1111/j.1460-9568.2008.06294.x, PMID: 18662342

Ruigrok TJ. 2011. Ins and outs of cerebellar modules. The Cerebellum 10:464–474. DOI: https://doi.org/10.1007/s12311-010-0164-y, PMID: 20232190

Ruigrok TJ, Hensbroek RA, Simpson JI. 2011. Spontaneous activity signatures of morphologically identified interneurons in the vestibulocerebellum. Journal of Neuroscience 31:712–724. DOI: https://doi.org/10.1523/JNEUROSCI.1959-10.2011, PMID: 21228180

Sanchez M, Sillitoe RV, Attwell PJ, Ivarsson M, Rahman S, Yeo CH, Hawkes R. 2002. Compartmentation of the rabbit cerebellar cortex. The Journal of Comparative Neurology 444:159–173. DOI: https://doi.org/10.1002/cne.10144, PMID: 11835188

Schonewille M, Belmeguenai A, Koekkoek SK, Houtman SH, Boele HJ, van Beugen BJ, Gao Z, Badura A, Ohtsuki G, Amerika WE, Hosy E, Hoebeek FE, Elgersma Y, Hansel C, De Zeeuw CI. 2010. Purkinje cell-specific knockout of the protein phosphatase PP2B impairs potentiation and cerebellar motor learning. Neuron 67:618–628.DOI: https://doi.org/10.1016/j.neuron.2010.07.009, PMID: 20797538

Schonewille M, Gao Z, Boele HJ, Veloz MF, Amerika WE, Simek AA, De Jeu MT, Steinberg JP, Takamiya K,Hoebeek FE, Linden DJ, Huganir RL, De Zeeuw CI. 2011. Reevaluating the role of LTD in cerebellar motor learning. Neuron 70:43–50. DOI: https://doi.org/10.1016/j.neuron.2011.02.044, PMID: 21482355

Schonewille M. 2019. iMove: Analysis tools for eye movements analysis Routine. GitHub. https://github.com/MSchonewille/iMove

Schreurs BG, Tomsic D, Gusev PA, Alkon DL. 1997. Dendritic excitability microzones and occluded long-term depression after classical conditioning of the rabbit's nictitating membrane response. Journal of Neurophysiology 77:86–92. DOI: https://doi.org/10.1152/jn.1997.77.1.86, PMID: 9120599

Sekerková´ G, Kim JA, Nigro MJ, Becker EB, Hartmann J, Birnbaumer L, Mugnaini E, Martina M. 2013. Earlyonset of ataxia in moonwalker mice is accompanied by complete ablation of type II unipolar brush cells and purkinje cell dysfunction. Journal of Neuroscience 33:19689–19694. DOI: https://doi.org/10.1523/JNEUROSCI.2294-13.2013, PMID: 24336732

Shadmehr R. 2017. Distinct neural circuits for control of movement vs. holding still. Journal of Neurophysiology117:1431–1460. DOI: https://doi.org/10.1152/jn.00840.2016, PMID: 28053244

Simpson JI, Wylie DR, De Zeeuw CI. 1996. On climbing fiber signals and their consequence(s). Behavioral and Brain Sciences 19:384–398. DOI: https://doi.org/10.1017/S0140525X00081486

Stahl JS. 2004. Using eye movements to assess brain function in mice. Vision Research 44:3401–3410. DOI: https://doi.org/10.1016/j.visres.2004.09.011, PMID: 15536008

Sugihara I, Quy PN. 2007. Identification of aldolase C compartments in the mouse cerebellar cortex by olivocerebellar labeling. The Journal of Comparative Neurology 500:1076–1092. DOI: https://doi.org/10.1002/cne.21219, PMID: 17183552

Sun Y, Sukumaran P, Bandyopadhyay BC, Singh BB. 2014. Physiological function and characterization of TRPCs in neurons. Cells 3:455–475. DOI: https://doi.org/10.3390/cells3020455, PMID: 24852263

Suvrathan A, Payne HL, Raymond JL. 2016. Timing rules for synaptic plasticity matched to behavioral function. Neuron 92:959–967. DOI: https://doi.org/10.1016/j.neuron.2016.10.022, PMID: 27839999

ten Brinke MM, Boele HJ, Spanke JK, Potters JW, Kornysheva K, Wulff P, IJpelaar AC, Koekkoek SK, De Zeeuw CI. 2015. Evolving models of pavlovian conditioning: cerebellar cortical dynamics in awake behaving mice. Cell Reports 13:1977–1988. DOI: https://doi.org/10.1016/j.celrep.2015.10.057, PMID: 26655909

Thach WT, Goodkin HP, Keating JG. 1992. The cerebellum and the adaptive coordination of movement. Annual Review of Neuroscience 15:403–442. DOI: https://doi.org/10.1146/annurev.ne.15.030192.002155,PMID: 1575449

Tian J, Zhu M. 2018. GABAB receptors augment TRPC3-Mediated slow excitatory postsynaptic current to regulate cerebellar purkinje neuron response to Type-1 metabotropic glutamate receptor activation. Cells 7:90.DOI: https://doi.org/10.3390/cells7080090

Vinueza Veloz MF, Zhou K, Bosman LW, Potters JW, Negrello M, Seepers RM, Strydis C, Koekkoek SK, De Zeeuw CI. 2015. Cerebellar control of gait and interlimb coordination. Brain Structure & Function 220:3513–3536. DOI: https://doi.org/10.1007/s00429-014-0870-1, PMID: 25139623

Voges K, Wu B, Post L, Schonewille M, De Zeeuw CI. 2017. Mechanisms underlying vestibulocerebellar motorlearning in mice depend on movement direction. The Journal of Physiology 595:5301–5326. DOI: https://doi.org/10.1113/JP274346, PMID: 28586131

Wadiche JI, Jahr CE. 2005. Patterned expression of purkinje cell glutamate transporters controls synaptic plasticity. Nature Neuroscience 8:1329–1334. DOI: https://doi.org/10.1038/nn1539, PMID: 16136036

White JJ, Sillitoe RV. 2017. Genetic silencing of olivocerebellar synapses causes dystonia-like behaviour in mice. Nature Communications 8:e14912.Witter L, Canto CB, Hoogland TM, de Gruijl JR, De Zeeuw CI. 2013. Strength and timing of motor responses mediated by rebound firing in the cerebellar nuclei after purkinje cell activation. Frontiers in Neural Circuits 7:133. DOI: https://doi.org/10.3389/fncir.2013.00133, PMID: 23970855

Womack M, Khodakhah K. 2002. Active contribution of dendrites to the tonic and trimodal patterns of activity in cerebellar purkinje neurons. The Journal of Neuroscience 22:10603–10612. DOI: https://doi.org/10.1523/JNEUROSCI.22-24-10603.2002, PMID: 12486152

Wu B, Schonewille M. 2018. Targeted Electrophysiological Recordings in Vivo in the Mouse Cerebellum. In: Extracellular Recording Approaches, Roy Sillitoe. New York: Humana Press. p. 19–37.

Xiao J, Cerminara NL, Kotsurovskyy Y, Aoki H, Burroughs A, Wise AK, Luo Y, Marshall SP, Sugihara I, Apps R,Lang EJ. 2014. Systematic regional variations in purkinje cell spiking patterns. PLOS ONE 9:e105633.DOI: https://doi.org/10.1371/journal.pone.0105633, PMID: 25144311

Yang Y, Lisberger SG. 2014. Purkinje-cell plasticity and cerebellar motor learning are graded by complex-spike duration. Nature 510:529–532. DOI: https://doi.org/10.1038/nature13282, PMID: 24814344

Zhou H, Lin Z, Voges K, Ju C, Gao Z, Bosman LW, Ruigrok TJ, Hoebeek FE, De Zeeuw CI, Schonewille M. 2014.Cerebellar modules operate at different frequencies. eLife 3:e02536. DOI: https://doi.org/10.7554/eLife.02536,PMID: 24843004

Zhou H, Voges K, Lin Z, Ju C, Schonewille M. 2015. Differential purkinje cell simple spike activity and pausingbehavior related to cerebellar modules. Journal of Neurophysiology 113:2524–2536. DOI: https://doi.org/10.1152/jn.00925.2014, PMID: 25717166

Chapter 6

Purkinje cell axonal swellings enhance action potential fidelity and cerebellar function

Daneck Lang-Ouellette, François G. C. Blot, Chloe A. Stewart, Pauline de Vanssay de Blavous, Connie H. Li, Carter Van Eitrem, Charlotte Rosen, Phyllis L. Faust, Martijn Schonewille, and Alanna J. Watt

Abstract

Axonal plasticity allows neurons to control their output, which critically determines the flow of information in the brain. Axon diameter can be regulated by activity, yet an understanding of how morphological changes in an axonal structure impact its function remains poorly understood. Axonal swellings have been found on Purkinje cell axons in the cerebellum both in healthy development and in neurodegenerative diseases where they have been thought to contribute to axonal pathophysiology. Here we report that Purkinje cell axons with swellings propagated action potentials with higher fidelity than those without, and that axonal swellings form when axonal failures are high. Furthermore, we observed that healthy young adult mice with more axonal swellings learned better on cerebellar-related tasks than mice with fewer swellings. Our findings suggest that axonal swellings underlie a novel form of axonal plasticity that optimizes the fidelity of action potential propagation in axons, resulting in enhanced learning.

Keywords

Axon, morphology, plasticity, Purkinje cell, cerebellum, two-photon imaging, light-sheet imaging, action potential, spike failures, motor learning, torpedoes.

Introduction

Information is transmitted in the nervous system primarily by action potentials traveling along axons. This means that a neuron's ability to maintain high-fidelity axonal propagation is of fundamental importance for its function[1]. Indeed, instances when axonal propagation is delayed or interrupted can produce devastating consequences. For example, in multiple sclerosis (MS), axonal impairments resulting from the break-down of myelin that surrounds axons lead to severe sensory and motor symptoms. Conversely, alterations in axonal structure can also be adaptive: for example, neurons respond to elevated levels of activity by restructuring their axon initial segment (AIS) to homeostatically regulate their excitability[2].

Since Purkinje cell axons carry information out of the cerebellar cortex, changes in the structure of their axons could impact cerebellar function dramatically. Purkinje cell axonal swellings appear transiently during

cerebellar development[3,4] and are observed during normal aging[5], including in healthy human samples[6,7]. These data suggest that axonal swellings play a physiological role in the brain. However, axonal swellings have also been associated with axon dysfunction in several neurodegenerative diseases[8-11], indicating that axonal swellings may be implicated in pathological function. Likewise, computational modeling has proposed that axonal swellings serve a pathophysiological role, as models predict that action potentials will be delayed, filtered, or fail when propagating across an axonal swelling[12-14].

To determine the impact of axonal swellings on Purkinje cell axonal function, we performed visually-targeted dual recordings from the soma and axon of individual Purkinje cells from young mice, and found that Purkinje cell axonal failures were reduced in axons with swellings. In other words, axonal propagation was more reliable when swellings were present. Pharmacologically mimicking high levels of axonal failures led to the formation of focal axonal swellings, and we uncovered that their formation is Ca^{2+}-dependent and requires Ca^{2+} entry through voltage-gated Ca^{2+} channels. Finally, by examining cerebellar-related behavior, we observed that mice exhibiting higher levels of cerebellar learning had higher numbers of axonal swellings. These data suggest that the enhancement of action potential propagation associated with axonal swellings in healthy young animals positively impacts behaviour.

Results

Action potential propagation is enhanced in axons with swellings:

Purkinje cell axonal swellings are present in healthy developing rodents[4] and are also observed in several neurodegenerative diseases[8-11]. However, functional measurements of the impact of axonal swellings on axons have been lacking. We used dual targeted loose-patch recordings with fluorescently-tagged Quantum dot-coated glass electrodes[15] to measure action potentials simultaneously in Purkinje cell somata and axons (**Fig. 1a**) in acute brain slices prepared from the cerebellar vermis of juvenile, healthy transgenic mice expressing GFP in Purkinje cells, including in their axons[16,17]. Since computational models suggest that axonal swellings increase axonal failure rates[13], we monitored action potential failures in Purkinje cells with and without focal axonal swellings (**Fig. 1b**). Since the vast majority of swelling appeared as single swellings on axons (> 95%; **Supplementary Fig. 1**), we targeted axons with single swellings only. Surprisingly, we found that the

axonal failure rate in Purkinje cells with swellings was significantly lower than that in Purkinje cells without axonal swellings (Control Axon: 6.07 ± 1.36 per 1000 spike; n = 11; Axon with Swelling: 1.12 ± 0.41 per 1000 spike; n = 9; Mann Whitney *U* test, P = 0.002; **Fig. 1c**). A large proportion of axons with swellings propagated action potentials with very high fidelity (having very few axonal failures), whereas only the occasional axon without a swelling propagated with similar fidelity (9.1% of control axons were high-fidelity; 55.5% of axons with swellings were high-fidelity; Mann Whitney *U* test, P = 0.05; **Fig. 1d**). We found no differences in the propagation speed in axons with swelling and control axons, suggesting that swellings do not change the propagation speed of action potentials, or at least not over the relatively short distances that we have measured (**Supplementary Fig. 2; Supplementary Table 1**). Taken together, these data argue that axonal swellings enhance rather than impair axonal propagation.

As changes in intrinsic firing have been observed in several ataxia and autism mouse models[18-21], we wondered whether firing properties would differ in Purkinje cells with axonal swellings. We found that Purkinje cells with axonal swellings fired action potentials at rates that were indistinguishable from those with axons without swellings and observed no changes in regularity (**Supplementary Fig. 3**). Furthermore, we observed no relationship between baseline firing rate and axonal failure rate for axons with or without swellings (**Supplementary Fig. 3**). This was surprising because axonal failures are enhanced when Purkinje cell firing is driven at extremely high frequencies (> 250 Hz)[22-24]. This observation suggests that baseline axonal failure rate is regulated in a manner that is distinct from the processes that contribute to axonal failures at high frequencies.

To examine axonal swellings in greater detail, we studied their ultrastructure by imaging anterior lobules of cerebellar vermis with transmission electron microscopy (TEM; from N = 7 mice). We identified 15 myelinated spheroid-shaped structures with smallest diameters greater than 4 µm as putative axonal swellings (**Fig. 2a, b;** swelling diameter average = 8.1 µm; range from 4.1 to 11.8 µm). We found no evidence of presynaptic or postsynaptic specializations, confirming that axonal swellings are not presynaptic terminals or specialized postsynaptic structure for axo-axonal synapses. Axonal swellings were myelinated and we fortuitously found two instances where an axonal swelling had intact flanking axonal segments (one example shown in **Fig. 2a**) which revealed that the myelin surrounding the axonal swelling was similar to that around flanking axons. Occasionally, we observed perinodal protrusions proximal to an axonal swelling (**Fig. 2a**, white asterisk), which agrees with our findings that about half of axonal

swellings are near the paranodal protein CASPR (contactin-associated protein 1; n = 58 axonal swellings; **Supplementary Fig. 4**), suggesting that swellings are frequently found close to paranodal junction, and therefore are proximal to nodes of Ranvier. Additionally, we occasionally observed periaxonal oligodendrocyte cytoplasm associated with axonal swellings (**Fig. 2a** cyan box inset, observed in ~20% of swellings), as has been previously described[25]. Although the function of specialized oligodendrocytic structures like perinodal protrusions is poorly understood, it suggests that axonal swellings may preferentially form close to them. Given that perinodal and internodal structures play a role in saltatory conduction[26], our results suggest that oligodendrocytic specialization and perinodal protrusions proximal to axonal swellings may contribute to enhanced action potential propagation in Purkinje cell axons.

TEM revealed that axonal swellings are rich in intracellular organelles including mitochondria and endoplasmic reticulum (ER) (**Fig. 2a, b** yellow box inset). We also found that the majority (~80 %) of axonal swellings were positive for ER-located IP3R (inositol 1,4,5-trisphosphate receptors) using immunocytochemistry (**Supplementary Fig. 5**), as previously reported[27]. Furthermore, the majority of axonal swelling contained close co-localization of ER and mitochondria (**Fig. 2b** yellow box inset), which has been linked to axonal repair in peripheral axons[28]. Surprisingly, we did not observe a significant enrichment in the density of intracellular organelles in axonal swellings compared to control axons (**Fig. 2c; Supplementary Table 1**), although dense packing of organelles has been reported for axonal swellings in disease models[29], suggesting that swellings in healthy and diseased brains differ in their subcellular composition. Even without enrichment, however, all swellings contained intracellular organelles such as mitochondria and ER, which may lead to specialized biochemical signaling which could contribute to the enhancement of action potential propagation that we have observed (**Fig. 1**).

A distinguishing morphological feature of disease-related axonal swellings in human post-mortem tissue is disorganized neurofilament[29]. Interestingly, we detected disorganized neurofilament in most axonal swellings from healthy young mice (**Fig. 2b** inset). The prevailing interpretation of disorganized neurofilament as a marker of impaired axonal transportation appears incongruous with our observation of their presence in axonal swellings that enhance axonal function, and highlight that some similarities exist between swellings from healthy brains and disease.

We found that axons flanking axonal swellings were similar in diameter to control axons without swellings, suggesting that axonal swellings occur on

axons that are not morphologically distinct (**Supplementary Fig. 6**). Axonal propagation is influenced not only by the size of the axonal diameter, but also by the thickness of the myelin sheath surrounding it, which is reflected in an axon's g-ratio (g-ratio = axonal diameter/axonal diameter + total diameter including myelin sheath)[30]. In agreement with what has been reported for axons with large diameters[31,32], the myelin sheath around putative axonal swellings is thicker than that around thin axons (**Supplementary Fig. 6**). However, the increase in myelin thickness is modest, and not proportional to the increase in diameter, where the g-ratio for axonal swellings is higher and farther from the theoretical optimal g-ratio (**Fig. 2d; Supplementary Table 1**). This data appears at odds with our findings of unchanged propagation velocity (**Supplementary Fig. 2**), since higher g-ratios are thought to be associated with decreased propagation velocity[30]. Interestingly, despite enhanced myelination, large central axons tend to have larger g-ratios than smaller axons[33,34], which is reminiscent to what we have reported for axonal swellings, and suggests that optimal g-ratios may differ for different classes of axons[24]. Since dynamic regulation of myelin structure may impact axonal propagation[35]; the modest increase in myelination we measured around putative axonal swellings, together with their close proximity to nodes of Ranvier, could contribute to the enhanced propagation fidelity that we have observed (**Fig. 1**).

Axonal swellings form when action potential failure rate is high in the axon:

Recent and classic studies have determined that axonal diameter can vary in response to changes in activity[36,37]. Since axonal swellings are associated with reduced axonal propagation failures, we predicted that axonal failures may be involved in their formation. To test this, we perfused a sub-saturating concentration of tetrodotoxin (10 nM; "*low TTX*", which is estimated to block ~ 75% of the Na^+ current in Purkinje cells)[38,39] onto live acute cerebellar slices. By recording spontaneous activity from the soma and/or axon of Purkinje cells, we observed that perfusing *low TTX* significantly reduced firing in axons more extensively than in Purkinje cell somas (**Fig. 3a-c**; n = 17 for somatic and axonal recordings), thereby mimicking high axonal failures pharmacologically. Through time-lapse imaging of GFP-expressing Purkinje cell axons, we discovered that swellings formed on a subset of Purkinje cell axons after 3 hours of *low TTX* application (*low TTX*: 7.11 ± 0.94 new swellings per 100 Purkinje cells; significant difference over time, P < 0.0001; n = 38 acquisitions; **Fig. 3d-f**; **Supplementary Movie 1**), while no swelling formation was observed in axons imaged over a 3 hour time period

without TTX (*no TTX*: 1.45 ± 0.95 new swellings per 100 Purkinje cells; n = 6; no difference over time, P = 0.74; **Fig. 3d-f**). To confirm that the TTX-induced formation of focal axonal swellings was due to differential activity in the soma and axon, and not the binding of Na^+ channels, we applied saturating levels of TTX (200 nM, "*high TTX*") and found that swelling formation was minimal (*high TTX*: 2.26 ± 0.79 new swellings; n = 6; not significantly different over time, P = 0.74; **Fig. 3d-f**). This posits that the swellings formed in *low TTX* arise from axonal failures. To gain insight into the time window over which axonal failures are integrated, we applied *low TTX* briefly for 30 minutes followed with a firing blockade by applying *high TTX* for 2.5 hours, or reversed the order, perfusing of *high TTX* first for 30 minutes followed by *low TTX* for 2.5 hours. We observed that in both cases, shorter periods of axonal failure produced no formation of new swellings **(Supplementary Fig. 7)**, suggesting that swellings only form when a sufficient level of axonal failure has occurred.

Upon pharmacologically mimicking axonal failures, we observed that axonal swellings form on a subset of axons, and wondered whether this selectivity arose from morphological differences between axons. We created 3-D reconstructions from time-lapse images, in *low TTX* conditions, of axons that formed new swellings and neighboring axons that did not (**Fig. 3g**). Over time, the axonal volume increased as axonal swellings formed. However, at time zero, their initial volume was indistinguishable from that of neighboring axons (control axon: 12.5 ± 3.4 μm^3; axon before swelling formed: 19.2 ± 7.7 μm^3; n = 8; P = 0.96; **Fig. 3h, i**). As expected, we observed that following three hours of *low TTX* perfusion, axons that formed swellings had significantly larger volumes than those that did not (control axon: 20.9 ± 6.8 μm^3; axon with a newly-formed swelling: 71.4 ± 17.4 μm^3; n = 8; P = 0.0047; **Fig. 3h, j**). The similarity in volume at the initial time point suggests that there is no obvious morphological signature for axons that will form a swelling, and that swellings do not originate from the local rearrangement of axoplasm in already-thicker axons.

If axonal swellings develop in response to axonal failures, what is the signal that reports when failure occurs? Since activity is implicated, we wondered whether calcium might be playing a role. To address this, we perfused *low TTX* in artificial cerebrospinal fluid (ACSF) without calcium (0 mM Ca^{2+}), and found that the absence of calcium was sufficient to block the formation of axonal swellings (1.86 ± 0.58%; n = 15; not significantly different over time, P = 0.16, **Fig. 4a-c**). Meanwhile, both 2 mM (the concentration in ACSF used in all other experiments) and 3 mM of calcium resulted in robust swelling formation (2 mM Ca^{2+}: 5.99 ± 1.14%; n = 14; 3 mM Ca^{2+}: 6.81 ± 1.23%; n = 12; both are significantly different over time, P < 0.0001 for both,

Fig. 4a-c). Importantly, 0 mM Ca^{2+} in the absence of *low TTX* did not cause formation of axonal swellings (0 mM Ca^{2+}: 1.65 ± 0.56%; n = 12; no difference over time, P = 0.25, **Fig. 4a-c).** If extracellular calcium is critical for axonal swelling formation, how might it be involved in signaling? Since voltage-dependent calcium channels are found in Purkinje cell axons, including T-type[40], we predicted that they might be implicated. We applied a saturating concentration of Ni^{2+} (1 mM) that blocks most T-type calcium channels[40-42], but may also impact other voltage-dependent calcium channels as well[43]. We found that 1 mM Ni^{2+} in the presence of *low TTX* prevented the formation of axonal swellings (Ni^{2+} + *low TTX*: 1.19 ± 0.61%; n = 8; *low* TTX: 6.09 ± 1.39%; n = 14 ; *low* TTX significantly different from Ni^{2+}+ *low* TTX, Mann-Whitney U-test, P = 0.0027; **Fig. 4d, e**) while Ni^{2+} without TTX had no effect (1 mM Ni^{2+}: 1.58 ± 0.81%; n = 6; **Fig. 4d, e**). A sub-saturating concentration of Ni^{2+} partially blocked the formation of axonal swellings, (**Supplementary Fig. 8**). These findings suggest that axonal action potential failures trigger axonal swelling via calcium entry through voltage-dependent calcium channels.

Elevated numbers of axonal swellings are linked to enhanced cerebellar learning:

Does the increase in axonal action potential propagation fidelity associated with axonal swellings have an impact on cerebellar function? To address potential functional changes, we conducted Rotarod (**Fig. 5a**), a motor task implicated in motor coordination and learning[19], and took advantage of the natural variability in learning that is observed across young adult mice (**Fig. 5b**). After performing behavioral assays, we quantified the number of Purkinje cell axonal swellings found in the granule cell layer in lobule III of the vermis, a cerebellar region that is important for locomotion[44]. We observed variability in the number of swellings across animals (**Fig. 5b**) which positively correlated with the amount of learning on the Rotarod task (R = 0.544; P = 0.011; **Fig. 5c**). High-learning mice had significantly more axonal swellings (**Fig. 5d**) than low-learning mice (low learner: 29.8 ± 3.3% axonal swellings; n = 10; high learners: 39.2 ± 3.0% axonal swellings; n = 11; P = 0.046; **Fig. 5e**). These results highlight the positive effect that axonal swellings have on cerebellar-related motor learning. Based on these data, we developed a Monte Carlo simulation to understand the differences in information content in a cerebellar network with varying numbers of axonal swellings. This model enabled us to estimate the amount of learning that can be accounted for by variation in axonal swelling occurrence. The amount of learning that the model predicted varied dramatically depending on the number of swellings (**Supplementary Fig. 9**).

We further investigated the difference in motor learning with a cerebellar-specific assay, the Erasmus ladder[45]. We trained mice to cross an Erasmus ladder every day for 4 days (**Fig. 5f**), noting the amount of learning that occurred. As we observed for Rotarod, there was significant heterogeneity in learning across mice (**Fig. 5g**). Still, learning was positively correlated with the number of axonal swellings found in lobule III of the cerebellar vermis (R = 0.776; P = 0.008; **Fig. 5h, i**). When mice were grouped into low and high learners on the Erasmus ladder, we found that high learners had significantly more axonal swellings than low learners (low learners: 34.9 ± 4.2%; n = 5; high learners: 46.6 ± 2.2%; n = 5; P = 0.039; **Fig. 5j**).

To determine whether axonal swellings influence behavior in a cerebellar region with a well-defined associated behavior, we tested the adaptation of the vestibular ocular reflex (VOR; **Fig. 5k**). VOR adaptation is known to be encoded by Purkinje cells in the flocculus[46], which differ in intrinsic firing rate from those in lobule III[47,48]. There is relatively little variability across animals for VOR adaptation (**Fig. 5l**). These experiments were also conducted in C57Bl/6J mice and axonal swellings were labeled with IP3R, which we have shown labels the majority (~ 80%), but not all, of axonal swellings in both Lobule III and the flocculus (**Supplementary Fig. 3**). We observed a positive correlation between the number of axonal swellings and learning in the flocculus that was reminiscent of the correlation seen in the anterior vermis, although not significant (R = 0.627; P = 0.052; **Fig. 5m, n**); furthermore, no significant difference was observed between the low and high learners (R = 0.627; P = 0.052; **Fig. 5m, n**; low learners: 13.2 ± 1.5%; n = 5; high learners: 17.8 ± 2.2%; n = 5; P = 0.12; **Fig. 5o**). This suggests that variability in axonal swellings in the flocculus does not account for the variability in learning in this task. However, taken together, our data suggest that axonal swellings have a modest but positive impact on cerebellar function, a trend that is consistent with their ability to ameliorate axonal spike fidelity.

As we observed fewer axonal swellings in the flocculus than in the anterior vermis of mice, we harnessed tissue clearing and light-sheet imaging techniques to determine whether the number of swellings varied across cerebellar region (**Supplementary Movie 2**). Focusing on the cerebellar vermis, we found that the number of swellings varied dramatically across cerebellar lobules, with lower numbers of swellings in posterior lobules (**Supplementary Fig. 10**). Having conducted the Rotarod task prior to imaging, we were also able to observe the positive correlation between the density of axonal swellings and learning: greater density of swellings tended to coincide with more learning (**Supplementary Fig. 10**).

Discussion

Here we describe the unexpected observation that Purkinje cell axonal swellings in young mice are associated with enhanced axonal fidelity and cerebellar performance. Using targeted paired recordings, we report that Purkinje cell axons presenting focal swellings have significantly fewer axonal failures than Purkinje cell axons without swellings, with no detectable changes in firing properties. Purkinje cell axonal swellings are myelinated, show no evidence of being synaptic structure, but are frequently observed in proximity to nodes of Ranvier or at locations enriched with oligodendrocytic cytoplasm, and have a moderately thicker myelin sheath than those surrounding smaller axons, and a higher g-ratio. These characteristics of swellings observed at the ultrastructure level may contribute to the enhanced action potential fidelity observed in axons with swellings. We wondered if axonal failures are instrumental in the formation of axonal swellings, and found that by mimicking high axonal failures, we could induce the formation of swellings on Purkinje cell axons within 2 to 3 hours. Axonal swelling formation required extracellular calcium entry and was blocked by a voltage-dependent Ca^{2+} channel blocker, suggesting that neurons detect axonal failures by the integration of calcium influx through voltage-dependent channels. Finally, using three different cerebellar-related behavioral assays, we demonstrated a positive correlation between motor learning and the number of axonal swellings in related cerebellar structures in young adult mice. Light-sheet imaging revealed that the density of axonal swellings even varies within an animal across cerebellar lobules. These data suggest that there is a behavioral read-out to the enhancement of axonal propagation associated with axonal swellings.

Modeling studies have mostly predicted that action potentials moving across axons that swell will be delayed, filtered, or fail to propagate[12-14], although this depends greatly on the precise geometry of the swelling, with small differences leading to large and at times opposite outcomes[14]. Furthermore, these models have typically focused on non-myelinated axons, so it is unclear how they apply to myelinated axons like Purkinje axons. For myelinated axons, the g-ratio is a concept that relates the thickness of myelination to an axon's diameter, which has been studied extensively. There is a theoretically optimal g-ratio that produces the fastest propagation velocity[30]. However, since g-ratios assume regular shape[30], it is difficult to interpret g-ratios for axonal swellings. These pitfalls may explain why our experimentally-determined findings of enhanced action potential propagation fidelity with no detectable change in propagation velocity appear at odds with model predictions.

Does the ultrastructure composition of axonal swellings impact axonal propagation? There are several possible ways this may occur. First, enriched organelles observed in disease-related swellings[29] may alter axonal axial resistance, although we did not observe significant enrichment in axonal swellings from young healthy mice. Moreover, IP3 receptors in axonal swellings on ER in proximity to mitochondria likely result in biochemical signal compartmentalization in the axon swelling. Whether the proximity of these signaling cascades to perinodal structures directly impacts saltatory conduction is an unresolved but exciting possibility that is raised by our observations. It is possible that the compartmentalization of intracellular signaling in axonal swellings, rather than any biophysical properties conferred by their morphology, is largely responsible for the enhancement of action potential propagation fidelity in the axon by axonal swellings.

Axonal plasticity is used by neurons to modulate their excitability and optimize neuronal output. For example, activity-dependent modulation of the axon initial segment (AIS), where action potentials are initiated, enables neurons to homeostatically adapt to alterations in their activity[2,49,50,51]. The formation of axonal swellings is reminiscent of homeostatic synaptic and intrinsic alterations like synaptic scaling or firing rate homeostasis that optimize network output[52,53], although for swellings, axon propagation fidelity appears to be the output that is being optimized. Additionally, activity-dependent myelination has been observed in several brain regions, where axons with heightened activity trigger oligodendrocytes to increase myelination[54-56]. We observed differences in the density of axonal swellings across individual mice that relates to behavior, suggesting that axonal swellings represent a novel form of structural plasticity that the nervous system utilizes to influence its function. Understanding how neurons decode axonal failures leading to the formation of axonal swellings is an important question to be answered. The signaling pathway involving calcium influx may take place directly in the axon, since voltage-dependent calcium channels are expressed in axons[40]; however, it is also possible that signaling occurs in distal locations that then are relayed to the axon, or that signals originate in the surrounding myelin sheath rather than the axon[57], which might explain the relatively slow time course of swelling formation.

We observed a correlation between the density of axonal swellings and different cerebellar-related forms of behavioral learning. These findings were surprising to us, since learning and memory are thought to be largely determined by synaptic plasticity[58]. However, many factors contribute to successful learning, including the reliable transmission of information. Indeed, we found that the number of axonal swellings correlates with motor

performance on the last day of the motor assay as well with the amount of learning, albeit this correlation was weaker for some behaviour (data not shown). A parsimonious explanation of our data is that the correlation between learning and axonal swellings arises because information is more reliably propagated in the cerebellum, and that the effect on learning could thus be indirect. Chaisanguanthum and colleagues recently showed that even a single extra action potential in Purkinje cells in the cerebellar flocculus could impact eye-movement behavior variability[59]. These data argue that reliable transmission of action potentials in axons is essential for the engagement of appropriate forms of synaptic plasticity in the brain.

Purkinje cells transmit information in vivo with two distinct patterns: simple spikes and complex spikes. Purkinje cell axons have been reported to have relatively low propagation failure rates for simple spikes with higher failures for complex spikes[23,38,40]. Our study has focused on spontaneous action potentials, which correlate with simple spikes. How and if axonal swellings impact complex spike propagation down the axon is an interesting question to be explored.

Our study has focused on Purkinje cell axons, which are important because they transmit information from the cerebellar cortex to downstream targets. Interestingly, similar axonal swellings, or spheroids, have been observed in several locations, including frontal lobe white matter[60,61], hippocampus[62], basal ganglia[63], brain stem[64], and spinal cord[65,66]. Axonal swellings in other brain regions have frequently been associated with neurodegenerative diseases[60-63,65]. However, axonal swellings have also been reported in other brain regions from healthy humans[64,66] and animal models[66]. Whether axonal swellings on axons in other brain regions cause enhanced action potential propagation as we have observed, or whether our results arise from a unique property of Purkinje cell axons remains to be determined.

Axonal swellings in neurodegenerative diseases have typically been regarded as morphological signatures of neuronal dysfunction[8-11]. Although one suggestion raised by our findings is that disease-related axonal swellings might also serve an adaptive role, several alternative explanations exist. It is possible that disease-related axonal swellings differ from those observed in healthy states; mice used in our study were young and healthy and did not suffer from a neurodegenerative disease. Furthermore, axonal swellings in neurodegenerative diseases exhibit heterogeneity in their myelination; that is, some diseases are associated with axonal swellings that are myelinated while others are associated with predominantly unmyelinated swellings[67]. It is possible that differences in underlying axonal dysfunction produces axonal

swellings with different properties, and that these swellings, which appear similar at the light-microscopic level, are nonetheless distinct structurally. It would be interesting to test the functional properties of axonal swellings arising from disease models to gain insight into whether disease-related swellings show similar properties to those characterized here. Regardless of whether they are similar or distinct from one another, our findings highlight the importance of empirically determining the impact of morphological specializations on neuronal function.

In conclusion, our data demonstrate that Purkinje cell axonal swellings constitute an adaptive alteration to morphology that maintains optimal axonal propagation. Given the central role that Purkinje cell axonal conductance plays in transmitting information from the cerebellar cortex, it appears that axonal swellings are structures that can form dynamically and enable a Purkinje cell to maintain axonal propagation fidelity, thereby optimizing cerebellar function[53].

Methods

Animals:

We used *pcp2-tau-eGFP* mice[16,17] to characterize the functional properties of axonal swellings as well as for time-lapse visualization of their formation and for Rotarod and Erasmus Ladder behavioral studies. C57BL/6J mice were used for vestibular ocular reflex (VOR) behavioral study. All animal procedures were approved either by the McGill Animal Care Committee, in accordance with guidelines established by the Canadian Council on Animal Care, or for experiments from Fig. 5K-O by the Dutch Ethical Committee for animal experiments in accordance with the Institutional Animal Care and Use committee at the Erasmus Medical Centre.

Behavior:

Mice were used at 1-2 months of age for all behavioral studies. *Rotarod Assay.* We used a Rotarod (Stoelting Europe, Dublin, Ireland) as previously described [19] to assess the natural variability of individual mice motor coordination. After an hour of acclimatization, mice were placed on an accelerating (from 4 to 40 RPM, over 5 min) Rotarod and latency to fall (4 trials/day for 7 days) was recorded. Motor learning was determined by subtracting the average time on the rod of the last two trials for day 1 from day 7. *Erasmus*

Ladder Assay. We used the Erasmus Ladder (Noldus Inc., Wageningen, GE, Netherlands) to assess motor learning [45]. Mice walked across a horizontal ladder (42 trials/day for 4 days), which consisted of 2 parallel rows of 37 pressure monitored rungs between two dark chambers. Mice typically used short steps (stepping between two upper rungs) to traverse the ladder. The change in the number of short steps across days was used to measure motor learning in individual animals. *VOR Assay*. Mice were equipped with a construct for immobilization ("pedestal") under general anesthesia with isoflurane/O_2. After a 2–3 days of recovery, mice were head-fixed with the body loosely restrained in a custom-made restrainer and placed in the center of a turntable (diameter: 60 cm) in the experimental set-up. A round screen (diameter 63 cm) with a random dotted pattern ('drum') surrounded the mouse during the experiment. VOR Phase reversal was induced by training mice over 4 days (6 x 5 min. per day) using in-phase sinusoidal drum and table rotation at 0.6 Hz (amplitude table 5° on all days, drum 5° on day 1, 7.5° on day 2, 10° on day 3-4) and probed by recording VOR in the dark before and after training sessions. A CCD camera fixed to the turntable monitored the eyes of the mice using eye-tracking software (ETL-200, ISCAN systems, Burlington, NA, USA). For eye illumination during the experiments, two infrared emitters (output 600 mW, dispersion angle 7°, peak wavelength 880 nm) were fixed to the table and a third emitter, which produced the tracked corneal reflection, was mounted to the camera and aligned horizontally with the optical axis of the camera. Eye movements were calibrated by moving the camera left-right (peak-to-peak 20°) during periods that the eye did not move[48]. Gain and phase values of eye movements were calculated using custom-made Matlab routines (MathWorks, Natick, MA, USA).

Acute Slice Preparation:

Acute slices were prepared from young juvenile mice (postnatal (P)9-14), when axonal swellings are numerous[4]. Mice were deeply anesthetized using isoflurane and checked for foot-paw reflex. Mice were decapitated, and the brain quickly removed in ice-cold artificial cerebrospinal fluid (ACSF; in mM: 125 NaCl, 2.5 KCl, 2 $CaCl_2$, 1 $MgCl_2$, 1.25 NaH_2PO_4, 26 $NaHCO_3$ and 20 glucose, bubbled with 95% O_2 and 5% CO_2 to maintain pH at 7.3; Osmolarity 320 ± 5 mOsm). Parasagittal cerebellar vermis slices (200 µm thick) were made using a Leica VT 1000S vibratome. Slices were incubated in ACSF at 37°C for 45 min and then incubated at room temperature (RT) until used for experiments. All chemicals were purchased from Sigma-Aldrich (Oakville, ON, Canada).

Electrophysiology:

All recordings were taken in lobule III from the cerebellar vermis, using a Multiclamp 700B amplifier (Molecular Devices, Sunnyvale, CA, USA), at 33°C. An upright microscope (Scientifica, Uckfield, UK) combined with a custom-built two-photon Ti:Sapphire laser (MaiTai; Spectra Physics, Santa Clara, CA, USA) was used to identify Purkinje cells soma with intact axons (GFP). Glass pipette dipped in CdSeS/ZnS alloyed quantum dots (Sigma-Aldrich, Oakville ON, CA) were visually positioned using the scanning two-photon laser as previously described[15]. Loose cell-attached or extracellular recording of Purkinje cells soma and axons was performed using a custom-designed Igor Pro acquisition and data analysis software (Wavemetrics, Portland, OR, USA). Axons were recorded in the granule cell layer, downstream from axonal swellings (50-200 μm from the parent soma), or an equivalent distance down a control axon without swellings. Approximately 30% of axons display swellings at this age[4]. Of these, the majority had single swellings (96.4%, or 187/194 of axons with swellings had single swellings, N = 4; **Supplementary Fig. 1**), we only recorded from axons with single swellings.Imaging: Parasagittal cerebellar slices were imaged with a custom-built two-photon microscope (Scientifica) with a Ti:Sapphire laser (MaiTai; Spectra Physics, Santa Clara. CA, USA) tuned to 890 nm (GFP) or 775 nm (non-GFP). Images acquisition was done using ScanImage running in MatLab (Mathworks, Natick, MA, USA). For live imaging, cerebellar slices were kept alive by continuously perfusing buffered ACSF (with drugs) at 33°C. For fixed tissue, slices from the vermis were imaged on a LSM800 laser scanning confocal microscope (Zeiss, Oberkochen, Germany), while slices from the flocculus were imaged using an LSM700 laser scanning confocal microscope (Zeiss).

Pharmacology:

Tetrodotoxin (TTX; Biotium Inc., Fremont, CA, USA) was used at a concentration of 10 nM (*low TTX*) or 200 nM (*high TTX*) and Nickel chloride (NiCl; Sigma-Aldrich, Oakville, ON, Canada) was used at a concentration of 1 mM in ACSF. Extracellular Ca^{2+} was also manipulated by changing its concentration in the ACSF (3 mM or 0 mM); the concentration of other positively-charged divalent ions (e.g. Mg^{2+}) were not altered when Ca^{2+} was altered.

Immunocytochemistry:

Mice were anesthetized using an intraperitoneal (IP) injection of Avertin (2,2,2-tribromoethanol; dosage: 0.25 mL/10 g body weight), and transcardially perfused with 4 % paraformaldehyde (PFA; Electron Microscopy Sciences, Hatfield, PA, USA). Perfused brains were removed and stored at 4°C on a rotary shaker at 70 RPM for 24 hours in 4 % PFA. Brains were then transferred into phosphate-buffered saline (PBS) with 0.05 % sodium azide. Brain were sliced on a Leica vibratome 3000 into 100 µm-thick parasagittal slices or on a cryostat Leica CM into 40 µm-thick coronal slices. In some cases, brain slices were briefly washed in a 0.1mg/ml pepsin solution dissolve in 1x phosphate buffer (PB), for 5min at RT for antigen retrieval. Slices were washed in 1x PBS - 0.4% Triton X, blocked with 5 % BSA, and primary antibodies (anti-mouse CASPR, used at a dilution of 1:200, Antibodies Incorporated, Davis, CA, US, Cat#75-001; anti-rabbit IP3R, used at a dilution of 1:200, Abcam, Cambridge, UK, abID#5804) were applied to slices for 3 days while incubated on a rotary shaker at 70 RPM at RT. After washing, secondary donkey anti-mouse or anti-rabbit antibodies conjugated to Alexa Fluor-594 (1:500, Life Technologies, Carlsbad, CA, USA, product # A12203; Jackson Immunoresearch Labs, West Grove, PA, USA, product # 711-585-152, respectively) were applied to slices while incubated on the rotary shaker for 90 min at RT. Slice were mounted on slides with Prolong gold anti-fade mounting media (Life Technologies). For imaging of axonal swellings in the flocculus, experiments differed from above in the following manner: mice were deeply anesthetized through IP administration of sodium pentobarbital, and brains were post-fixed for 1 hour instead of 24 hours, and were subsequently transferred to a 10% sucrose solution overnight at 4°C. The following day they were embedded with 10% sucrose/14% gelatin (Wako) and placed in a 30% sucrose/10% formaldehyde for 1 hour at RT, and then were switched to a 30% sucrose solution overnight at 4°C. Embedded brains were sectioned transversally into 40 µm-thick slices with a freezing microtome. Sections were rinsed with 0.1 M PB and incubated for 2 hours in 10 mM sodium citrate (pH 6) at 80 °C for 2 hours for antigen retrieval. 10% horse serum was used instead of 5% BSA to block non-specific binding, and antibodies were applied for 2 instead of 3 days. Primary antibodies used were Calbindin (1:7000 mouse monoclonal, Sigma C9848), and IP3R (1:1000 rabbit polyclonal, Abcam 5804). Secondary antibodies used were coupled to Alexa Fluor-488 or Cy3 (1:200). Sections were mounted on coverslips in Chromaluin (genatin/chromate) and covered with Mowiol mounting medium (Polysciences Inc., Bergstrasse, Germany).

Electron Microscopy:

Mice were anesthetized using an IP injection of Avertin and transcardially perfused with a combination of 2% Glutaraldehyde (Electron Microscopy Sciences) and 2% paraformaldehyde (Electron Microscopy Sciences) in 1X PBS at a perfusion rate of 5mL/min. The brain was then removed and placed in 2.5% Glutaraldehyde in 0.1M sodium cacodylate (Electron Microscopy Sciences) buffer at 4°C, overnight. Brains were dissected to isolate the anterior lobules of the cerebellar cortex. TEM was performed of axons located in the anterior cerebellar lobules 3, 4, and 6. Lobules were kept at 4ºC in fixative no longer than a week before being processed for TEM. Subsequently, samples were washed 3 times with 0.1M sodium cacodylate washing buffer (Electron Microscopy Sciences) for 1hr. The samples were then post-fixed using 1% aqueous osmium tetraoxide (Mecalab, Montreal, QC, Canada) and 1.5% aqueous potassium ferrocyanide for 2 hours, followed by 3 washes of washing buffer for a total of 15 minutes. Then, samples were dehydrated with acetone (Fisher Scientific) in increasing concentrations (30%, 50%, 70%, 80%, 90%, 3 X 100%) for 8-15 min per concentration. Samples were then infiltrated with Epon (Mecalab) in acetone as follows: 1:1 overnight, 2:1 the next day, 3:1 the following night, and pure Epon the last day for 4 hr. Samples were embedded and allowed to polymerize in a 60ºC oven for 48 hrs. Samples were trimmed and cut at 90-100 nm thick sections with UltraCut E ultramicrotome (Leica Microsystems, Wetzlar, HE, Germany, formerly Reichert-Jung) and placed onto slotted grids (Electron Microscopy Sciences). Finally, sections were stained with uranyl acetate (Electron Microscopy Sciences) for 8 min, followed by Reynold's lead (Electron Microscopy Sciences) for 5 min. Samples were imaged using FEI Tecnai G2 Spirit Twin Cryo-TEM (FEI Company, Hillsboro, OR, USA) at 120 kV and visualized with an AMT XR80C 8 megapixel CCD camera (Advanced Microscopy Techniques, Woburn, MA, USA).Tissue Clearing: Mice were anesthetized and transcardially perfused as above. The brain was removed and transferred into 4% PFA and stored at 4°C on a rotary shaker at 70RPM for 24h after which the cerebellar cortex was isolated and transferred into a hydrogel solution (10% v/v 10X PBS, 10% v/v 40% Acrylamide; 0.025% v/v 10% VA-044 and filled up to 15ml with ddH$_2$O) at 4°C for 24h. The cerebella were then transferred to the X-Clarity Polymerization system (Logos Biosystem, Annandale, VA, USA) at 37°C, under 90 kPa vacuum for 3h, followed by the X-Clarity Tissue Clearing system, using the electrophoretic tissue clearing solution (Logos Biosystem, Annandale, VA, USA) set at a current of 1 Amp at 37°C for 24h. A Lightsheet Z.1 with the Zen 2014 SP1 (black edition) software (Zeiss, Oberkochen, Germany) was used to image the whole cerebellum.

6

Data Analysis:

We used a custom-designed Igor Pro 8 software for electrophysiology data analysis of spike timing, frequency, regularity and failures. Image analysis of 2-photon image stacks was conducted out with Fiji/ImageJ2 or Zen 2014 SP1 (black edition: Zeiss). Lightsheet image processing was done using Zen 2.5 (blue edition), Imaris File Converter and Stiching 9.2.1 software, and analysis was completed using Imaris 9.3.0 software (Bitplane Inc., Zurich, Switzerland). For axonal reconstructions in **Fig. 3**, we used Neurolucida software (MBF Biosciences, Williston, VT, USA) to reconstruct an axonal swelling and the sections of axon flanking both sides of the swelling, in addition to an equivalent length of neighboring axon without a swelling. For measurement of velocity, axons were reconstructed from the recording location to the soma using Simple Neurite Traces, a plugin for ImageJ. For EM images, axons were unbiasedly identified and imaged using the presence of myelin. Using Fiji/ImageJ2, the axonal circumference was traced and minimum Feret diameter was measured. In one case where minimum Feret diameter was not applicable (i.e. in **Fig. 2a** when the axon was not spherical but rather was observed in cross-section, and thus rectangular in shape), the diameter was taken by averaging 4 diameters along the axon. Myelin thickness was quantified by measuring myelin width at 4 cartesian points, although care was taken to avoid locations where myelin infiltration occurred. Organelle density was measured by tracing organelle bodies and was quantified as the ratio between the area covered by organelles to the total axonal area.Statistics: Data normality and equality of variance were determine using Shapiro-Wilk and Levene's test. Multiple comparisons with repeated measures ANOVA were made using IBM SPSS Statistics (IBM Corp., Armonk, NY, USA), all reported data are interaction effect of conditions over time corrected for sphericity using Greenhouse-Geisser test, post-hoc analysis with Bonferroni correction were done between all conditions over time (data not shown). Due to low degree of freedom, the assumption of normality is not always respected, to address that concern non-parametric multiple comparisons were made using Kruskal-Wallis H test to compare all conditions at the latest time point, followed by Mann-Whitney U test corrected with Bonferroni. Simple comparison were made using either paired or unpaired two-tailed Student's T tests for parametric data, or the Mann Whitney U test for non-parametric data, and correlations were made using the Pearson (r) correlation test in SPSS software. Data were reported as mean ± SEM. Statistical comparisons were made with the level of significance (α) set at P* < 0.05; P** < 0.01; P*** < 0.005, unless corrected with Bonferroni.

Acknowledgements

6

Author contributions

D. L.-O. designed and ran experiments and analyzed data for all Figures, and helped write the manuscript, F.C.G.B. designed and ran experiments for Fig. 5 and helped write the manuscript, C. S. designed, ran experiments and analyzed data for Fig. 2 and helped write the manuscript. P.V.B. ran experiments for Fig. 5. C.H.L. designed and ran experiments for Fig. 3 and Fig. S6 and helped write the manuscript. C.V.E. designed and ran Monte Carlo simulation for Fig. S5. C.R. ran experiments for Fig. 1. P.H.F. helped interpret data for Fig. 2 and helped write the manuscript. M.S. designed experiments and analyze data for Fig. 5 and helped write the manuscript. A.J.W conceived of the project, designed experiments and analyzed data, supervised the project, and wrote the manuscript.

Supplementary Information

Supplementary Figs. 1-10
Supplementary Table 1
Supplementary Movies 1-2

1. Debanne, D. Information processing in the axon. *Nat Rev Neurosci* **5**, 304-316 (2004).
2. Grubb, M.S. & Burrone, J. Activity-dependent relocation of the axon initial segment fine-tunes neuronal excitability. *Nature* **465**, 1070-1074 (2010).
3. Gravel, C., Leclerc, N., Plioplys, A. & Hawkes, R.B. Focal axonal swellings in rat cerebellar Purkinje cells during normal development. *Brain Res* **363**, 325-332 (1986).
4. Ljungberg, L*., et al*. Transient Developmental Purkinje cell axonal torpedoes in healthy and ataxic mouse cerebellum. *Frontiers in cellular neuroscience*, 1-15 (2016).
5. Baurle, J. & Grusser-Cornehls, U. Axonal torpedoes in cerebellar Purkinje cells of two normal mouse strains during aging. *Acta neuropathologica* **88**, 237-245 (1994).
6. Kato, T. & Hirano, A. A Golgi study of the proximal portion of the human Purkinje cell axon. *Acta neuropathologica* **68**, 191-195 (1985).
7. Louis, E.D., Faust, P.L., Vonsattel, J.P. & Erickson-Davis, C. Purkinje cell axonal torpedoes are unrelated to advanced aging and likely reflect cerebellar injury. *Acta neuropathologica* **117**, 719-721 (2009).
8. Louis, E.D., Kuo, S.H., Vonsattel, J.P. & Faust, P.L. Torpedo formation and Purkinje cell loss: modeling their relationship in cerebellar disease. *Cerebellum* **13**, 433-439 (2014).
9. Babij, R*., et al*. Purkinje cell axonal anatomy: quantifying morphometric changes in essential tremor versus control brains. *Brain* **136**, 3051-3061 (2013).
10. Louis, E.D*., et al*. Torpedoes in Parkinson's disease, Alzheimer's disease, essential tremor, and control brains. *Mov Disord* **24**, 1600-1605 (2009).
11. Redondo, J*., et al*. Purkinje Cell Pathology and Loss in Multiple Sclerosis Cerebellum. *Brain Pathol* **25**, 692-700 (2015).
12. Manor, Y., Koch, C. & Segev, I. Effect of geometrical irregularities on propagation delay in axonal trees. *Biophys J* **60**, 1424-1437 (1991).
13. Maia, P.D*., et al*. Diagnostic tools for evaluating the impact of Focal Axonal Swellings arising in neurodegenerative diseases and/or traumatic brain injury. *J Neurosci Methods* **253**, 233-243 (2015).
14. Goldstein, S.S. & Rall, W. Changes of action potential shape and velocity for changing core conductor geometry. *Biophys J* **14**, 731-757 (1974).
15. Andrasfalvy, B.K*., et al*. Quantum dot-based multiphoton fluorescent pipettes for targeted neuronal electrophysiology. *Nat Methods* **11**, 1237-1241 (2014).
16. Sekirnjak, C., Vissel, B., Bollinger, J., Faulstich, M. & du Lac, S. Purkinje cell synapses target physiologically unique brainstem neurons. *J Neurosci* **23**, 6392-6398 (2003).
17. Watt, A.J*., et al*. Traveling waves in developing cerebellar cortex mediated by asymmetrical Purkinje cell connectivity. *Nature neuroscience* **12**, 463-473 (2009).
18. Walter, J.T., Alvina, K., Womack, M.D., Chevez, C. & Khodakhah, K. Decreases in the precision of Purkinje cell pacemaking cause cerebellar dysfunction and ataxia. *Nature neuroscience* **9**, 389-397 (2006).
19. Jayabal, S., Chang, H.H., Cullen, K.E. & Watt, A.J. 4-aminopyridine reverses ataxia and cerebellar firing deficiency in a mouse model of spinocerebellar ataxia type 6. *Sci Rep* **6**, 29489 (2016).
20. Ady, V*., et al*. Altered Synaptic and Intrinsic properties of cerebellar Purkinje cells in a mouse model of ARSACS. *Journal of Physiology* **596**, 4253-4267 (2018).
21. Stoodley, C.J*., et al*. Altered cerebellar connectivity in autism and cerebellar-mediated rescue of autism-related behaviors in mice. *Nature neuroscience* **20**, 1744-1751 (2017).
22. Khaliq, Z.M. & Raman, I.M. Axonal propagation of simple and complex spikes in cerebellar Purkinje neurons. *J Neurosci* **25**, 454-463 (2005).
23. Monsivais, P., Clark, B.A., Roth, A. & Hausser, M. Determinants of action potential propagation in cerebellar Purkinje cell axons. *J Neurosci* **25**, 464-472 (2005).
24. Hirono, M*., et al*. BK Channels Localize to the Paranodal Junction and Regulate Action Potentials in Myelinated Axons of Cerebellar Purkinje Cells. *J Neurosci* **35**, 7082-7094 (2015).
25. Watanabe, S*., et al*. Glycosphingolipid synthesis in cerebellar Purkinje neurons: roles in myelin formation and axonal homeostasis. *Glia* **58**, 1197-1207 (2010).
26. Cohen, C.C.H*., et al*. Saltatory Conduction along Myelinated Axons Involves a Periaxonal Nanocircuit. *Cell* **180**, 311-322 e315 (2020).
27. Ishibashi, T., Kodama, A. & Baba, H. Disruption of paranodal axo-glial interaction and/or absence of sulfatide causes irregular type I inositol 1,4,5-trisphosphate receptor deposition in cerebellar Purkinje neuron axons. *J Neurosci Res* **93**, 19-27 (2015).
28. Lee, S., Wang, W., Hwang, J., Namgung, U. & Min, K.T. Increased ER-mitochondria tethering

promotes axon regeneration. *Proc Natl Acad Sci U S A* **116**, 16074-16079 (2019).

29. Louis, E.D., Yi, H., Erickson-Davis, C., Vonsattel, J.P. & Faust, P.L. Structural study of Purkinje cell axonal torpedoes in essential tremor. *Neurosci Lett* **450**, 287-291 (2009).

30. Rushton, W.A. A theory of the effects of fibre size in medullated nerve. *The Journal of physiology* **115**, 101-122 (1951).

31. Michailov, G.V.*, et al.* Axonal neuregulin-1 regulates myelin sheath thickness. *Science* **304**, 700-703 (2004).

32. Fraher, J.P. Axon-myelin relationships in rat cranial nerves III, IV, and VI: a morphometric study of large- and small-fibre classes. *The Journal of comparative neurology* **286**, 384-390 (1989).

33. Chomiak, T. & Hu, B. What is the optimal value of the g-ratio for myelinated fibers in the rat CNS? A theoretical approach. *PloS one* **4**, e7754 (2009).

34. Guy, J., Ellis, E.A., Kelley, K. & Hope, G.M. Spectra of G ratio, myelin sheath thickness, and axon and fiber diameter in the guinea pig optic nerve. *The Journal of comparative neurology* **287**, 446-454 (1989).

35. Dutta, D.J.*, et al.* Regulation of myelin structure and conduction velocity by perinodal astrocytes. *Proc Natl Acad Sci U S A* **115**, 11832-11837 (2018).

36. Chereau, R., Saraceno, G.E., Angibaud, J., Cattaert, D. & Nagerl, U.V. Superresolution imaging reveals activity-dependent plasticity of axon morphology linked to changes in action potential conduction velocity. *Proc Natl Acad Sci U S A* **114**, 1401-1406 (2017).

37. Costa, A.R., Pinto-Costa, R., Sousa, S.C. & Sousa, M.M. The Regulation of Axon Diameter: From Axonal Circumferential Contractility to Activity-Dependent Axon Swelling. *Front Mol Neurosci* **11**, 319 (2018).

38. Khaliq, Z.M. & Raman, I.M. Relative contributions of axonal and somatic Na channels to action potential initiation in cerebellar Purkinje neurons. *J Neurosci* **26**, 1935-1944 (2006).

39. Swensen, A.M. & Bean, B.P. Robustness of burst firing in dissociated purkinje neurons with acute or long-term reductions in sodium conductance. *J Neurosci* **25**, 3509-3520 (2005).

40. Grundemann, J. & Clark, B.A. Calcium-Activated Potassium Channels at Nodes of Ranvier Secure Axonal Spike Propagation. *Cell reports* **12**, 1715-1722 (2015).

41. Mouginot, D., Bossu, J.L. & Gahwiler, B.H. Low-threshold Ca2+ currents in dendritic recordings from Purkinje cells in rat cerebellar slice cultures. *J Neurosci* **17**, 160-170 (1997).

42. Isope, P. & Murphy, T.H. Low threshold calcium currents in rat cerebellar Purkinje cell dendritic spines are mediated by T-type calcium channels. *The Journal of physiology* **562**, 257-269 (2005).

43. Zamponi, G.W., Bourinet, E. & Snutch, T.P. Nickel block of a family of neuronal calcium channels: subtype- and subunit-dependent action at multiple sites. *J Membr Biol* **151**, 77-90 (1996).

44. Reeber, S.L., Otis, T.S. & Sillitoe, R.V. New roles for the cerebellum in health and disease. *Front Syst Neurosci* **7**, 83 (2013).

45. Vinueza Veloz, M.F.*, et al.* Cerebellar control of gait and interlimb coordination. *Brain Struct Funct* (2014).

46. Ito, M. Cerebellar control of the vestibulo-ocular reflex--around the flocculus hypothesis. *Annual review of neuroscience* **5**, 275-296 (1982).

47. Zhou, H.*, et al.* Cerebellar modules operate at different frequencies. *Elife* **3**, e02536 (2014).

48. Wu, B.*, et al.* TRPC3 is a major contributor to functional heterogeneity of cerebellar Purkinje cells. *Elife* **8**(2019).

49. Evans, M.D., Dumitrescu, A.S., Kruijssen, D.L.H., Taylor, S.E. & Grubb, M.S. Rapid Modulation of Axon Initial Segment Length Influences Repetitive Spike Firing. *Cell reports* **13**, 1233-1245 (2015).

50. Kuba, H., Ishii, T.M. & Ohmori, H. Axonal site of spike initiation enhances auditory coincidence detection. *Nature* **444**, 1069-1072 (2006).

51. Kuba, H., Yamada, R., Ishiguro, G. & Adachi, R. Redistribution of Kv1 and Kv7 enhances neuronal excitability during structural axon initial segment plasticity. *Nat Commun* **6**, 8815 (2015).

52. Turrigiano, G.G. & Nelson, S.B. Homeostatic plasticity in the developing nervous system. *Nat Rev Neurosci* **5**, 97-107 (2004).

53. Marder, E. & Goaillard, J.M. Variability, compensation and homeostasis in neuron and network function. *Nat Rev Neurosci* **7**, 563-574 (2006).

54. Purger, D., Gibson, E.M. & Monje, M. Myelin plasticity in the central nervous system. *Neuropharmacology* **110**, 563-573 (2016).

55. Chorghay, Z., Karadottir, R.T. & Ruthazer, E.S. White Matter Plasticity Keeps the Brain in Tune: Axons Conduct While Glia Wrap. *Frontiers in cellular neuroscience* **12**, 428 (2018).

56. Gibson, E.M.*, et al.* Neuronal activity promotes oligodendrogenesis and adaptive myelination in

the mammalian brain. *Science* **344**, 1252304 (2014).

57. Yin, X*., et al.* Myelin-associated glycoprotein is a myelin signal that modulates the caliber of myelinated axons. *J Neurosci* **18**, 1953-1962 (1998).

58. Suvrathan, A. Beyond STDP-towards diverse and functionally relevant plasticity rules. *Current opinion in neurobiology* **54**, 12-19 (2019).

59. Chaisanguanthum, K.S., Joshua, M., Medina, J.F., Bialek, W. & Lisberger, S.G. The Neural Code for Motor Control in the Cerebellum and Oculomotor Brainstem. *eNeuro* **1**(2014).

60. Jin, C., Washimi, Y., Yoshida, K., Hashizume, Y. & Yazawa, I. Characterization of spheroids in hereditary diffuse leukoencephalopathy with axonal spheroids. *J Neurol Sci* **352**, 74-78 (2015).

61. Trapp, B.D*., et al.* Axonal transection in the lesions of multiple sclerosis. *N Engl J Med* **338**, 278-285 (1998).

62. Galvin, J.E., Uryu, K., Lee, V.M. & Trojanowski, J.Q. Axon pathology in Parkinson's disease and Lewy body dementia hippocampus contains alpha-, beta-, and gamma-synuclein. *Proc Natl Acad Sci U S A* **96**, 13450-13455 (1999).

63. Ohgami, T., Kitamoto, T. & Tateishi, J. Alzheimer's amyloid precursor protein accumulates within axonal swellings in human brain lesions. *Neurosci Lett* **136**, 75-78 (1992).

64. Liberski, P.P. & Budka, H. Neuroaxonal pathology in Creutzfeldt-Jakob disease. *Acta neuropathologica* **97**, 329-334 (1999).

65. Carpenter, S. Proximal axonal enlargement in motor neuron disease. *Neurology* **18**, 841-851 (1968).

66. Clark, A.W., Parhad, I.M., Griffin, J.W. & Price, D.L. Neurofilamentous axonal swellings as a normal finding in the spinal anterior horn of man and other primates. *J Neuropathol Exp Neurol* **43**, 253-262 (1984).

67. Yagishita, S. Morphological investigations on axonal swellings and spheroids in various human diseases. *Virchows Arch A Pathol Anat Histol* **378**, 181-197 (1978).
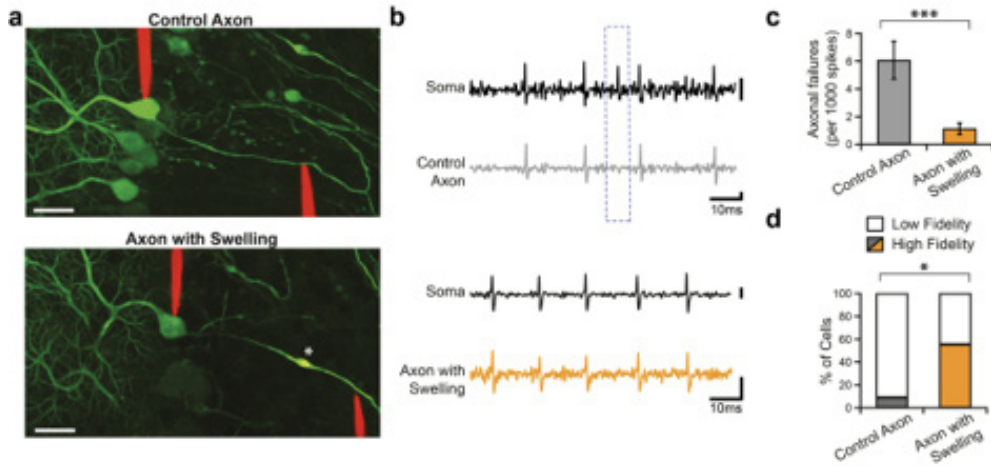
Fig. 1. Axonal swellings are associated with improved axonal propagation of action potentials.

(a) Representative images of a Purkinje cell with placement of electrodes showing simultaneous dual recording from Purkinje cells soma (left electrode) and axon (right electrode) from a control axon (top) and an axon with a swelling (bottom; asterisk indicates swelling). Scale bar, 25 µm. (b) Representative traces of dual recordings from soma (black) and axon corresponding to Purkinje cell axons without (top, grey) and with (bottom, orange) an axonal swelling. Scale bar: 0.5 mV for top two traces, 1 mV and 0.5 mV for bottom two traces, respectively. (c) Axonal spike failure rate is significantly reduced in axons with swellings (Control Axon, n= 11; Axon with Swelling, n=9; significantly different, Mann Whitney U test; ***P < 0.005). (d) Purkinje cell axons with swellings are more likely to be high fidelity transmitters (high fidelity: < 1 of 1000 action potentials fail; low fidelity > 1 in 1000 action potentials fail) than axons without swellings (Mann Whitney U test; P* < 0.05).
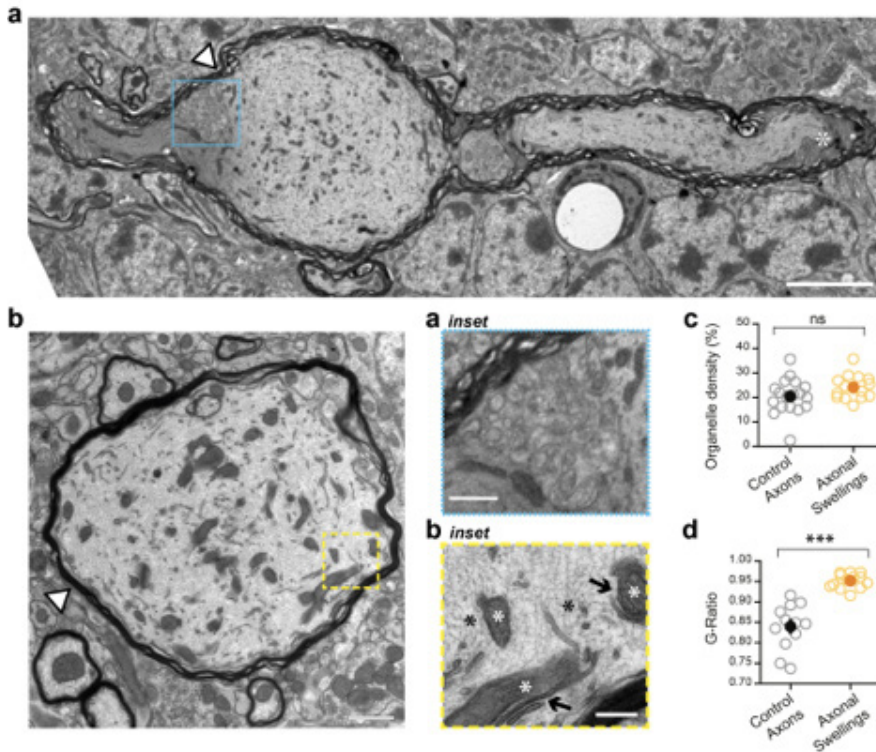
Fig. 2. Purkinje cell axonal swellings are myelinated and are not synaptic structures.

*(a) Representative TEM image showing longitudinal cut of axon with swelling and non-swollen sections extending from both sides of swelling. White asterisk shows perinodal protrusions (PNP) indicating proximity of node of Ranvier. Axon dips out of plane of image to the right of the swelling. Scale bar, 5 µm. Inset below middle: Region of interest delineated by cyan dashed outline in (a) shows periaxonal oligodendrocyte cytoplasm. Scale bar, 1 µm. (b) Representative TEM image showing crosswise cut of a putative axonal swelling (centre) with 5 neighbouring control axons, discernable by presence of dark myelin outline. Scale bar, 1 µm. Inset right: Region of interest delineated by yellow dashed outline in (b) shows mitochondria (white asterisks) that is in close proximity to EM (black arrows), and disorganized neurofilament (black asterisks). Scale bar, 500 nm. (c) Axonal swellings are not enriched in organelles compared to control axons. (n = 18 control axons; n = 15 putative axonal swellings, unpaired Student T test, P = 0.097). (d) G-ratio as a function of axonal diameter of control axons (grey) and axonal swellings (orange). Myelin is measured only in compact regions, indicated by the white arrowheads in (a) and (b). Axonal swellings have a larger g-ratio than smaller axons do. (n = 12 control axons; n = 13 putative axonal swellings, Mann Whitney U test; *** P < 0.001)*
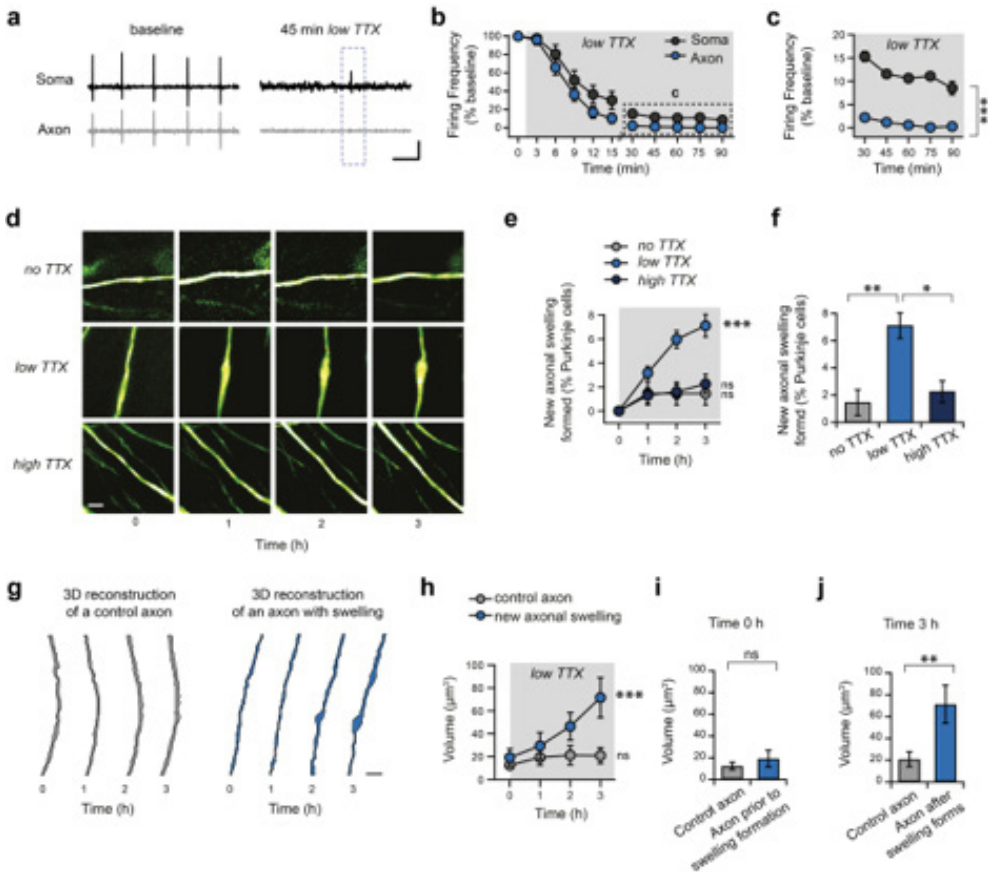
Fig. 3. Enhancing axonal failures causes axonal swellings to form.

(a) Sample recordings from Purkinje cell soma (top, black) and axon (bottom, grey) prior to (left) and 45 minutes after (right) low TTX has been applied onto an acute cerebellar slice. Action potential amplitudes are reduced and axonal failures become prominent. Scale bar, 1 mV, 25 ms. n = 17 for both soma and axon recordings. (b) Summary data showing that firing in Purkinje cell axons is reduced to a great than in the soma, mimicking axonal failures. In some cases, axons and soma recordings were not from the same cell. Frequency was normalized to initial frequency prior to TTX wash-in in order to compare in these cases. (c) Replotting data in panel (b) showing expanded y-axis. Axonal firing rates are significantly reduced than somatic firing rates, indicating that more failures occur in the axon and that this persists throughout the recording (repeat-measured ANOVA followed by pairwise comparisons using Bonferroni correction shows significant difference at each timepoint, *** P < 0.001). (d) Representative images of axons at 1 hour intervals after bath application of regular ACSF (no TTX, top); low TTX (10nM) and high TTX (200nM). Scale bar, 5 µm. (e) Low TTX treatment results in the formation of

new axonal swellings (no TTX, n = 6; low TTX, n = 38; high TTX, n = 6; repeated measures ANOVA showed a significant difference over time for low TTX but not the other conditions, *** P < 0.001). (f) Summary data showing significant differences in the number of swellings formed in low TTX condition after 3 hours. (Kruskal-Wallis H test followed by Mann-Whitney U test, with Bonferroni correction; * α = 0.016; ** α = 0.0033). (g) 3-D reconstruction of new axonal swelling (right) and neighbouring axons without the formation of swellings (left) demonstrate that axons that later produce swellings are not morphologically distinct at the initial timepoint (time 0). Scale bar, 5 μm. (h) Summary data from 3-D reconstructions reveals that volume of axons with swellings differs after 3 hours, but is not different from control axons at time 0 (control axon, n = 8; new axonal swelling, n = 8; repeated measures ANOVA followed by pairwise comparison corrected with Bonferroni ; P*** < 0.005). (i) No differences in axon volume was observed between controls and those that will form new swellings at time 0 (Mann-Whitney U test, P = 0.959), whereas (j) significant differences were observed once the swelling formed after 3 h (Mann-Whitney U test, P = 0.0047).
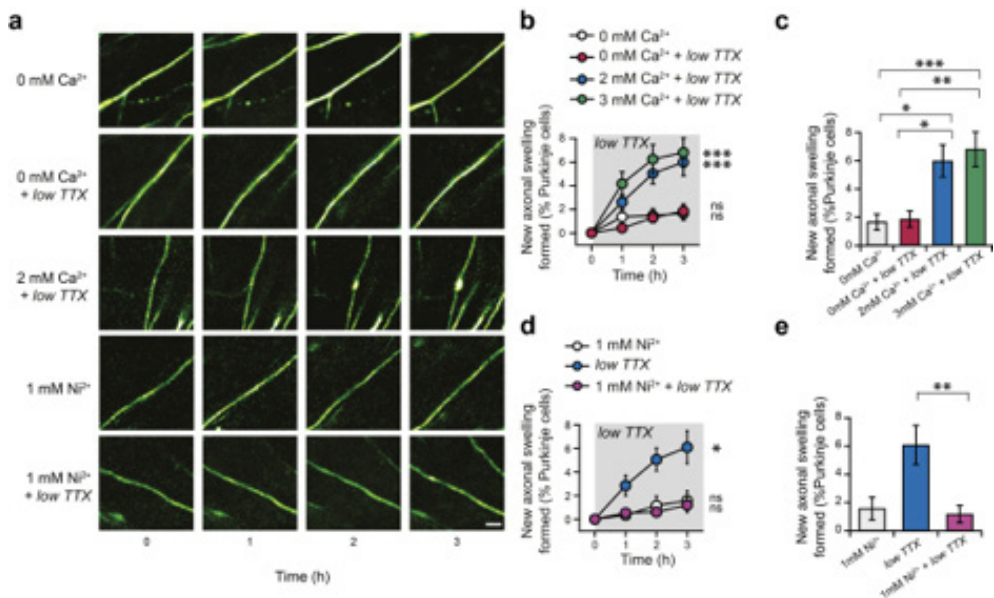

Fig. 4. Axonal swelling formation requires calcium influx through voltage-gated Ca^{2+} channels.

(a) Representative time-lapse images during bath application of ACSF containing no Ca^{2+} (0 mM Ca^{2+}, top), 0 mM Ca^{2+} with low TTX (second row), low TTX with 2 mM Ca^{2+} (third row). The formation of axonal swellings in low TTX is occluded by the presence of 1 mM Ni^{2+} (fourth row), and Ni^{2+} without TTX does not produce axonal swelling formation. Scale bar, 5 μm. (b) Axonal swellings do not form in low TTX with 0 mM Ca^{2+}, but do form in both 2 mM and 3 mM Ca^{2+} (repeated measures ANOVA; 0 mM Ca^{2+}, n = 12, P = 0.25; 0 Ca^{2+} + low TTX, n = 15, P = 0.16; 2 mM Ca^{2+} (2mM) +

low TTX, n = 14, P < 0.001; 3 mM Ca²⁺ + low TTX, n = 12, P < 0.001). (c) Summary data showing after 3 h, significantly fewer swellings are observed with 0 mM Ca²⁺ and with 0 mM Ca²⁺ + low TTX than with higher concentrations of Ca²⁺ (2 mM and 3 mM; one-way ANOVA, P = 0.0004, followed by Mann-Whitney U tests with Bonferroni correction). * α = 0.0083; ** α = 0.00167; *** α = 0.00083, data is not significantly different if not shown. (d) Summary data showing low TTX ACSF containing 1 mM Ni²⁺ occludes the formation of axonal swellings. (repeated measures ANOVA; ACSF containing 1 mM Ni²⁺, n = 6, P = 0.78; low TTX, n = 14, P < 0.001; 1mM Ni²⁺ + low TTX, n = 8, P = 0.80). (e) Summary data showing that after 3 h, Ni²⁺ + low TTX is significantly reduced compared to low TTX alone (one-way ANOVA, P = 0.0027). ** α = 0.00333; data is not significantly different if not shown.
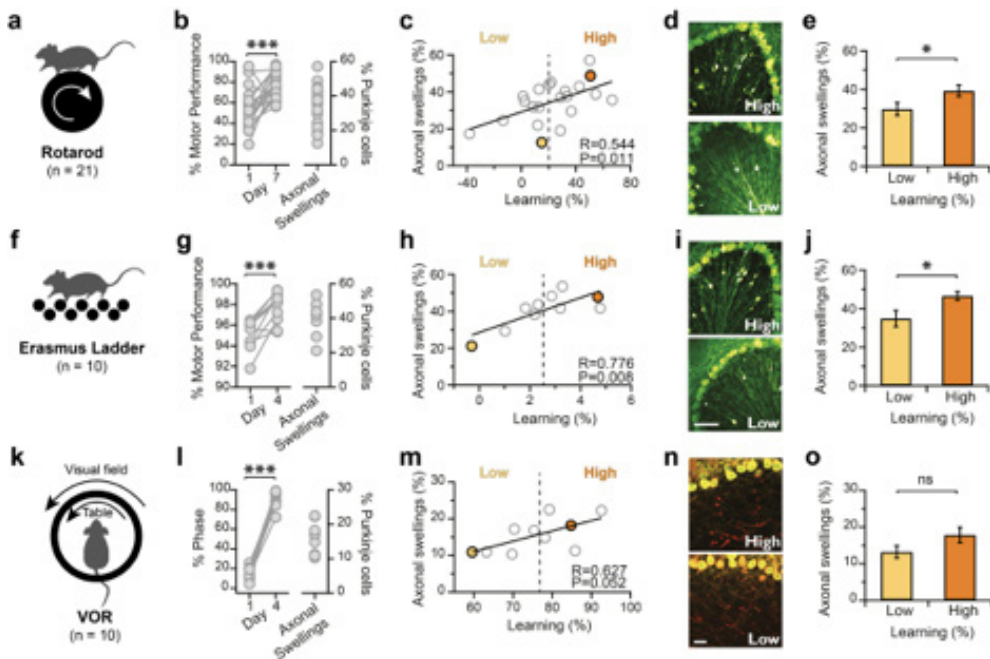

Fig. 5. Axonal swelling density is positively correlated with cerebellar-related learning.
(a) Rotarod assay. (b) Variability in motor learning (left; ***P < 0.005) and the density of axonal swellings in anterior vermis lobule III (right) across mice. (c) The variability in motor learning is positively correlated with the density of axonal swellings. Filled orange marker indicates representative high learner in (d), while filled yellow marker indicates representative low learner in (d). (d) Representative images of anterior cerebellar vermis from high learners (top) and low learners (bottom). Note the differences in the number of axonal swellings. (e) When mice are separated into high and low learner groups, they have significantly different numbers of axonal swelling, with high learners having more than low learners. (f) Erasmus ladder assay. (g) Variability in motor learning (left) and anterior lobule swelling density (right) are also

*observed with Erasmus ladder. (**h**) This variability is positively correlated across animals. (**i**) Representative images from high (top) and low (bottom) learners on the Erasmus ladder assay. (**j**) High learners on Erasmus ladder show more axonal swellings in lobule III of the vermis than low learners. (**k**) VOR assay. (**l**) Some but less variability in learning is observed in VOR (left) and in the density of axonal swellings in the flocculus (right). (**m**) Variability in learning and axonal swelling density in the flocculus is correlated across animals for VOR. (**n**) Representative images showing axonal swellings (stained with IP3R) in high learners (top) and low learners (bottom) for VOR task. (**o**) The density of axonal swellings in the flocculus is not significantly different in low and high VOR learners, perhaps due to a subset of swellings being labelled with IP3R, although the same trend is observed as for the Rotarod and Erasmus ladder tasks.*
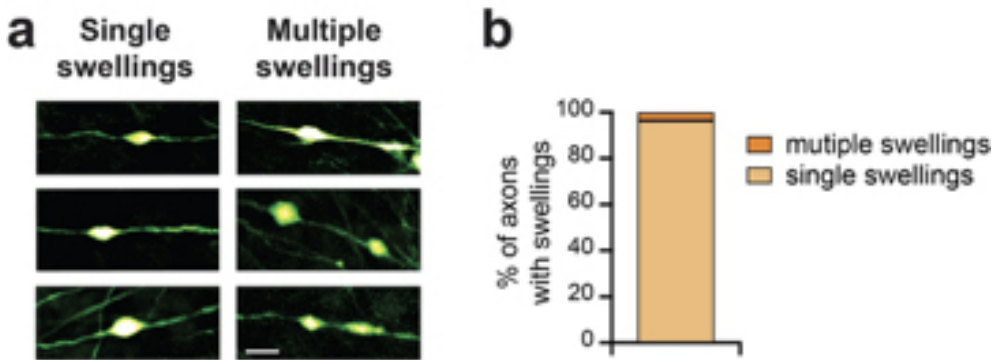

Supplementary Fig. 1. Majority of axons with swellings have single swellings.
*(**a**) Sample images of axons with single swellings (left) and rare axons with multiple swellings (right). Scale bar, 10 µm. (**b**) The majority of axons that have swellings have a single swelling in the granule cell layer (96.4%, or 187/194 of axons with swellings had single swellings, N = 4 animals). Axons with single axonal swellings were targeted for recording.*
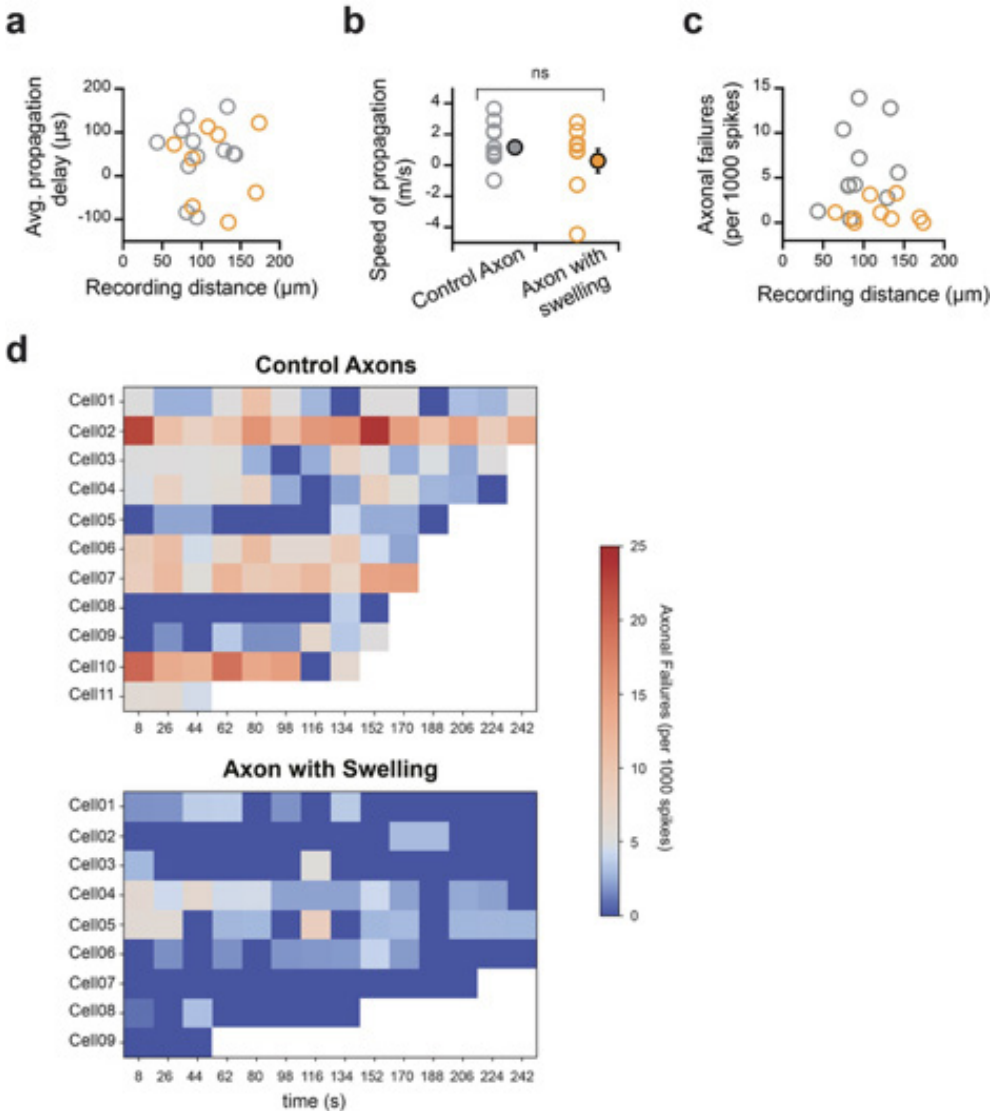
**Supplementary Fig. 2. Propagation velocity is not altered in axons with swellings.**
*(**a**) The propagation delay as a function of recording distance for control axons (grey circles) and for axons with swellings (orange circles). Propagation delay can be negative when the action potential reaches the axonal recording electrode before the somatic electrode, due to the spike initiation zone being located on the axon initial segment. (**b**) No significant difference is observed for the speed of action potential propagation for axons with and without swellings. Mann-Whitney U test, P = 0.66. (**c**) Axonal failures as a function of recording distance. There is no relationship between the failure rate and the distance of the axonal recording from the soma for control*

*axons or for axons with swellings. (**d**) Axonal failures as a function of time for each pair of cells recorded for control axons (top) and axons with swellings (bottom). Cells that display higher axonal failures tend to do so throughout their recording, and cells that display lower axonal failures tend to do so throughout their recording.*
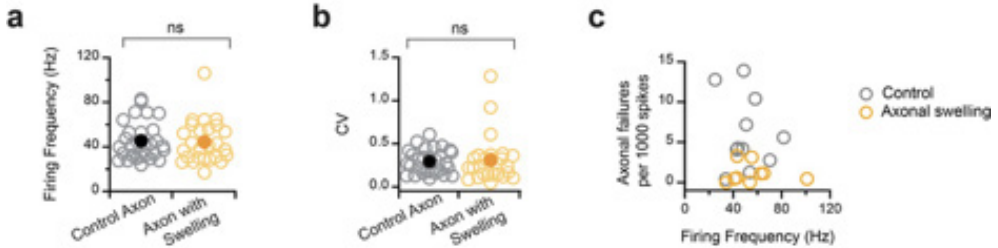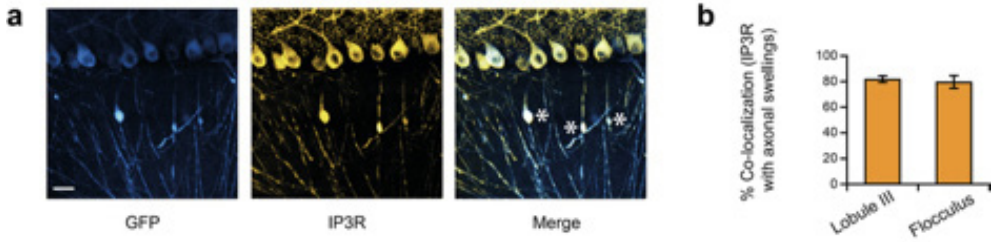

Supplementary Fig. 3. Axonal swellings and failure rate are not correlated with firing properties.
*(**a**) Firing frequency in Purkinje cells with axonal swellings is not statistically different from cells without swellings on their axons. (Firing Frequency: Control axon: 45.2 ± 3.15 Hz; n = 29; Axon with swelling: 44.3 ± 3.71 Hz; n = 26; not significantly different, P = 0.70). (**b**) The coefficient of variation (CV), a measure of the regularity of Purkinje cell firing is not different in neurons with and without axonal swellings. (CV: Control Axon: 0.293 ± 0.026; Axon with Swelling: 0.307 ± 0.053; P = 0.40). Control Axons, n = 29; Axon with Swelling, n = 26. (**c**) Axonal failures as a function of firing frequency. There is no significant correlation between firing rate and failure rate for either control axons or axonal swellings. Control axons, n = 11; Axons with Swellings, n = 9.*
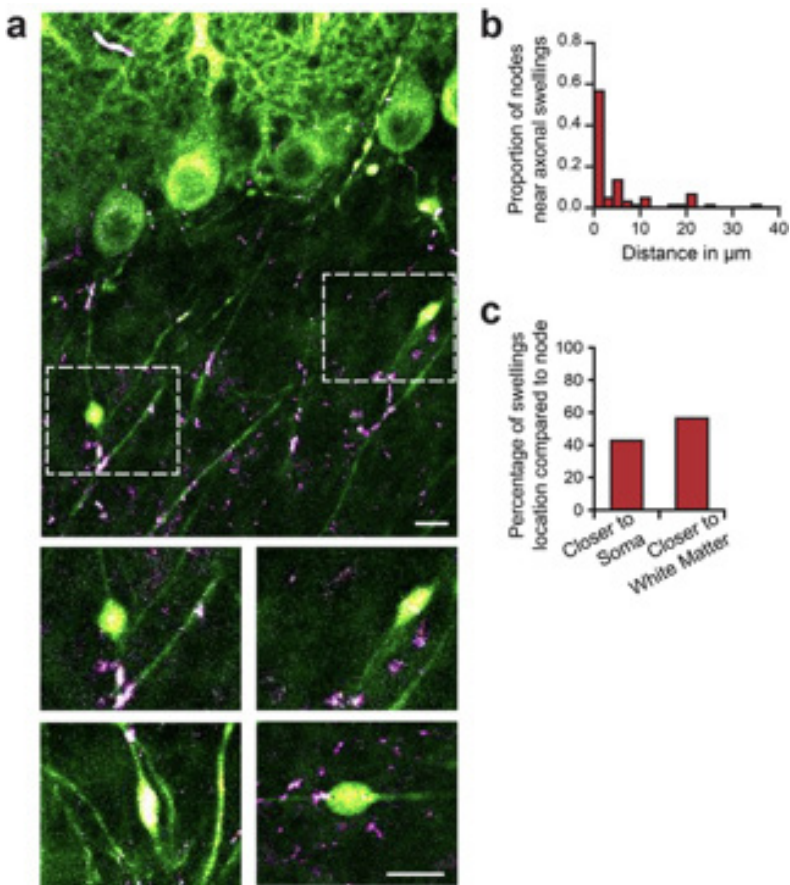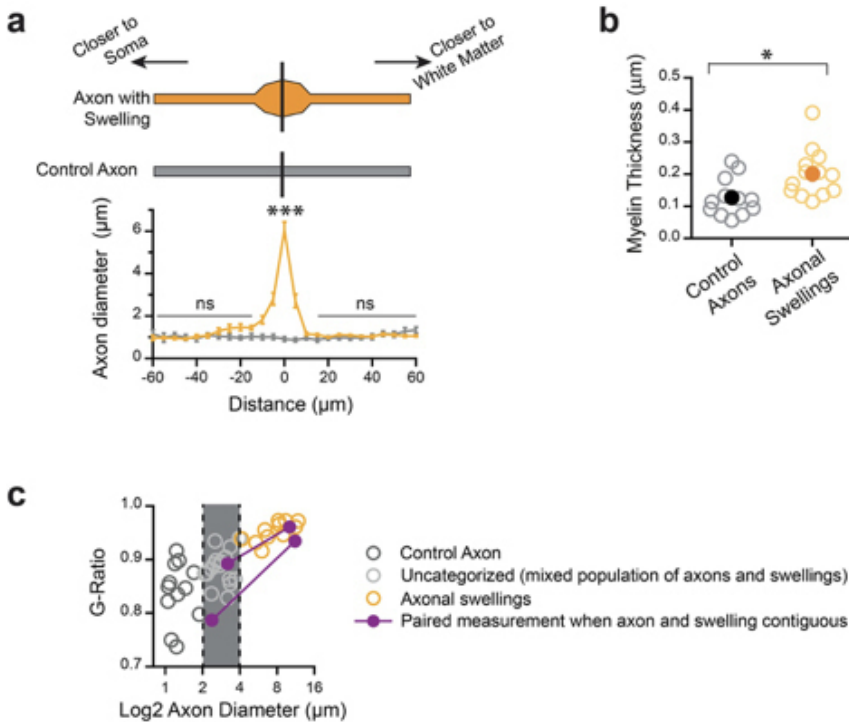
Supplementary Fig. 4. Axonal swellings are often located close to nodes of Ranvier.

(**a**) Examples of Purkinje cell axons (green) stained for the paranodal protein CASPR (purple). CASPR labeling was almost never observed directly on axonal swellings, suggesting that these structures are not typically located precisely at nodes of Ranvier. However, CASPR puncta were often observed near axonal swellings, suggesting that they were frequently close to nodes of Ranvier. Top: image shows Purkinje cells and several swellings. Second row: axonal swellings shown in top image (white boxes) are expanded. Paranodal CASPR is near but no co-localized with swellings. Bottom row: further examples showing paranodal CASPR staining that is close (left) or very proximal (right) to axonal swellings. Scale bar, 20 µm (top); 10 µm (middle and bottom rows). Note that CASPR staining labels paranodal structures on non-Purkinje axons as well as Purkinje axons. (**b**) Nearly 50% of axonal swellings were located within 2 µm of CASPR puncta. (**c**) Axonal swellings did not show preferential up- or down-stream localization in comparison to CASPR puncta: roughly half were located closer to the soma and half closer to the white matter. N = 3 mice, n = 58 axonal swellings.

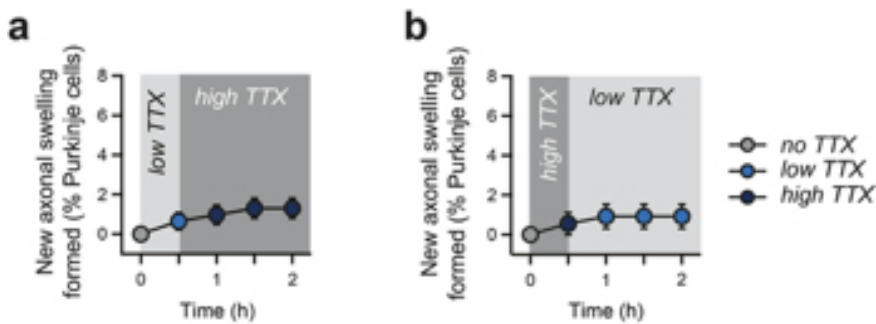**Supplementary Fig. 5. Axonal swellings express IP3Rs.**
(a) Representative image showing the majority of axonal swellings (GFP, blue) colocalize with IP3R (yellow). Asterisks show axonal swellings co-labeled for IP3R in merged image (right). Scale bar, 20 µm. (b) Summary data showing that the majority of axonal swellings are positive for IP3R staining in both lobule III (left) and in the flocculus (right).

Supplementary Fig. 6. Axonal swellings occur on axons of similar diameters to control axons but have a moderate increase in myelin thickness.
(a) To determine whether swellings occurred on axons that were already thicker, we measured the diameter of axons with swellings and those without and found no significant difference in the diameter 15 µm from the centre of the axonal swelling on either side (centred on the swelling; left: negative values are closer to the soma; right: positive values are closer to the white matter), and equivalent locations from control axons. The diameter of the axonal swelling was significantly larger than that

of control axons(Mann-Whitney U test, P = 0.004; n = 15 axons with swellings, n = 13 control axons). (b) Myelin around axonal swellings (> 4 µm) was measured on the subset of axons where the myelin was compact, and was found to be slightly but significantly thicker than myelin around control axons (< 2 µm; N = 13 axonal swellings, N = 12 control axons; unpaired Student's T test, P = 0.013). (c) G ratio was measured for axons (< 2 µm), uncategorized because they represent a mixed population of large axons and small swellings (between 2 and 4 µm), and axonal swellings (> 4 µm). Two instances where a swelling and an axon were connected in the image (e.g. **Fig. 2a***) are shown in purple, and follow the general observation that the g-ratio is larger for swellings than for axons (***Fig. 2d***).*

Supplementary Fig. 7. Insufficient exposure to low TTX will not lead to axonal swelling formation.

(a) To determine the minimum time course over which the formation of axonal swellings occurs, we perfused slices with low TTX for 30 minutes followed by 90 minutes of high TTX (that will block all action potentials). This duration was insufficient to induce the formation of axonal swellings (low TTX followed by high TTX: 1.30 ± 0.50 new axonal swellings % Purkinje cell; n = 8; not significantly different over time when compared to ACSF, P = 0.74). (b) We then reversed the order of application, perfusing high TTX for 30 minutes which will completely block action potentials followed by 90 minutes of low TTX and found that no additional swellings were formed with this paradigm (high TTX followed by low TTX: 0.93 ± 0.06 new axonal swellings % Purkinje cell; n = 6; P = 0.65). These data suggest that sufficient levels of axonal failures are required for the formation of axonal swellings.
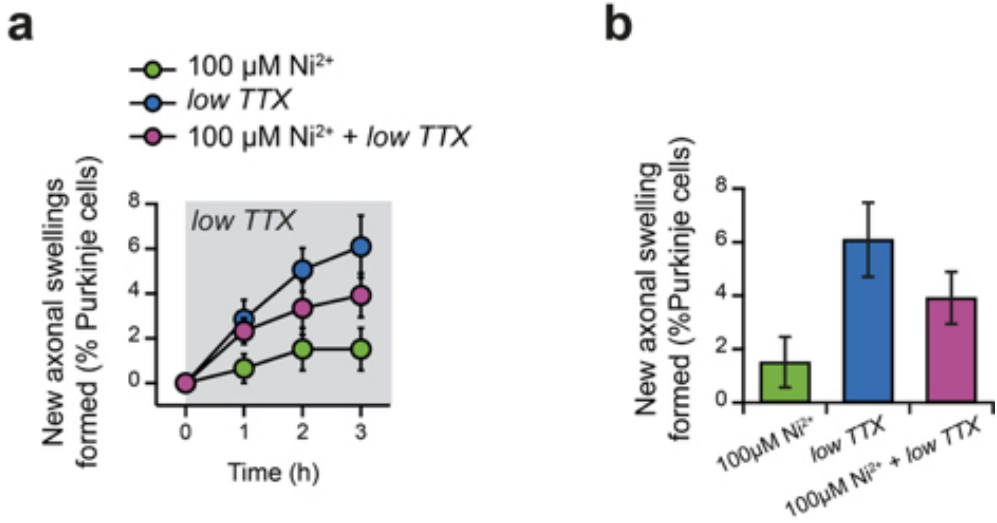
Supplementary Fig. 8. Partial blockade of new swelling formation with sub-saturating concentration of Ni^{2+}.

(**a**) We used a sub-saturating concentration of Ni^{2+} to partially block voltage-gated calcium channels and found that it partially blocked the formation of swellings in the presence of low TTX (repeated measures ANOVA showed no effect of the conditions over time). Sub-saturating Ni^{2+} concentration partially block torpedoes formation (100 mM Ni^{2+} + low TTX: 3.91 ± 0.98% new swellings; n = 6) compared to low TTX (low TTX: 6.09 ± 1.39%; n = 14) and Ni^{2+} only (100 mM Ni^{2+}: 1.51 ± 0.94%; n = 5; One-way ANOVA, P = 0.049). (**b**) However, further analysis showed no significant differences between Ni^{2+} + low TTX and low TTX or Ni^{2+} only (Mann-Whitney U tests, P = 0.15 and P = 0.24, respectively). The difference between low TTX and Ni^{2+} only (Mann-Whitney U tests, P = 0.034) was not significant in this case due to the Bonferroni correction, *α = 0.017.
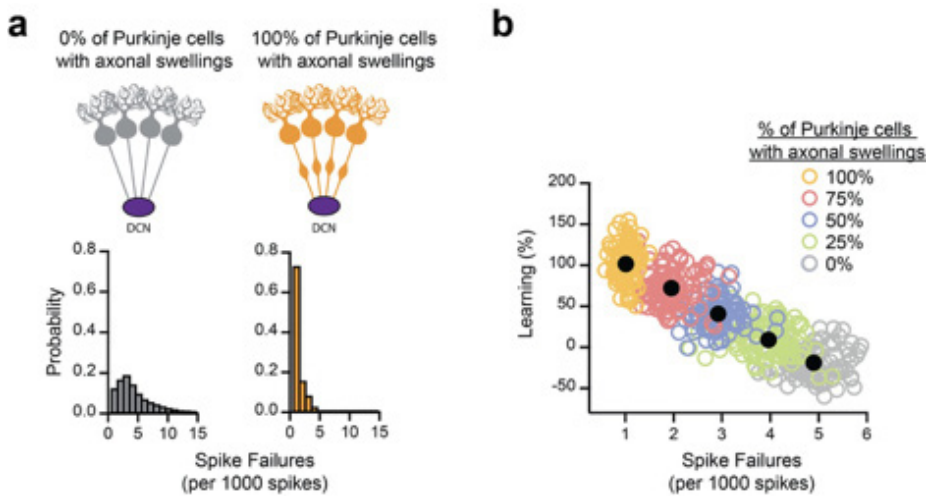
Supplementary Fig. 9. Monte Carlo simulation relating learning to axonal swellings in a network model.

(**a**) *Percentage of spike failures for simulated output of a 200,000-Purkinje cell network (representing the whole cerebellum) that has either 0% of Purkinje cells with axonal swellings (left) or 100% (right). Each simulation was run 5000 times and the incidence of network output failures is shown in the histogram, using experimental data to populate the simulation. The probability of spike failures in a network is more likely to be closer to 0 with a greater percentage of axonal swellings. (**b**) Subsequent projection of the amount of learning on the Rotarod tasks given that the Monte Carlo simulation of the network of 200,000 Purkinje cells predicts behavior. Simulation was run sampling from experimentally-determined data 100 times (individual dots) for different percentages of Purkinje cells with axonal swellings (0, grey; 25, green; 50, blue; 75, rose; 100%, yellow). Note that the amount of learning observed shifts dramatically depending on the percentage of Purkinje cells with axonal swellings.*
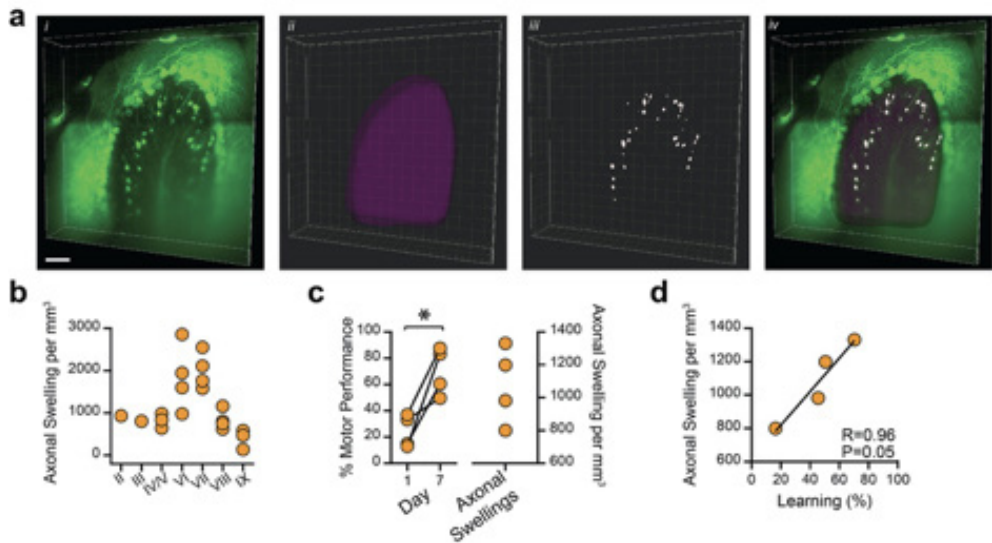
Supplementary Fig. 10. Light-sheet imaging reveals that the density of axonal swellings varies across lobule within the cerebellar vermis.

Left to right images: (**a**) Analysis pipeline. (i) Small vermal section from lobule II expressing GFP in Purkinje cells. (ii) Granule cell layer delineation, enabling axonal swellings to be detected in this area (area in purple). (iii) Automatic detection of axonal swellings in delineated area based on size, sphericity, and intensity. (iv) Merge of (i- iii) shows good detection of swellings. Scale bar, 100 µm. (**b**) The density of axonal swellings varies across lobule of vermis. (**c**) Mice exhibit variable learning on the Rotarod task, and variable overall density of axonal swellings. (**d**) The number of axonal swellings demonstrates a trend to vary proportionally to the overall axonal swelling density (including lobules where > 2 mice were imaged). N = 4 mice.

Supplementary Table 1 Cellular and subcellular properties of axonal swellings and control axons.

Category	Control axons	Axonal swellings	P value
	Average ± SEM (range, n)	Average ± SEM (range, n)	
Location of Recordings (μm from soma)	95.3 ± 8.79 (43.5 – 142.8 μm; n = 11)	121.2 ± 12.43 (65.1 – 173.8 μm; n = 9)	0.098
Failure rates (per 1000 spikes)	6.07 ± 1.36 (0.41 – 13.90; n = 11)	1.12 ± 0.41 (0 – 3.28; n = 9)	0.0023
Organelle density (% area)	20.4 ± 1.68 (2.47 – 35.54; n = 18)	24.1 ± 1.25 (16.68 – 35.68; n = 15)	0.097
g ratio	0.84 ± 0.16 (0.74 – 0.92; n = 12)	0.95 ± 0.005 (0.92 – 0.97; n = 13)	0.009
Firing rate (Hz)	45.16 ± 3.15 (23.88 – 82.75; n = 29)	44.32 ± 3.71 (16.75 – 106.16; n = 26	0.22
CV	0.29 ± 0.03 (0.098 – 0.61; n = 29)	0.31 ± 0.05 (0.044 – 1.28; n = 26	0.40

P values are reported for t tests when distributions are normal, or for Mann-Whitney U tests when distributions are not. The g ratio was measured only for a subset of axons where compact myelin could be measured reliably (due to fixation artefacts).
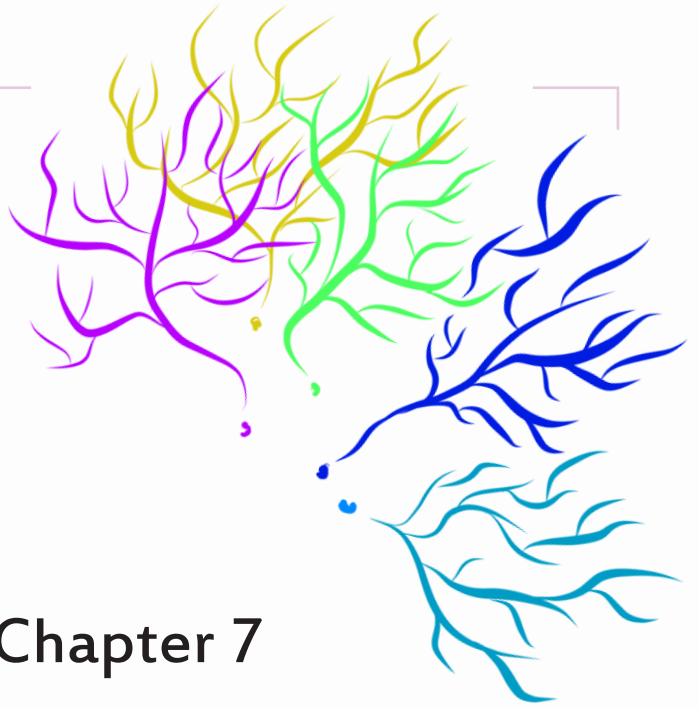
Chapter 7

General Discussion

"Speaking for myself, I'm absolutely amazed by the way our bodies work. In my eyes, this is something extremely beautiful. I'm exploring natural aesthetics and translate it into my own language, my own style. And I'm repeatedly surprised how much there is to explore, how much deeper you can dive into this world. On a surrealistic level, anatomy cannot be exhausted in art. For me, it's absolutely fascinating to discover how nature has designed all that and how living organisms are constantly optimizing to nature, evolutionarily. So yeah, dissection is my kind of research on life and beauty, so to say."

`

Nychos the Weird, Street Anatomist – Interview "Visual Atelier 8"
– January 2019

The anatomical literature of the twentieth century delineated brain structures and traced the neuronal routes sketching the connectome. But as detailed these studies might have been, they all ended up being limited by the technics of their time. For example, neuronal tracing performed with biotin dextran amine (BDA), cholera toxin subunit B (CTb), horseradish peroxidase (HRP), or rabies virus can be focal or sparse but they always confine neuronal populations to their physical proximity. The recent rapid evolution of tools and methods of neuroanatomy brings new perspectives. Single-cell transcriptomic, multiplex immunohistochemistry, conditional neuronal tracing, tissue clearing and other approaches showed that all major brain structures are composed of discrete neuron subtypes integrated in compartmentalized networks (1). The findings presented in these chapters showed that high resolution anatomical descriptions coupled with molecular profiling are essential to understand fundamental as much as pathological brain processes. In light of the data presented, one can draw inferences on the properties granted by the molecular diversity of the cerebellum.

Purkinje cell plurality:

Single cell recording and sequencing approaches (Patch-seq) offer the high spatial resolution that allows to correlate electrophysiological properties with transcriptomic profiles (1, 2). However, the direct correlation between gene expression and neuronal properties appears sometimes elusive. For example, while GABAergic interneurons can be divided in 60 subtypes defined by their transcriptional profile, only 28 subtypes could be defined based on morphoelectrical properties. This dichotomy between molecular and biophysical diversity can be explained by both technical and biological

reasons. From the biological standpoint theoretical and experimental work showed that the diversity of current types gives a range of neuronal outputs lower than what could be expected (2–4). Such predictions and observations are attributed to current compensation. With the large reservoir of genes and the flexibility of the transcriptome (5) it becomes challenging to identify the proteins and mechanisms responsible for the diversity of eletrophysiological properties within a single neuronal type.

The discovery of distinct intrinsic firing properties among Purkinje cell (PC) subtypes was a colossal break-through in the cerebellar field. Morphologically identical neurons segregated on the basis of one molecular feature were found to exhibit distinct biophysical properties (6, 7). The role of AldoC differential expression on PC intrinsic properties has been discussed due to the metabolic function of the protein. While the impact of AldoC enzymatic activity on the neuronal activity cannot be excluded, it would be indirect and insufficient to explain the radical differences in electrophysiological signatures between the subtypes. Previous investigations on EAAT4 and GLAST protein functions showed that properties of each PC subtypes are driven by independent mechanisms (8). The authors discussed that respective biophysical properties are the results of complex metabolic and membrane currents regulations involving multiple molecular actors. Several pieces of evidence led us to investigate TRPC3 channel as potential actuator of these subtypes' heterogeneity. We observed that both gain or loss of function of TRPC3 channels has notable effect on AldoC-negative (AldoC-) PCs but limited to no effect on AldoC-positive (AldoC+) PCs (**Chapter 5**). Similar to the study of Perkins *et al.*, our results clearly demonstrate the independency of subtypes properties. One of the interesting characteristics of the study is the slight disparity between histological and physiological data. TRPC3 immunolabeling showed observable but hardly distinguishable differential expression. At first, TRPC3 appeared to be expressed in all PCs along the cortex but comprehensive analysis of the expression profile revealed nuances in protein levels. This differential expression draws a pattern complementary to AldoC immunoreactivity. However, while the patterning of TRPC3 expression was observable in the vermis, it appeared virtually absent in the hemispheres. The generally low immunoreactivity for TRPC3 protein brings the question whether these observations relate to the expression of the protein or point at the resolution limit of the method. Nonetheless, the low contrast of TRPC3 expression still has a preponderant role in contrasting the biophysical properties of PC subtypes. Is TRPC3 directly responsible? The relatively mild effect of the conditional knock-out (pcp2^{CreERT2}) compared to the constitutive knock-out (pcp2^{Cre}) on PC properties makes one question the mechanism behind TRPC3

7

mutant phenotypes. Deletion of the protein in the constitutive mutant occurs during the first post-natal week, while in the constitutive it occurs following Tamoxifen injections at 12 to 31 week few days prior to the recordings. These data suggest that long term compensatory mechanisms established following the loss of TRPC3 have more impact than the deletion per se. Together with the nuanced differential expression this shows the complex stability of currents compensation in neuronal subtypes.

The observed nuances in protein levels brings a recurring question. Where is the line between biological relevance and noise? The essential challenge is first to disentangle biological variance and experimental artefacts. Fujita *et al.* (9) recently brought to light anatomo-molecular data questioning a possible partition of the flocculus based on the distribution of PC subtypes. While the direct immunolabeling of AldoC hardly distinguish PC subtypes in the flocculus, the detailed reconstruction of an AldoC promoter-driven VENUS expression mouse model advocates for a division of the flocculus in two domains. We aimed to test the veracity of these data as they were brought by the examination of a mutant mouse, and confirmed the existence of the floccular domains (**Chapter 4**). The validation came from a poorly characterized pattern marker, KCTD12 (10). The expression of KCTD12 essentially follows that of AldoC throughout the cerebellum with the major distinction that KCTD12 expression appeared generally more contrasted. This allowed to effectively discriminate floccular domains 9+ and 9- where AldoC expression remained lightly contrasted between both domains. We proved that this division translate distinct biophysical and anatomical attributes. Interestingly, our data showed that AldoC expression and electrophysiological properties of PCs draw correlated continuums of variability, as previously suggested (6). Such continuity in protein levels and electrophysiological properties were also observed in cortical interneurons (11), striatum (12) and hippocampus (13). With the absence of clear boundaries, it becomes difficult to classify these neuronal populations. Zheng and Sanes (14) on their conceptualization of neuron classification suggested that continuous and discontinuous variations need to be approached differently as the latter is more decisive to define types and subtypes. In the case we are presenting, such affirmation is dubious. The neuronal tracing from 9+ and 9- domains present strongly divergent long-range projections despite the barely perceptible AldoC expression change. Such anatomical distinctions among continuum of variability are rarely demonstrated. The implication of our work is that continuous variations can also have decisive impact in classifying network properties. Multiple simultaneous readouts per cell might be necessary to act if the variability in a single measure reflect valuable intrinsic diversity. To

assess the diversity of PC subtypes one cannot restrict the analysis to AldoC expression profile. From AldoC to KCTD12 to Hsp25 we tracked patterned expressions to see populations nested in one another like *матрёшки* (Russian dolls). The complementary expression profiles of PLCβ4 and Nfh add in complexity in several lobules. Nfh expression was previously shown to be complementary to AldoC expression in the anterior and posterior zones, while partially overlapping AldoC expression in the central and nodular zones to complement Hsp25 expression (15). In the flocculus we then observe three populations AldoC+/KCTD12+/Hsp25+, AldoC+/KCTD12+/Hsp25- and the PLCβ4+/Nfh+. The latest corresponds to the 9- domain which, at midway between AldoC- and AldoC+, is significantly distinct from the two common modules. In the nodulus, the differential patterning of these marker describes a fourth population AldoC+/Nfh+/Hsp25-. The overlay of these readouts draws already a high diversity of molecular footprint (**Fig. 1**). Our

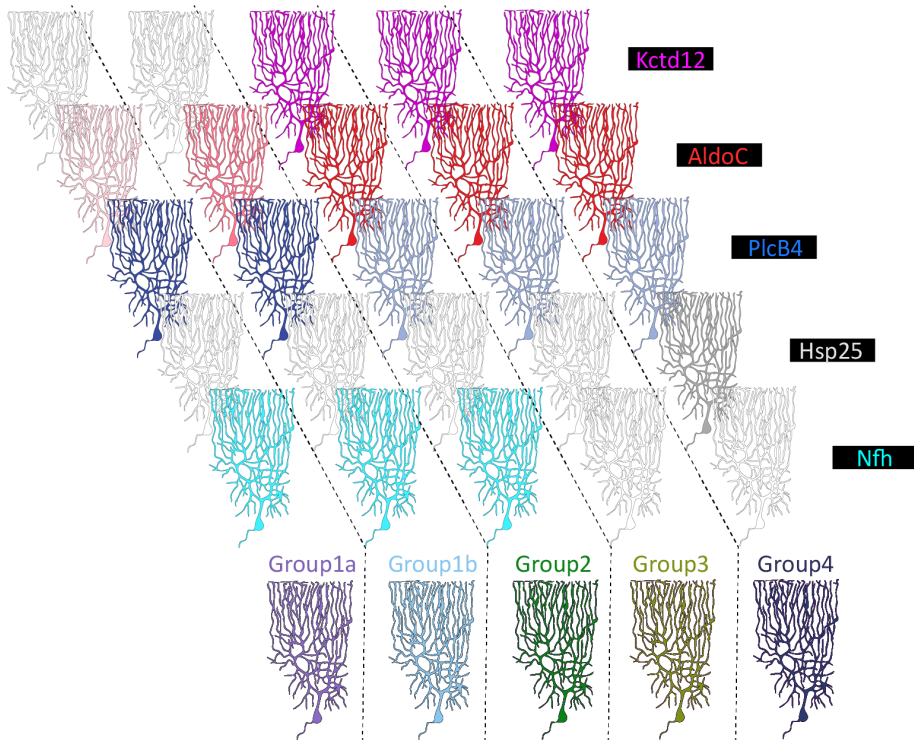**Figure 1. Diversity of PC molecular profiles.**
Overlapping the expression profiles of KCTD12, AldoC, PlcB4, Hsp25, and Nfh reveals at least four group of PCs. The group 1 is divided in 1a and 1b based on variations of AldoC expression only. In the flocculus, groups 1b (9-), 3 (9+) and 4 (subregion of 9+) can be identified. PC illustration is adapted from the original drawing of S. Ramón y Cajal.

data prove that these distinctions have anatomical implications. Therefore, the cerebellar cortex has to be described as a multimodal structure, and not as the bimodal system commonly portrayed. The panel of PC attributes grants distinct properties that have repercussions at several scales, from cellular metabolism to information processing.

Patterned degeneration:

The gradual degeneration of discrete populations of neurons is a feature observed in several neurodegenerative disorders (16, 17). The key challenge to decipher the mechanisms behind selective vulnerability is to isolate the molecular pathways relevant for the cellular fate. The difficulty is to identify them among the multitude of unique gene expressions and protein interactions that define the respective morphology, location, and intrinsic properties of neuronal types. An ideal model would be to explore the metabolism of seemingly identical neurons with distinct vulnerabilities to the same insult. Such model would allow to identify molecular predispositions to cell death. Cerebellar pathologies offer such ideal model as PC subtypes frequently manifest selective vulnerability (18). The term "patterned" neurodegeneration emerged to illustrate the topographically organized loss of PCs. Most cases identified to date showed that PCs located in AldoC+ domains or in the flocculo-nodular lobule are commonly preserved in the first stages of cerebellar degeneration. Such traits are observed in a model of spino-cerebellar ataxia type one, the Atxn1[82Q]-/+. Commonly used as a model of cerebellar degeneration, little was known about the impact and origins of the observed pattern degeneration.

It was established that the absence of cerebellar cortex prevails to an unhealthy cerebellar cortex (19). The strong inhibition driven by PCs on motor planning and execution circuits becomes deleterious as PC intrinsic properties and synapses are pathologically altered. Removal of the afflicted PCs in ataxic models was showed to improve these motor functions, due to the reorganization and sprouting of inhibitory circuits in the cerebellar and vestibular nuclei (20). The substantial loss of PCs in some ataxic models was even shown to be ultimately beneficial compared to the survival of unhealthy PCs. In Atxn1[82Q]-/+ model the degeneration is characterized by affected morphology and intrinsic electrophysiological properties. At early stages the loss of PCs is minimal. Thereby, the conservation of altered PCs prohibit plasticity mechanisms, leading to the strong impairments observed (21). We found that the locomotor adaptation is indeed heavily affected. This relates to the degeneration observed in the vermis of lobule I-VIII. However,

the motor functions associated with seemingly spared cortical regions were preserved (**Chapter 3.1**). The conserved eye movement adaptation relates to the predominant preservation of PCs in the flocculo-nodular lobule. Such behavioral output demonstrates that PCs in these regions not only appear healthy but they actually maintain their proper functions. It also demonstrates the strong compartmentalization of the network driving this behavior, as altered PCs in the rest of the cerebellum do not appear to impact the flocculo-nodular circuit. We showed in this study that cerebellar patterned degeneration offers ways to study cerebellar circuits and neuronal physiology.

Some reports proposed that the metabolism of sphingolipids might be a key element in patterned degeneration (22). The notorious role of sphingolipids in PCs survival and the differential expression of Sphingosine kinase 1 (SPHK1) among PC subtypes supported this theory (23–25). We pursued this lead and investigated the metabolic pathway of sphingolipids synthesis in the cerebellum and its role in patterned degeneration (**Chapter 3.2**). Our data showed that the regional equilibrium of sphingosine-1-phosphate (S1P) correlates with the selective vulnerability of PC subtypes. The regional changes in levels of sphingolipids and Sphk1/2 in the Atxn1[82Q]-/+ transgenic model are coherent with a role of S1P in selective vulnerability. Finally, the partial rescue of the Atxn1[82Q]-/+ cellular phenotype following Sphk1 deletion confirms the essential role of sphingolipid metabolism on PCs cellular fate. The exact mechanistic of S1P signaling pathway in neuron survival remains ambiguous. Two recent studies illustrate the conflict existing in the literature. Rashad *et al.* (26) suggested that the increase of S1P levels via Sphk1 up-regulation following brain ischemia promotes neuronal survival. In contrast, Zheng *et al.* (27) presented opposite findings as they argue that Sphk1 up-regulation post ischemia activate the inflammatory responses and drive neuronal apoptosis. Without arguing on the validity of the data presented in each study, we can first observe that Zheng *et al.* were able to reduce the infarction of brain tissue thanks to Sphk1 inhibitor or siRNA pre-treatment. Rashad *et al.* failed to reduce the infraction following S1P agonist treatment. The antinomy of both studies translates the complexity of studying sphingolipid homeostasis. Hagen *et al.* (28) explained that the pro-apoptotic or pro-survival effect of S1P depends on its cellular and sub-cellular provenance. Our data do not allow us to conclude on the molecular signaling behind the rescue, nor can it conclude on the pro-apoptotic role of S1P. Nevertheless, we can affirm that PCs subtypes hold different sphingolipid metabolisms driven by the differential expression of several enzymes. While the patterned expression of Sphk1 was clearly established, recent RNA-seq analysis suggested the

differential expression of ceramide kinase (Cerk), ceramide synthase 4 (CerS4), sphingomyelin phosphodiesterase 1 (Smpd1) and Sphk1 interactor (Sphkap) (29). Interestingly, on the 669 genes identified in this study, with non-homogeneous expression in PC, only 126 correlate or anti-correlate with the AldoC pattern. Authors stressed that other spatial distributions exist, such as lobule IX-X specific or excluded expressions. It implies that the diversity of metabolic profiles cannot solely be attributed to the AldoC- and AldoC+ populations. One could suggest at least four distinct sphingolipid metabolic profiles related to AldoC-, AldoC+, Hsp25+ and flocculo-nodular PC populations, which would explain the three types of pattern degeneration known to date. Each metabolic profile would grant predispositions to cell death dependent on the pathological machinery triggered. To confirm the canonical role of sphingolipids in patterned degeneration it would be necessary to test Sphk1 deletion on other models. For example, the *Moonwalker* mouse model is one of the few mutants with preferential survival of AldoC- PCs. Dulneva *et al.* (30) showed that sphingolipid homeostasis is affected in the cerebellum of the *Moonwalker* mouse. However, the authors did not perform the refine anatomical dissection to independently analyze preserved and afflicted regions, treating the cerebellum only has a homogenate.

One may ask if such selective neuroprotection is the result of an evolutionary pressure to preserve essential behavioral functions. Another way to see it would be that selective vulnerability is a mechanism employed to rapidly eliminate unhealthy PCs in key regions. However, defining cellular fate base on behavioral functions would be deeply deterministic. One would then suggest that patterned cerebellar degeneration is a by-product of the different attributes of PC subtypes acquired through evolution. It is established by now that PCs subtypes must comply to distinct intrinsic and network properties. Sphingolipids are known actors of several signal transduction processes. Thereby, local sphingolipid balance might be the result of distinct cellular needs and not of behavioral needs.

Theory on the functional implications:

The vast heterogeneity of neuronal properties predicts a certain diversity of coding. At a population level it is predicted that intrinsic diversity lowers output correlation and would allow individual neuronal events to spread within a larger highly synchronized population activity to offer more depth in information coding (31). Transient mechanism can also appear to give unique properties to a single cell in response to specific conditions (**Chapter 6**). But how do subtype properties integrate at the network level?

In 2004, Prinz *et al.* (32) proposed a three neurons circuit of seven synapses and virtually create 20 250 000 models by diversifying synaptic strengths and intrinsic properties. The three-neuron network aimed to reproduce the pyloric rhythm circuit of the stomatogastric ganglion which controls the striated muscles of crustacean's stomach. Among these models, 4 047 375 were able to produce pyloric-like rhythm (based on subjective criteria) in which 452 516 were able to reproduce the exact biological characteristics of the pyloric rhythm (based on recorded data). One can argue that the representation of pyloric rhythm was produced by only 2.2% of their models, but they used a very large range of intrinsic properties (1.7 million neuronal models) attributed randomly, not taking into account that channel expression is non-stochastic. Nevertheless, they have demonstrated that networks composed of different intrinsic and synaptic features can achieve similar output. In other words, while at a population level one can expect decreased correlation, at the network level we could see increased correlation. This dichotomy could be explained by ways of **molecular compensations of the network**. These terms do not refer here to the conventional activity-dependent gene expression mechanisms, or how the expression profile of neurons change at a given time in response to specific stimuli. It refers to mechanisms in which several neurons of the same circuit tune their fundamental transcriptomic profiles with respect to each other. Schultz *et al.* demonstrated that electrically coupled neurons of the same type share more similar expression of ion channels then non-couple neurons from the same population (2). This suggests that connected neurons tune their molecular processes in respect to each other, and could be true even for neurons of different types. Several pieces of evidence already suggested that PC molecular diversity, in adult cerebellum, is the result of molecular adaptation to the baseline network activity. The specific disruption of PC output on cerebellar nuclei neurons (L7[Cre]; Vgat [flox/flox] mouse) was shown to alter the differential expression of AldoC (33). We showed in our own study that the abnormal physiology of PCs in the Atxn1[82Q]-/+ model leads to the disruption of AldoC expression (**Chapter 3.2**). The idea that PC transcriptomic profile adapts to the circuit is supported by the fact that the majority, if not all, proteins with a patterned expression in the adult cerebellum are uniformly expressed during early developmental periods. Thereby, the adult patterning correlates with the maturation of the cerebellar activity (34). One can expect that some intra-type diversity (e.g. PC to PC) of molecular profiles might be explained by some inter-type correlations (e.g. MF to PC). We observed in our data such inter-types correlations. The SST28+ MF terminals in the flocculus segregate with KCTD12+ PCs (**Chapter 4**). Moreover, the density

of SST28+ MF is increased in the subdomain defined by KCTD12+/HSP25+ PCs. Interestingly, these MFs do not all originate from the same nuclei but from both PrH and MVe, suggesting the convergence of the molecular profile of two anatomically distinct class of inputs. This is supported by electrophysiological and modeling work on MF diversity (35). All these data could support the theory of the molecular adaptation of the network to increase output correlation among networks despite highly uncorrelated inputs. What could be the function of networks output correlation? A possible reason why non-redundant network would have high output correlation could be the large range of input modalities to integrate in order to give unique and precise motor execution. For example, the desired motor execution of the floccular network is the eye movement. This eye movement can be triggered by visual only (OKR), vestibular only (VOR), or visuo-vestibular (VVOR) inputs. The modalities to integrate are diverse. The sensory organs, retina and semi-circular canals, have very distinct biophysical properties, and the anatomical pathways are extremely distinct despite some convergence. Nevertheless, the different outputs of these networks require to be highly correlated to produce this unique response that requires precise muscle synergy.

However, this may not represent the entire picture. Through my investigations on atypical molecular expression in the cerebellum, I have identified NECAB2 protein as marker discriminating a subset of MFs in the granular cell layer. Several lines of evidence suggested that these MFs originate solely from the external cuneate nucleus, which means they carry upper limb proprioceptive information. NECAB2 delineate clear clusters of MFs which partially correlate with AldoC defined compartments, but generally span through several domains. This seemingly unique modality is integrated in several cortical compartments. Such anatomical features would be more in line with the principle of decorrelation of the input. In this case, a unique sensory modality would produce decorrelated outputs as it spreads among diverse PC subsets. Then, what could be the function of output decorrelation? I would suggest that unimodal input would pass through different cortical modules to obtain a larger potential range of motor responses. This would make sense in contexts such as locomotor adaptation. The predominant input modality is the proprioception of the limbs, but in case of perturbations one might need to select the optimal strategy to adapt among a panel of options. Therefore, the input would need to decorrelate to properly integrate other minor inputs and select the proper action once even the least significant parameter is taken in consideration. To summarize, this theory consists of two elements:

1) Behaviors with various sensory modalities that need highly synchronous response (e.g. vestibule-ocular reflex) would solicit compartmentalized networks in which strong inter-type correlations are needed to produce correlated output activities driving a unique motor response (**Fig. 2A**).
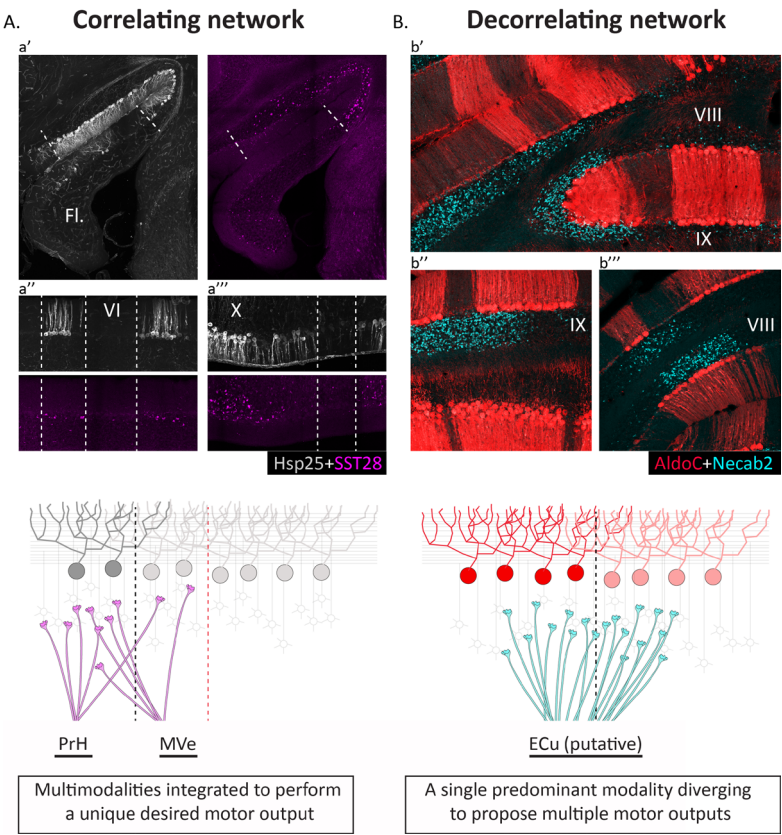

Figure 2. Theory of modular function.
SST28+ Mossy Fibers (purple) originate from multiple nuclei but converge toward clearly defined cerebellar compartments. NECAB2+ MFs (blue) supposedly originate from a single nuclei and diverge to contact several cerebellar compartments. The origin of NECAB2+ MFs was assessed by the mean of several tracing experiments. NECAB2 immunostaining following BDA or AAV injections of either Vestibular nuclei, Reticular formation, Pontine nuclei, Spinal cord, and Cerebellar nuclei did not show any colocalisation of the marker with labelled fibers. The territory of the traced spinal fibers (Clark's column) appeared to complement NECAB2+ terminals fields, characteristic of the complementation between Clark's column fibers and External Cuneate (ECu) projections. The large majority of ECu neurons appeared strongly immunoreactive for NECAB2.

2) Behaviors with a predominant sensory modality that need a wide range of possible strategies (e.g. locomotor adaptation) would solicit interlaced networks of various biophysical properties to produce decorrelated outputs offering a panel of possible motor responses (**Fig. 2B**).

From this view, it is impossible to detach gene expression from anatomical pathways. Detecting correlations between distinct but connected neuron types requires to integrate transcriptomic and morphoelectrical profiling with high resolution connectomics. Such approaches start to emerge, combining several multiplex immunolabeling protocols, clearing and expansion methods to obtain what some call "spectral connectomics" (36). However, these studies still limit the anatomical characterization to close range morphology. Whole mount brain tissue clearing would expose possible divergence in long-range projections.

Evolutionary perspectives:

Throughout evolution, emergence of paralog genes and splicing variants expanded the library of channel subunits and protein isoforms (37). These available resources allow neurons to adapt to a larger range of input modalities with little to no changes in neuron morphology or network cytoarchitecture. The comparative anatomical studies investigating the AldoC expression pattern, from fish to mammals, suggested that the molecular diversity of PCs and their parasagittal organization was acquired by the amniotes common ancestor 300 million years ago (38, 39). The expression of AldoC was indeed found homogeneously high in zebra fish and stingray cerebella. Heterogeneous expression of AldoC can still be observed in some mormyrid fish (40) and weekly-electric elephant nose fish, but all fish present a predominant AldoC+ population. This led to the theory that the most ancestral cerebellum was made of a homogeneous population of PCs which might share more characteristic with the AldoC+ PCs we know today. We have emphasized through this thesis that AldoC expression depict only a fraction of cerebellar diversity. Nevertheless, as AldoC expression segregates with a panel of biophysical and molecular features, we can assume that homogeneity of AldoC implies uniformity of PC properties. In this ancestral cerebellum the available pool of proteins might not have been sufficient to adapt PC properties to new input modalities.

One could assume that other evolutionary strategies have been implemented to adapt to the increasing range of input modalities despite molecular restrictions. As example, the UBCs which are commonly associated to vestibular input are densely present in the mormyrid fish (40). One could

assume that they represent the adaptation process of a rapidly appearing vestibular sensory network during evolution. The presence of UBCs in all cerebella investigated to date suggest that the sensory modality they process cannot be operate by the standard MF-GC-PC pathway, despite the range of molecular profiles. Following the same logic, one can assume that the input of the Basal Interstitial Nucleus of the cerebellum (BIN) represent such a unique modality to the floccular cortex for which the network had to adapt its cytoarchitecture. We observed that indeed the BIN receives a singular input which do not project to the cerebellar cortex in any other ways (**Chapter 2**). Detailed studies of UBCs and BIN neurons might give precious information regarding the limits of the operative range of the MF-GC-PC pathway.

1. N. W. Gouwens, *et al.*, Integrated Morphoelectric and Transcriptomic Classification of Cortical GABAergic Cells. *Cell* (2020) https:/doi.org/10.1016/j.cell.2020.09.057.
2. D. J. Schulz, J. M. Goaillard, E. Marder, Variable channel expression in identified single and electrically coupled neurons in different animals. *Nat. Neurosci.* (2006) https:/doi.org/10.1038/nn1639.
3. M. S. Goldman, J. Golowasch, E. Marder, L. F. Abbott, Global structure, robustness, and modulation of neuronal models. *J. Neurosci.* (2001) https:/doi.org/10.1523/jneurosci.21-14-05229.2001.
4. E. Marder, A. A. Prinz, Current compensation in neuronal homeostasis. *Neuron* (2003) https:/doi.org/10.1016/S0896-6273(02)01173-X.
5. R. J. Greenspan, The flexible genome. *Nat. Rev. Genet.* (2001) https:/doi.org/10.1038/35072018.
6. H. Zhou, *et al.*, Cerebellar modules operate at different frequencies. *Elife* (2014) https:/doi.org/10.7554/eLife.02536.
7. J. Xiao, *et al.*, Systematic regional variations in Purkinje cell spiking patterns. *PLoS One* (2014) https:/doi.org/10.1371/journal.pone.0105633.
8. E. M. Perkins, *et al.*, Loss of cerebellar glutamate transporters EAAT4 and GLAST differentially affects the spontaneous firing pattern and survival of Purkinje cells. *Hum. Mol. Genet.* (2018) https:/doi.org/10.1093/hmg/ddy169.
9. H. Fujita, *et al.*, Detailed expression pattern of Aldolase C (Aldoc) in the cerebellum, retina and other areas of the CNS studied in Aldoc-Venus knock-in mice. *PLoS One* (2014) https:/doi.org/10.1371/journal.pone.0086679.
10. M. Metz, M. Gassmann, B. Fakler, N. Schaeren-Wiemers, B. Bettler, Distribution of the auxiliary GABAB receptor subunits KCTD8, 12, 12b, and 16 in the mouse brain. *J. Comp. Neurol.* (2011) https:/doi.org/10.1002/cne.22610.
11. F. Scala, *et al.*, Phenotypic variation within and across transcriptomic cell types in mouse motor cortex. *bioRxiv* (2020) https:/doi.org/10.1101/2020.02.03.929158.
12. A. B. Muñoz-Manchado, *et al.*, Diversity of Interneurons in the Dorsal Striatum Revealed by Single-Cell RNA Sequencing and PatchSeq. *Cell Rep.* (2018) https:/doi.org/10.1016/j.celrep.2018.07.053.
13. K. D. Harris, *et al.*, Classes and continua of hippocampal CA1 inhibitory neurons revealed by single-cell transcriptomics. *PLoS Biol.* (2018) https:/doi.org/10.1371/journal.pbio.2006387.
14. H. Zeng, J. R. Sanes, Neuronal cell-type classification: Challenges, opportunities and the path forward. *Nat. Rev. Neurosci.* (2017) https:/doi.org/10.1038/nrn.2017.85.
15. A. Demilly, S. L. Reeber, S. A. Gebre, R. V. Sillitoe, Neurofilament heavy chain expression reveals a unique parasagittal stripe topography in the mouse cerebellum. *Cerebellum* (2011) https:/doi.org/10.1007/s12311-010-0156-y.
16. W. W. Seeley, R. K. Crawford, J. Zhou, B. L. Miller, M. D. Greicius, Neurodegenerative Diseases Target Large-Scale Human Brain Networks. *Neuron* (2009) https:/doi.org/10.1016/j.neuron.2009.03.024.
17. S. Saxena, P. Caroni, Selective Neuronal Vulnerability in Neurodegenerative Diseases: From Stressor Thresholds to Degeneration. *Neuron* (2011) https:/doi.org/10.1016/j.neuron.2011.06.031.
18. J. R. Sarna, R. Hawkes, Patterned Purkinje cell death in the cerebellum. *Prog. Neurobiol.* (2003) https:/doi.org/10.1016/S0301-0082(03)00114-X.
19. U. Grüsser-Cornehls, J. Bäurle, Mutant mice as a model for cerebellar ataxia. *Prog. Neurobiol.* (2001) https:/doi.org/10.1016/S0301-0082(00)00024-1.
20. M. Blosa, *et al.*, Reorganization of synaptic connections and perineuronal nets in the deep cerebellar nuclei of purkinje cell degeneration mutant mice. *Neural Plast.* (2016) https:/doi.org/10.1155/2016/2828536.
21. H. B. Clark, *et al.*, Purkinje cell expression of a mutant allele of SCA1 in transgenic mice leads to disparate effects on motor behaviors, followed by a progressive cerebellar dysfunction and histological alterations. *J. Neurosci.* (1997) https:/doi.org/10.1523/jneurosci.17-19-07385.1997.
22. J. Matsuda, A. Yoneshige, K. Suzuki, The function of sphingolipids in the nervous system: lessons learnt from mouse models of specific sphingolipid activator protein deficiencies. *J. Neurochem.* (2007) https:/doi.org/10.1111/j.1471-4159.2007.04709.x.
23. N. Terada, *et al.*, Compartment of the Mouse Cerebellar Cortex by Sphingosine Kinase. *J. Comp. Neurol.* (2004) https:/doi.org/10.1002/cne.11002.
24. S. Furuya, J. Mitoma, A. Makino, Y. Hirabayashi, Ceramide and Its Interconvertible Metabolite Sphingosine Function as Indispensable Lipid Factors Involved in Survival and Dendritic

Differentiation of Cerebellar Purkinje Cells. *J. Neurochem.* (2002) https:/doi.org/10.1046/j.1471-4159.1998.71010366.x.

25. K. Wang, *et al.*, Alkaline Ceramidase 3 Deficiency Results in Purkinje Cell Degeneration and Cerebellar Ataxia Due to Dyshomeostasis of Sphingolipids in the Brain. *PLoS Genet.* (2015) https:/doi.org/10.1371/journal.pgen.1005591.

26. S. Rashad, *et al.*, Intracellular S1P Levels Dictate Fate of Different Regions of the Hippocampus following Transient Global Cerebral Ischemia. *Neuroscience* (2018) https:/doi.org/10.1016/j.neuroscience.2018.05.015.

27. S. Zheng, *et al.*, Sphingosine kinase 1 mediates neuroinflammation following cerebral ischemia. *Exp. Neurol.* (2015) https:/doi.org/10.1016/j.expneurol.2015.03.012.

28. N. Hagen, *et al.*, Subcellular origin of sphingosine 1-phosphate is essential for its toxic effect in lyase-deficient neurons. *J. Biol. Chem.* (2009) https:/doi.org/10.1074/jbc.M807336200.

29. S. Rodriques, *et al.*, Slide-seq: A Scalable Technology for Measuring Genome-Wide Expression at High Spatial Resolution. *Slide-seq A Scalable Technol. Meas. Genome-Wide Expr. High Spat. Resolut.* (2019) https:/doi.org/10.1101/563395.

30. A. Dulneva, *et al.*, The mutant Moonwalker TRPC3 channel links calcium signaling to lipid metabolism in the developing cerebellum. *Hum. Mol. Genet.* (2015) https:/doi.org/10.1093/hmg/ddv150.

31. K. Padmanabhan, N. N. Urban, Intrinsic biophysical diversity decorrelates neuronal firing while increasing information content. *Nat. Neurosci.* (2010) https:/doi.org/10.1038/nn.2630.

32. A. A. Prinz, D. Bucher, E. Marder, Similar network activity from disparate circuit parameters. *Nat. Neurosci.* (2004) https:/doi.org/10.1038/nn1352.

33. J. J. White, *et al.*, Cerebellar zonal patterning relies on purkinje cell neurotransmission. *J. Neurosci.* (2014) https:/doi.org/10.1523/JNEUROSCI.0122-14.2014.

34. N. Leclerc, C. Gravel, R. Hawkes, Development of parasagittal zonation in the rat cerebellar cortex: MabQ113 antigenic bands are created postnatally by the suppression of antigen expression in a subset of Purkinje cells. *J. Comp. Neurol.* (1988) https:/doi.org/10.1002/cne.902730310.

35. F. P. Chabrol, A. Arenz, M. T. Wiechert, T. W. Margrie, D. A. Digregorio, Synaptic diversity enables temporal coding of coincident multisensory inputs in single neurons. *Nat. Neurosci.* (2015) https:/doi.org/10.1038/nn.3974.

36. F. Y. Shen, *et al.*, Light microscopy based approach for mapping connectivity with molecular specificity. *Nat. Commun.* (2020) https:/doi.org/10.1038/s41467-020-18422-8.

37. A. L. Goldin, Evolution of voltage-gated Na+ channels. *J. Exp. Biol.* (2002).

38. R. L. Puzdrowski, Anti-Zebrin II Immunopositivity in the Cerebellum and Octavolateral Nuclei in Two Species of Stingrays. *Brain. Behav. Evol.* (1997) https:/doi.org/10.1159/000113346.

39. C. Gutiérrez-Ibáñez, *et al.*, Zebrin Expression in the Cerebellum of Two Crocodilian Species. *Brain. Behav. Evol.* (2020) https:/doi.org/10.1159/000505897.

40. J. Meek, T. G. M. Hafmans, L. Maler, R. Hawkes, Distribution of zebrin II in the gigantocerebellum of the mormyrid fish Gnathonemus petersii compared with other teleosts. *J. Comp. Neurol.* (1992) https:/doi.org/10.1002/cne.903160103.

7

Appendix

Summary

Neurons exist in many sizes, shapes and colors. This diversity has profound implications in regards to brain functions and pathologies. The works compiled in this thesis aim to expand our conception of neuronal diversity. Along the chapters we address the subtle cellular or network specificities that shape the cerebellum.

A substantial number of neuronal types remain poorly characterized until today. Far from the commonly studied pathways , they can define discrete circuitries hidden within the principal anatomical routes. We showed in chapter 2 that the so far neglected Basal Interstitial Nucleus of the cerebellum (BIN) projects massively to a restricted region of the cerebellar cortex and receives an input modality never identified before. The BIN traces a unique neuronal pathway to the cerebellum, highly conserved among mammals, with potential major implication in the oculomotor control.

Novel single cell sequencing tools revealed a vast range of heterogeneity within neuronal types. Continuums of transcriptomic variability among neurons with similar morphology define several neuronal subtypes. The relevance of such diversity remains unknown at the cellular, network and behavioral level. The Purkinje cell (PC) population, the principal neurons of the cerebellum, can be divided in subtypes which appear to have different sensitivities to pathological insult s. In chapter 3.1 we investigated the impact of such selective neurodegeneration on cerebellar functions. We showed that preserved PCs maintain a proper execution of their behavioral output. Concluding that some neuronal pathways are deeply compartmentalized and degeneration of neighboring regions does not impact their functions. The molecular mechanisms behind the selective vulnerability of neuron subtypes remain largely unknown. In chapter 3.2, we analyzed the metabolism of sphingolipids, complex lipids involved in cell apoptosis, in a mouse model presenting selective neurodegeneration of PC subtypes. We found that sphingolipids accumulate in the cerebellar region primarily affected by the neurodegeneration. Disrupting the sphingolipid metabolism via genetic mutation resulted in a neuroprotective effect on PCs. Thus, our data indicate that sphingolipid metabolism varies between neuronal subtypes and is determinant in the predisposition to neurodegeneration.

Variations in gene expression between subtypes reflect major differences in neuron intrinsic properties. We demonstrated in chapter 4 that subtle nuances in Aldolase C protein expression profile among PC

population correlates with variations in electrophysiological properties. The newly defined subtypes contrast essentially by their respecting projections to the vestibular formation that draw different compartmentalized networks. The identification of the molecular processes responsible for the unique biophysical properties of a neuron subtype can be challenging. Often, the differences of electrophysiological signatures observed between subtypes are the result of several current compensations and involve a large range of ionchannels and protein interactions. In chapter 5 we identified one of the key elements behind the unique electrophysiological properties of a PC subtype. We showed that the Transient Receptor Potential Cation Channel Subfamily C Member 3 (TRPC3) mediated current is a major contributor to the specific high firing frequency of so-called Aldolase C-negative PC subtype. We demonstrated that the expression profile of TRPC3 in the cerebellum supports these conclusions as the protein appeared to be differential expressed between PC subtypes.

The attributes of a neuron are not necessarily genetically encoded. Profound morpho-electric rearrangement may occur in response to a change in the activity state of the network. In chapter 6 we explored a transient morphological feature of PC's axon. These "swellings" impact the fidelity of propagation of the action potential. With this work it becomes evident that our conception of neuronal subtypes needs to take account for such state-relative variables.

Samenvatting

Neuronen bestaan in een groot aantal maten, vormen en kleuren. Deze diversiteit heft grote gevolgen voor hersenfuncties en hersenaandoeningen. Met het werk in deze thesis beoog ik om de huidige ideeën over neuronale diversiteit uit te breiden. Door de hoofdstukken heen bespreken we de subtiele cellulaire en netwerk-eigenschappen die het cerebellum vormen.

Een groot aantal neuronale subtypes zijn tot op heden beperkt gekarakteriseerd, terwijl ze de mogelijkheid hebben om verborgen circuits in de reeds bekende anatomische routes aan het licht te brengen. In Hoofdstuk 2 bespreken wij dat de tot nu toe weinig belichtte Basal Interstitial Nucleus (BIN) van het cerebellum een groot aantal projecties heeft naar een zeer beperkte regio van de cerebellaire cortex, alsook input ontvangt van een tot dusver niet gedefinieerde modaliteit. De BIN omvat een unieke neuronale verbinding met het cerebellum, zeer goed geconserveerd in zoogdieren, met mogelijk grote consequenties voor hoe wij denken over oculomotore aansturing.

Nieuwe single cell sequencing technieken onthullen een grote diversiteit aan neuronale types. Variabiliteit in het transcriptoom binnen neuronen met dezelfde morfologie, ontrafelen verdere onderverdelingen in neuronale subtypes. De relevantie van een dergelijke diversiteit op celullair, netwerk- en gedragsniveau is op dit moment nog onbekend. De Purkinje Cel (PC) populatie, het primaire neuron in het cerebellum, kan worden onderverdeeld in subtypes die verschillend gevoelig lijken voor pathologiën. In Hoofdstuk 3.1 onderzoeken wij de impact van een dergelijke, selectieve neurogeneratie op cerebellaire functies. We tonen aan dat onaangetaste PCs een intacte output vertonen. Hieruit concluderen wij dat de neuronale banen zeer gecompartimentaliseerd zijn en dat de degeneratie van naburige regio's geen invloed heeft op hun functies.

De moleculaire mechanismen onderliggend aan deze selectieve gevoeligheid van neuronale subtypes zijn op dit moment grotendeels nog ongekend. In Hoofdstuk 3.2 analyseren we het metabolisme van sphingolipiden - complexe lipiden met een rol in cel apoptose - in een muis model met selectieve neurodegeneratie van PC subtypes. Wij rapporteren dat sphingolipiden zich ophopen in de cerebellaire regio die primair is aangedaan bij deze neurodegeneratie. Het ingrijpen in het sphingolipide metabolisme met een genetische mutatie, had een beschermend effect op de PCs. Derhalve toont onze data aan dat sphingolipide metabolisme variabel

is in verschillende neuronale subtypes en bepalend is in de predispositie voor neurodegeneratie.

Variabele gen expressie in neuronale subtypes reflecteren de grote verschillen in intrinsieke eigenschappen van deze neuronen. In Hoofdstuk 4 tonen wij aan dat de subtiele verschillen in Aldolase C eiwitexpressie in de PC populatie correleert met variaties in elektrofysiologische eigenschappen. De nieuw gedefinieerde subtypes tonen essentiële verschillen in hun respectievelijke projecties naar de vestibulaire formatie, duidend op uniek gecompartimentaliseerde netwerken. De identificatie van de moleculaire processen die verantwoordelijk zijn voor de unieke biofysische eigenschappen van een neuronaal subtype kan erg uitdagend zijn. Vaak zijn de verschillen in elektrofysiologische eigenschappen tussen subtypes het gevolg van verschillende stroom compensaties en verschillende betrokkenheid van een range aan ionkanalen en eiwitinteracties. In Hoofdstuk 5 identificeren wij een van de kernelementen verantwoordelijk voor de ynieke elektrofysiologische eigenschappen van een PC subtype. Wij demonsteren dat de door Transient Receptor Potential Cation Channel Subfamily C Member 3 (TRPC3) gemedieerde stroom, een belangrijke factor is in de hogere vuurfrequentie van het zogenaamde Aldolase C-negatieve PC subtype. Wij tonen ook aan het expressie profiel van TRPC3 in het cerebellum deze conclusie verder ondersteunt, aangezien het eiwit verschillend tot expressie lijkt te komen tussen verschillende PC subtypes.

De eigenschappen van een neuron hoeven niet per se genetisch bepaald te zijn. Verregaande morfo-elektrische veranderingen kunnen plaatsvinden als reactie op een verandering in de activiteit-status binnen een netwerk. In Hoofdstuk 6 onderzoeken wij een transiënte, morfologische eigenschap van PC axonen. Deze 'zwellingen' hebben een impact op de propagatie van het actiepotentiaal. Door dit werk wordt duidelijk dat wij in ons idee over neuronale subtypes, ook zulke status-afhankelijke variabelen moeten meenemen.

Acknowledgements & Ema

I would need to write another book just to properly thank everyone who helped me to arrive here, but I will try to keep it short.

Chris, thank you for the environment you provide for all of us. In the past six years in the department, I never woke up thinking I was going at work. I just felt like I was going to play science with the other kids. I can only imagine that you feel the exact same way. I hope it will never change. **Martijn**, you offered me the opportunity I dreamed of since I took the path of science. Thank you for entrusting me with that. For four years, you faced the storms of my bad temper, and all the problems that it carries along, and you survived! Everyone who knows me would acknowledge that it might not have been easy for you. When I doubted that I would reach the end of my PhD, you helped me to keep calm, to not panic and to see that I would make it through.

To my committee, I hope for us to have a passionate discussion during the defense. Dear **Gerhild**, for me you embody the complex and charming world of sphingolipids that I discovered back in Sicily, in 2017. When I came later to visit you in Bonn, I could see that you are fundamentally amused by the unpredictability of this metabolism. It did not take much time to see how passionate you are about it. I hope we will have the occasion to dance again at a Sphingolipid Club meeting, as we will not be able to do it at my graduation. **Monique**, without the providential help of both you and Sandra, this project would have remained an embryo of an idea. Thank you for guiding me and Maaike in a field so novel to us. **Alanna**, I wish I could have come to visit you and Daneck in Canada and see more of this amazing work you have accomplished. I feel somehow ashamed for the little contribution I brought to our collaboration, but you gave me the opportunity to learn and be part of a fascinating discovery. Thank you for letting me join you on board. **Geeske**, I don't know if I should wish for you to become professor or not. I am certain the title would suit you perfectly, but seeing how much you love the bench work, I am not sure whether you can breathe outside a molecular lab. You showed me that only a good teacher can be a good scientist. Your eclectic approach of fundamental sciences is really used at its best when battling developmental disorders, and I am curious to see where it will bring you. **Freek**, I need to thank you for guiding me toward the nearest light sheet microscope. Now I can say that my passion for microscopy was pushed by the craziest professor of the Netherlands. **Gao**, you are as sharp as you

are caustic. The upside with someone that do not hesitate to point out your stupid ideas, is that when he spots a good one, it gives it more value.

My dear paranymphs, I am truly honored to have both of you by my side. **Sadaf**, couple years back we had this heated conversation regarding whether or not one could excel at being both a clinician and a hardcore fundamental scientist. You are the only one that could have proven me wrong! You are the most ambitious, smart and honest (future) MD-PhD I had the chance to meet. I am certain you can reach higher than anyone of us, so, do not forget to put me as co-author. I hope we will have other Christmas mysteries to add to our collection "Sadaf & François little detectives". **Aaron**, your knowledge appears to be infinite. I am constantly amazed by this deep and pure interest you have for science, by your dedication towards your students, and of course, by your climbing skills. But I will put that aside for a minute to write about your real greatness. I saw you taking the lead to defend the rights of your city and your people even thousands of kilometers away, exhausted by a fight impossible to win. You might feel that the battle is lost, but what really matters is that you were and are still standing. If you cannot find a home in Hong Kong anymore, a spirit like yours always has a place in France. Of course, your perfectly counterbalancing crazy half is also included in this. Even if **Ursula** knows she will always be the third wheel. Standing next to you the day of your wedding will remain one of the happiest moments of my life, and I cannot wait to meet baby Wong.

Dr. Dick "dingetje" Jaarsma, I had the chance to meet many devoted teachers sharing their interest for science along the way, but none as singular as you are. Looking at you and how you approach science makes me feel like I will never get bored by the surprising tricks of nature. Everyone knows I am the first to torment you, but very few understand that my sarcasm only equals the respect I have for you since the day we met. You are the only mentor I could have wished for.

Dr. Ruigrok, like two-thirds of the doctors in this country, I have learned everything I know about neuro-anatomy from you. I don't think I will ever acquire the precision you demonstrate in your work, or your encyclopedic knowledge, but at least I hope to share the little I know as much as you do.

Catarina, I think you are among the people without whom I would have never made it out alive. We share the same furious passion about... almost every debatable point. I rarely saw you backing down on your opinions,

and I even more rarely saw you being wrong about them. You may not have noticed but you made me become a better scientist on many aspects, thank you for that. **Josh**, it is sad to think that now that I am gone, absolutely no one will get your jokes. Someone needs to be here to remind you they are terrible. It is rare to meet someone with whom we are so in phase on our view of science. We have been able to constantly tackle each other's blind spots. The balance between your genuine kindness and my obnoxious behavior made us the perfect team. There are not enough people like you but luckily a new White joined our world. **Bin**, I remember my first weeks as a master student and you as a young PhD, feeling like neither of us knew what we were supposed to do. Thankfully, we helped each other to, years later, reach a point where we can both proudly hold this title. **Lisanne**, unfortunately for you I am like your boss, I am the worst to people of whom I have high expectations. But I saw you gain confidence in the last 2 years and I hope I have helped a bit in that. I will be back for your graduation party; it will be HUGE! **Maaike**, you know what we say?! You never forget your first. Only someone kind, patient and optimistic like you could survive a supervisor like me. Thanks for letting me learn by your side how to be a better teacher. **Vaishnavi**, I have pushed you so much to start your PhD only because I think you will excel at it. You are probably the smartest young student I had the chance to meet. You question every step you take, both in your work and your life, you are made for science in the core. I am very excited to see how your path will unfold. Just one advice, stop overthinking! Sometimes, taking a wrong step is necessary to go forward in science. **Amy**, you are indefatigable. You are polyvalent and have acquired more skills in your repertoire then I have, while always trying to learn new ones. If I am sometimes harsh with you it is only because I can see your potential to evolve further when pushed to your limit. The rest, I will keep it for your ceremony to come.

  Elise, the histolab has always been more than just a work place to me. With your kindness, your homemade cookies and our shared love for Queen, you made it the heart of this department. We helped each other, we argued sometimes, but more importantly, we got infuriated together when people mistreated this place. **Erika**, even from Paris I can hear your laugh echoing from the histolab. Thanks to both of you for everything you taught me.

  Patrick, **Brandon**, **Zeb**, thanks to all of you I had the chance to

experience what only few humans in the history have tried... Vomit in zero gravity! At two occasions! You offered me one of the most unique adventures of my life. Now I know that there are two things that my stomach cannot handle, abrupt changes of gravity, and the rhymes of MC PaddhyPad. It has been fun (and painful) to be your lab rat for the past years. Call me when you have built up an Iron Man suit.

Gerard, I am proud to be able to write in my curriculum that I was the bully of the eminent professor Borst.

Edwin, after Dick, you are probably the one that I have mistreated the most in the department. But you really deserved it, you are despicable! Ahahah I wanted to do a last one for the occasion. The few times we have been able to stop bashing each other for fun, I could see the great scientist you are, in addition to the caring teacher I already knew you were.

Martijn, your perspectives on brain physiology and anatomy helped me tremendously to start building up my own conception of this mysterious organ. I felt slightly less lost in my new department when I saw your name tag on a door. I was not surprised to see that you left a nice impression on everyone you have met at la Vision. And you were right, French administration is a nightmare!

Vincenzo, you made this department a home for yourself and any student joining it. I don't know the "party guy" well, but I do know the scientist in you well. You explained me a lot about the cerebellum, and I wish we could have collaborated on a combined physiology/anatomy project. You always respected my opinions even when they went against yours which made me respect your points of view even more, except regarding "le …"!

To the "Brain Awareness Week" team. Where to begin?! **Sashini**, thank you for starting this initiative. It is an exhausting but rewarding work. You helped us to remember that as academics we need to share our work and knowledge with the world. **Sander**, **Martijn**, **Marlou**, **Simo**, **Aaron**, **Carmen** it felt like an honor for a young PhD student like me to walk in your steps. **Isabella**, we suffered together to hold this flag up again and to see it cancelled after the tremendous work we all did together with **Anna**, **Maurits**, **Eva**, **Francesca**, **Roberta**, **Sadaf** and **Lucas**. I hope you will take the lead as soon as we can reopen the doors of the department. **Yarmo**, by now we know two things, you don't hold alcohol very well, and you always put others before yourself. You are a brilliant scientist, creative and eager to discover

new horizons. The only reason why you could not achieve the goal you aimed for is that you lack this part of selfishness that all of us need to make it to the end. Never try to change that, it is the best part of you.

Thanks to **Laura**, **Gerco**, **Rike**, **Hei Ling**, **Ines**, **Peter**, **Bastian**, **Laurens**, **Stephanie**, **Nikki**, **Stijn**, **Mattijs**, **Monica**, **Martina**, **Ilse**, **Diana**, **Linda**, **Guy**, **Marcel**, **Mario** and all other students, Technicians, PhDs, Postdocs, P.I.s and Professors that I might have forgotten. Sorry to not be able to list all of you, but thank you for sharing the science, the projects, the interests, the alcohol, and the fun with me.

Sara, at 5 a.m., after a long night at the confocal, there is only you who can make me go out for a cigarette. While I don't even smoke! Five years of complaining together, five years of you force feeding me amazing homemade pastries, all to come to a single conclusion, only a crazy Algerian can stand along a crazy French. So, go for it, do the best "youyou" you can. **Malik**, luckily people around us do not understand French well enough to grasp our conversations. You always reminded me of my brother, telling me to go out, party and meet people (mainly girls in your case). It felt like I was getting back a little part of myself every time we could complain together in French.

Daniel, you are probably the only person I know sharing the same musical taste as me. And the only one that disgusts me with his culinary taste… Broodje egg, curry, brie?! I still have nightmares of it. **Tim**, what a strange little Dutchy you are! Spontaneity is not something frequent in this country, I guess you took it all for you. I am ready to go on a 7h trip to Fontainebleau again whenever you want. **Wouter**, **Annemiek**, **Caroline**, **Paul**, **Deb**, **Brit**, **Emiel**, **Adriana**, **Johanna**, **Nina**, **Timo**, **Serge**, Neoliet is the only bar in the city where I want to spend my nights… and also climb sometimes. Thank you for making me love the spirit of this discipline.

Simona, first of all, shabbat shalom! You were the first sign of the Italian invasion in my life. This surge of passion, craziness, but mostly love coming from the south. I would never have thought that I would end up floating in the dead sea with the girl who was doing a patch clamp demo during my second week in the Netherlands. That is the kind of surprises that come along with you. That, and this clearly distinctive laugh! **Francesca**, you have forced me out of my bubble to make me meet all these fantastic people. Sorry, I meant all these Italian people. Luckily, we counterbalanced

by emptying bottles of French liquor. You helped me to preserve a certain sense of sanity in corona times, more than anyone else. I can always count on you when I am at the lowest, and I hope you feel that you can do the same. **Lorenzo**, my little beam of light. The biggest regret I have of these past six years is that I have not realized sooner how amazing you are. It is surprising to see how people revolve around you, like we have always been part of your family. I know a long list of people ready to do anything for you, and I felt free to put my name on that list as well. I just want to end up barbecuing in Vroesenpark with **Ele**, **Matteo**, **Marta**, **Gonofredo the romantic**, **Roberta**, **Thomas**, **Agnese**, **Carlos**, **Joana**, **Enrico**, **Georgia**, **Ema** and **Cris**. What most of them might not realize is the passionate scientist you are. It is for people like you that I wanted to be part of this community. **Livia**, at the moment I am writing, you are squatting the bed that I was supposed to squat, in an anti-squat! You really bring everything to another level. You always pop out of the blue to bring stories, parties, and pieces of Sahara, while craving as much as I do for "the Look"! **Agnese**, you are the best medication when I feel down. Who needs psychedelics when we have a crazy hyperactive and hyper-loud Agnese?! But I go easy on it because it is addictive, and can lead to deafness. **Amore**, what do you want me to say?! You are the only person that can turn a worldwide pandemic into one of the best year of my life. If only we could hang out in Almondestraat forever. Complaining about our thesis, going to the sauna, recovering from passed nights. Everything seems to flow so naturally around you. It is like we fall in the orbit of a rogue planet, take speed, before all colliding into a memorable party. That is the kind of imagery that comes in mind after you play the little chemist with my brain. I am never bored of your "projects". Even if I love to make fun of them, I love even more to be part of them. I still don't know what is so special about me to be included in your adventures, but I wish for it to never stop. **Cris**, **Elena**, you made me feel at home when I was feeling the loneliest. You both bring with you an entire universe wherever you go. When you moved in, the house became so loud! Now I cannot stand the silence anymore. You have changed me so much in a time that felt so short. I love you Chiquitas.

      Little Sun, I could not take you out of this list. Thank you for everything you are. Life with you is made of never ending surprises. We are so childish together but I still hope it will never end. More than anyone else, you know my best and my worst. Kali kuqe ka nje huqe. We are like an Albanian saying,

we are a mess but somehow, we make sense. Të dua pa fund.

My little editor in chief, **Izi**, thanks for the help in this last months and of course the Almondstraat parties at 217 with **Pietro** and his Teletubbies shows. I am ready for the graduation party and we will need a fire extinguisher.

Maman, tu dis toujours que tu n'es pas "plus bête qu'une autre". T'as fait un fils docteur en neurosciences ! Je dirais même que t'es pas mal au-dessus de la moyenne. Je sais que ce diplôme ne change pas ce que tu penses de moi, mais moi ça me permet de montrer au monde que vous avez quand même assuré. **Papa**, tu m'as montré qu'on était libre à partir du moment où l'on portait l'entière responsabilité de nos actions. J'ai l'impression d'avoir toujours vécus sans contraintes. Je sais que j'ai parfois étais un enfant un peu étrange, mais c'est juste que ça m'a pris un peu de temps pour trouver à quel univers j'appartenais. Merci pour m'avoir laissé être comme je suis. Je vois que vous vous intéressez à mon monde, que vous êtes curieux et que vous apprenez aussi. Grâce à vous, j'ai la chance d'observer et d'explorer des territoires que peu d'hommes ont vu avant moi.

Thomas, tu m'as poussé pour ma première descente d'halfpipe, poussé à mes premières soirées, mes premiers dessins, mes premiers boulots. Tu m'as ouvert la route pour tout. C'est facile de réussir quand la personne devant dégage la voie. **Vaness**, t'es l'addition parfaite a une famille tordue. Je ne sais pas comment tu fais pour nous supporter tous.

Mich, tout ce qui sort de ton imaginaire est poétique et fascinant. Après presque 15 ans, même la plus anecdotique de tes idées me surprend toujours. Je t'observe observer le monde depuis le jour où tu m'as faits m'arrêter pour regarder les étoiles. Je pourrais passer une vie à t'étudier, mais **Geneviève** ne me laissera jamais ouvrir ta boite crânienne. J'espère un jour vous convaincre qu'une étude approfondie de la si extravagante famille Michelet serait une aubaine pour la science. **Lucie**, on s'est engueulé tellement de fois que je commence à croire qu'on est de la même famille. **Jana**, merci pour l'œuvre en couverture et les moments hors du temps dans ton petit sous-marin. **Leonet**, on fait grosse soirée au Chinois pour ma soutenance, le thème de la semaine prochaine c'est « musique traditionnelle bulgare » ! **Clément**, je te promets de venir au FestiFun cette année pour célébrer ma thèse

Mr Delanys, vous m'aviez dit au cours d'une réunion parents-

professeurs une phrase sans doute toute banale pour vous : "tes résultats sont correct, mais tu pourrais faire beaucoup mieux si tu t'y mets vraiment." Allez savoir pourquoi, elle est restée bloquée dans ma tête les 15 années qui ont suivis. Mais la vraie raison qui me pousse à vous écrire quelques lignes est que c'est lors de l'un de vos cours que j'ai découvert pour la première fois la structure de l'ADN. Je n'aurai jamais imaginé que cela changerait autant le cours de ma vie. Merci pour ça. Je n'aurai jamais votre rigueur mais je vais essayer de m'y mettre vraiment.

Mme Clavé, **Mme Ducret**, **Mr Ross**, **Mr Cullin**, **Mr Thoraval**, **Mr Doignon** et toutes/tous celles/ceux que j'oublie de citer, merci de partager votre amour des sciences. De nous montrer que cela n'a rien d'un monde froid et cartésien, mais est peuplé de gens passionnés et passionnant, d'une imagination débordante, tournés vers l'observation de l'univers.

Curriculum Vitae

Professional Experiences

2021-02 to today PostDoc researcher, Department of Wavefront Engineering Microscopy, Institue De La Vision, Paris, France.
Project : "Development of 2-photon scanning micro-endoscope. for in vivo neuronal activity imaging and holographic photostimulation"

2016-08 to 2020-08 PhD Candidate, Neuroscience Department , ErasmusMC, Rotterdam, Netherlands.
Project : "Heterogeneity of the Cerebellar Cortex"

2014-09 to 2016-07 Internship at the Neurocience Department, ErasmusMC, Rotterdam, Netherlands.
Project : "The Basal Interstitial Nucleus : characterization of a novel nucleus of the cerebellum"

2014-01 to 2014-06 Internship at the Membrane Transport Biophysics Department, Institute of Physiology, Czech Academy Of Sciences, Prague, Czech Republique.
Project : "Investigation of early stages of mitochondrial ribosome assembly pathway in humans cells"

2013-04 to 2013-06 Internship at the Institute Of Biochemistry And Cellular Genetics, Bordeaux, France.
Project : "Identification of actors in the incompatibility system het-Z1/het-Z2, in Podospora anserina"

Education

2016-08 to 2020-08 PhD, Neuroscience Department, ErasmusMC, Rotterdam, Netherlands.

2014-08 to 2016-08 Master of Science: Neuroscience, Neuroscience Department, ErasmusMC, Rotterdam, Netherlands.

2012-09 to 2014-08 Master of Science: Molecular and Cellular Genetics, Bordeaux II University, Bordeaux, France.

2009-09 to 2012-09 Bachelor of Science : Biology-Animal Physiology specialty, Bordeaux II University, Bordeaux, France.

Publications

- F.G.C. Blot, W.H.J.J. Krijnen, S. Den Hoedt, C. Osório, J.J. White, M. Mulder, M. Schonewille. Sphingolipid metabolism controls cerebellar Purkinje cell predisposition for patterned degeneration. In revision Aug.2020.

- J.J. White*, L.W.J. Bosman*, F.G.C. Blot, C. Osório, B.W. Kuppens, W.H.J.J. Krijnen, C. Andriessen, D. Jaarsma, C.I. De Zeeuw, M. Schonewille. Region-specific preservation of Purkinje cell morphology and motor behavior in the ATXN1[82Q] mouse model of Spinocerebellar Ataxia 1. In revision Aug.2020.

- D. Lang-Ouellette, F.G.C. Blot, Chloe Stewart, P. de Vanssay de Blavous, C.H. Li, Carter Van Eitrem, C. Rosen, P.L. Faust, M. Schonewille, and A.J. Watt. Purkinje cell axonal swellings act homeostatically to enhance axonal spike fidelity and cerebellar function. In revision Feb.2020.

- B. Wu, F.G.C. Blot, A. Benson Wong, C. Osório, Y. Adolfs, R.J. Pasterkamp, J. Hartmann, E.B.E. Becker, H-J. Boele, C.I. De Zeeuw, M. Schonewille (2019). TRPC3 is a major contributor to functional heterogeneity of cerebellar Purkinje cells. Elife ;8:e45590. doi: 10.7554/eLife.45590.

- D. Jaarsma, F.G.C. Blot, B. Wu, S. Venkatesan, J. Voogd, D. Meijer, T.J.H. Ruigrok, Z. Gao, M. Schonewille, C.I. De Zeeuw (2018). The basal interstitial nucleus (BIN) of the cerebellum provides diffuse ascending inhibitory input to the floccular granule cell layer. J Comp Neurol. ;526(14):2231-2256